Microscopic physics of transition edge sensors

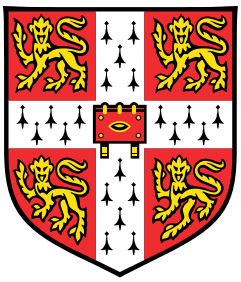

Rebecca Claire Harwin

Department of Physics
University of Cambridge

This dissertation is submitted for the degree of
Doctor of Philosophy

Jesus College

May 2020

Be thankful for problems.

Jim Lovell

Declaration

This thesis is the result of my own work and includes nothing which is the outcome of work done in collaboration except as declared in the Preface and specified in the text. It is not substantially the same as any that I have submitted, or, is being concurrently submitted for a degree or diploma or other qualification at the University of Cambridge or any other University or similar institution except as declared in the Preface and specified in the text. I further state that no substantial part of my thesis has already been submitted, or, is being concurrently submitted for any such degree, diploma or other qualification at the University of Cambridge or any other University or similar institution except as declared in the Preface and specified in the text. This dissertation contains fewer than 60,000 words including summary/abstract, tables, footnotes and appendices.

Rebecca Claire Harwin
May 2020

Acknowledgements

First and foremost, I would like to thank my supervisor Stafford Withington, who has helped me grow as a scientist throughout my PhD. Despite his many commitments, he has always had the time to teach and guide me, and I am particularly grateful for his help demystifying circuit analysis. His careful proof-reading of this thesis has been much appreciated. My research on superconducting detectors started with David Goldie, who introduced me to the world of bilayer physics. I would like to thank him for all of his help with my experimental and theoretical work throughout the years. I am also very grateful to him for all of his guidance on figure design for my publications and my thesis.

I am very grateful to Christopher Thomas, for his ability to come up with a solution to any problem, his help in proof reading my thesis and his willingness to listen. Along with Michael Crane, he has carried out the fabrication of all of the devices for my experimental work, and I am thankful to both of them for their exceptional expertise in device processing. I would also like to thank Dorota Glowacka, who was involved in the processing of some of the previous devices that I used in my modelling work.

I am forever indebted to David Sawford and Dennis Molloy, for building the cryogenic refrigerator that made my experimental work possible and for their help in troubleshooting all of the experimental problems that I encountered. David also created the electronics and Labview software that I used in my work, and Dennis made the mechanical parts that were required. I would like to thank them both for their encouragement that 'If it was easy, someone else would have already done it!'

My thanks go also to all of my fellow research students, for their support and advice: Tejas Guruswamy, Dan Moinard, Rachel Chen, Jonah Sun, Emily Williams, Tess Skyrme, Songyuan Zhao, Ben Jacot, Andrea Muni, Vincent Lim, Bram Lap and Denis Thiem. In particular, I wish Jonah, Emily, Tess and Songyuan the very best as they complete their theses in the next few months. I have enjoyed our many trips to the Maxwell Centre for hot chocolate and research discussions!

I have been fortunate enough to be involved in several collaborations throughout my PhD, and would like to thank my collaborators at Lakeshore Cryotronics, the Spanish National Research Council (CSIC) and the Netherlands Space Agency (SRON). In particular, I would like

to thank Ian Perry, Ryan Oliver, Carlos Pobes and Pourya Khosropanah. Lakeshore Cryotronics provided me with a new Hall probe for the calibration measurements in Chapter 4, and SRON and CSIC provided me with data to test my model in Chapter 3.

I would also like to thank everyone who encouraged me to study Physics, particularly my parents William Harwin and Jill Kirby, and my Physics teacher Theresa Conlon. My parents' love and support has been invaluable throughout my PhD and I am fortunate that since both of them have completed doctoral degrees, they understand what life as a PhD student is like. I am sorry that my sisters Caroline and Katherine Harwin do not share my enthusiasm for Physics but am glad they have been able to study subjects they find more interesting!

Throughout my studies in Cambridge, I have been fortunate to be supported by a wonderful college, so my thanks go to all at Jesus College who have made my time here so enjoyable. In particular, I would like to thank Noel Rutter, Jim Bellingham and Siân Dutton, for all of the guidance and wisdom they have shared with me. My thanks go also to my wonderful friend and housemate Joanna Wolstenholme.

I would like to thank all of those I have lived with throughout my PhD studies, from my original housemates Matthew Daggitt, Elliott Bussell, Lisa McCarthy, Tom Atherton, Kim Liu and Izabela Kujawiak, to my more recent housemates Orla Woodward, Jake Moscrop, James Walpole, Raphael Henkes, Olivia Shears, Ella Monkcom and my writing-up companion Charlotte Jackson. It's been fantastic to hear about your research projects, and I wish you all the best of luck in the future.

The Ultimate community has provided me with a much-needed break from my PhD studies throughout my time in Cambridge, and I would like to thank all of those I've trained and played with over the years. In particular, I would like to thank Emily Hoyt and Laura Rogers, and wish them all the best as they complete their PhD projects.

I am especially grateful to my fiancé, Chris Lewis-Brown, for always believing in me. Choosing to do PhDs at the same time in different cities has not been easy, but I'm glad we both made it to the end! In particular, I was not expecting to complete my thesis in lockdown following the outbreak of a new virus strain, so I am very thankful that Chris' wonderful family David Brown, Ruth Lewis and Jonny Lewis-Brown have allowed us to stay with them for the last few weeks, providing us with everything we needed to finish writing our PhD theses.

Finally, I also wish to acknowledge the Engineering and Physical Sciences Research Council (EPSRC) for their financial support throughout my PhD.

Abstract

Transition Edge Sensors (TESs) are ultra-sensitive superconducting detectors having a wide range of applications, from quantum cryptography to x-ray spectroscopy. Models of TESs often employ a circuit theory approach, taking TES parameters such as the temperature and current dependent resistance as inputs, but there are few microscopic models which allow prediction of these parameters. In this thesis, I develop a microscopic model to describe TESs based on the Usadel equations, allowing predictions of resistance surfaces, critical currents and the small signal electrothermal parameters. To test my model, I calculate $I(V)$ curves for device designs used by different research groups and compare them to experimental measurements.

Using my model, I design a TES wafer for a systematic study of the effects of bilayer size and patterning on performance. To investigate the effects of magnetic field, I also design and characterise a new cryogenic magnetic field test facility to apply fields of variable direction and magnitude. I present the results of this study, showing that bilayers of around 10-20 square micrometres present a good balance between low field susceptibility and predictable behaviour. I then investigate the use of a backing plate as an on-chip shield, to reduce the field susceptibility of the TESs by attenuating the perpendicular field component. I present the models used in this design process to ensure a good shielding factor as well as a high reflection coefficient, and repeat key measurements from my systematic study to show the reduction in field achieved using this prototype on-chip shield.

TES readout typically uses Superconducting Quantum Interference Detectors (SQUIDs), placing limitations on the readout frequency. I investigate the possibility of using a High Electron Mobility Transistor (HEMT) amplifier in parallel with an inductor for readout, increasing the bandwidth and allowing higher frequency operation, and discuss how TESs might be optimised for this new readout scheme.

Through this thesis I have explored a range of microscopic physics and discussed how this understanding can be used to enhance the performance of transition edge sensors.

Table of contents

List of figures

List of tables

Chapter 1

Introduction

Transition Edge Sensors (TESs) are highly sensitive detectors that use the sharpness of the resistive-superconducting transition to detect photons [1], giving them unparalleled performance in terms of energy resolution when used as microcalorimeters or noise equivalent power when used as bolometers. They are used or are being developed for use in a variety of fundamental physics experiments, including the SAFARI spectrometer on the SPICA far infra-red space telescope [2–5], the X-ray Integral Field Unit (X-IFU) on the ATHENA x-ray satellite [6, 7], the HOLMES experiment to measure neutrino mass [8, 9] and multiple x-ray calorimeters at the National Institute of Standards and Technology [10].

Device optimisation is typically carried out empirically, requiring the processing of many batches of devices and lots of time-consuming experimental characterisation for each batch. Using microscopic physics models to test possible device designs and instrument configurations before manufacture would significantly reduce the time required for TES development and optimisation. In this thesis I will develop a series of microscopic models to describe a TES and investigate to what extent these models can be used to predict device behaviour and hence to inform sensor development.

1.1 Description of a Transition Edge Sensor

Figure 1.1 shows a TES manufactured by the Quantum Sensors Group, with the key components labelled. The device consists of a superconducting thin film, typically about 100 nm thick and here made of a Mo/Au bilayer, operated close to its transition temperature T_c. It is connected to an external bias circuit by two superconducting leads of a higher transition temperature. These leads also modify the thin film transition temperature via the superconducting proximity effect, whereby Cooper pairs diffuse from a higher T_c to a lower T_c superconductor. In Figure 1.1 the thin film is patterned with two thicker Au bars, which are thought to reduce noise

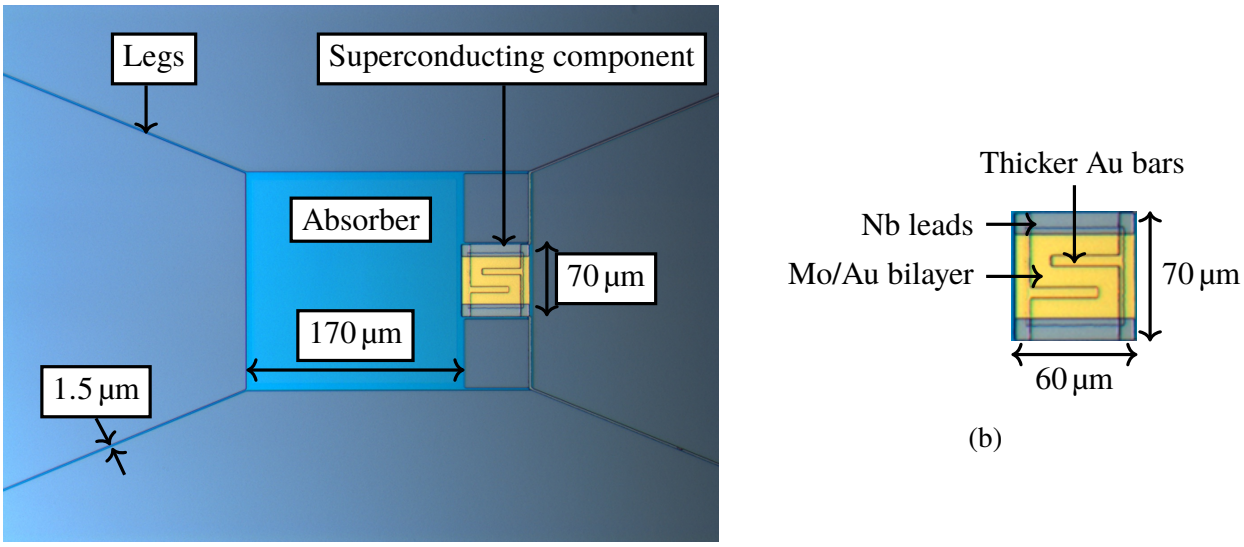

Figure 1.1 (a) Membrane-suspended Transition Edge Sensor (TES) manufactured by the Quantum Sensors Group, showing the supporting legs, the absorber and the superconducting component. This photo shows a device built for sub-mm and far infra-red detection but other devices are constructed similarly. (b) Close-up of the superconducting component of the device, indicating the superconducting leads used for bias and readout and the thin film, which for this device is a patterned Mo/Au bilayer.

[11]. An additional high resistivity beta-phase tantalum infra-red absorber is connected next to the bilayer. The superconducting component and absorber are suspended on a silicon nitride substrate by four thin legs for good thermal isolation (sometimes described as 'released'). To improve device performance, the thermal conductance between the TES and its surroundings can be adjusted by modifying the leg geometry [12, 13].

Figure 1.2 shows a model $R(T)$ curve of a thin film passing through its resistive transition. The overall TES structure has an effective T_c, the temperature where the superconducting transition occurs. This may be defined either as the temperature at which the first onset of resistance is observed, or the temperature at which the film resistance reaches a specified percentage of its normal state value R_n.

TESs can be used as either bolometers, when the response to a continuous input power is measured, or calorimeters, when the response to a pulse of energy is measured. In general, regardless of the planned application, the film size also impacts design decisions, as the transition temperature and the heat capacity of the thin film vary with size, in turn affecting the device response time. Furthermore, the length of the thin film affects the degree to which it is proximitised by the superconducting electrodes. For good spatial resolution in an imaging system, the TESs must be as tightly packed as possible to allow the focal plane to be sampled

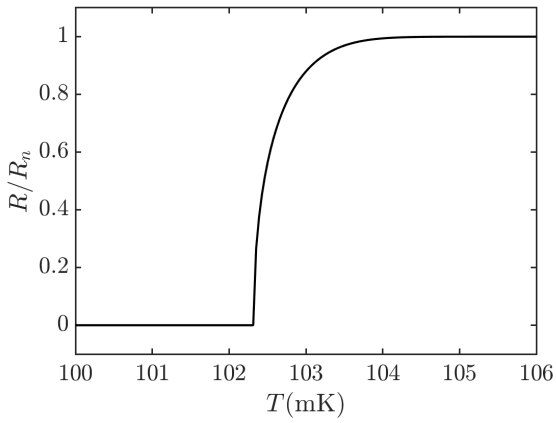

Figure 1.2 Model $R(T)$ curve for a TES thin film showing the resistive transition. The resistance is normalised to the TES normal-state resistance R_{n}.

more densely, making smaller films desirable [14]. However, for some applications where large absorbers are necessary, the absorber size will determine the maximum achievable spatial resolution.

The sharpness of the resistive transition means that devices must be carefully designed to avoid eletrothermal instability. When current-biased, positive electrothermal feedback can cause thermal runaway [15]. A TES is therefore operated under voltage bias, with the Joule power from the bias circuit used to heat the TES from the temperature of its surroundings to its superconducting transition temperature T_{c} [15]. The TES self-biases within its transition, and any increase in incident power is compensated for by electrothermal feedback, when the Joule power reduces to keep the operating temperature of the device constant [16]. The Joule power required to bias the TES is determined by the thermal conductance to the heat bath. Operating a TES under electrothermal feedback speeds up the device and reduces the noise, allowing the device to operate with extremely low limits on fundamental resolution [15]. The phonon noise defines the fundamental limit on both the noise-equivalent power of TES bolometers [17] and the energy resolution of TES calorimeters [15].

When TESs were first developed, initial readout schemes were often highly complex, as the low normal-state resistance of a TES makes it difficult to match to a field-effect transistor amplifier [18]. This problem was eliminated by the use of Superconducting Quantum Interference Devices (SQUIDs) as current amplifiers, which are easily impedance-matched to the low-resistance TESs [19]. Using SQUIDs for readout also means that the bias circuit and the readout circuit can be optimised independently of each other. It also enables multiplexed readout, which allows large detector arrays to have a manageable number of wires to room temperature [18].

Incident photons may be coupled into TESs by a thermal link from a microstrip transmission line, coupled to a small resistor on the TES substrate, or from an absorber. Microstrip transmission lines are used to couple in signals from antennae on CMB instruments [20, 21]. Multiple devices may be connected to a single antenna, to study different frequencies [22] or polarizations [23]. The filter-bank spectrometer instrument HYMAS also uses microstrip coupling to couple signals from the filter-bank to the TESs [24]. Absorbers may be mounted next to the TES, as in Figure 1.1, or above the TES, as in the X-IFU detector on ATHENA [6]. The geometry and material choice for the absorbers depend on the wavelength of interest [19].

For a thin film coupled directly to free space, there is a fundamental limit on the proportion of incident radiation that is absorbed. Optimum absorption occurs when the sheet impedance of the thin film is matched to the impedance of free space, Z_0, but even then, only 50 % of the incident photons are absorbed. By embedding the TES in a resonant cavity structure, consisting of a high reflectivity dielectric mirror behind the TES and dielectric anti-reflection coatings in front of the TES, the percentage of incident radiation that is absorbed can be increased and quantum efficiencies of 98 % can be achieved [25]. The choice of the materials in the resonant cavity structure is important, as the cavity must not affect the transition temperature of the TES, its heat capacity or its thermal coupling to the heat sink [26]. Changing any of these would affect detector performance metrics such as the maximum count rate and the system detection efficiency. Materials with extremely low heat capacities, such as Au-black coating, are therefore often used to make cavities [27].

1.1.1 Materials selection

The transition temperature T_c of the thin film should be chosen to match experimental requirements determined by bath temperature and power handling. The film may be fabricated as a bilayer such as Mo/Au [17], Mo/Cu [28], or Ti/Au [29], allowing precise control of $T_{c,S'}$ via the superconducting proximity effect within the thin film [30]. In order to optimise bilayer behaviour, additional metal layers may be added for adhesion, isolation or protection. For example, at the Argonne National Laboratory, Ti/Au/Ti/Au quadrilayers have been studied for use as the TES thin film [31]. Films may also be made from pure superconductor, such as Ti [25], or from a superconductor-normal metal alloy, such as AlMn [32]. These alloys have had T_c adjusted by tailoring the proportions of Al and Mn in the alloy and then annealing for a set amount of time - the time needed and proportions of metals in the alloy are determined by a series of calibration tests and checks. In this thesis, metals in bilayers will be written with a forwards slash between the metals, whilst metals in alloys will be written without the slash. Some experiments use two TESs in series, one with a higher transition temperature for laboratory testing and one with a lower transition temperature for observations [33].

The proximity effect within bilayer thin films will be discussed in Section 2.2.1 and a detailed description of the material combinations and device geometries used by different groups will be given in Section 3.2.

1.2 Applications of Transition Edge Sensors

As TESs can be manufactured to detect a wide range of photon energies, they have many different applications, including as optical photon counters [34], to study the cosmic microwave background [35], as x-ray and gamma ray spectrometers [36, 37] and as bolometers in infrared telescopes [38].

They are used widely for astronomical observations in ground based observatories, including the CMB experiments EBEX [39], SPTpol [40], CLASS [41], POLARBEAR-2 [42], BICEP2/Keck and SPIDER [35]. The GISMO detector for radio/IR observations [43], the SCUBA-2 camera [44], the MUSTANG bolometer camera [45] and several dark matter searches [46, 47] also utilise TESs. Additionally, TESs will be used or are proposed for use in a number of upcoming space missions such as SPICA [38] and ATHENA [7, 48]. The airborne observatory SOFIA will carry the HIRMES instrument, a TES direct detection spectrometer to study IR radiation [49]. The Micro-X sounding rocket flight in 2018 provided the first test of TES operation in space, demonstrating successful multiplexed readout with reasonable energy resolution [50].

Cameras utilising TESs can be engineered to provide photon-number-resolving capability, which has many applications in optical quantum information [51]. High performance photon-resolving detectors are required for the design of quantum optimal receivers [52] and for the monitoring of non-classical states of light, such as Fock states [53] and squeezed light, in quantum optics experiments [54, 55]. Single photon or few photon measurement techniques will also be needed for a definition of a quantum candela, a new standard unit for the intensity of light [56]. In quantum communication, TESs are being studied for quantum key distribution [57] and realisation of a quantum optical gate [58].

TESs are also used for spectral imaging [59], where differences in colour signals provide information about materials. This can be due to natural phenomena, such as stress-induced colour changes, or because certain molecules have been tagged with coloured markers. The HYMAS instrument will use superconducting on-chip filter bank spectrometers with TES readout to carry out measurements for astronomy and meteorology [24].

1.3 Advantages relative to other detectors

Although TESs are used as both calorimeters and bolometers, my research has focused more on photon counting applications. I compare TESs to other photon counting detectors to identify areas for future optimisation.

1.3.1 Detector characterisation

Photon detectors are assessed by a number of different characteristics and metrics, depending on the desired application:

- **Operating temperature**: low operating temperatures reduce thermal noise but may require expensive cooling systems.
- **Detection efficiency**: the probability of a detector generating a measurable current pulse and registering a count if a photon arrives at the detector [60], assuming that the time between photon arrivals is greater than the dead time of the detection system [61]. This may include the optical coupling efficiency to the detector, through free-space optics or optical fibres. In this case the overall detection efficiency is then the product of the coupling losses and the intrinsic detection efficiency.
- **Pulse width**: this affects the time taken after a photon is detected for the detection efficiency to return to its steady state value [62].
- **Dark count rate**: the rate of detector output pulses in the absence of any incident photons [63]. The origin of dark counts depends on the detector type, the properties of its constituent materials and the operating conditions [61], but some are always attributable to thermal excitations. In some detectors, dark counts may be triggered by detection events, a phenomenon known as afterpulsing [60]. The dark count rate is often measured with the detector completely shielded, but practically, the most useful dark count rate to measure is when the detector is embedded in an experimental setup.
- **Maximum count rate**: for calorimeters, the maximum number of particles per second that a detector can reliably distinguish.
- **Photon number resolution**: the ability of a calorimeter to distinguish the number of photons in each detected pulse [62].

Table 1.1 Selection of assessment metrics for existing photon detectors. Data taken from manufacturers where possible.

Detector	Operation temperature	Detection efficiency	Pulse width	Dark count rate	Max count rate	Resolves photon number?
PMT (visible-near IR) [64]	300 K	11 % at 500 nm	10 ns	600 Hz	5 MHz	yes
PMT (visible) [64]	300 K	15 % at 500 nm	10 ns	50 Hz	5 MHz	yes
Si SPAD [65]	250 K	35 % at 500 nm	35 ns	25 Hz	28 MHz	yes
Si SPAD [66]	300 K	78 % at 760 nm	-	125 MHz	2 GHz	no
Si SPAD (gated) [67]	300 K	50 % at 400 nm	200 ps	-	80 MHz	no
InGaAs APD [68]	230 K	32 % at 1550 nm	2 ns	5 kHz	100 MHz	yes
VLPC [69]	6 K	88 % at 694 nm	100 ns	20 kHz	-	yes
TES [25, 70]	0.1 K	98 % at 850 nm	100 ns	0.6 Hz	1 MHz	yes
TES [71]	0.1 K	95 % at 1550 nm	100 ns	-	100 kHz	yes
SNSPD [72]	2 K	90 % at 1550 nm	125 ns	10 Hz	-	yes
SNSPD [73, 74]	0.7 K	86 % at 1550 nm	60 ns	100 Hz	1 GHz	yes
QD [75]	4 K	12 % at 550 nm	150 ns	2 mHz	250 kHz	no
QDFET [76]	4 K	68 % at 805 nm	-	-	1 Hz	yes

1.3.2 Comparison of TESs to other photon detectors

Table 1.1 compares a number of detectors currently used for the detection of photons, looking at several useful performance metrics. From this table, it can be seen that TESs offer excellent detection efficiency, very low dark count rates and photon-number resolution. TES calorimeters allow energy resolution of 1.8 eV FWHM at 6 keV [77] and their increase in electrical resistance on absorption of a photon gives information about the energy of the photon [59]. TESs are also straightforward to calibrate and highly linear for small signals. Even during thermal recovery, TESs can still receive and detect photons, unique among photon counting detectors [78]. However, if multiple signals are received before the TES has returned to its bias point, the detector response becomes complicated and difficult to analyse. TESs must also be operated at cryogenic temperatures and are relatively slow, with wider pulse widths and lower maximum count rates. Recently, thermal recovery rates of less than 0.5 µs have been demonstrated [79] using Au heat sinks to improve the electron-phonon coupling in the TES whilst maintaining its weak link nature.

One main cryogenic alternative to the TES calorimeter is the superconducting nanowire single photon detector, consisting of a narrow superconducting wire current biased just below its critical current. When this nanowire absorbs a photon, a normal region or hot spot is produced, resulting in a breakdown of the superconducting state and giving a voltage spike.

Superconducting nanowire single photon detectors are faster than TESs, but their detection efficiency is very low, less than 1 % [61]. Additionally, they do not provide information about particle energy when used as photon counters. The detector can also get 'stuck' in the normal state due to self-heating of the normal region, requiring active resetting [63].

Superconducting microresonators such as Kinetic Inductance Detectors (KIDs) allow easy multiplexing of large numbers of detectors and have a faster response speed than TESs [80]. However, KIDs are difficult to manufacture for low-frequency operation, with many groups currently working to develop low-frequency KIDs [81].

Semiconductor bolometers allow higher temperature operation and and integration with conventional electronics, but are not capable of the same sensitivity as TESs and may be difficult to multiplex [19].

1.4 Design challenges

1.4.1 Microscopic modelling

Often, TESs are modelled using a circuit theory approach [18], setting up electrothermal circuits and describing the device in terms of a set of parameters that represent the sharpness of its transition, the shape of its response curve and its connection to a thermal heat sink. Typical values of these device parameters are taken as an input to the model. In this approach, the TES is either studied in the small signal limit [18] or the large signal limit [82].

The deposition of normal metal structures on the superconducting thin film can improve the device performance, reducing electrical noise [43] and altering response times [11, 40, 83, 84]. These structures are a relatively unexplored variable in optimising device performance. Many groups are now testing different arrangements of these normal metal structures, including bars, dots and stripes, to find the configuration that optimises the performance of their detectors. These normal metal features have been shown to control edge effects [85], modify the sharpness of the resistive transition [86] and reduce excess noise [11]. However, they also reduce the transition temperature [87], increase the heat capacity of the thin film and reduce the value of $\alpha = (\partial \ln R(T, I))/\partial \ln T)_I$, the sharpness of the resistive transition, [88], and so there is no widely accepted conclusion as to whether these normal metal structures improve device performance.

When designing TESs, it would be advantageous to be able to calculate expected values of TES parameters using a microscopic description of a device, accounting for the presence of normal metal structures, with easily measurable inputs such as the TES geometry, bath temperature and material composition. Models have been created to describe the thin film using

a network of resistors [89] and using a combination of supercurrents and quasiparticle currents [90]. Kozorezov et al. developed a detailed proximity effect model to describe simple thin film geometries operating close to their transition temperature, based on the diffusion of Cooper pairs from the superconducting electrodes into the thin film [91, 92]. Two dimensional models have been used to study magnetic effects [93]. None of these models account for the effects of normal metal structures.

1.4.2 Device speed

The recovery time of a detector is fundamentally limited by the thermal time constant of the detector element, typically 1 microsecond for a TES. Faster TESs can be made by using thin films with higher transition temperatures, or by modifying the thermal conductance between the TES and its surroundings, but this requires faster readout electronics [58, 60]. The transition temperature of a TES must be a tradeoff between speed and sensitivity, as a lower T_c TES has a smaller heat capacity and is more sensitive, whilst a higher T_c TES has a faster device response [26] and may also be more stable with respect to thermal cycling.

1.4.3 Magnetic field effects

TESs are magnetically sensitive devices and are therefore affected by electromagnetic interference and magnetic disturbances. As TESs have been developed for operation in a variety of different environments, they may be subjected to magnetic fields from a wide range of sources. These include electric currents, both in the surrounding wiring and in the devices themselves [94], components of the cooling system such as compressors [95] and ADRs [96], and other parts of the instrument, for example the beam deflectors in a telescope. In a large instrument, changes in configuration of the superstructure may cause variations in local field. Additionally, ground-based TESs will also be subject to the Earth's magnetic field.

It is known that square thin film structures act as weak superconducting links, exhibiting oscillatory, Fraunhofer-like behaviour of both the current and the critical current with applied magnetic field [97, 98]. These variations mean that a magnetic field will affect the onset of the normal-resistive transition, which is the basis on which the sensor operates. The small signal electrothermal parameters α and $\beta = (\partial \ln R(T, I))/\partial \ln I)_T$ also exhibit oscillatory behaviour with magnetic field, in turn affecting the signal responsivity, the noise and the predicted energy resolution [97]. Additionally, the response time of the TES oscillates with field [99], and fields can cause vortex formation in type II superconductors such as Nb [93]. Variations in magnetic field also lead to noise in the detected signals.

The choice of materials and geometry for the superconducting thin film of the TES may affect the device's sensitivity to magnetic fields, as well as its effective time constant [32, 99]. Measurements of TESs show that the magnetic field sensitivity is larger for fields normal to the detector plane than for fields parallel to the detector plane [95]. Since a SQUID is a very sensitive magnetometer, it is also important that the readout system is shielded from internal and external magnetic fields.

Magnetic shielding

In order to achieve good TES performance, the magnitude of the magnetic fields experienced by the device must be reduced during operation. TESs are therefore typically enclosed in a magnetic shield to reduce the impact of any fields on the sensors. For a given shield, the shielding factor is defined as the ratio of the internal magnetic field before the shield is installed to the internal magnetic field after the shield is installed. This factor allows the effectiveness of different magnetic shields to be quantified and compared.

There are two main types of shielding: active and passive shielding. Active shielding involves the use of coils, additional field sensors, such as Hall probes, and control circuits to measure and cancel out background magnetic fields [100]. It allows the shielding factor to be adjusted as required, to compensate for changes in field. Remote TES cameras do not typically employ active shielding as it requires power and control systems, resulting in a more complex system with a higher risk of failure.

Passive shielding uses a combination of high permeability and superconducting materials to prevent magnetic fields reaching the TESs. To minimise thermal noise, the innermost magnetic shield should be at the same temperature of the TES [95]. Typically, a superconducting shield will offer a higher shielding factor than a high-permeability shield, but the effectiveness of a superconducting shield can be compromised by external magnetic fields that become 'frozen in' during cooling. The most straightforward way to prevent this is to combine an outer shield made of high-permeability material with inner shielding made of superconducting material [32]. In some systems, recycling of the superconducting coolers may cause the temperature of any magnetic shields to rise as high as 4-6 K. If the transition temperature of any superconducting shield is lower than this, the shield will repeatedly be cooled through its transition and any trapped field will change between cooldowns, making reproducibility of measurements very difficult. Niobium is a very popular choice for a superconducting shield as its high transition temperature ensures it will remain superconducting even when the coolers are recycled.

There must be gaps in the magnetic shield, both to permit the entry of the signal of interest and the detector wiring. There may also be additional gaps required if some of the readout electronics are within the magnetic shield, to accommodate the suspension of stages at different

temperatures. All openings in a shield will reduce its effectiveness by allowing magnetic fields inside the shield. When we put a shield on a device, the shielding attenuation is calculated and measured with respect to three primary axes. For example, the shield might comprise a cylinder with a hole for the optical beam. Thus, it is enormously important to be able to predict and measure the angular dependence of an unshielded TES, since combining this with the orientation of the TES in the shield allows calculation of the angular dependence outside of the shield. This is highly applicable in developing effective magnetic shielding for TESs that will be operated in space. A detailed understanding of the field directions that a TES is most sensitive to will allow us to design shields where the openings in the shields allow through fields that will have the smallest possible impact on the TES performance.

Additionally, a baffle may be included at the opening to reduce the stray field [95]. For space-based TES instruments, it is important to keep the mass and volume of the shield as low as possible, to keep the payload small and to minimise the cooling requirements. There must therefore be a balance between effective shielding and meeting the mass budget of the spacecraft.

Although the magnetic fields from most sources can be attenuated by shielding, the fields generated by the currents in the wiring cannot be fully shielded. The wiring design should therefore aim to minimise the fields generated by currents in the wiring between the TESs and the readout electronics, for example, through use of a multiplexed readout scheme that requires fewer wires. The TESs themselves may also be modified to alter their field dependence. For example, the presence of normal metal banks on the thin film reduces the field sensitivity of the TESs [87], as does the spacing of the normal metal bars [101]. If the current in the film itself follows a meander pattern, this will generate a magnetic field [94] that cannot be compensated for by shielding, which will also affect device operation.

Radiation effects

All space-based telescopes will undergo cosmic ray impacts. These cosmic rays produce thermal drift and data glitches that must be accounted for and compensated for where possible to achieve good quality data [102]. Mitigating the effects of irradiation requires an understanding of the transfer of energy from the impact of a cosmic ray to the rest of the detector [103]. In a TES, a cosmic ray impact may produce quasiparticles (produced by Cooper pair breaking) and diffuse phonons. Possible ways to mitigate this include removing the sources of quasiparticles by reducing the number of superconducting elements and adding palladium, which suppresses low energy pulses through the membrane by absorbing diffuse phonons. GEANT-4, software that has a wide range of applications in radiation modelling, has been used to simulate the effects of cosmic ray impacts [104], but the subject is still under-developed.

1.4.4 Readout and multiplexing

TESs are typically read out using Superconducting Quantum Interference Devices (SQUIDs), with an appropriate multiplexing scheme to reduce the number of SQUIDs and the length of wiring required. Multiplexing allows large arrays of sensors to be read out with relatively small numbers of SQUIDS, reducing the instrumentation and wiring requirements at cryogenic temperatures [19]. Originally, TESs were time-division multiplexed [18], with a single SQUID switching between multiple DC-biased pixels. However, despite the simplicity of this scheme, the noise increases with the number of pixels per SQUID. Code-division multiplexing was developed as a response to this noise penalty, allowing the simplicity and DC operation of time-division multiplexing without the increased noise [19].

An alternative readout scheme is frequency-division multiplexing [105], where each TES is AC biased at a different frequency. The signals are then combined and read out by a single SQUID, and a digital frequency demultiplexer separates out the signals for the individual pixels [106]. However, readout via frequency-division multiplexing appears to degrade performance, with the AC readout producing frequency-dependent dissipative loss [107]. This has been attributed to low thin film resistance, with two different methods proposed to increase the resistance: using a thinner film and changing the aspect ratio of the thin film to make it long and narrow.

Another scheme for readout uses resonators to achieve a high multiplexing factor, inspired by the readout of Kinetic Inductance Detectors. This is known as microwave multiplexing [108] and can be achieved both with SQUID coupling and with direct readout via kinetic inductance effects [109]. Recently, multiplexing via the use of multiple absorbers coupled to a single TES has been demonstrated [110], showing excellent energy resolution for 1.5 keV x-rays.

All of these methods place different requirements on the TES parameters. For example, the bandwidth required for readout using frequency-division multiplexing is determined by the time constant [19]. The use of SQUIDs for readout places limitations on the readout frequency. If a readout scheme could be designed to allow TESs to operate at higher frequencies with wide-band readout, and at higher speeds, TESs would be used much more widely.

1.5 Outline of thesis

In this thesis, I will present a numerical microscopic model of the TES thin film based on the Usadel equations that accounts for the effects of normal metal bars as well as the film size. In the development of this model, I consider the overall 3D structure, including effects such as phase variations, due to a magnetic field B, and thickness variations. I will describe the modelling process and compare results from the model with the measured $I(V)$ characteristics

of representative devices to test its validity. Using this model to investigate proposed device designs prior to manufacture could enable the selection of TES designs with the required performance parameters for a particular application. This would avoid the time and expense associated with the fabrication and testing of a large number of prototype TESs.

I demonstrate the predictive power of my model to design a TES wafer for the systematic study of a series of TESs of varying size, with different numbers of normal metal bars. I characterise a set of devices from this wafer to determine the effects of film geometry on transition sharpness, response time, noise and transition temperature.

In addition to this, I investigate the effects of magnetic field on TES performance, which is an important input into instrument design, determining the degree of magnetic shielding required by the TESs. I develop simple models to calculate the magnetic fields produced by currents in the thin film and the surrounding wiring, as well as creating a model to predict the variation of the critical current with the direction of an applied magnetic field. I design and calibrate a new magnetic field system to extend my systematic experimental study of TESs. Using this system, I investigate the magnetic field sensitivity of different thin film geometries, including the first ever measurements of the TES directional magnetic field dependence.

Using a backing plate as an on-chip shield has enormous potential to reduce the fields experienced by a TES without the large mass requirements of a typical passive shield. I model different designs for such a shield to investigate materials choice and shield geometry, and repeat magnetic sensitivity measurements for TESs with on-chip shielding.

I develop a small signal model to investigate an alternative readout scheme using a High Electron Mobility Transistor (HEMT) in parallel with an inductor, providing higher frequency and wider band readout than existing schemes. I show how this scheme could be optimised by varying the circuit parameters and compare it with an equivalent scheme using a SQUID.

The chapter breakdown is as follows:

Chapter 2: I outline the mathematical basis for my proximity effect model, and present sample results for an idealised thin film geometry. These results are compared qualitatively with experimental observations to assess to what extent this mathematical model can be used to account for device behaviour. I then present three models for describing magnetic field phenomena, along with sample results for each model. These models describe, respectively, the directional response of a TES thin film to an applied magnetic field, the field produced by the current flow in the surrounding wiring and the self-field generated by the current flow in the thin film itself.

Chapter 3: I give an overview of device designs used by different groups, covering thin films made from elemental superconductors, bilayers and alloys. I then quantitatively compare the results of my model to experimental measurements for three sets of TESs: Ti/Au

devices from SRON, Mo/Au TESs made and tested by CSIC and Mo/Au TESs measured in a previous investigation by our group in Cambridge. I investigate any discrepancies between the measurements and the model and assess the predictive capability of my model.

Chapter 4: I describe the design process for a series of TESs to study the effects of film size and patterning. I explain the steps that were taken to ensure accurate comparisons could be made between TESs of different sizes, and present results from my model that were used to select the bilayer geometries of interest. An overview of the device fabrication process is then given, followed by the mask design procedure and details of tests carried out on the calibration structures. Following on from this, I show the design of a new TES jig to allow three-axis magnetic field measurements, and describe the characterisation of the magnetic field produced by this jig, using both a semiconductor Hall probe and a new Hall probe based on a 2D electron gas. Finally, I give a description of the overall measurement system used for the experimental study in Chapter 5, including the integration of the new TES jig.

Chapter 5: Firstly, I explain the order in which TESs were tested, before presenting the results of experimental characterisation of the TESs. I investigate the effects of bilayer geometry, showing measurements of the critical current as a function of temperature, calculations of T_c and the thermal parameters G and n, as defined in Section 2.2.2, from $I(V)$ curves, noise spectra, response time, α and β.

Chapter 6: I give details of the experiments carried out to ensure the SQUIDs were not affected significantly by the new magnetic field system, and then present measurements that show the magnetic field sensitivity of the TESs. These include critical current as a function of field and $I(V)$ curves for different field strengths, used to calculate the variation of transition temperature with field. I also present the variation of the TES current and resistance as a function of field, and determine the directional magnetic field sensitivity of the TESs. This is followed by measurements of the TES electrothermal parameters α and β for a series of fields, as well as risetime and noise measurements for different field strengths.

Chapter 7: I investigate the possibility of using an on-chip shield to reduce the perpendicular magnetic field experienced by a TES. Firstly, I present a model to predict the reduction in field that such a shield might provide, using the method of image dipoles. Next, I describe the selection of the materials to make the shield, setting up a model to calculate the reflection coefficient of the shield to compare different possible material choices. Following on from this, I detail the design and manufacture of the on-chip shield and finally present the results of experimental testing of TESs using this on-chip shield. I repeat key measurements from Chapter 6 to investigate the magnetic field sensitivity of the shielded devices, and use these to calculate shielding factors for the on-chip shield.

Chapter 8: I present the HEMT modelling work carried out to investigate the feasibility of using a HEMT in parallel with an inductor to read out a TES. Firstly, I show the development of a small signal model for HEMT readout, including simulations of the TES response for typical TES parameters. I then present an analysis of the noise sources in the HEMT readout circuit and SQUID readout circuit. This is followed by a stability analysis for the HEMT circuit. Finally I identify the key parameters for optimising the readout circuit and give details of how TESs might be optimised for readout using HEMTs and SQUIDs.

Chapter 2

Fundamental modelling of the thin film

2.1 Introduction

To achieve a microscopic model of a TES thin film that accounts for the effects of normal metal patterning, I formulate a proximity effect model based on the Usadel equations [30, 111], with suitable boundary conditions that ensure continuity of the supercurrent across the thickness discontinuities produced by normal metal structures. This model can be used to account for the variations in the superconducting phase produced by a magnetic field B as well as variations in temperature, allowing calculation of $R(T, I)$ surfaces and the electrothermal parameters α and β. The geometry of the bilayer and the material combinations used for the electrodes, the thin film and any normal metal patterning are all taken as inputs to my model. Therefore, this model can be easily adapted to describe different bilayer configurations, allowing investigation of a variety of designs before manufacture.

When carrying out experimental studies of TESs, it is beneficial to be able to compare the measurements with theoretical predictions. I develop a model to predict the variation of the critical current of the TES with the direction of an applied magnetic field, as well as two models to investigate the effects of the magnetic fields produced by current flow in the thin film and in the surrounding wiring, and will use the results of these models in later chapters.

I describe the formulation of my proximity effect model in Section 2.2, including a description of the proximity effect, the underlying equations for the model and the numerical modelling procedure used. In Section 2.3, I present results of the model for generalised devices, and qualitatively compare these predictions to observations made by other groups, to ensure the model gives a good account of TES behaviour. I will test this model in Chapter 3, to see how well it predicts the behaviour of existing bilayer geometries, and then use it to investigate possible bilayer designs and make predictions about optimal configurations in Chapter 4. Section 2.4 gives details of three models created to further investigate the magnetic field behaviour of thin

films: one model to predict the effects of magnetic field direction on the critical current, one to investigate the effects of the fields produced by the wiring and one to examine the self-field produced by the flow of current through the film itself.

Part of this work has been published in an article in the Journal of Superconductor Science and Technology, describing the theoretical basis for the model and studies of idealised TES thin films [112].

2.2 Mathematical description of proximity model

2.2.1 The Proximity Effect

Superconductivity is explained by the formation of Cooper pairs: bosons consisting of two electrons coupled by long-range electron-phonon interactions [113]. The energy of a pair of electrons coupled by phonon interactions is reduced below the Fermi energy, and so this electron pair can be considered as a bound state. The large number of Cooper pairs make it convenient to model a superconductor as a liquid. As the binding energy of a Cooper pair is relatively low, these pairs can only form for appreciable lengths of time at low temperatures. The temperature at which it is energetically favourable for a material to form Cooper pairs is the transition temperature T_c. Because a Cooper pair is a spin-1 or spin-0 boson, when large numbers of Cooper pairs are formed, many Cooper pairs can occupy the same energy state. This creates a state similar to a Bose-Einstein condensate in which all the pairs are in the ground state with a band gap between the pairs and the Fermi level. As this band gap allows the movement of electrons without scattering, there is no energy dissipation and hence no resistance when a current flows. A material in this state is said to be in a superconducting state.

When two superconductors of different transition temperatures are connected, Cooper pairs diffuse from the higher T_c superconductor into the lower T_c superconductor that may or may not be in its superconducting state, inducing or enhancing superconductivity. This phenomenon is known as the superconducting proximity effect and was first proposed by Cooper [114], in describing the change in superconducting properties at a superconductor-normal metal interface. The proximity effect can also be defined mathematically in terms of the suppression of the pair potential Δ in a superconductor at an interface with a normal metal or the induction of a non-zero pair potential at the normal side of the interface [115]. This pair potential is a measure of the pairing energy of the Cooper pair, and becomes the BCS energy gap between the Cooper pairs and quasiparticle states in a bulk superconductor whose superconducting properties are spatially uniform. It is also sometimes referred to as an order parameter [116], as it describes the phase transition of the superconductor from its superconducting state to its normal state. It

can therefore be used as a measure of the superconductivity of a system: for example in a TES, its spatial variation is linked to the spatial variations of other properties such as the supercurrent.

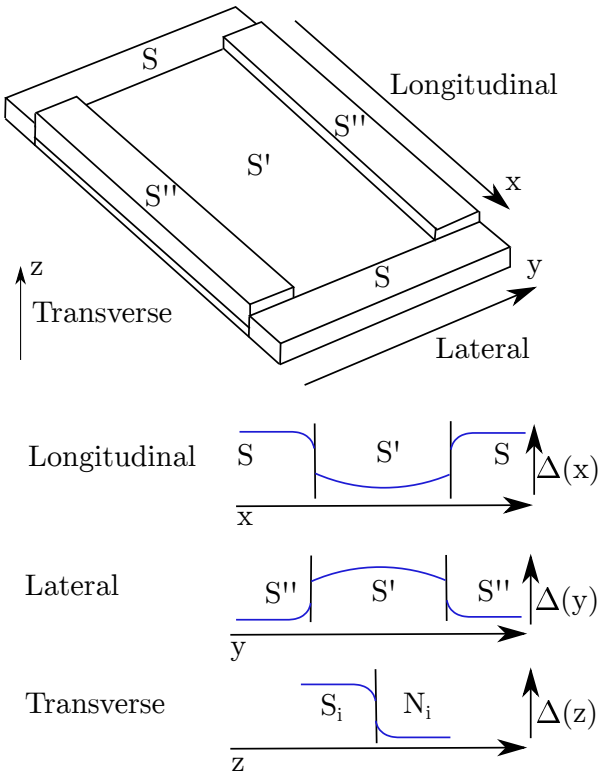

Figure 2.1 Diagram of the TES superconducting component illustrating the different descriptors used to refer to the proximity effect. The underlying physics of the effect is the same regardless of its direction. The superconducting leads are labelled S, the thin film is S' and the side stripes are S''. The regions S' and S'' are often composed of a superconductor S_i of uniform thickness and a normal metal N_i, whose thickness differs between S' and S''. The variations of the order parameter, a measure of the superconductivity, are indicated underneath the diagram as a function of position in the x, y and z directions. There is a longitudinal proximity effect acting in the x direction as Cooper pairs diffuse from the leads into the thin film; a lateral effect acting in the y direction as Cooper pairs diffuse from S' to S''; and, for a bilayer, a transverse effect acting in the z direction as Cooper pairs diffuse from the superconductor S_i to the normal metal N_i. Some aspects of the figure were inspired by Fig. 1 from [1].

Because a TES features components made from a range of superconducting materials with different transition temperatures, the superconducting proximity effect influences the behaviour of the device. It is common for the thin film to be made of two materials of different transition temperatures, and so the superconducting component of a TES can consist of a superconducting proximity structure in which the proximity effect acts in all spatial directions. This means that the superconducting properties of the thin film vary with position, which needs to be taken into consideration in the formulation of a microscopic model. A full microscopic model of this

film should therefore be a 3D proximity model, but approximations can be made to simplify this to either a 2D or a 1D model, containing all of the key physics whilst avoiding numerical complexity. Figure 2.1 shows the descriptors I use for the different directions of the proximity effect. The transverse proximity effect acts perpendicular to the plane of the film, in the z direction; the longitudinal proximity effect acts in the direction of current flow, the x direction, and the lateral proximity effect acts in the plane of the device perpendicular to the current flow, the y direction. In Figure 2.1, the superconducting leads are denoted S, the thin film region is labelled as S′ and any normal metal features are shown by S″.

Table 2.1 Resistivities, transition temperatures, coherence and correlation lengths of the materials used in the manufacture of the TESs under investigation. Data collected by the Quantum Sensors Group and from Ashcroft and Mermin [117]

Material	Resistivity, ρ_i ($10^{-8}/\Omega$ m)	Critical temperature, $T_{c,i}$/K	Coherence length, ξ_i/nm	Correlation length at 10K, ξ_i/nm
Nb	2.85	9.2	15.7	15.1
Au	2.2	N/A	N/A	46.6
Ti	43	0.39	43.1	8.5
Mo	9.2	1.1	75.3	25.0

A characteristic length scale of the proximity effect is the coherence length, given for a material i by $\xi_i^2 = \hbar D_i/2\pi k_B T_{c,i}$. Here D_i is the electron diffusion coefficient of the material and $T_{c,i}$ is its transition temperature. This coherence length gives the length scale of the Cooper pair [118], which is also the length scale over which the order parameter starts to vary and the position-dependence of the superconducting parameters needs to be taken into account. At temperatures above $T_{c,i}$, the coherence length becomes a correlation length, $\xi_i^2 = \hbar D_i/2\pi k_B T$. Table 2.1 shows typical coherence and correlation lengths, as well as resistivities and transition temperatures, for materials that are frequently used to make TES thin films. The thin film has length L and width W that are both much larger than the superconducting coherence length ξ.

Transverse proximity effect within the TES thin film

When designing a TES, it is important to have the flexibility to adjust and reproducibly control the effective $T_{c,S'}$ of the thin film to satisfy design specifications determined by power sensitivity, bath temperature and electrical impedance. One way to adjust the effective T_c is to exploit the transverse proximity effect in the S′ thin film, by making it out of a bilayer consisting of a superconducting metal layer S_i and a second metal layer M_j. This second metal layer may be a superconductor or a normal metal, and has a lower transition temperature than the S_i layer. Since the thickness of this bilayer satisfies $t \ll \xi_i$, the variation of the order parameter is small

and the bilayer may be considered as a single material of critical temperature $T_{c,S'}$ that satisfies $T_{c,M} < T_{c,S'} < T_{c,S}$. $T_{c,S'}$ of the superconducting film can be adjusted by thickening either the S_i layer or the M_j layer. The expected value of $T_{c,S'}$ can be calculated for S_i/N_i bilayers using the results of Martinis et al. [30], who use the linearised Usadel equations to predict T_c by determining the temperature at which $\Delta \rightarrow 0$. For S_i/S_j bilayers, the results of Zhao et al. [119] can be used.

The use of S_i/M_j bilayers to form the S′ thin film have other advantages. The S′ region should possess desirable characteristics such as mechanical stability, ease of deposition and patterning and resistance to environmental influences such as oxidation. Few elemental superconductors satisfy these requirements but the materials of the bilayer can be chosen to make sure it meets these specifications. Additionally, it is desirable for the thin film to have high electrical conductance to ensure good thermal conductance for rapid heat diffusion. Using a S_i/M_j bilayer means that M_j can be chosen to have high conductivity, producing a film that diffuses energy faster, uniformly and more completely. The work of Fominov and Feigel'man [120] emphasises the importance of S_i/M_j interface uniformity, suggesting that interface resistance is an important factor in determining the behaviour of the bilayer. A perfectly uniform S_i/M_j interface is not experimentally achievable, resulting in a local interface resistance that varies across the bilayer. Common metal combinations used in TES bilayers include Mo/Au, Ti/Au and Mo/Cu, and experimental measurements suggest that the different metal combinations produce thin films with different characteristics [121]. The choice of materials for the TES thin film will be discussed in more detail in Section 3.2.

Normal metal structures are often patterned on to the TES thin film as these have been shown experimentally to improve device performance [11]. Any additional normal metal structures are often formed by thickening the lower T_c material of the bilayer in selected areas, an additional advantage as this reduces the number of deposition steps involved in manufacturing. These thickened regions of the bilayer S″ can also be considered as a single material with a lower critical temperature than the S′ regions as the condition $t \ll \xi_i$ is still satisfied. Several different types of structure have been investigated, as shown in Figure 2.2, but there is no consensus as to the optimal patterning design.

Lateral and longitudinal proximity effects in the thin film

Considering the S′ and S″ regions to be uniform in the transverse (z) direction, as defined in Figure 2.1, the thin film is reduced to a 2D proximity system, with effects acting in both the longitudinal (x) and lateral (y) directions. This can be further reduced to a 1D proximity model by assuming uniform behaviour in the lateral direction. In the case where a magnetic field causes the phase to vary in the lateral direction, the thin film can be alternatively assumed to be

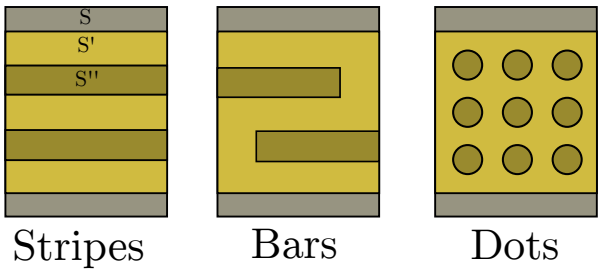

Figure 2.2 Different types of normal metal structures used to pattern the TES bilayer with the aim of reducing the device noise. The grey regions labelled S are the superconducting leads, the light golden yellow regions are the thin film S′ and the dark golden brown regions are the normal metal structures S″. Stripes (or full-length bars) are defined to cover the whole width of the thin film and bars to extend only partially across the film. These diagrams are all for thin films without side stripes.

formed of a series of independent slices, each with a different phase difference and therefore a different contribution to the overall current. In the 1D proximity model, bars, dots and stripes can all be modelled in the same way, as in one dimension all three structures are equivalent to thicker regions of the film.

A general method for describing the spatial proximity effect in materials with short electronic mean-free-paths is provided by the diffusive Usadel equations [111] with suitable boundary conditions. These equations will be presented in detail in Section 2.2.2. They have been used widely to describe S S′ S structures near T_c [116, 122–124]. The Usadel equations are a quasiclassical approximation of quantum field theoretical methods [125]. This approximation is valid for mesoscopic proximity systems, where relevant length scales such as coherence lengths and sample thicknesses are much larger than the atomic scale.

The equations employ a Green's function description of superconductivity [125], where the Green's functions in this case represent generalised densities of states. The off-diagonal elements of the matrix Green's function describe superconducting correlations and therefore vanish in a normal metal [120]. The coherence length gives the scale of variation of the Green's functions.

This Green's function description can be parameterised in different ways for different equations. For example, the Riccati parameterisation is often used in equilibrium problems for arbitrary strengths of impurity scattering as a convenient parameterisation of the more general Eilenberger equations of superconductivity [125]. The parameterisation used here for the Usadel equations is the θ-parameterisation in imaginary time [125]. In the θ parameterisation, the matrix Green's function is expressed in terms of the real functions θ and χ, where θ is the pairing angle, giving the proportions of quasiparticles and pairs; and χ is the superconducting phase [120]. The phase difference between the extremities of the superconducting leads is

labelled as ψ, assuming that the leads are wider than the superconducting overlap region so that bulk superconducting behaviour is reached within the superconducting element. The value of θ can also be used to determine the quasiparticle and pair densities of states [126].

Using these variables makes it straightforward to describe the boundary conditions at the edges of the electrodes, the external boundaries, where the behaviour is assumed to be that of a bulk superconductor. To fully specify a solution to the Usadel equations, suitable internal boundary conditions must be used, to account for the proximity effect and ensure that current is conserved between dissimilar materials and in the presence of a boundary resistance [127].

2.2.2 Numerical modelling of TES thin films

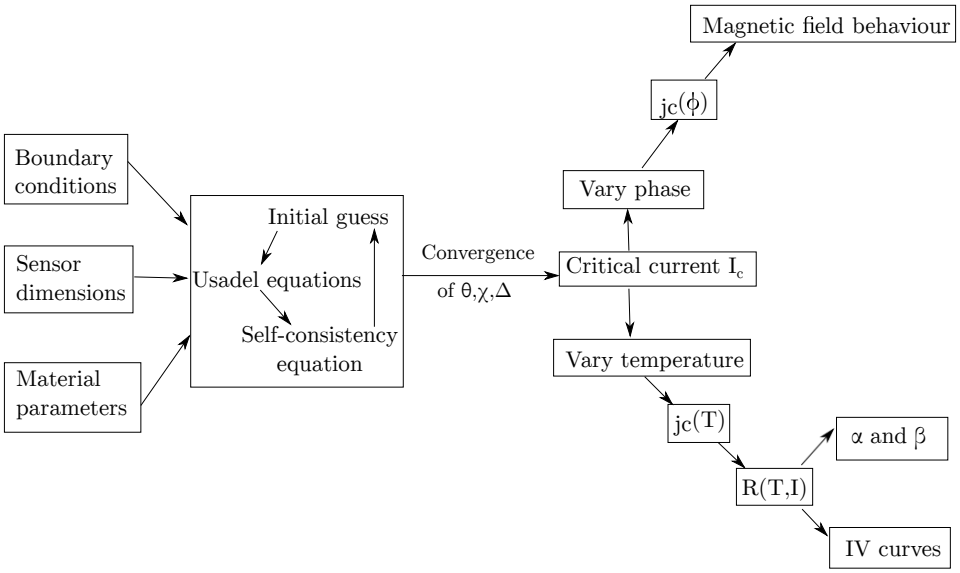

Figure 2.3 I devised this procedure to use a proximity model to predict experimental measurements. Taking the dimensions and material parameters of a particular device design and suitable boundary conditions, the Usadel equations are solved iteratively in conjunction with the self-consistency equation to determine the critical current. By varying the environmental conditions, such as T and ψ, the variation of j_c with these conditions can be investigated. From the critical current variation as a function of ψ, predictions of magnetic field behaviour can be made, whilst the variation of I_c as a function of temperature allows predictions of experimentally obtainable measurements such as $I(V)$ curves and the values of α and β.

As described in the previous section, the Usadel equations can be used to describe a system in which the superconducting proximity effect is present. I wanted to use the Usadel equations to create a model of a TES thin film that could be used to predict key device parameters, in order to use the model to test and characterise potential device designs. As well as this, the ability to predict experimental data such as $I(V)$ curves was required for verification and testing

of my model. As discussed in Section 2.2.1 and Section 2.2.1, I made simplifying assumptions to reduce the system to 1D. I devised a scheme to numerically solve the Usadel equations in order to describe and characterise devices, shown in the flowchart in Figure 2.3. This represents an advance on previous methods as it allows modelling over a range of temperatures and can account for different bilayer geometries, as well as the influence of magnetic fields. I wrote software to implement this modelling scheme, which requires three inputs: the film dimensions, the material parameters, and a set of boundary conditions. With these inputs, the software solves the Usadel equations iteratively and looks for convergence of the variables θ, χ and Δ. By varying the phase difference between the electrodes ψ and the temperature T, I used this software to predict experimentally obtainable results, such as $I(V)$ curves, providing a good test of the model.

Once the model has been tested, it is beneficial to be able to calculate parameters that can be used to characterise and compare the responses of different TES designs. For this, the small signal electrothermal parameters α and β can be used. For a TES with resistance $R(T, I)$ and bias current I, $\alpha = (\partial \ln R(T, I))/\partial \ln T)_I$ characterises the sharpness of the superconducting-normal resistive transition at constant current and determines the thermal response time. Large values of α enhance the current-to-power sensitivity of a TES operated as a bolometer and reduce its response time, whilst at the same time reducing its in-band Johnson noise. $\beta = (\partial \ln R)/(\partial \ln I)_T$ is the dynamic resistance of the sensor at constant temperature and influences the electrical response time. Large values of β increase the response time and also reduce the electrical stability of the TES when biased optimally at low bias voltage V_b.

In this chapter, I will apply my model to an idealised TES thin film and see if any of the following experimental observations can be accounted for by my model:

1. The effective T_c scales approximately as $(1/L^2)$ [1].

2. α is reduced by the addition of lower $T_{c,S''}$ bars (and likewise increased by higher-T_c bars) [84, 88].

3. α and β show oscillations when a magnetic field is applied. As the maximum of these oscillations reduces with increasing field, both parameters are maximised in the zero field case [97, 99].

4. The ratio α/β is typically in the range $10 - 200$ [16, 97, 128, 129].

5. The measured critical current as a function of magnetic flux through the film, $I_c(\Phi)$, shows a mostly Fraunhofer-like dependence, although the dependence is not exact [87, 97, 121, 130]. Some measurements on thin films with bars show a more complicated field dependence [121].

Description of thin film in terms of Usadel equations

Cuevas and Bergeret [93] solved the Usadel equations at low temperatures, $T/T_c \approx 0.01$, in two dimensions for short wires, $L/\xi = 2$, with varying widths, $0.5 \leq W/\xi \leq 50$. Kozorezov et al. [91, 131] extended the modelling to long one-dimensional superconducting structures, $L/\xi_{S'} \gg 1$, in simple S S′ S geometries at low temperatures, $T/T_{c,S} \ll 1$, and showed how to describe a thin film in the context of the resistively shunted Josephson junction (RSJ) model. I refer to this latter work as the '1D model' and extend this model to investigate the effects of normal metal patterning.

I make the following assumptions:

1. I assume that electron diffusion in the lateral, y, direction can be ignored so that electron trajectories are parallel to the x axis (see Figure 2.4). In this approximation, the effects of stripes, bars and dots become identical, as all can be modelled as thickened regions of the superconducting film.

2. In the transverse direction, z, I assume that the superconducting film is sufficiently thin (thickness $t \ll \xi_{S'',S'}$) that its properties are spatially invariant , even if the film is a proximity bilayer [30], as discussed in Section 2.2.1. I denote the composite bilayer simply as S′, S″ as required, but include the effect of thickness changes.

3. I ignore pair-breaking by the current.

4. In the lateral, y, direction I assume that the film is uniform. The problem is then reduced to the $x-$dimension.

In order to present the most general form of my model and its predictions, I initially have not assumed any particular material parameters for the bias leads, thin film or stripes. I use normalized parameters and dimensions wherever possible to emphasize the generic nature of this study.

Figure 2.4 shows the geometry that I used to set up a proximity model of a thin film, taking the example of a film with a single normal metal stripe. I assume that the supercurrent flow is entirely in the x direction, with the y direction parallel to the width of the film and the z direction perpendicular to the plane. I describe the thin film using a series of one dimensional slices, and then integrate the critical current density across these slices to obtain the overall critical current. The superconducting electrodes are shaded in blue and labelled S, the thin film is unshaded and labelled S′ and the normal metal stripe is shaded in red and labelled S″. The film has length L and width W, and each region has thickness t_i and length d_i.

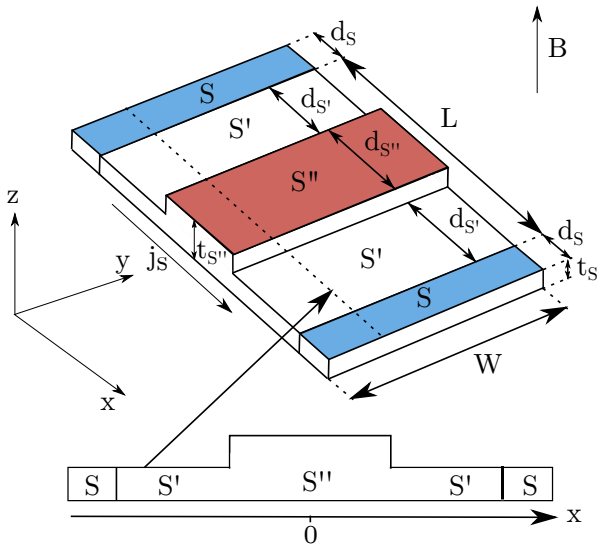

Figure 2.4 Geometry used to set up a proximity model of a TES thin film, shown here for a film with one normal metal stripe. The axes indicate the coordinate system used to describe the thin film. In order to apply the Usadel equations to the film, I assume that each region (S, S′ S″) is uniform in the z direction. I take the film to be formed of a series of independent slices, each of width δy, as indicated by the cut-through in the diagram. For each slice, I solve the Usadel equations in the x direction to find the critical current density. These densities are summed to calculate the overall critical current. I assume here that the supercurrent density j_s is entirely in the x direction. The (blue) regions labelled S are the superconducting electrodes; the unshaded regions labelled S' are the unpatterned areas of the thin film and the (red) region labelled S" is the normal metal stripe. L and W are the length and width of the film, respectively, d_i is the width of region i and t_i its thickness. I take $t_S = t_{S'}$, and so the only discontinuity in thickness is between the S′ and S″ regions. If a magnetic field is applied it is assumed to be perpendicular to the thin film as indicated.

Usadel equations, self-consistency equation and supercurrent density

In terms of the matrix Green's function $\hat{G}$, the Usadel equations can be written as [111]

$$\hbar D \frac{\partial}{\partial x}\left(\hat{G}\frac{\partial}{\partial x}\hat{G}\right) = \left[\hbar\omega\sigma_z + \hat{\Delta}, \hat{G}\right]. \tag{2.1}$$

Here σ_z is the Pauli matrix, $\hat{\Delta}$ is the matrix form of the order parameter and the square brackets denote the commutator of the two matrices. ω represents the Matsubara frequencies given by $\hbar\omega = \pi k_B T(2n+1)$ for integer n.

I follow Vasenko et al. [124], parameterizing the normal and anomalous Green's functions using the θ parameterisation from Section 2.2.1 to give $G = \cos\theta$ and $F = \sin\theta e^{i\chi}$ respectively.

With this parameterisation, the matrix Green's function $\hat{G}$ can be expressed as

$$\hat{G} = \begin{pmatrix} G & F \\ F^* & -G \end{pmatrix} = \begin{pmatrix} \cos\theta & \sin\theta\, e^{i\chi} \\ \sin\theta\, e^{-i\chi} & -\cos\theta \end{pmatrix}, \tag{2.2}$$

meaning that the normalisation condition,

$$\hat{G}^2 = I, \qquad G^2 + FF^* = 1, \tag{2.3}$$

is automatically satisfied. The matrix form of the order parameter is

$$\hat{\Delta} = \begin{pmatrix} 0 & \Delta(x) \\ \Delta^*(x) & 0 \end{pmatrix}, \tag{2.4}$$

where Δ is the spatially varying superconducting order parameter.

From this, I obtain the parameterised form of the one-dimensional Usadel equations [91, 116, 124]

$$\hbar D\left(\frac{d^2\theta}{dx^2} - \left(\frac{d\chi}{dx}\right)^2 \cos\theta\sin\theta\right) = 2\hbar\omega\sin\theta - \cos\theta(\Delta\, e^{-i\chi} + \Delta^*\, e^{i\chi}), \tag{2.5a}$$

$$\hbar D\frac{d}{dx}\left(\sin^2\theta\frac{d\chi}{dx}\right) = i(\Delta\, e^{-i\chi} - \Delta^*\, e^{i\chi})\sin\theta. \tag{2.5b}$$

The Usadel equations (2.5) make no assumptions about the relationship between the phase of Δ and the superconducting phase χ. Solving these equations for each Matsubara frequency produces a series of solutions for θ and χ, which can then be used in the summations in Equations (2.6) and (2.7).

The order parameter varies as a function of χ and θ according to the self-consistency equation

$$\Delta\ln\left(\frac{T}{T_c}\right) + 2\pi k_B T\sum_{\omega>0}\left(\frac{\Delta}{\hbar\omega} - \sin\theta\, e^{i\chi}\right) = 0, \tag{2.6}$$

and the supercurrent density is

$$j_s(x,\psi) = -\frac{2\sigma\pi k_B T}{e}\sum_{\omega>0}\sin^2\theta\frac{d\chi}{dx}. \tag{2.7}$$

Boundary conditions

The Usadel equations (2.5) and (2.6) must be solved in conjunction with suitable boundary conditions. The required boundary conditions were first devised by Zaitsev [127] for arbitrary interface transmission and these conditions were then simplified in the dirty limit for low interface transparency by Kuprianov and Lukichev [132]. The conditions ensure the conservation of current at the interfaces.

I assume bulk superconductor behaviour at the external boundaries $\pm(L/2 + d_S)$, the outer edges of the superconducting electrodes, and so here $\Delta = \Delta_{BCS}$, $\theta = \text{atan}\,(\Delta_{BCS}/\omega)$ and $\partial\chi/\partial x = 0$. I set $\chi(\pm(L/2 + d_S)) = \pm\psi/2$ [116, 124]. The boundary conditions at the S-S′ and S′-S″ internal interfaces are given in terms of the Green's functions of Equation (2.2) by [124, 132]

$$\xi_j \gamma \frac{t_j}{t_i}\left(\hat{G}_j \frac{\partial}{\partial x}\hat{G}_j\right) = \xi_i\left(\hat{G}_i \frac{\partial}{\partial x}\hat{G}_i\right), \tag{2.8}$$

and

$$2\xi_j \gamma_B\left(\hat{G}_j \frac{\partial}{\partial x}\hat{G}_j\right) = \pm[\hat{G}_i, \hat{G}_j]. \tag{2.9}$$

γ_B is a measure of the boundary resistance [132], inversely proportional to the transmission coefficient [91, 116]. $\gamma = \xi_i\rho_i/\xi_j\rho_j$ accounts for the differences in material properties at the interface and is sometimes referred to as a conductivity gradient [116]. In the direction of increasing x, the positive sign in (2.9) refers to the interface from material i to material j and the negative sign to the interface from material j to material i.

I modify the first boundary condition (2.8) compared with the condition given by Kuprianov et. al. [132] with an additional factor t_j/t_i, the ratio of the layer thicknesses. This takes into account the discontinuities in thickness between the S′ and S″ regions, ensuring conservation of supercurrent.

I solve the Usadel equations (2.5) iteratively and check for convergence of the order parameter $\Delta(x = 0)$ to better than 0.1%. This method will work for any value of ψ.

Magnetic field behaviour and R(T,I)

From the supercurrent density $j_s(x, \psi)$, I define the critical current density as $j_c(\psi) = \min_x(j_s(x, \psi))$. With zero applied magnetic field ψ is constant as a function of y, and the total critical supercurrent

$$I_c(x, \psi) = Wt(x)j_c(x, \psi) \tag{2.10}$$

follows directly by integration with respect to y.

In the presence of a magnetic field B_z, the gauge-invariant phase difference between the electrodes varies as a function of y such that [93, 98, 123]

$$\psi(y) = \frac{2\pi\Phi(y)}{\Phi_0} + \psi_0, \tag{2.11}$$

where $\Phi_0 = h/2e$ is the magnetic flux quantum and the flux $\Phi(y) = B_z y(L + 2\lambda_L)$, with λ_L the penetration depth in S.

From this, I can find the total critical current

$$I_c(\Phi) = t \int_{y=-L/2}^{y=L/2} j_c(\psi(y))\,\mathrm{d}y. \tag{2.12}$$

It is only necessary to calculate $j_c(\psi)$ for $\psi \in (0, \pi)$, due to the properties of the current-phase relation [116]. This analysis assumes a relatively weak magnetic field, and so the order parameter Δ is not altered by the field.

By varying the temperature T at which I solve the Usadel equations, I can find the variation of I_c with T. From this, I model the overall thin film resistance using a resistively shunted Josephson junction (RSJ) model [131, 133], which is a circuit theoretic description of a TES in terms of a Josephson junction and resistor in parallel. Although here I am developing a microscopic model, this description is appropriate as it accounts for the energy flow in a system with the same boundary conditions, allowing the calculation of the resistance of the system in equilibrium. Previous applications of the $R(T, I)$ model to TESs use a simple model for I_c [97], and so this represents the first use of the RSJ model with a detailed microscopic calculation of I_c. From the RSJ model, the resistance is given by

$$R(T, I) = R_n \left\{ 1 + \frac{1}{\kappa} \mathrm{Im} \left[\frac{\mathcal{I}_{1+i\zeta\kappa}(\zeta)}{\mathcal{I}_{i\zeta\kappa}(\zeta)} \right] \right\}, \tag{2.13}$$

where $\zeta = \hbar I_c/2eT$ describes the effect of thermal fluctuations, and $\mathcal{I}_\mu(\nu)$ are modified Bessel functions of the first kind of complex order μ and real variable ν. The ratio of current to critical current is $\kappa = I/I_{c,T}$. The Bessel functions are calculated using a continued fraction method [134]. For these calculations, in the zero-magnetic field case I use the value of $\psi = \psi_0$ that maximizes I_s. From $R(T, I)$, $I(V)$ curves and the electrothermal parameters α and β can be calculated.

Calculation of IV curves

I need to be able to use my model to predict experimental measurements such as $I(V)$ curves, to test whether it is sufficiently predictive to be used in device characterisation. The two equations

that determine the $I(V)$ behaviour of a TES are

$$V = IR(T, I) \tag{2.14a}$$

$$P = \frac{V^2}{R(T, I)} = K(T^n - T_{\mathrm{b}}^n) \tag{2.14b}$$

The second equation here comes from the requirement that the heat dissipated in the TES, V^2/R must be equal to the power flow P to a thermal sink at temperature T_b. This power flow depends on the temperature difference between the TES and the thermal sink, as well as the thermal exponent n and the constant of proportionality K, which may be obtained from a fit to experimental data. The value of n is determined by the mechanism of heat transport between the TES and the thermal sink [135, 136]. For the TESs made by our group, typically $n \approx 2$ [137], indicative of the diffusive heat transfer that takes place in longer legs. In TESs with shorter legs, the heat transfer along the legs is ballistic and the corresponding values of n are higher [13]. The power flow is often characterised by the thermal conductance G, which when the device is at its transition temperature, is given by

$$G = \frac{\mathrm{d}P}{\mathrm{d}T} = nKT_{\mathrm{c}}^{n-1}. \tag{2.15}$$

As the analytical form of R(T,I) includes Bessel functions, I solve Equations (2.14) using the following numerical procedure:

1. Calculate $V - IR(T, I)$ and $V^2 - R(T, I)K(T^n - T_b^n)$. As this is a numerical procedure, $R(T, I)$ is represented by a matrix calculated using Equation (2.13).

2. Find the zero intercepts in the $I - T$ plane of each equation from the previous step as a function of I and T, defining two curves. One equation is satisfied on each curve.

3. Find the intersection of these lines, which will be the point at which Equations (2.14) are simultaneously satisfied.

4. Record the I and T values of this point and repeat for a series of voltages.

I repeated this procedure for each bath temperature to obtain a series of $I(V)$ curves.

2.3 Model results

I applied this proximity effect model to calculate $I_{\mathrm{c}}(T)$ and $I_{\mathrm{c}}(\psi)$ for a set of generalised thin films, in order to test the qualitative predictions of the model. For my generalised films, I

assumed that $T_{c,S'}/T_{c,S} = 0.01$ and $T_{c,S''}/T_{c,S} = 0.005$. I took $\gamma_{(S,S')} = 0.1$, $\gamma_{B(S,S')} = 1$ to describe S-S′ interfaces, and $\gamma_{(S',S'')} = 1$, $\gamma_{B(S',S'')} = 0$ to describe any S′-S″ interfaces. Where additional S″ features were included, I denoted their number by N and I assumed that they were uniformly positioned with respect to the centre of the TES film.

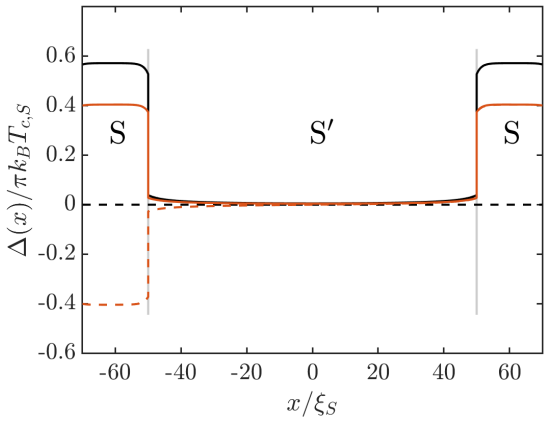

Figure 2.5 Real (solid line) and imaginary (dashed line) components of $\Delta(x)$ across a unpatterned TES thin film with $L/\xi_S = 100, T/T_{c,S} = 0.02$. The phase difference $\psi = 0$ for the black lines and $\psi = \pi/2$ for the red lines. The units used are dimensionless: Δ is normalised by a factor of $\pi k_B T_{c,S}$ and x by a factor of ξ_S.

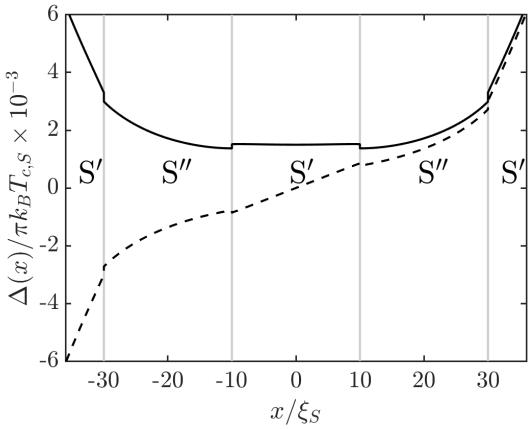

Figure 2.6 Real (solid line) and imaginary (dashed line) components of $\Delta(x)$ in the central region of a thin film with $N = 2, \psi = \pi/2, T/T_{c,S} = 0.02$.

Here I present representative results of the modelling. Figure 2.5 shows the variation of the superconducting order parameter Δ with position for a thin film with $L/\xi_S = 100$, $N = 0$. The phase differences of 0 and $\pi/2$ were chosen for comparison to the earlier calculations of Kozorezov et al. and show good qualitative agreement with their published results [91].

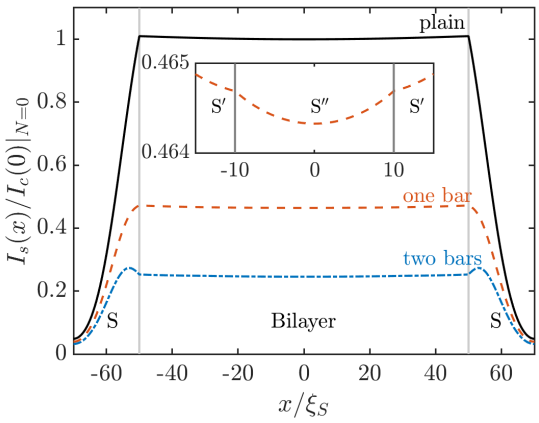

Figure 2.7 Supercurrent I_s for TES thin films with $N = 0$ (solid line), 1 (dashed line) and 2 (dot-dashed line). Inset is a magnification of the central region of the plot for $N = 1$ to illustrate the effects of the lower-T_c S″ structure. The phase difference of $\psi = \pi/2$ means that the supercurrent is close to its maximum value; and $T/T_{c,S} = 0.02$. I_s is normalized to I_c in a thin film with $N = 0$ and no magnetic flux ($I_c(0)|_{N=0}$)

Although the temperature used here, $T/T_{c,S} = 0.02$, is above the superconducting transition temperature of S′, there is still a non-zero order parameter throughout the length of the film due to the long-range proximity effect. Figure 2.6 shows the effect on the order parameter of adding two S″ sections each of length $d_{S''}/\xi_S = 20$. The magnitudes of both the real and imaginary components of the order parameter are reduced inside these stripes.

Figure 2.7 shows how the supercurrent I_s varies with position in thin films with $N = 0, 1, 2$ stripes of length $d_{S''}/\xi_S = 20$ and fixed overall length $L/\xi_S = 100$. $I_s(x)$ is normalized by the critical current for a unpatterned film with zero applied field $I_c(0)|_{N=0}$. As N is increased, both the overall supercurrent and hence the critical current are reduced. The inset shows the slight reduction of the supercurrent magnitude within the metal stripes themselves. However, consistent with my modified boundary conditions at the S-S′ and S′-S″ interfaces (2.8), the current I_s is continuous. At the far edges of S, $I_s \to 0$ as required by the boundary conditions.

Figure 2.8a shows the $R(T, I)$ surface calculated from the above model as a function of normalised temperature $T/T_{c,S}$ and normalised current I/I_{c0}. I_{c0} is the critical current in the film for $T/T_{c,S} = 0.05$. The TES thin film has $N = 0, L/\xi_S = 100$. The effective superconducting transition occurs at $T/T_{c,S} \simeq 0.12$ dependent on current. This is considerably higher than the intrinsic transition temperature of the thin film, $T_{c,S'}/T_{c,S} = 0.01$, due to the proximity effect of the electrodes, the film geometry and the choice of boundary conditions. The film length chosen is relatively small and the value of γ_B relatively low - increasing both the length and the value of γ_B would reduce the transition temperature. Figure 2.8b shows the calculated $R(T, I)$ surface for a thin film with $L/\xi_S = 100$ and $N = 2$. Both lower-T_c stripes have length

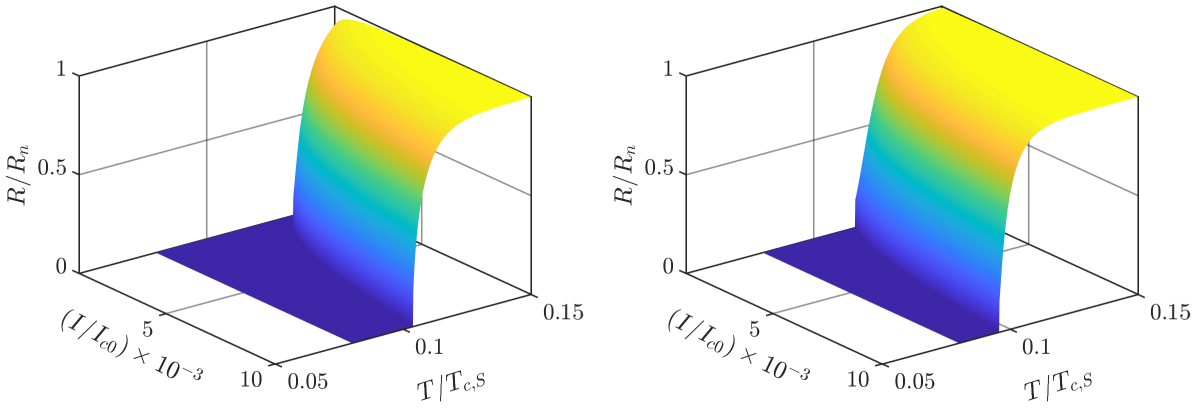

(a) $N = 0$. (b) $N = 2$.

Figure 2.8 $R(T, I)$ surfaces for two thin films with different numbers of bars, both with $\psi = \pi/2$. The temperature is normalised to $T_{c,S}$, the transition temperature of the superconducting leads; the current to I_{c0}, the critical current in the film for $T/T_{c,S} = 0.05$; and the resistance to R_n, the normal state film resistance.

$d_{S''}/\xi_S = 20$. A reduction in the effective T_c relative to Figure 2.8a is immediately evident. There is also a suggestion that the $R(T, I)$ surface becomes less steep. This represents the first calculation of a $R(T, I)$ surface directly from the microscopic physics properties of a TES.

The effect on $\alpha(T, I)$ and $\beta(T, I)$ for the same geometries is shown in Figure 2.9. Figure 2.9a shows the logarithmic resistance-temperature sensitivity $\alpha(T, I)$ with $N = 0$ and phase difference $\psi = \pi/2$. Figure 2.9c shows $\beta(T, I)$ for the same parameters. These can be compared with Figures 2.9b and 2.9d, which show the same surfaces for a TES thin film with $N = 2$. A reduction in both α and β caused by the stripes is evident and the ratio $\alpha/\beta \approx 10$, agreeing with experimental measurements [83, 97, 128]. This shows that the predictions of this model successfully describe experimental results found in the literature, allowing me to use this model to make predictions of device behaviour.

Having demonstrated the predictive ability of my model, I use it to further explore trends in α and β, as shown in Figure 2.10. The left panel shows the effects on $\alpha(T)|_I$ of increasing the number of stripes and the magnetic flux for a fixed film length and operating current. In (a) $N = 0, \Phi/\Phi_0 = 0$; (b) $N = 1, \Phi/\Phi_0 = 0$; (c) $N = 2, \Phi/\Phi_0 = 0$; (d) $N = 2, \Phi/\Phi_0 = \pi/2$. The right panel shows the effect on $\alpha(T)|_I$ of lengthening the thin film for films with $\Phi = 0, N = 2, I/I_{c,0} = 0.1$: (e) $L/\xi_S = 100$ (f) $L/\xi_S = 150$; and (g) $L/\xi_S = 200$. Comparison of curves (a) to (c) shows how, as observed experimentally [19, 88], α and hence β are reduced as N increases. Comparison of curves (c) and (d) shows the reduction of α and hence β by an applied field. Comparison of curves (e) to (g) shows the effect of increasing the TES film length with fixed N. The effective T_c is reduced by increasing either N or L and

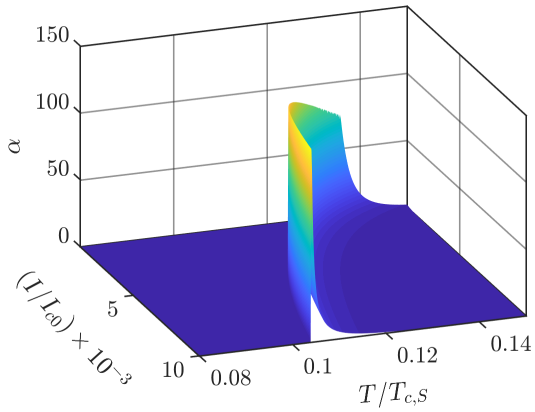

(a) $N = 0$.

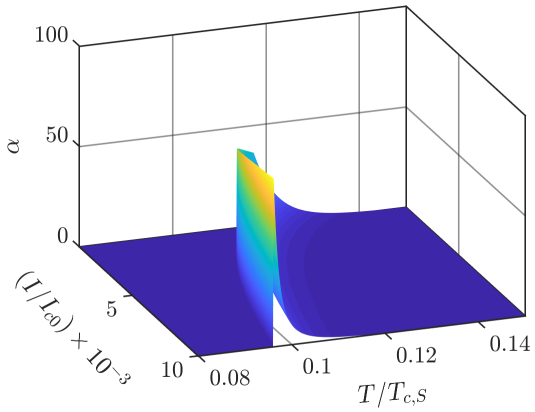

(b) $N = 2$.

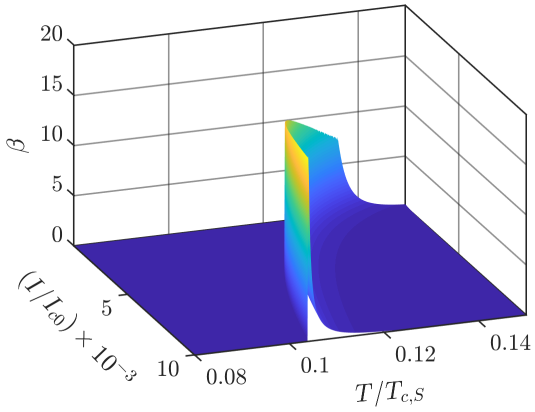

(c) $N = 0$.

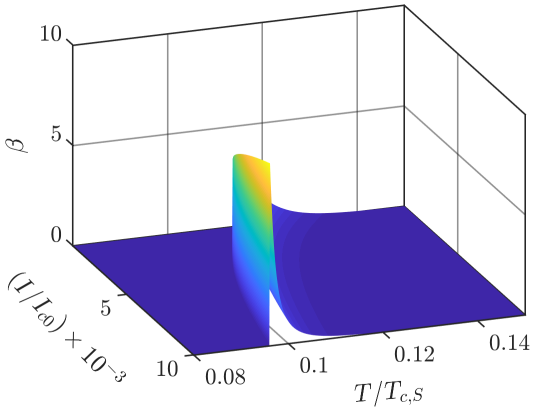

(d) $N = 2$

Figure 2.9 α and β surfaces for two TES thin films with different numbers of bars, all calculated with $\psi = \pi/2$.

here $T_c \propto L^{-0.7}$ in this instance with $N = 2$. These predictions enable me to quantify the effects of adding stripes and lengthening the thin film on key device parameters. The variation of transition temperature with film size could be exploited as a way of changing the transition temperature of a device, regardless of the material composition of the thin film. This would allow a series of devices with varying transition temperatures to be easily deposited on a single chip.

Figure 2.11 shows the variation of critical current with magnetic flux $I_c(\Phi)$, normalized to $I_c(0)|_{N=0}$. The maximum critical current is reduced as the number of bars increases, but the predicted critical current-phase relationships still have the form of a Fraunhofer diffraction pattern. Such Fraunhofer-like flux-dependencies have been observed experimentally [87, 138]. The left inset shows the calculated current-phase relationship $j_c(\psi)$, which is not perfectly

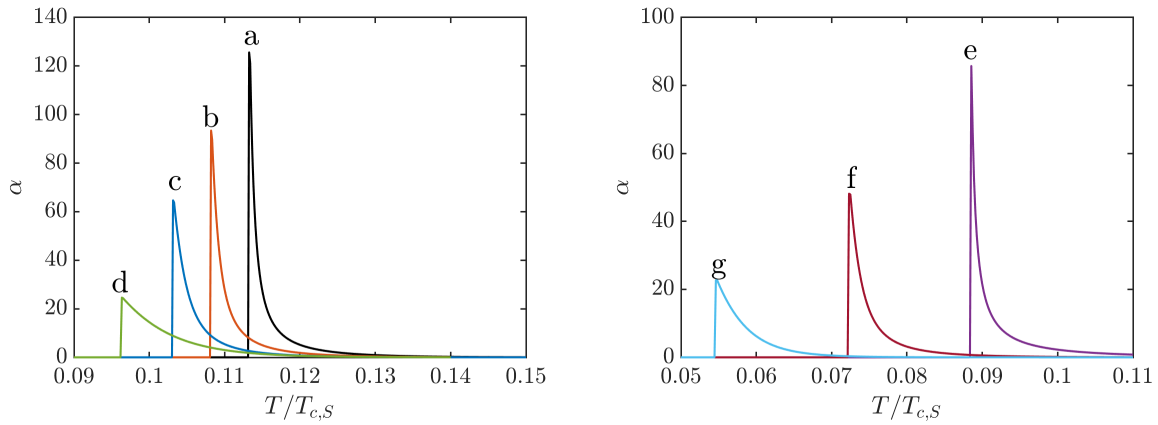

(a) (b)

Figure 2.10 (a) $\alpha(T)|_I$ for TES thin films with different numbers of stripes and applied magnetic flux: a. $N = 0, \Phi/\Phi_0 = 0$; b. $N = 1, \Phi/\Phi_0 = 0$; c. $N = 2, \Phi/\Phi_0 = 0$; d. $N = 2, \Phi/\Phi_0 = \pi/2$. $L/\xi_S = 100$ and $I/I_{c0} = 0.005$ throughout. (b) $\alpha(T)|_I$ for TES thin films of different lengths: e. $L/\xi_S = 100$ f. $L/\xi_S = 150$; and g. $L/\xi_S = 200$. $\Phi = 0, N = 2, I/I_{c,0} = 0.1$ throughout. β shows the same trends as α - from Figures 2.9a to 2.9d, $\alpha/\beta \approx 10$.

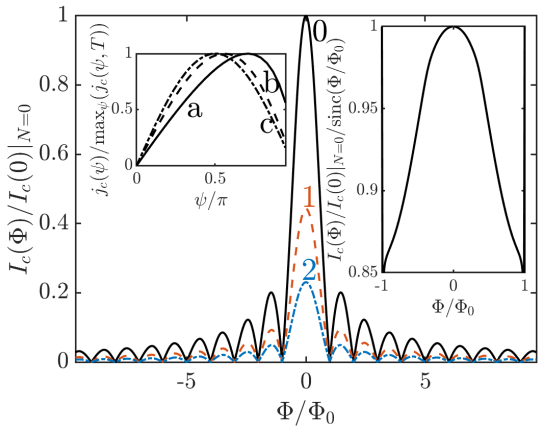

Figure 2.11 Critical current in the film I_c as a function of magnetic flux Φ, for TES thin films with (0) $N = 0$, (1) $N = 1$ and (2) $N = 2$. $T/T_{c,S} = 0.02$ and $L/\xi_S = 100$. Magnetic field is applied perpendicular to the film, in the z direction, and I_c is normalized to the zero-field critical current for a unpatterned TES thin film, $I_c(0)|_{N=0}$. Φ is in units of the magnetic flux quantum Φ_0. Left inset shows $j_c/\max_\psi(j_c(\psi,T))$, the critical current density normalized to its maximum value, as a function of phase difference ψ across the film, at $T/T_{c,S}$ = (a) 0.01, (b) 0.02 and (c) 0.05. Right inset shows the ratio of the normalised critical current for $N = 0$ to a sinc function of the same period and magnitude.

sinusoidal, instead showing a temperature-dependent skew. As the temperature reduces, the degree of skew increases and the maximum of $j_c(\psi)$ moves to higher values of ψ. These observations are consistent with the predictions of other groups [116, 122]. As described in Section 2.2.2, I use the $j_c(\psi)$ relationship calculated directly from the Usadel equations to determine the field dependence. The right inset demonstrates that using a sinc function to approximate the variation of critical current with field gives a prediction that deviates by up to 15% from the full model prediction. A sinc function approximation therefore can be used to give a general idea of the field dependence, especially at higher temperatures when the skew in the current-phase relationship is relatively small.

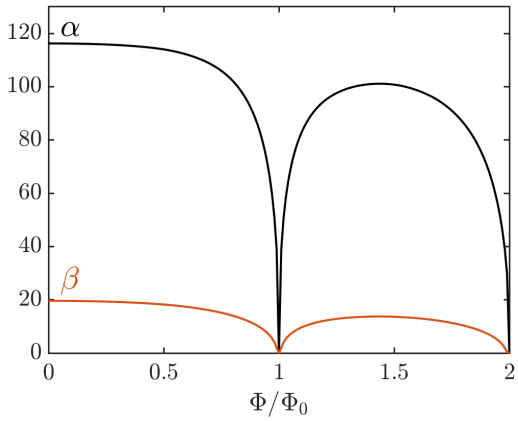

Figure 2.12 α and β as a function of magnetic flux in units of the magnetic flux quantum Φ/Φ_0. The calculations of both parameters were carried out for a resistance of $R/R_n = 0.015$. For α, $I/I_{c0} = 0.8$ and for β, $T/T_{c,S} = 0.063$.

A periodic dependence of the electrothermal parameters α and β on applied magnetic field is also seen, as demonstrated by Figure 2.12. Again, the relationship is not perfectly symmetric - there is a slight skew in the curve. This behaviour agrees qualitatively with measurements made by Smith et al. [97]. Calculations of this kind are important in quantifying the effects of stray magnetic fields on device performance.

Figure 2.13 shows the $I(V)$ curves calculated for two model devices. (a) is for a TES where the film has $N = 0$, whilst (b) is for a TES where the film has $N = 2$. The curves show the expected trend in temperature - as the temperature increases, the superconducting transition shifts to lower voltages and becomes broader. The higher transition temperature and sharper transition of the TES with $N = 0$ are reflected in the $I(V)$ curves, which show a steeper transition for the TES with a plain film than for the TES with stripes on the film.

Overall, this model shows excellent agreement with existing qualitative observations of TES behaviour, and in this chapter I have already demonstrated its predictive capability, using it to

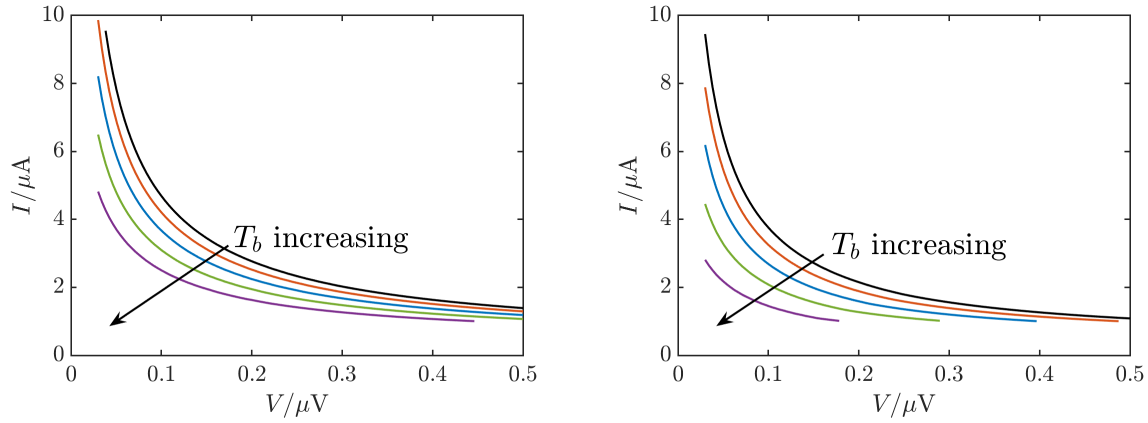

(a) $N = 0$. (b) $N = 2$.

Figure 2.13 $I(V)$ curves calculated by the model for two TESs with different numbers of bars. The set of temperatures used is the same for both figures.

show how a series of devices with different properties, such as transition temperature, could be manufactured on the same chip.

2.4 Magnetic field simulations

As seen in Figures 2.11 and 2.12, the behaviour of a TES is significantly changed by the presence of any magnetic flux through the device. From Section 1.4.3, knowing the effect of magnetic flux on TES performance is important as it means the level of shielding required for the TESs can be specified.

2.4.1 Device response as a function of magnetic field direction

When a magnetic field is applied in the z direction in Figure 2.14 of magnitude B_z, this alters the phase between the points $y = a$ and $y = b$. I wanted to find the phase difference between these points, i.e. $\psi(\mathrm{b}) - \psi(\mathrm{a})$. I follow the analysis of Gross and Marx [139], neglecting edge effects. Around the red dashed loop shown in Figure 2.14, denoted here as the contour C,

$$\oint_{\mathrm{C}} \nabla\theta \cdot d\mathbf{l} = 2\pi n, \tag{2.16}$$

so

$$\oint_{\mathrm{C}} \nabla\theta \cdot d\mathbf{l} = (\theta_{\mathrm{R_a}} - \theta_{\mathrm{L_a}}) + (\theta_{\mathrm{R_b}} - \theta_{\mathrm{R_a}}) + (\theta_{\mathrm{L_b}} - \theta_{\mathrm{R_b}}) + (\theta_{\mathrm{L_a}} - \theta_{\mathrm{L_b}}) + 2\pi n, \tag{2.17}$$

using the labels in Figure 2.14.

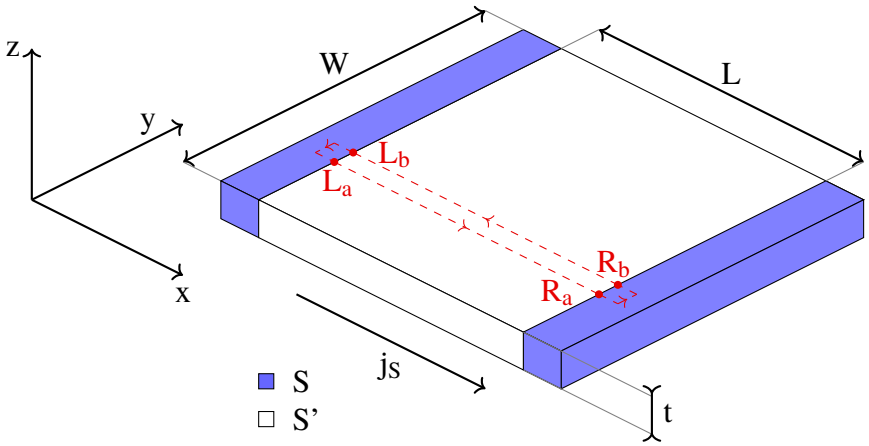

Figure 2.14 Schematic of a plain TES film of width W, length L and thickness t, including the electrodes. The electrodes (S) are shown in blue and the thin film (S′) is unshaded. The red dashed line indicates the contour used to determine the magnetic field response, and the co-ordinate system used to describe the film is indicated to the left of the diagram. The supercurrent density j_S is taken to be entirely in the x direction.

The phase difference across a weak link, between points 1 and 2, is

$$\psi = \theta_2 - \theta_1 - \frac{2\pi}{\Phi_0}\int_1^2 \mathbf{A}\cdot d\mathbf{l}, \tag{2.18}$$

which can be used to substitute in Equation (2.17) for $(\theta_{R_a} - \theta_{L_a})$ and $(\theta_{L_b} - \theta_{R_b})$,

$$(\theta_{R_a} - \theta_{L_a}) = -\psi(a) + \frac{2\pi}{\Phi_0}\int_{L_a}^{R_a} \mathbf{A}\cdot d\mathbf{l} \tag{2.19}$$

$$(\theta_{L_b} - \theta_{R_b}) = \psi(b) + \frac{2\pi}{\Phi_0}\int_{R_b}^{L_b} \mathbf{A}\cdot d\mathbf{l}. \tag{2.20}$$

From the London Equation, in a bulk superconductor,

$$\nabla\theta = \frac{2\pi}{\Phi_0}(\Lambda\mathbf{J}_S + \mathbf{A}), \tag{2.21}$$

where $\mathbf{A}$ is the magnetic vector potential and $\mathbf{J}_S$ is the supercurrent. This equation can be used to find $(\theta_{R_b} - \theta_{R_a})$ and $(\theta_{L_a} - \theta_{L_b})$,

$$(\theta_{R_b} - \theta_{R_a}) = \int_{R_a}^{R_b} \nabla\theta\cdot d\mathbf{l} = \frac{2\pi}{\Phi_0}\int_{R_a}^{R_b} \Lambda\mathbf{J}_S\cdot d\mathbf{l} + \frac{2\pi}{\Phi_0}\int_{R_a}^{R_b} \mathbf{A}\cdot d\mathbf{l} \tag{2.22}$$

$$(\theta_{L_a} - \theta_{L_b}) = \int_{L_b}^{L_a} \nabla\theta\cdot d\mathbf{l} = \frac{2\pi}{\Phi_0}\int_{L_b}^{L_a} \Lambda\mathbf{J}_S\cdot d\mathbf{l} + \frac{2\pi}{\Phi_0}\int_{L_b}^{L_a} \mathbf{A}\cdot d\mathbf{l}. \tag{2.23}$$

Substituting Equations (2.19) and (2.22) into Equation (2.17) gives

$$\psi(\mathrm{a}) - \psi(\mathrm{b}) = \frac{2\pi}{\Phi_0}\oint_{\mathrm{C}} \mathbf{A}\cdot d\mathbf{l} + \frac{2\pi}{\Phi_0}\int_{\mathrm{R_a}}^{\mathrm{R_b}} \Lambda \mathbf{J}_{\mathrm{S}}\cdot d\mathbf{l} + \frac{2\pi}{\Phi_0}\int_{\mathrm{L_b}}^{\mathrm{L_a}} \Lambda \mathbf{J}_{\mathrm{S}}\cdot d\mathbf{l}. \tag{2.24}$$

The integration of $\mathbf{A}$ is around a closed contour and is therefore equal to the total flux Φ enclosed by the contour. I consider the x and y components of the integral of $\mathbf{J}_{\mathrm{S}}$ separately. The current density along one segment of the path in the x direction cancels with the contribution of the adjacent path, which is only an infinitesimal distance dy away. In the y direction, the current is flowing in the x direction, perpendicular to the integration path along y, and contributes nothing to the integral of the current density. In addition to this, the path in the y direction is assumed to be deep inside ($\gg \lambda_L$, the London penetration depth), where the current density induced by the applied field is negligible. For the same reasons, any field applied in the x direction will not affect the current flowing through the junction. Therefore the line integral of the current density vanishes to give

$$\psi(\mathrm{b}) - \psi(\mathrm{a}) = -\frac{2\pi\Phi}{\Phi_0}. \tag{2.25}$$

The total flux enclosed by the contour is dependent on the applied magnetic field and the length of the thin film L,

$$\Phi = B_z(L + 2\lambda_{\mathrm{L}})dz. \tag{2.26}$$

Substituting this into Equation (2.25),

$$\psi(\mathrm{b}) - \psi(\mathrm{a}) = \frac{\partial\psi}{\partial y}dz = -\frac{2\pi}{\Phi_0}B_z(L + 2\lambda_{\mathrm{L}})dz, \tag{2.27}$$

so

$$\frac{\partial\psi}{\partial y} = -\frac{2\pi}{\Phi_0}B_z(L + 2\lambda_{\mathrm{L}}). \tag{2.28}$$

Repeating this analysis for a contour in the $y - z$ plane,

$$\frac{\partial\psi}{\partial z} = \frac{2\pi}{\Phi_0}B_y(L + 2\lambda_{\mathrm{L}}). \tag{2.29}$$

These two equations can be combined to give

$$\nabla\psi(\mathbf{r}, t) = \frac{2\pi}{\Phi_0}(L + 2\lambda_{\mathrm{L}})\,[\mathbf{B}(\mathbf{r}, t) \times \hat{\mathbf{x}}] \tag{2.30}$$

, where $\hat{\mathbf{x}}$ is the unit vector in the x direction.

Integrating Equation (2.28) gives

$$\psi(y) = \frac{2\pi}{\Phi_0} B_z(L + 2\lambda_\mathrm{L})y + \psi_0, \tag{2.31}$$

where ψ_0 is the constant of integration and is equal to the phase difference at $y = 0$. To create a simple model of the response of a TES thin film to a magnetic field I assume a sinusoidal critical current-phase relation, which is a reasonable approximation to the critical current-phase relation seen using my full proximity effect model. This gives a supercurrent density of

$$J_\mathrm{c}(y, z, \Phi) = J_\mathrm{c}(y, z) \left| \sin\left(\frac{2\pi}{\Phi_0} B_z(L + 2\lambda_\mathrm{L})y + \psi_0 \right) \right|. \tag{2.32}$$

The integral current is then

$$I_\mathrm{c}(\Phi) = \int \int J_\mathrm{S}(y, z) dy dz. \tag{2.33}$$

Assuming that the critical current J_c is spatially homogeneous and setting $\psi_0 = 0$, the integral in the z direction can be carried out to give

$$I_\mathrm{c}(\Phi) = t \int_{-W/2}^{W/2} J_\mathrm{c} \left| \sin\left(\frac{2\pi}{\Phi_0} B_z(L + 2\lambda_\mathrm{L})y \right) \right| dy, \tag{2.34}$$

so, carrying out the integration in the y direction,

$$I_\mathrm{c}(\Phi) = I_\mathrm{c} \left| \mathrm{sinc}\left(\frac{\Phi}{\Phi_0} \right) \right|, \tag{2.35}$$

where $I_\mathrm{c} = tWJ_\mathrm{c}$ and $\Phi = \pi B_z WL$. The current is therefore predicted to have a dependence on flux that is analogous to the Fraunhofer diffraction pattern.

If the applied field is in an arbitrary direction, neglecting the x component as from Equation (2.30), this will have no effect on device response,

$$\mathbf{B} = B_y \hat{\mathbf{y}} + B_z \hat{\mathbf{z}}, \tag{2.36}$$

for a spatially homogeneous critical current, the double integral in Equation (2.33) separates. Each integral can be evaluated separately to give the overall current response,

$$I_\mathrm{c}(\Phi) = I_\mathrm{c} \left| \mathrm{sinc}\left(\frac{\pi \Phi_y}{\Phi_0} \right) \right| \left| \mathrm{sinc}\left(\frac{\pi \Phi_z}{\Phi_0} \right) \right|, \tag{2.37}$$

where $\Phi_y = B_y Lt$ and $\Phi_z = B_z LW$.

I applied this model to calculate the device response for a 100 µm side length TES thin film as a function of magnetic field direction, by working out the critical current at zero applied field, then calculating the critical current as a function of magnetic field direction for a fixed magnitude of magnetic field strength using Equation (2.37). In Figures 2.15 to 2.17, I plot the direction of the applied field, scaled by the magnitude of the change in critical current from the zero field value. A device that is equally sensitive to magnetic fields applied in any direction would show a spherical response surface.

For all field strengths, a field applied in the $x-y$ plane produces no change in critical current, whilst a field applied in the z direction produces a large change in critical current. For the smaller field strengths, the change in critical current is at a maximum for fields in the z direction. As the magnetic field strength increases, the response surface becomes less smooth and displays oscillatory behaviour, as shown in Figure 2.17, and there is no longer a clear maximum change for fields in the z direction. As the field strength increases, the sensitivity to in-plane fields also increases, with a flattening of the response surface into the $x-y$ plane visible from the cuts through the $x-z$ and $y-z$ planes.

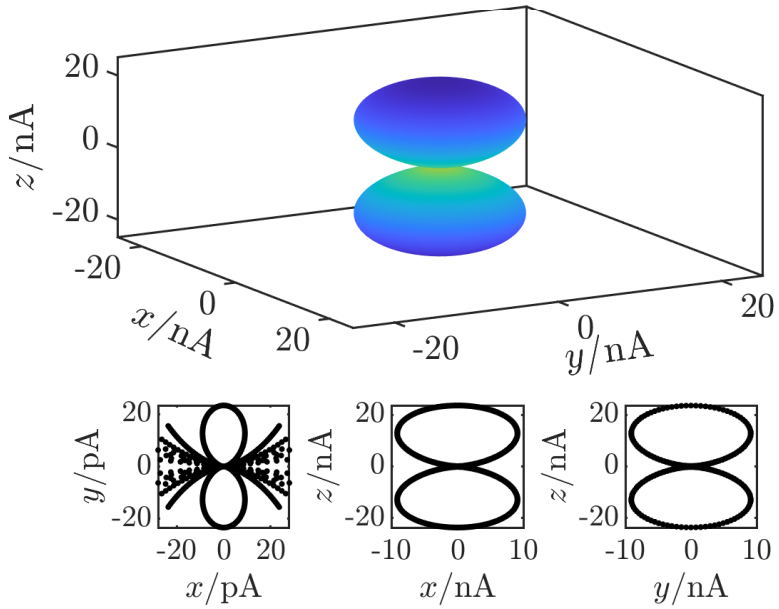

Figure 2.15 (Top) Direction of the magnetic field applied to the TES scaled by the critical current response in nA, for an applied field of 5nT. The shading corresponds to the magnitude of the critical current response. (Bottom) Cuts through the response surface in the $x-y$, $x-z$ and $y-z$ planes.

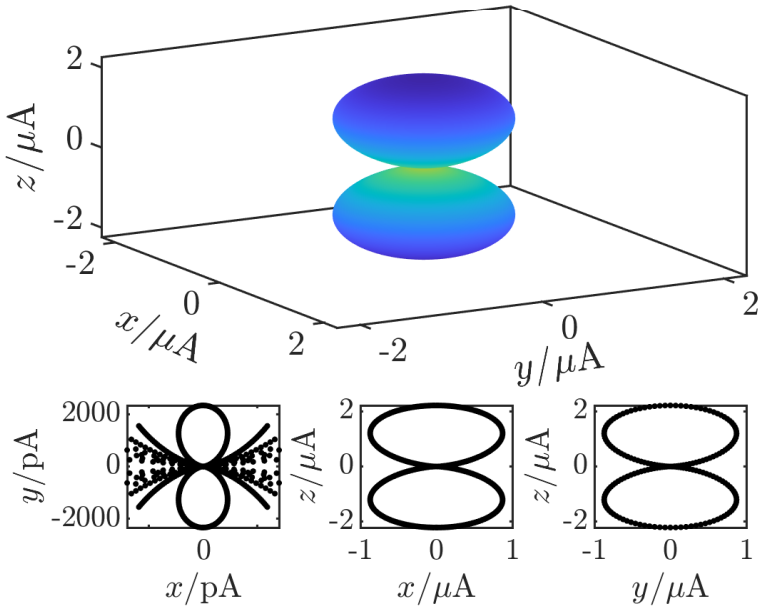

Figure 2.16 (Top) Direction of the magnetic field applied to the TES scaled by the critical current response in μA, for an applied field of 50nT. The shading corresponds to the magnitude of the critical current response. (Bottom) Cuts through the response surface in the $x-y$, $x-z$ and $y-z$ planes.

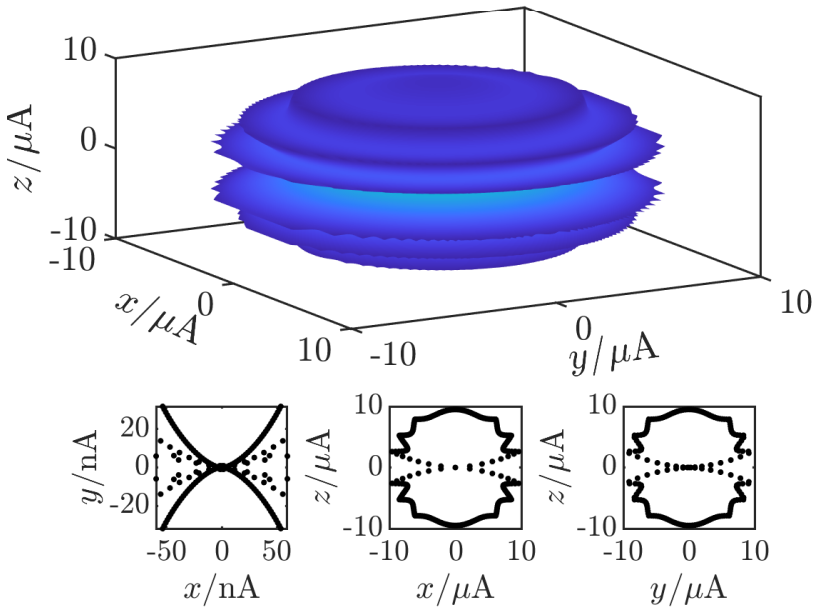

Figure 2.17 (Top) Direction of the magnetic field applied to the TES scaled by the critical current response in μA, for an applied field of 500nT. The shading corresponds to the magnitude of the critical current response. (Bottom) Cuts through the response surface in the $x-y$, $x-z$ and $y-z$ planes.

2.4.2 Magnetic field due to current flow in the surrounding wiring

In an array of TESs, all the devices have to be wired up to the SQUID and this wiring will produce magnetic fields. Additionally, a space-based array of TESs will experience the effects of the magnetic fields within a spacecraft. These magnetic fields will degrade the sensitivity and energy resolution of the TESs so it is important to understand both the magnitude of the magnetic fields and the subsequent effect of these fields on device performance.

The magnetic fields generated by the wiring may have a significant effect on the magnetic flux through the TES thin film [140]. To investigate this phenomenon, I created a basic model to investigate the effects of these fields for a range of different TESs, studying common wiring geometries for unreleased or partially released devices. Unreleased devices have not had their supporting membrane etched, so are not suspended at all. Partially released devices may have some sections of the supporting membrane removed to reduce the thermal conductance, but are not fully suspended.

Reduction of wiring to basic model

The wiring geometry used for unreleased TESs can be seen in Figure 2.18. The current flow is round three sides of a square and can be approximated by three infinitely long wires on three sides of a square, as shown in Figure 2.19. In creating this model, I also assumed all three wires have the same current I flowing through them and that the wires were infinitely thin. I neglected any crossing effects and assumed additionally that all three wires were the same perpendicular distance r away from the centre of the TES thin film. As the superconducting contacts are superconducting at all operating temperatures, they were not included in this model.

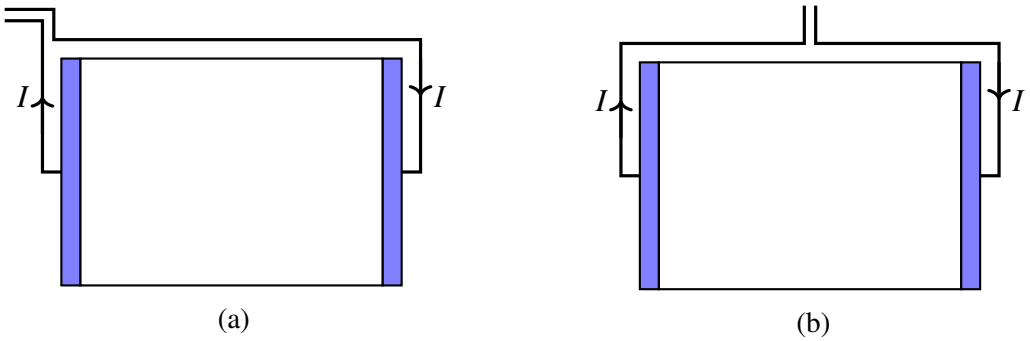

Figure 2.18 Two different wiring arrangements (a) and (b) used for unreleased TESs. The unshaded region is the thin film S′, which may or may not be patterned, and the blue regions are the superconducting electrodes S. In both cases, the current effectively flows round three sides of a square current loop.

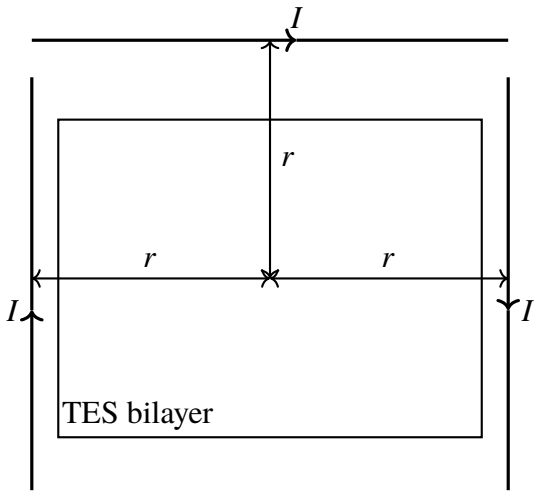

Figure 2.19 Simple model created to approximate the wiring of these unreleased devices. All three leads have the same current I flowing through them and are assumed to be infinitely long and infinitely thin. Any crossing effects are neglected. The leads are all taken to be the same distance r from the centre of the TES thin film. The superconducting lead contacts S are not included in this model.

Results from basic model

Figure 2.20 shows the magnetic field variations across the thin film. Figure 2.20a illustrates the comparatively high magnetic field strengths at the edges of the thin film and Figure 2.20b shows the smaller variations in magnetic field in the y direction.

In Figure 2.21, I investigate how the distance of the wiring from the centre of the TES thin film, r, affects the total flux through the film, calculated by integrating the magnetic field strength in Figure 2.20 across the film surface. The flux shown has been divided through by the bias current as different bias currents may be used for a single device so magnetic flux for different currents can be quickly calculated. The calculation is for a TES thin film of dimensions $140{\times}100\,\mu m^2$. The flux experienced by the device drops off very rapidly as the distance of the wiring is increased.

Calculation of operating currents

To compare the effects of the wiring on different devices, my simple model requires the device dimensions and the maximum operating current. The device dimensions are usually stated in the literature but some papers do not give the operating current. If the thermal conductance G, the value of T_c and the device resistance are known, the operating current can be estimated by taking Equation (2.15) with $n = 2$ to calculate the value of K, and then substituting this into the power balance equation, (2.14b), using the I^2R form of the power. Using this equation, I

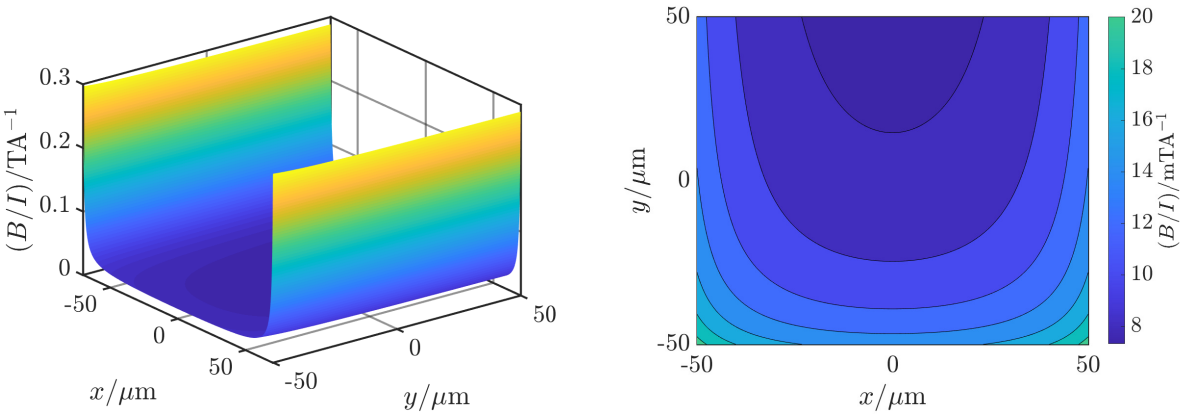

(a) (b)

Figure 2.20 (a) Magnetic field per unit bias current across the $x-y$ plane of a TES thin film due to the wiring. (b) Projection of the magnetic field surface onto the $x-y$ plane to demonstrate the variation of the magnetic field in the y direction.

calculated estimates for the values of I where needed. I assumed that $T_b \approx 0.5T_c$, the desired operating point for a TES, and took R to be the normal-state resistance of the device, as this gave the correct order of magnitude for R_0.

The effects of the magnetic field produced by the wires can be accounted for in a number of different ways. The most straightforward way is to use the code that I have already generated to account for magnetic field effects - as the magnetic flux produces a shift in the total phase across the thin film, this shift can be included in the value of ψ used in the calculations. Another method is to include the effects of the wiring directly in the Usadel equations, by using the covariant form of the gradient operator that includes the magnetic vector potential A.

Figure 2.22 shows the deviations of I_c, α and β from their zero-magnetic-field values as a result of the magnetic flux produced by the bias current in the wiring for a range of TES thin films with different dimensions and bias currents, as reported by a number of different researchers. The maximum percentage deviation is strongly dependent on the application. X ray devices such as those of Smith et al. require high powers and high currents, producing significant percentage deviations whereas the ultra-low noise devices such as those studied by Hijmering et al. [121] use low powers and low currents to minimise the noise, producing negligible percentage deviations. Since the deviations are significant for high power devices, it is surprising that no group has reported TESs that do not superconduct due to the fields produced by the surrounding wiring. Experimental measurements, as described in Chapter 3 and Chapter 6, will be important in probing the effects of the fields in the surrounding wiring.

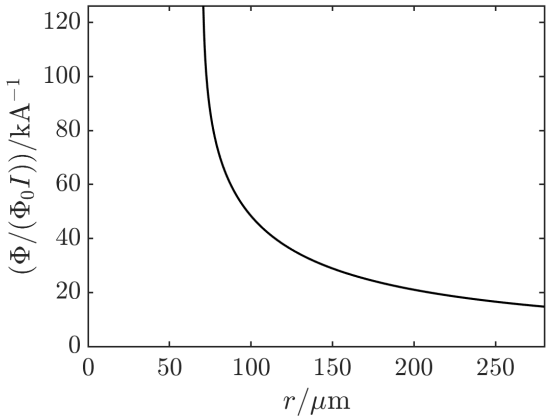

Figure 2.21 Normalised flux divided by bias current, as a function of wire distance from the centre of the film r, for a TES thin film of dimensions $140\times100\,\mu\mathrm{m}^2$.

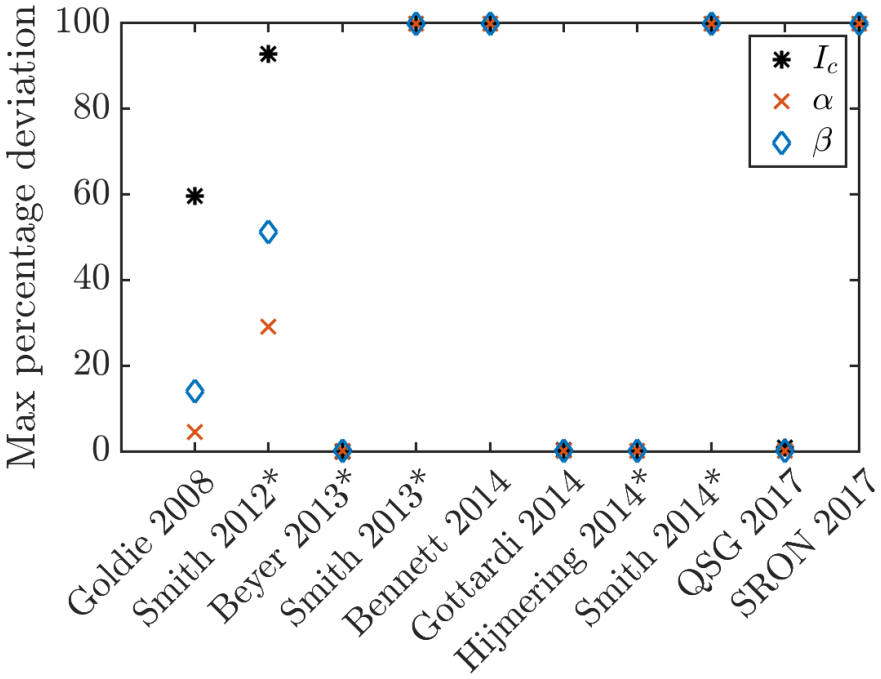

Figure 2.22 Maximum percentage deviations that could occur in I_c, α and β as a result of the flux produced by the current in the wires, for TESs with a variety of different dimensions and bias currents, including devices tested in Chapter 3 [14, 16, 87, 90, 97, 101, 121, 138, 141]. For the data points labelled *, an approximate operating current was calculated from other parameters given in the work, as detailed in Section 2.4.2.

2.4.3 Self-field produced by current flow in the TES film

It is also valuable to calculate the field produced by currents flowing in the TES thin film itself. In this model, I set up an example path for current flow as a first order illustration of the effects of current meander. The resulting field calculated was not used to update the expected current flow. The contribution to the magnetic field from a segment of current-carrying wire is given by the Biot-Savart law as

$$d\mathbf{B}(\mathbf{r}) = \frac{\mu_0}{4\pi} \frac{I d\mathbf{l} \times \hat{\mathbf{r}}'}{|\mathbf{r}'|^2}, \tag{2.38}$$

where $\mathbf{r}$ gives the position at which the field is being calculated and $\mathbf{r}' = \mathbf{r} - \mathbf{l}$ is the displacement between the wire element $d\mathbf{l}$ and the point $\mathbf{r}$. The wire segment has current I flowing through it.

I studied the magnetic field due to the expected current flow in four thin film configurations. In one configuration, I calculated the field in a thin film with current flowing perpendicular to the electrodes, which I refer to as a film with $N = 0$. This pattern of current flow would also take place in a film with normal metal bars when the current flows directly through the bars instead of bending around them. I also considered three thin films where the current flow bends around normal metal bars, with $N = 1 - 3$.

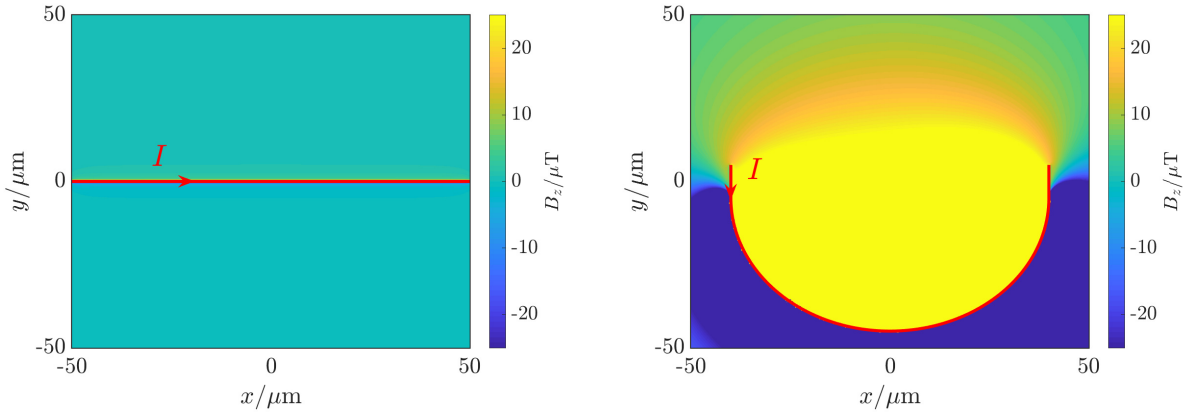

(a) $N = 0$. (b) $N = 1$.

Figure 2.23 Magnetic field magnitude in the z direction, over the surface of the TES thin film, produced by a current of 20 µA flowing through the wires shown in red. (a) is for an unpatterned TES with $N = 0$, whilst (b) is for a TES with $N = 1$.

Figure 2.23a shows the first order prediction of the magnetic field in a TES thin film with $N = 0$, where the current flows perpendicular to the electrodes. The magnetic field produced by this current flow is very small, and so would not significantly impact the device behaviour. Figures 2.23b to 2.24b show the fields for three TES films with $N = 1, 2$ and 3. The addition of any number of bars increases the overall magnetic field across the TES film to the order of

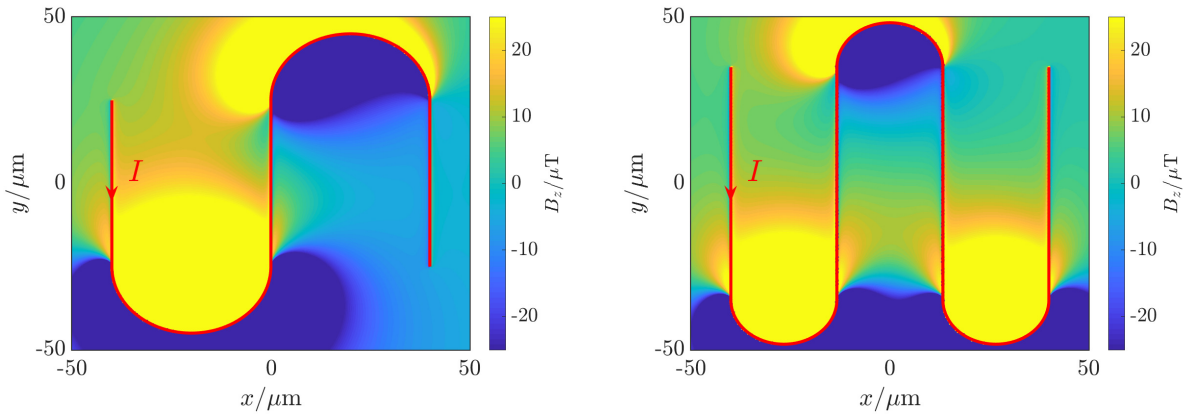

(a) $N = 2$. (b) $N = 3$.

Figure 2.24 Magnetic field magnitude in the z direction, over the surface of the TES thin film, produced by a current of 20 µA flowing through the wires shown in red. (a) is for a TES with $N = 2$ whilst (b) is for a TES with $N = 3$.

tens of µT, which is of the same magnitude as the fields I applied in my magnetic field study in Chapter 6. It can also be seen that current flow around adjacent bars produces magnetic fields that oppose each other, suggesting that TES films with even numbers of bars will have a smaller self-field than TES films with odd numbers of bars.

In order to quantify the effects of the field produced due to current flow in the TES film and compare devices with different numbers of bars, I calculated κ, which is a measure of the total self-inductance of each TES thin film. The inductive energy stored in the TES thin film per unit volume is

$$U = \frac{\int \mu_0 |\mathbf{B}|^2 \, \mathrm{d}A}{L^2} = \frac{1}{2}\kappa I^2, \tag{2.39}$$

from which κ can be defined,

$$\kappa = \frac{2\int \mu_0 |\mathbf{B}|^2 \, \mathrm{d}A}{L^2 I^2}. \tag{2.40}$$

The values of κ are shown in Table 2.2 for all of the film designs modelled, with $N = 0 - 3$. From this, it can be seen that the total self-inductance is indeed smaller for TES thin films with even numbers of bars compared to TES films with odd numbers of bars. This may affect device properties such as magnetic field suceptibility, transition sharpness, response time and noise. This observation will be returned to in Chapters 5 and 6.

Table 2.2 κ, a measure of the total self inductance, calculated to compare the self-field for TES thin films with $N = 0 - 3$. All thin films have the same area and the same current flowing along the sample path.

N	κ/mH m^{-3}
0	2.7×10^{-5}
1	170
2	28
3	70

2.5 Conclusions

In this chapter, I have developed a microscopic model of TES thin films operating at low temperatures $T/T_{c,S} \ll 1$ to explore the effects of normal-metal structures on the thin film, describing the film in terms of the diffusive Usadel equations. I have presented boundary conditions that account for thickness discontinuities in the film, ensuring supercurrent conservation. I wrote software to numerically solve the equations of this model, allowing me to explore the effects of bilayer stripes on the principal TES characteristics: α, β, T_c and $I_c(\Phi)$. I can also calculate the effect of magnetic field on α and β for structures both with and without stripes.

I return here to my initial list of experimental observations and see which of these are accounted for by my model.

1. *The effective T_c scales approximately as $(1/L^2)$ [1].* From Figure 2.10, I find the values of T_c for different film lengths. This gives a dependence $T_c \propto L^{-0.7}$ for the TES parameters used here. This observation will be returned to in subsequent chapters, following device testing.

2. *α is reduced by the addition of lower T_c, S″ bars (and likewise increased by higher-T_c bars) [84, 88].* Comparing Figure 2.9a and 2.9b shows the reduction in the value of α when stripes are added. This reduction in α is further demonstrated in Figure 2.10, which shows that as the number of stripes is increased, the value of α decreases. The effects of higher T_c stripes have not yet been investigated.

3. *α and β show oscillations when a magnetic field is applied. As the maximum of these oscillations reduces with increasing field, both parameters are maximised in the zero field case [97, 99].* The model predicts these oscillations, as shown in Figure 2.12. As expected, when the flux is an integer number of flux quanta, α and β are both zero.

4. *The ratio α/β is typically in the range $10 - 200$ [16, 97, 128, 129].* Comparison of Figure 2.9a with Figure 2.9c and Figure 2.9b with Figure 2.9d shows a ratio of approximately 10.

5. *The measured $I_c(\Phi)$ shows a mostly Fraunhofer-like dependence, although the dependence is not exact [87, 97, 121, 130]. Some measurements on TESs with partial bars show a more complicated field dependence [121].* The Fraunhofer-like dependence of $I_c(\Phi)$ is predicted by the model, as shown in Figure 2.11. The dependence is not perfectly sinusoidal, as shown in the right inset to the figure, but a sinc function gives a reasonable approximation. The more complicated field dependence observed by Hijmering et al. [121] is not accounted for by my model.

The results of my model agree well with trends seen in the literature, which is a qualitative validation of the predictive power of this model, and supports the idea that models of this kind can be important in device design. I envisage that this model would be used to validate designs prior to device processing work being undertaken. For example, the ability to check whether the electrothermal parameters and transition temperature meet instrument specifications would be immensely beneficial.

I have also carried out several studies into the effects of magnetic fields on TES thin film behaviour. My model of directional dependence of critical current shows that TES thin films are most sensitive to applied fields perpendicular to the thin film, especially for small field strengths. For larger fields, clear oscillations in the response surface are seen. These predictions will be compared to experimental measurements in Chapter 6.

The currents in the superconducting leads produce a magnetic field that may cause significant suppression of the device current and electrothermal parameters, considerably degrading the performance of the TES. However, no group has reported devices that do not superconduct, suggesting that there may be other factors affecting the critical current. I return to this observation in Section 6.3.1 of Chapter 6, where I will present measurements of $I_c(B)$. Throughout Chapters 5 and 6, I will discuss the results of Section 2.4.3, to examine whether the larger self-field of TES thin films with odd numbers of bars affects their behaviour.

I conclude that my modelling work gives a good first-order account of the behaviour of structured TES thin films. The next chapter will describe the quantitative verification of my proximity effect model, comparing my calculated $I(V)$ curves with those measured for a real device. I will use the results from both the proximity effect model and the magnetic models throughout this thesis, to inform design decisions and interpret experimental results.

Chapter 3

Agreement between model and theory

3.1 Introduction

In the previous chapter, I developed a proximity effect model to describe thin films with and without normal metal stripes, and showed that this model gave a good qualitative account of the behaviour of transition edge sensors. Before using my model to design and characterise my own devices, I wanted to test the ability of the model to make quantitative predictions about device behaviour, taking into account the wide range of TES bilayer geometries and material combinations that are currently in use. I worked with other groups from the Netherlands Space Agency (SRON) and the Spanish Research Council (CSIC) to apply my model to a range of existing device designs. This enabled me to assess the effectiveness of this proximity effect model.

In this chapter, I present a summary of the device designs used by different groups in Section 3.2. I then show the predictions of my model for two Ti/Au devices developed at SRON in Section 3.3. Section 3.4 describes the modelling of a set of Mo/Au sensors made and tested by CSIC, whilst Section 3.5 shows the modelling of three Mo/Au TESs manufactured and measured as part of a previous investigation by our group.

The results of the modelling of the SRON TESs were presented at the SPIE Astronomical Telescopes and Instrumentation conference and have been published in the conference proceedings [142].

3.2 Overview of device designs used by different groups

There is no general consensus on the optimal geometry or material composition of a TES thin film, with material choices often determined by the previous processing experience of the group

and the proposed application of the TESs. Once a device process route has been optimised, the TES performance is typically well within the specifications for most applications, and so the materials used are not changed unless there is a compelling reason to do so. TES thin films are typically made from either elemental superconductors, bilayers or alloys.

3.2.1 Elemental superconductors

Tungsten

- **Applications:** Tungsten has been used for the thin films of some early TESs [143] and is still widely used to make optical TESs [71, 144, 145]. Tungsten TESs are also used in the CRESST experiment to try and detect the weakly interacting massive particles that would provide evidence for dark matter [46, 47].
- **Geometry:** Films are relatively small and thin, typically about 20 µm long and 20-40 nm thick.
- **Optimisation:** Groups are working to improve the timing capabilities [145]. Studies have been carried out to see whether geometrical modifications can improve performance, for example, including notches to try and reduce the quasiparticle density and including inactive regions of tungsten to act as quasiparticle traps [27].
- **Tunable transition temperature:** The transition temperature is strongly dependent on the deposition conditions and the substrate [146], allowing T_c of the TES thin films to be tuned without the need for a bilayer. However, this tuning is unpredictable and experiments must be carried out to determine the required processing conditions for a given T_c.
- **No membrane suspension needed:** Weak coupling between tungsten's electron and phonon systems provides a weak thermal link without the need for membrane suspension [71].
- **High optical efficiency:** When combined with optical structures to promote photon absorption, tungsten devices have demonstrated high optical efficiencies, with system detection efficiencies of at least 95 % [71] at a wavelength of 1556 nm, important for telecommunications applications.

Aluminium and titanium

- **Applications:** TES bolometer arrays for BICEP-2 and KECK telescopes featured pairs of aluminium and titanium thin films connected in series [35]. The use of a pair of TESs increases the dynamic range and the saturation power of the detectors. The aluminium devices were designed to be used for optical characterisation in a laboratory whilst the titanium devices were designed for science operations.
- **Optimisation:** These pairs of TESs have been used to study the polarisation of the cosmic microwave background, requiring the detectors to have low noise performance. The inductance to the readout SQUIDs was carefully chosen to avoid any degradation due to aliasing, and a thick layer of gold was added to the membrane next to each TES thin film to slow the devices down and prevent electrothermal instabilities.
- **Stable transition temperature:** The use of elemental superconductors means the transition temperature of the TES thin film is less sensitive to changes in film thickness than a bilayer-based thin film [147].
- **Native oxide layer:** Elemental titanium forms a native oxide layer, affecting properties such as the refractive index and resulting in a degradation of superconducting behaviour [148].

3.2.2 Bilayers

Many TES thin films are made from bilayers, as this allows the transition temperature of the film to be tailored in a predictable way [30, 119]. These bilayers typically consist of a superconductor and a normal metal, with the three most common being Mo/Au, Ti/Au and Mo/Cu. These TES films are typically 30-100 µm long and 80-400 nm thick. Different material combinations may produce TES thin films that are more or less sensitive to magnetic field [121], but no systematic study has previously been carried out. Some detectors, such as those used on the EBEX experiment to study CMB polarisation, are made of superconductor/superconductor bilayers, in particular Ti/Al [39]. The order in which the metals in the film are deposited may be important [149], with Portesi et al. reporting a cleaner interface between titanium and gold when the gold is deposited first [29].

Mo/Cu

- **Applications:** Mo/Cu bilayer devices are commonly used as high energy photon calorimeters, with applications including gamma ray spectroscopy [150] and x-ray

spectrometry [10]. They have also been developed for bolometric applications [16], on-chip materials characterisation [151] and space applications [2].

- **Geometry:** The Cu layer is commonly patterned with normal metal stripes to reduce excess noise [11, 152].
- **Gold heat sinks:** The use of copper means that gold features can be used for heat-sinking [10].
- **Passivation step:** Mo/Cu thin films require a passivation layer of SiO_2 [28]. Residual stress in this passivation layer can result in unwanted curvature [2], and the additional heat capacity increases response times and contributes to device noise.
- **Reactivity of copper etch:** The chemistry of copper etching is complex [137] and uses chemicals that can also etch other components of the TES.
- **Choice of wiring material:** Using titanium instead of niobium for the wiring produces TESs with sharper transitions which are less susceptible to unwanted longitudinal proximity effects [141].

Mo/Au

- **Applications:** Mo/Au bilayer devices are widely used or planned for use on a variety of astronomical experiments, including SPTpol [84], CLASS [41] and ATHENA [6].
- **Geometry:** The bilayer is typically around 200-400 nm thick, frequently patterned with normal metal bars to reduce excess noise [137, 152], and often features normal metal side stripes or banks to prevent undercutting [153]. However, these normal metal bars may not be necessary to achieve the required performance levels [154].
- **Insolubility of Mo:** Mo is insoluble with normal metals [40].
- **Advantages of Au:** Au has a high density and resistivity, low reactivity, and high corrosion resistance [40], producing more rugged devices [28]. The use of Au in the bilayer also makes the fabrication of gold absorbers easier [77].
- **Gold multilayer:** As these TES films are often fabricated with relatively thick layers of gold to achieve the required transition temperature, a mixture of sputtered and e-beam deposited gold may be used in order to achieve films with a higher residual resistance ratio [155, 156].

- **Irreproducibility of Mo:** The superconducting properties of Mo are influenced by the fabrication process used, making the thin films less reproducible. RF biasing during fabrication has been shown to improve the quality of the Mo films obtained [40].
- **Potential weak link effect:** Structure has been observed in the $I(V)$ curves for some Mo/Au TESs, especially for smaller film areas. This is attributed to a weak link effect [157]. The structure means that the operating temperature and thermal conductivity may vary significantly with small changes in bias current [158].

Ti/Au

- **Applications:** Ti/Au bilayer devices are used both for optical applications [59] and astronomical applications [22].
- **Thinner gold layer:** As Ti has a much lower transition temperature than Mo, a thinner Au layer may be used to produce films of the required T_c.
- **Additional metal layers:** It may be necessary to add metal layers above or below the Ti/Au bilayer to improve TES performance. TES thin films made for SPT-3G feature a Ti/Au/Ti/Au thin-film stack [159], with a thin Ti base layer for good adhesion to the substrate, an underlayer of Au to shield from substrate effects and improve transition sharpness, and a top layer of Au to prevent oxidation of Ti. This structure also showed a much more reproducible transition temperature [22].
- **Choice of wiring material:** The choice of wiring material also impacts device performance, with direct contact between Ti and Nb affecting the behaviour of the TES. Ti and Nb both absorb active gas molecules such as CO and H_2O, and if the two materials have different concentrations of these impurities, the diffusion of impurities results in a high concentration of impurities at the Ti-Nb interface [160]. Portesi et al. [29] fabricated two sets of Au/Ti TESs, one set with Al wiring and one set with Nb wiring. They observed that the TESs with Al wiring were more stable, showing less degradation under repeated thermal cycling than TESs with Nb wiring.
- **Electrode caps:** Posada et al. also observed that Nb-Ti contacts resulted in roughened Ti surfaces [23]. They solved by depositing thin (30 nm) gold caps on the titanium to act as a protective layer between the titanium and the niobium. The use of this protective layer produced TESs with sharper transitions. A study into the best material to use for the protective cap was carried out [160], in which Ti/Au TESs were made without any caps and with 30 nm Au, Mo and Pd electrode caps. Au caps were found to provide the

largest improvement in device performance, removing interface defects and producing interfaces with no residual resistance and good reliability of the electrical contact.

3.2.3 Alloys

TESs may alternatively be made from superconductor-normal metal alloys, with the most popular choice being AlMn, although the QUBIC experiment used a NbSi alloy for the thin film [161].

- **Applications:** Many different experiments use or will use AlMn TESs, among them SPT-3G [162], POLARBEAR-2 [42], Spider-2 [163] and ACTPol [164]. A TES of a higher T_c may be included in series for on-ground pixel characterisation [163].
- **Ability to adjust T_c and R_n separately:** The transition temperature and normal state resistance can be adjusted separately [162], with the transition temperature depending on the level of Mn doping and the degree of film heating post-deposition and the normal-state resistance depending on the film thickness and geometry.
- **Calibration needed for T_c:** Fine-tuning of the thin film transition temperature requires many calibration experiments, as the variation in T_c due to changes in doping level and film heating cannot be easily predicted.
- **Processing complexity:** Fewer processing steps are typically needed than for bilayer-based TESs [32]. However, some AlMn TES films are covered with a Ti/Au cap layer [162], with the Au cap layer protecting the film and the Ti layer preventing a reaction between the Au and the AlMn. The deposition of this cap layer adds more processing steps than the deposition of a second metal layer, and so in this case the alloy-based TES does not provide a significant reduction in processing complexity relative to bilayer TESs.
- **Difficulty of modelling:** Calibration testing is necessary as alloy-based TESs are not well described by existing TES models, with the TES Johnson noise model requiring a scaling factor to describe AlMn TESs [164]. The presence of the cap layer requires more calibration testing, as the proximity effect between the cap layer and the thin film will alter T_c. Once calibration is carried out, films with excellent reproducibility of T_c and uniformity can be manufactured [32, 162].
- **Insensitivity to magnetic field:** It has been suggested that these alloy-based devices may be less sensitive to magnetic fields than bilayer-based TESs [32].

3.3 Ti/Au devices developed and characterised by SRON

The Netherlands Space Agency, SRON, are developing x-ray TES detectors for the approved ESA-NASA space observatory ATHENA [7, 48]. ATHENA is designed to study the growth of large scale gas structures and black holes, with a particular focus on high-energy phenomena [165, 166]. The observatory will consist of an x-ray optic with two interchangeable focal plane detectors, one of which, the X-ray Integral Field Unit (X-IFU), is based on a large array of TESs [167]. The X-IFU will achieve greater sensitivity than previous instruments, as the TES energy resolution is specified to be 2.5 eV FWHM [130].

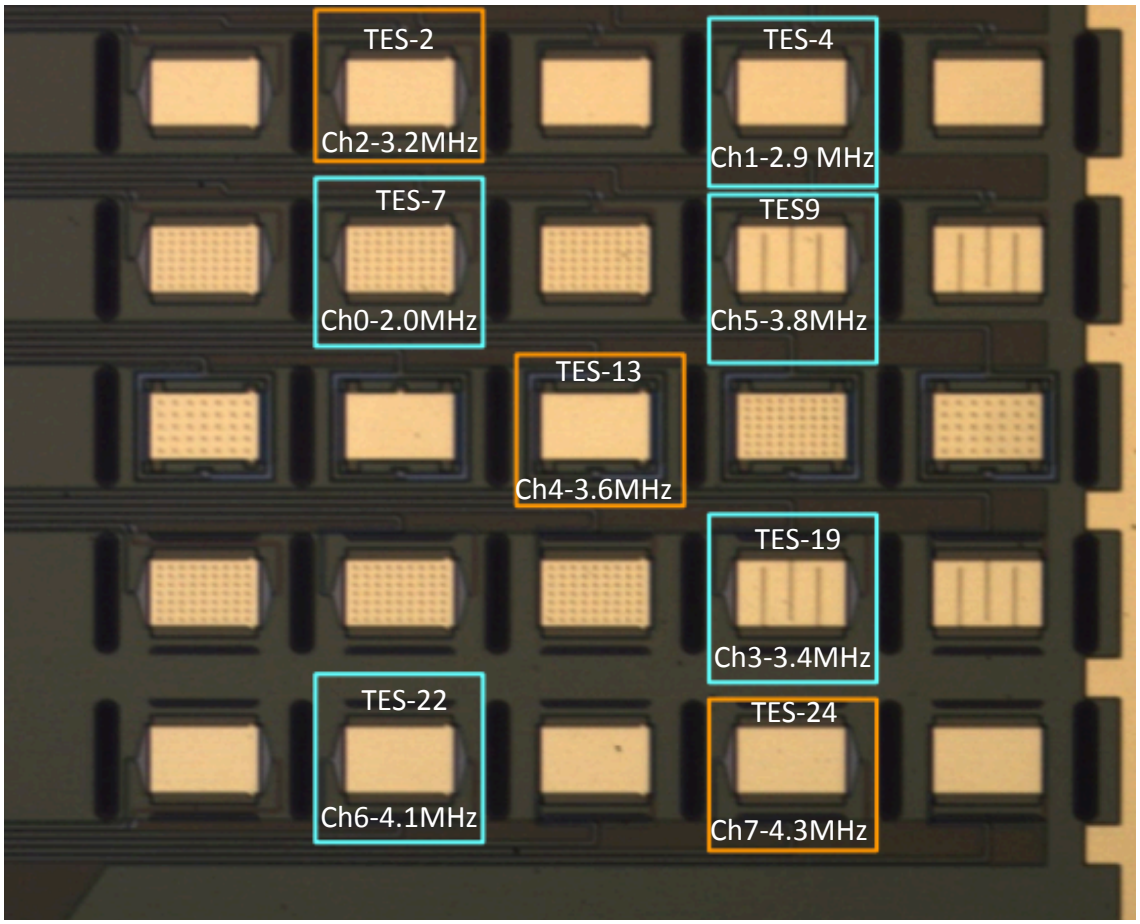

Figure 3.1 Image of a chip being tested at SRON, featuring 25 devices. All bilayers are $100\times140\,\mu m^2$ and made of Ti/Au of thickness 16/65 nm. The chip is designed to compare devices with different thermal conductances and normal metal designs. The highlighted devices were all tested in the same cooldown. The devices studied here are TES-4, a bare TES (Device 1), and TES-9, a TES with three bars (Device 2), designed to have the same thermal conductance and power plateau. Image from [142].

Our colleagues at SRON, the Netherlands Institute for Space Research, are in the process of testing Ti/Au TESs to investigate the optimal bilayer design. This work involves manufacturing and characterising devices with a range of different properties, including different normal metal patterns, and so they were able to provide me with data for two devices with the same thermal conductance and power plateau, one with metal bars and one without. The power plateau refers to the region where the TES is passing through its resistive transition and the power as a function of voltage remains constant. Figure 3.1 shows the chip containing these two TESs, with devices of interest highlighted.

In experimental testing the two TESs studied were labelled TES-4 and TES-9, but in my modelling work I refer to these devices as Device 1 and Device 2 for clarity. Top-down schematic views of the designs are shown in Figure 3.2. Device 1 was a Ti/Au TES with no normal metal patterning, whilst Device 2 had three partial gold bars across the width of the film. Both TESs had tapered electrodes to reduce manufacturing defects and improve device yield. However, in my model it was not necessary to account for this, as the taper will not affect the critical current of the bilayer, providing the electrodes are long enough that at some point bulk superconductor behaviour is exhibited across the full electrode width.

The important device parameters are given in Table 3.1. Both TESs were based on a Ti/Au bilayer (S′) of thickness 19/70 nm, with W=100 µm and L=140 µm, and had a normal resistance of approximately 250 µΩ. The additional gold bars (S″) were of thickness 100 nm.

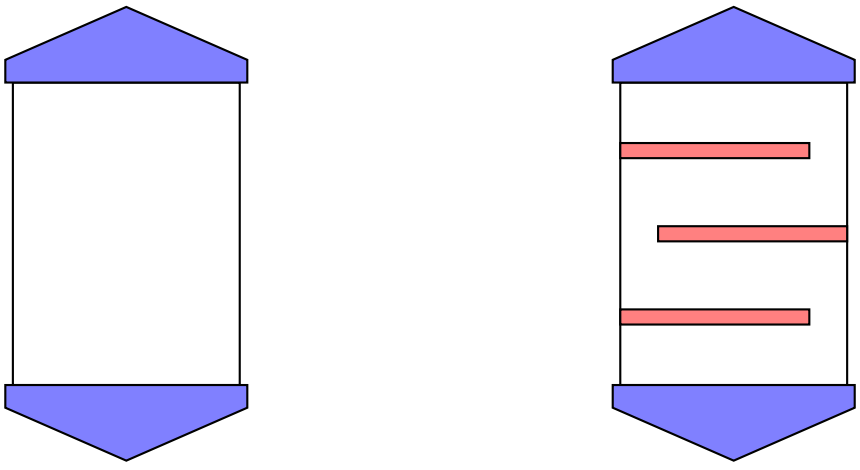

(a) (b)

Figure 3.2 Device designs are shown here in top-down view, with electrodes (S) in blue, bilayers (S′) in white, and normal metal patterning (S″) in red. Both TESs had tapered electrodes (S). Device 1 was of design (a), with no normal metal patterning. Device 2 had three partial normal metal bars (S″), as in design (b). Neither device had normal metal side stripes.

Table 3.1 Key device parameters for the two devices studied. Both devices had a normal state resistance of 250 mΩ. The unpatterned bilayer (S′) consisted of 19/70 nm of Ti/Au, with coherence length ξ=0.94 µm and dimensions W=100 µm, L=140 µm

	Device 1	Device 2
Design type	(a)	(b)
Number of additional Au bars	0	3
Length of Au bars/µm	n/a	90
Thickness of Au bars/nm	n/a	50
Width of Au bars/µm	n/a	5
Transition temperature/mK	102.4	101.7
n, the exponent in the power balance equation	3.63	3.62

3.3.1 Model results for SRON devices

In order to make quantitative comparisons between my model and the SRON devices, taking into account the dimensions, material composition and structure of the SRON devices, I altered the model to accept arbitrary model parameters. The material compositions of the different regions and the device dimensions can be quickly and easily altered in the source code to model the SRON devices. Additionally, as the SRON devices were much larger than my sample model devices, I increased the number and density of sampling points provided to the differential equation solver to ensure the solver could find a solution efficiently.

Firstly, I calculated the current-phase behaviour for Device 1 to find a value of ψ that maximised I_c, as described in Section 2.2.2. This calculated $I_c(\psi)$ relationship is shown in Figure 3.3, for zero magnetic flux. As this relationship was calculated at a temperature of 150 mK, significantly higher than the transition temperature, I_c is very small. A maximum device response at around $\psi = \pi/2$ can still be seen, and so for the calculation of the $I(V)$ curves, ψ was set to $\pi/2$. The shape of the $I_c(\psi)$ relationship is consistent with that shown in the left inset to Figure 2.11 and with the work of Likharev [122], as it displays a sinusoidal shape and a critical current that tends to zero for a phase difference $\psi = \pi$.

Figure 3.4 shows the prediction of $I_c(T)$ for Device 1 with a phase difference $\psi = \pi/2$. The shape of the log plot is consistent with experimental measurements [101]. Some measured $I_c(T)$ profiles display fluctuations at low critical current [1] but this effect was not accounted for by my model.

Figure 3.5 shows the calculated $R(T, I)$ surfaces for Device 1 and Device 2, over a temperature range ΔT =20 mK. The $R(T, I)$ surface corresponding to Device 2, the sensor with normal metal bars, shows a much broader transition than that for Device 1, the plain sensor. This indicates that the metal bars widen the transition, reducing the value of α of the device. Additionally, the

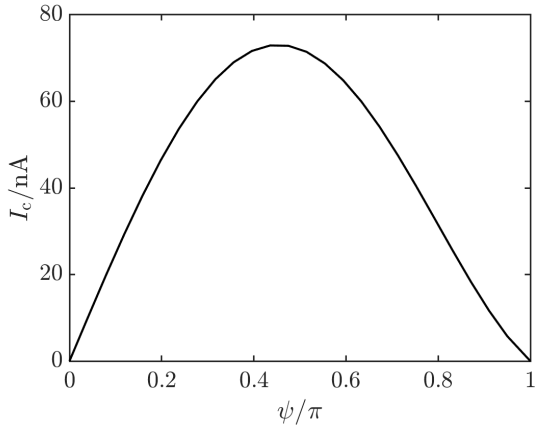

Figure 3.3 Calculated $I_c(\psi)$ relationship for Device 1, at a temperature of 150 mK. Magnetic flux $\Phi = 0$.

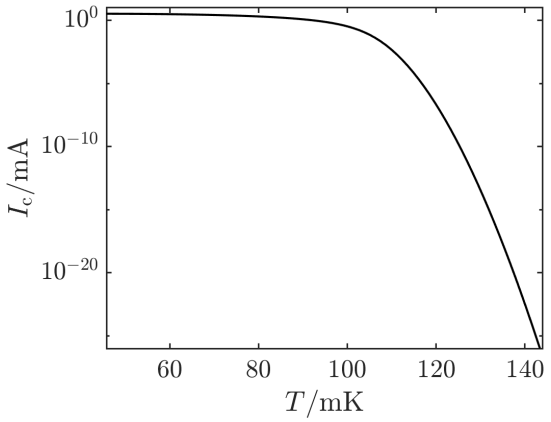

Figure 3.4 Calculated $I_c(T)$ for Device 1 with a phase difference of $\pi/2$. Magnetic flux $\Phi = 0$.

presence of the metal bars lowers the initial onset of resistance from just above 100 mK to about 93-94 mK at a current of 25 µA. For lower currents, the transition temperature is approximately the same for both devices, agreeing with experimental observations.

To see how effectively my model could describe the quantitative behaviour of actual devices, I used it to calculate $I(V)$ curves for these two TESs. Figure 3.6a shows the measured $I(V)$ curves (points) for Device 1 over a range of different bath temperatures, with the corresponding calculated $I(V)$ curves shown as dashed lines. The $I(V)$ curves calculated using the proximity effect model agree extremely well with the $I(V)$ curves measured experimentally. The model correctly predicts both the shape of the $I(V)$ curves and their variation with bath temperature. No attempt was made to fit the model to the data, with one free parameter in the modelling, $\gamma_{B(S,S')}$, a measure of the interface resistance between the niobium (S) electrodes and the Ti/Au

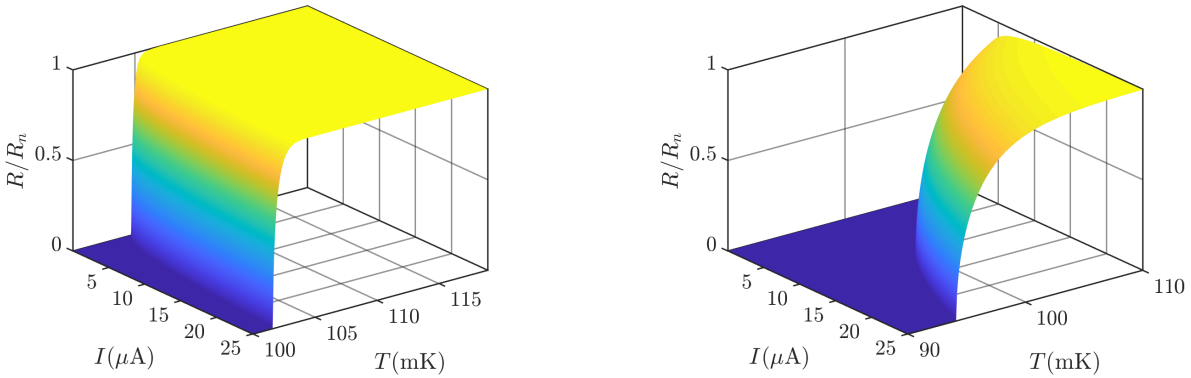

(a) (b)

Figure 3.5 $R(T, I)$ surfaces calculated using the proximity effect model for (a) Device 1 and (b) Device 2. Resistance is normalised to the normal state resistance of the device R_n. For both devices, the temperature range shown is $\Delta T = 20$ mK.

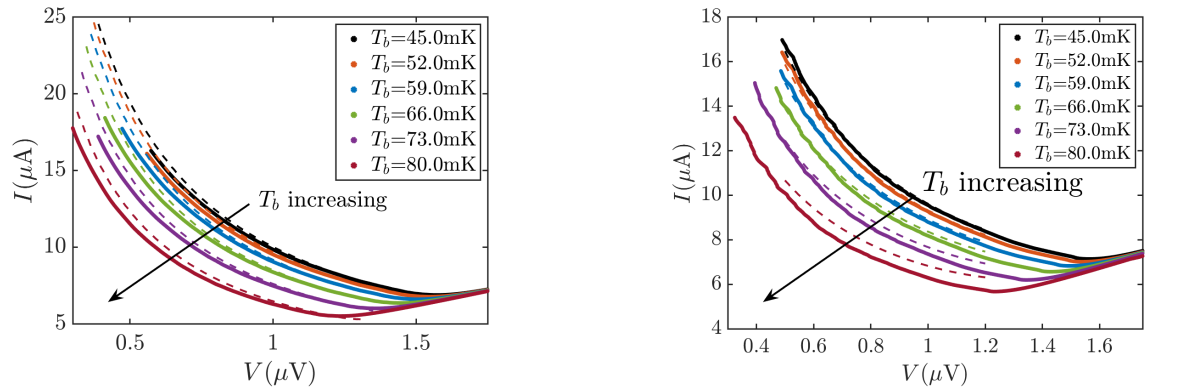

(a) (b)

Figure 3.6 $I(V)$ curves as measured (points) and calculated using the proximity effect model (dashed lines) over a range of bath temperatures T_b. The normal metal bars on Device 2 have an effective transition temperature $T_{c,S''} = 0.67\, T_{c,S'}$

(S') bilayer. I took $\gamma_{B(S,S')} = 10$ for all bath temperatures, showing that the same value of the boundary resistance gives good agreement between the model and the experimental data for a range of different bath temperatures.

Figure 3.6b shows the measured (solid lines) and calculated (dashed lines) $I(V)$ curves for the device with three normal metal bars, Device 2. The agreement is very good, although there is an additional free parameter: the transition temperature of the S″ region is not always known from experiments and cannot always be predicted easily. For example, in Device 2, there was a thin (3 nm) adhesive layer of titanium between the bar and the bilayer, preventing the use of the Martinis model [30] to calculate T_c. For this device I calculated the transition temperature of the regions with normal metal bars $T_{c,S''}$ to be equal to 0.67 $T_{c,S'}$, based on the $I(V)$ curves at T_b=45 mK. This transition temperature was taken to be the same for all of the different bath temperatures. I again took $\gamma_{B(S,S')} = 10$ for the interface between the niobium electrodes and the Ti/Au bilayer, and I assumed that the resistance of the interface between the S" region and the S' region is negligible so the interface parameter for this interface $\gamma_{B(S,S')} = 0$. For both devices, the fact that the one-dimensional model does well at predicting the $I(V)$ curves implies that any two-dimensional effects are not significant. This implies that the current in Device 2 was mostly flowing perpendicular to the electrodes and not taking a meandering path to avoid passing through the S″ regions, as has been previously suggested [94].

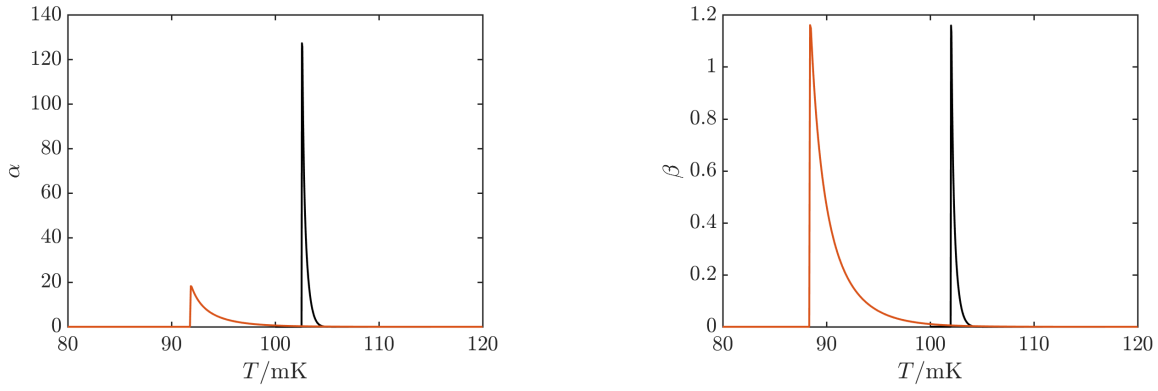

(a) (b)

Figure 3.7 Electrothermal parameters (a) $\alpha(T)$ and (b) $\beta(T)$ for Device 1 (black) and Device 2 (red), calculated using the proximity effect model at a current of 12.5 µA.

Calculations of the small signal electrothermal parameters $\alpha(T)$ and $\beta(T)$ for Device 1 and Device 2 are shown in Figure 3.7. The presence of the normal metal bars is expected to significantly reduce the maximum value of α by a factor of about 10, due to the broadening of the transition with temperature. The expected maximum value of β is not significantly altered

by the addition of normal metal bars, although the temperature broadening is predicted to produce a slower decay of β.

Throughout this modelling, I assumed $\Psi = 0$, suggesting that the effects of the field produced by current flow in the wiring do not need to be taken into account here, despite the results of Section 2.4.2 suggesting otherwise.

3.3.2 Conclusions from modelling SRON devices

For these Ti/Au devices, the model gives a good account of both quantitative and qualitative observations, and so can be used to accurately predict device behaviour for different device geometries. Predictions for devices patterned with normal metal bars may be slightly less accurate than those for unpatterned devices, due to the difficulty of estimating the transition temperature of the S″ region.

3.4 Mo/Au devices developed and characterised by CSIC

The Spanish National Research Council (CSIC) are also developing TESs for x-ray detection [156], using a different material combination. Their TES thin films are made from a Mo/Au bilayer and have no additional normal metal patterning. In developing their TESs, they have tested films of different aspect ratios with two electrode designs, giving a range of different geometries to investigate. They provided me with data for these devices to use in the quantitative testing of my model.

3.4.1 Description of devices

Figure 3.8 shows the general design of the Mo/Au TES superconducting components studied in this section. These Mo/Au TES thin films had a double layer of gold: following Mo sputtering (55 nm), a thin (15 nm) protective layer of gold was sputtered for protection, and the majority of the gold layer (325 nm) was then deposited via e-beam deposition. This could result in a trilayer if the transition temperatures of the sputtered gold and e-beam gold are very different, or if there is some boundary resistance between the two gold layers. Normal metal side banks may be added to prevent transition broadening, but for this study, the simpler device designs without these banks were selected.

Three TESs were used to test my model, with two different electrode geometries, as shown in Figure 3.9. Design (a) has tapered electrodes like the SRON TESs, whilst design (b) has square electrodes. As discussed in Section 3.3, the electrode shape was not important in the application of my model. Two of the TESs, Devices 2 and 3, were of design (a) whilst Device 1

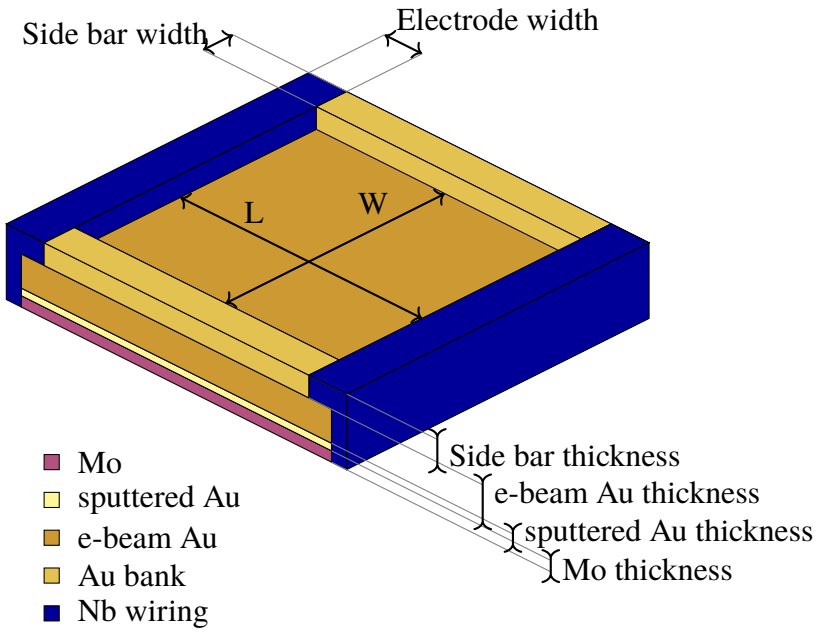

Figure 3.8 Schematic of the superconducting component of the Mo/Au devices studied by CSIC, indicating the different layers of Au in the thin film. Although some devices feature Au side stripes, the devices studied in this chapter did not.

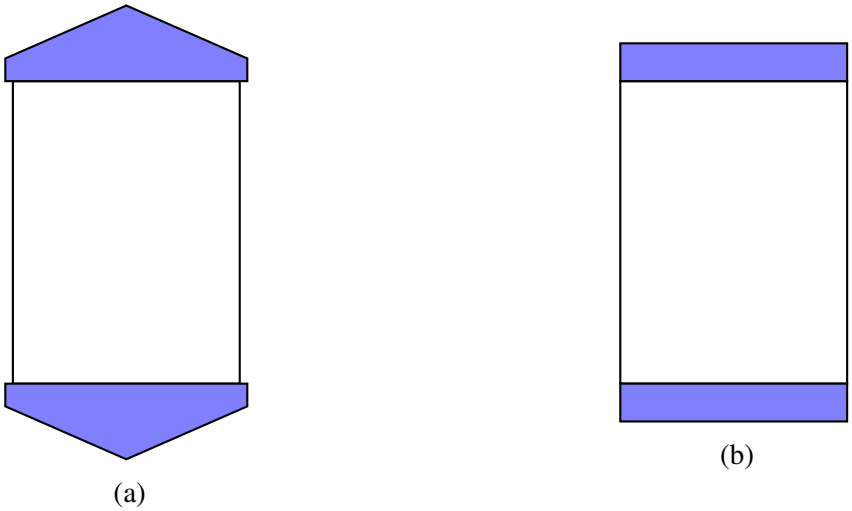

Figure 3.9 Device designs are shown here in top-down view, with electrodes (S) in blue and bilayers (S′) in white. Design (a) has TESs with tapered electrodes, whilst design (b) has rectangular electrodes. Of the three TESs studied, Devices 2 and 3 were of design (a) and Device 1 was of design (b).

was of design (b). The TES thin films also had different aspect ratios, as shown in Table 3.2. Device 1 had a bilayer with $W > L$, Device 2 was square and for Device 3, $W < L$.

Table 3.2 Key device parameters for the three devices from CSIC that were modelled. The length given for Device 1 is an effective length. All TESs were made from 55/15/325 nm Mo/sputtered Au/e-beam Au.

Device number	1	2	3
Design type	(b)	(a)	(a)
Width/μm	150	120	100
Length/μm	115*	120	140
R_n/mΩ	16	23	29

3.4.2 Initial calculations of IV curves

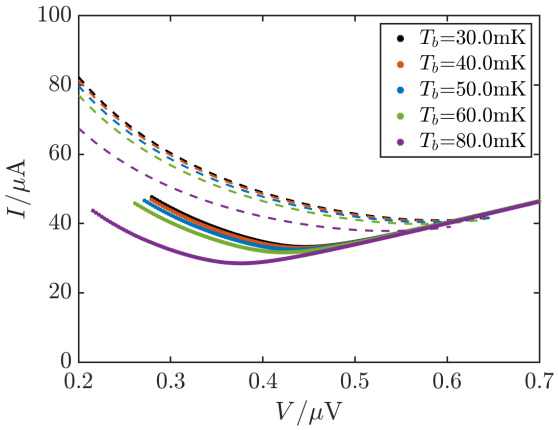

Figure 3.10 $I(V)$ curves measured (points) and calculated using a proximity effect model (dashed lines) over a range of bath temperatures T_b, for CSIC Device 1.

Figures 3.10 to 3.12 show the $I(V)$ curves (dashed lines) calculated using an initial set of material parameters and device geometries. The corresponding measured curves are shown as points. Where the values of parameters had not been measured experimentally, for example γ_B, the values used to model the SRON devices were taken as a first approximation. Although the model does a reasonable job of predicting the tracking in temperature of the $I(V)$ curves, for a given voltage, the calculated currents are higher than the measured currents for all three devices and at all bath temperatures. I therefore set about investigating the source of this discrepancy in the application of my model to Device 1.

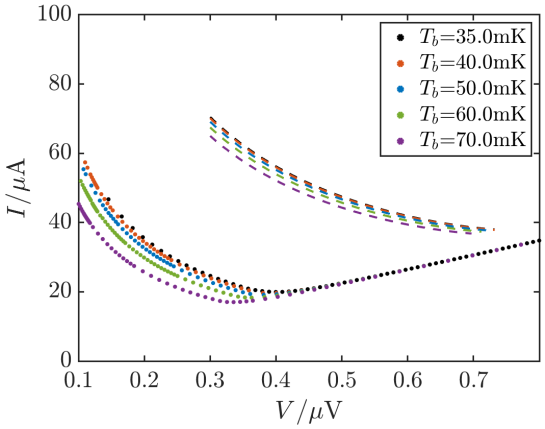

Figure 3.11 $I(V)$ curves measured (points) and calculated using a proximity effect model (dashed lines) over a range of bath temperatures T_b, for CSIC Device 2.

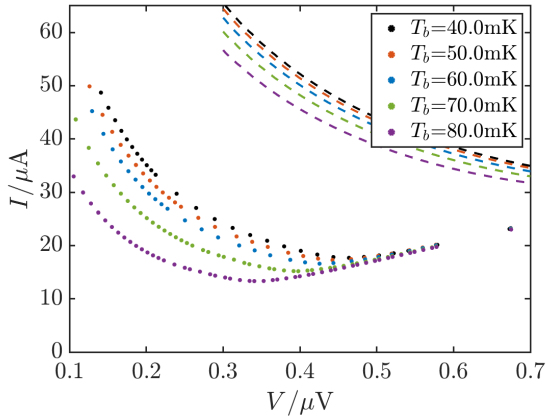

Figure 3.12 $I(V)$ curves measured (points) and calculated using a proximity effect model (dashed lines) over a range of bath temperatures T_b, for CSIC Device 3.

3.4.3 Investigating the source of the differences between the model and the data

Figure 3.13 shows a sample $I(V)$ curve at 40 mK for Device 1. The red dashed line indicates the initial model prediction, whilst the blue dashed line shows the effect of including a magnetic field, the green line shows the effect of increasing the boundary resistance and the purple line was calculated for a decreased bilayer transition temperature. For all simulations except the initial model, updated material parameters were used for the niobium leads.

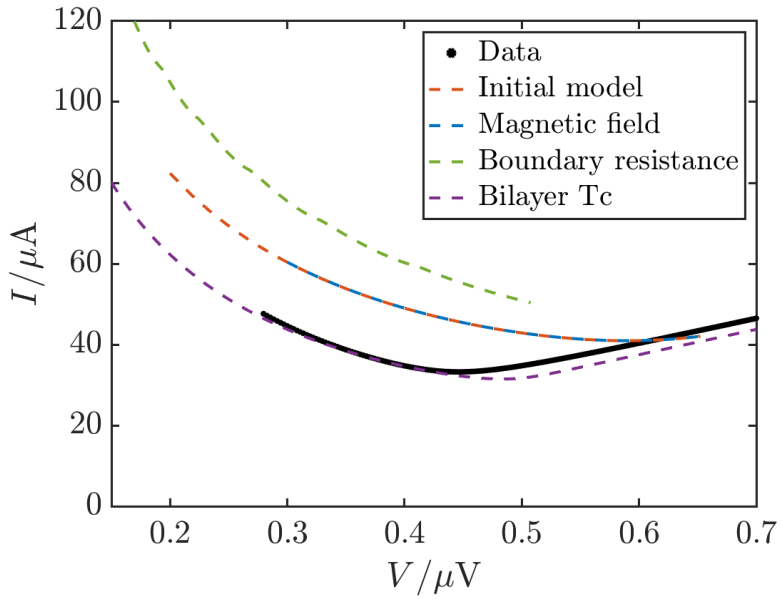

Figure 3.13 Black points show the $I(V)$ curve measured for Device 1 at a temperature of 40 mK. Dashed lines show a series of predictions using the proximity effect model for the $I(V)$ curve at 40 mK. The red dashed line shows the initial model prediction, whilst the blue, green and purple lines show the effects of including a magnetic field, increasing the boundary resistance and decreasing the critical temperature of the bilayer respectively.

Inclusion of magnetic field

The $I(V)$ curves measured may have been affected by stray magnetic fields, as the TESs were not fully shielded when the measurements were taken. Stray magnetic fields would act to suppress the current measured, explaining the discrepancy between the predicted and measured $I(V)$ curves. I therefore changed the value of ψ from 0.5π to 0.4π in the model to reflect suppression of the critical current by magnetic fields. The result of this change is shown by the blue dashed line in Figure 3.13. Combined with the change in material parameters, this did not produce a significant decrease in the critical current. This suggests that a large stray magnetic field would be needed to explain the difference between the model and the measurement.

Choice of γ_B

As the calculated currents were higher than the measured currents for a particular value of voltage, the initial model prediction of critical current was higher than the actual critical current of the thin film. One possible explanation for this would be a low boundary resistance in the model, as the lower the boundary resistance, the greater the diffusion of Cooper pairs from the electrodes to the bilayer and the higher the critical current of the thin film. Increasing the

boundary resistance and hence γ_B should lower the critical current of the film and hence the calculated currents in the $I(V)$ curves.

From previous projects, the simulation results are relatively insensitive to small changes in γ_B. For the SRON data, there was no significant difference in the modelling between using $\gamma_B = 9$ and $\gamma_B = 10$. I therefore hypothesised that a large change in γ_B would be required to significantly alter the current, and ran a simulation with $\gamma_B = 100$.

Initially, increasing the boundary resistance parameter to $\gamma_B = 100$ whilst keeping the temperature and current ranges the same did not allow me to access the required parameter space for the $I(V)$ curves. I therefore also had to alter the temperature and current ranges for the simulations. As seen in Figure 3.13, this larger value of γ_B, combined with the change in material parameters, increased the prediction for the current so did not explain the difference between the model and the measurement.

Calculation of an exact transition temperature for the bilayer

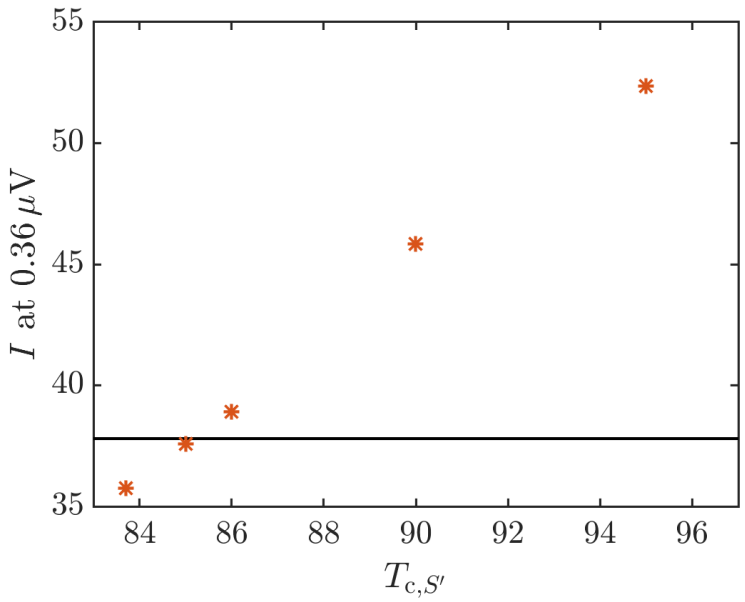

Figure 3.14 Current at a fixed voltage value, predicted using the proximity effect model, as a function of the bilayer transition temperature $T_{c,S'}$ used for the modelling. The black line indicates the measured value of current at that voltage.

Another source of discrepancy would be if the model used a value of transition temperature for the bilayer that was higher than the true value. The closer the bilayer to its transition temperature, the lower the critical current and hence the current, suggesting that the value I was using for the transition temperature of the bilayer was likely to be too high. As the transition

temperature of the bilayer was not known exactly, I carried out several simulations at different bilayer transition temperatures and used these results to interpolate a value of bilayer transition temperature that gave the expected current at a fixed voltage value.

Figure 3.14 shows the currents predicted by the model for a series of bilayer transition temperatures $T_{c,S'}$ at a voltage of 0.36 µV. Based on a linear interpolation, the bilayer transition temperature was around 85 mK. Using this transition temperature for the bilayer gave a prediction that was very close to the measured $I(V)$ curve, as shown by the purple dashed line in Figure 3.13. This transition temperature was used to recalculate $I(V)$ curves for all three sets of devices, to see whether a single updated transition temperature could explain the discrepancy between the model and the measurement for all three TESs.

3.4.4 Updated calculations of $R(T, I)$ surfaces and $I(V)$ curves

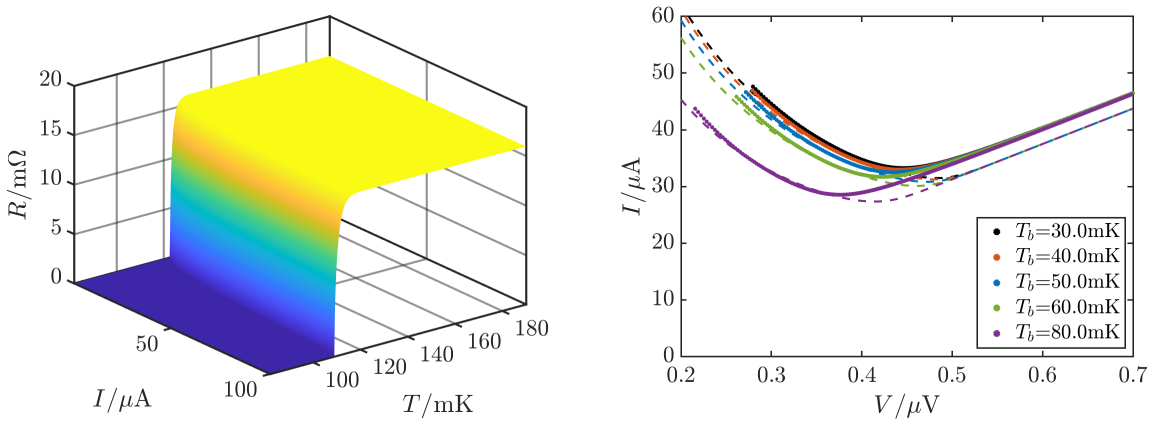

(a) (b)

Figure 3.15 (a) Calculated $R(T, I)$ for Device 1 with updated material parameters and an updated bilayer transition temperature. (b) Measured $I(V)$ curves (points) and calculated $I(V)$ curves (dashed lines) for this device at a series of bath temperatures.

Figures 3.15 to 3.17 show the $R(T, I)$ surfaces and $I(V)$ curves calculated for all three devices with an updated bilayer transition temperature and updated material parameters. The agreement between model and theory is improved for all three devices, and for Device 1, the model gives a reasonable description of both the individual $I(V)$ curves and the tracking of these curves with temperature. For Devices 2 and 3, there is still an offset between the model and the data, suggesting that the bilayer transition temperature was not the same for all three devices. This may be because molybdenum is highly sensitive to changes in deposition conditions, and so since Devices 2 and 3 were not from the same chip as Device 1, the transition temperature of the Mo may be different for these devices. There could also be a different

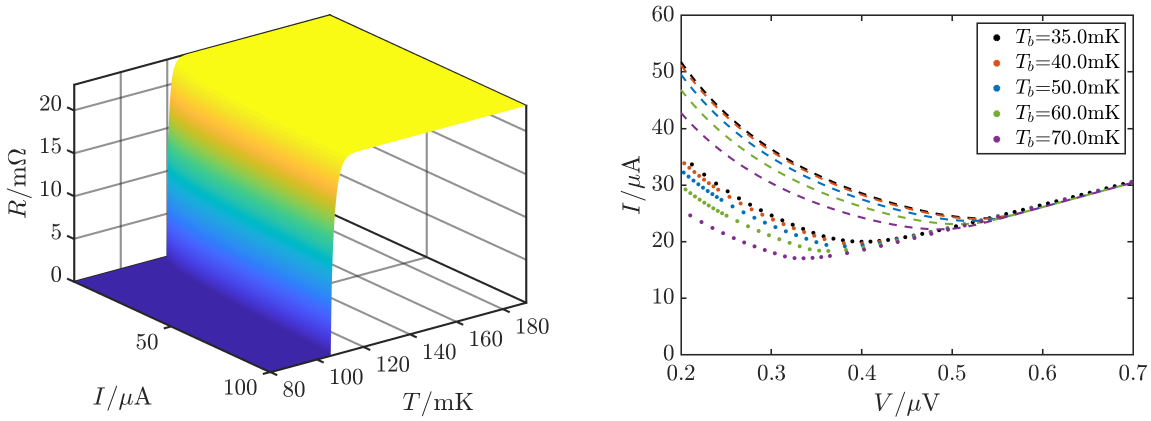

(a) (b)

Figure 3.16 (a) Calculated $R(T, I)$ for Device 2 with updated material parameters and an updated bilayer transition temperature. (b) Measured $I(V)$ curves (points) and calculated $I(V)$ curves (dashed lines) for this device at a series of bath temperatures.

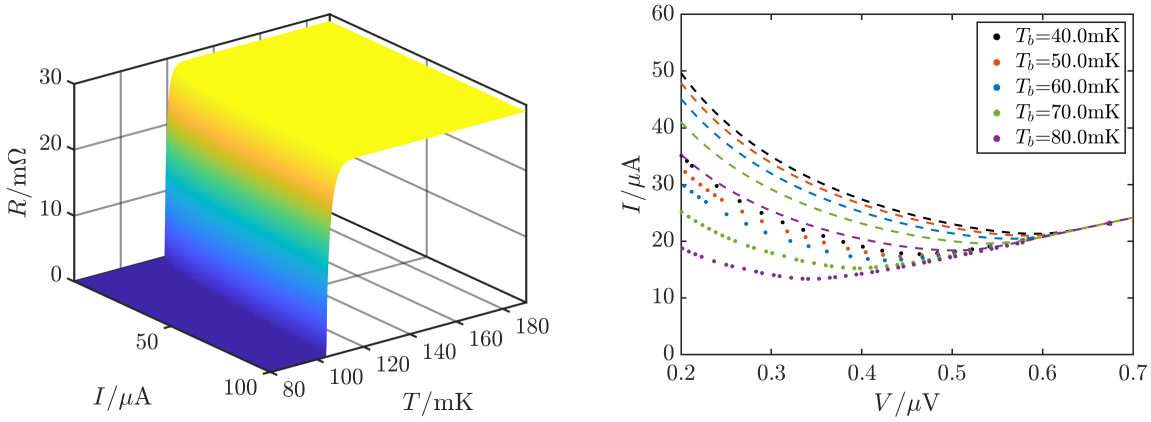

(a) (b)

Figure 3.17 (a) Calculated $R(T, I)$ for Device 3 with updated material parameters and an updated bilayer transition temperature. (b) Measured $I(V)$ curves (points) and calculated $I(V)$ curves (dashed lines) for this device at a series of bath temperatures.

boundary resistance between the sputtered and e-beam Au for these devices, affecting the bilayer transition temperature.

Checking for zero offsets

It was observed that there is still a constant offset when the TESs are normal, and the relationship $V = IR$ should hold for all TESs. The $I(V)$ curves in this region should be straight lines that interpolate back to the point $V = 0, I = 0$. I therefore carried out this interpolation to investigate the magnitude of the zero offset.

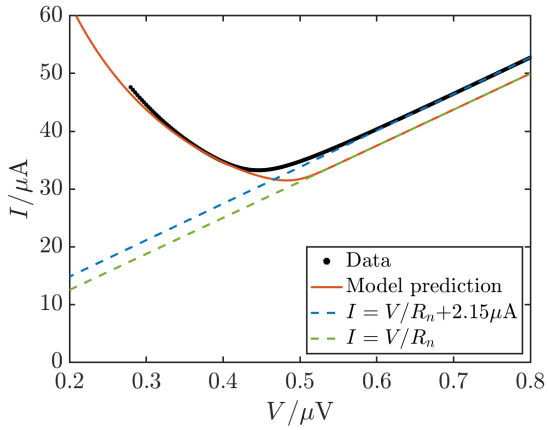

Figure 3.18 Measured $I(V)$ curve (black points), calculated model prediction (red line) and fits of $I = V/R_\mathrm{n} + I_0$ to both the data (blue dashed line) and model prediction (green dashed line). The measurement and model prediction were carried out at a bath temperature of 40 mK.

Figure 3.18 shows the data and model prediction at a bath temperature of 40 mK, along with fits of $I = V/R_\mathrm{n} + I_0$ to both the data (blue dashed line) and model prediction (green dashed line). There is a zero offset in the data, of the order of 2 µA. This may mean that the calculated bilayer transition temperature is not the true value of the bilayer transition temperature.

Checking $I(V)$ curves lie on $R(T, I)$ surface

As an additional check, the calculated $I(V)$ curves for Device 1 were plotted on the $R(T, I)$ surface to ensure the curves were within the surface, and the resulting plot is shown in Figure 3.19. The $I(V)$ curves lie within the surface as expected, showing that my method of calculating $I(V)$ curves was working as expected.

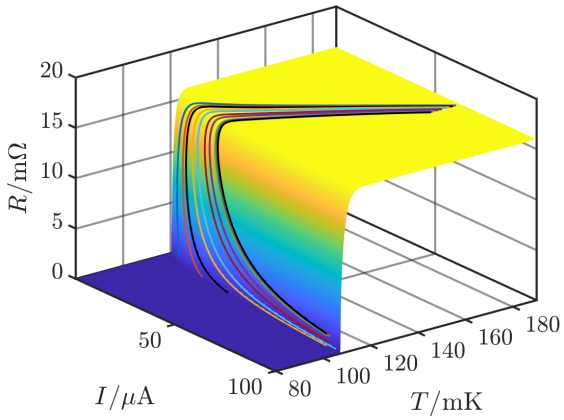

Figure 3.19 Calculated $R(T, I)$ surface for Device 1. The lines show the trajectories followed by the device for each of the calculated $I(V)$ curves.

3.4.5 Small devices

CSIC have also manufactured and tested much smaller TESs, in order to explore weak link behaviour. These devices were designed to have higher transition temperatures for ease of testing. The sizes, normal state resistances and transition temperatures for these TESs can be seen in Table 3.3. All three TESs were of design (b), as shown in Figure 3.9, and had $W = L$. Although the normal state resistances were different for these three TESs, their transition temperatures were very similar. I used my model to calculate transition temperatures for TES thin films of these geometries to see whether my model could account for this result, with a bilayer transition temperature $T_{c,S'}$=580 mK.

Table 3.3 Key device parameters for the three small CSIC TESs.

Device number	4	5	6
Design type	(b)	(b)	(b)
Width/μm	10	15	20
Length/μm	10	15	20
R_n/mΩ	94	80	75
T_c/mK	552	548	550

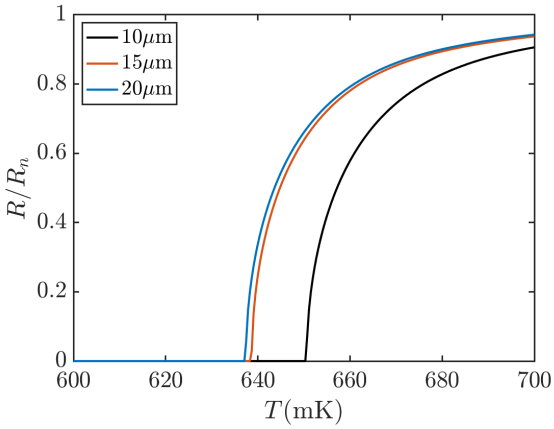

Figure 3.20 Calculated $R(T)$ curves at a fixed current for three TESs of different side lengths: 10 μm (black line), 15 μm (red line) and 20 μm (blue line). For all TESs, $L = W$.

Figure 3.20 shows the $R(T)$ curves at fixed current for Devices 4, 5 and 6. For all three devices, the $R(T)$ curves are very broad, indicating small values of α and a wide transition. The transition temperatures are also much higher than the measured bilayer transition temperature of 580 mK, suggesting a significant proximity effect from the electrodes. From Table 3.4, the calculated transition temperatures are much higher than the measured transition temperatures,

suggesting that there is a competing factor acting to reduce the proximity effect in the real devices. The model predicted similar transition temperatures for the 15 µm side length and 20 µm side length TESs, as observed experimentally. However, the predicted transition temperature for the 10 µm side length TES was around 10 mK higher, which does not agree with the trends obeyed by the measured transition temperatures.

Table 3.4 Measured and calculated transition temperatures for the three small CSIC TESs.

Device number	4	5	6
Measured T_c/mK	552	548	550
Calculated T_c/mK	650	638	637

3.4.6 Conclusions from modelling CSIC devices

Overall, for these devices the model gives a reasonable quantitative account of the $I(V)$ behaviour, but is highly sensitive to the transition temperature of the bilayer. This transition temperature appears to differ between the two sets of larger devices, possibly due to differences in manufacturing conditions. For the smaller devices, the model can account for trends in transition temperature but does not predict the exact changes in T_c that are observed experimentally. As a result, it is harder to use the model for exact predictive purposes, but modelling can still be used to investigate general trends with bilayer geometry.

3.5 Mo/Au devices developed and characterised in Cambridge

I also applied my model to three Mo/Au TESs made and tested in previous investigations by our group in Cambridge, in order to study a set of Mo/Au TESs with partial normal metal bars. The three designs used are shown in Figure 3.21, with all TESs having rectangular electrodes and normal metal side stripes to prevent underetching of the Mo layer. Design (a) is a plain TES, whilst design (b) has two partial normal metal bars and design (c) has six partial bars. I studied one TES of each design, with sizes, transition temperatures and normal state resistances as shown in Table 3.5. All of these TESs include absorbers, which were not included in the mathematical model.

3.5.1 Results for our group's TESs

From Figure 3.22, the predicted $I_c(T)$ is of the right magnitude for the plain device but is much smaller than expected for the two TESs with bars, suggesting that only a very small supercurrent

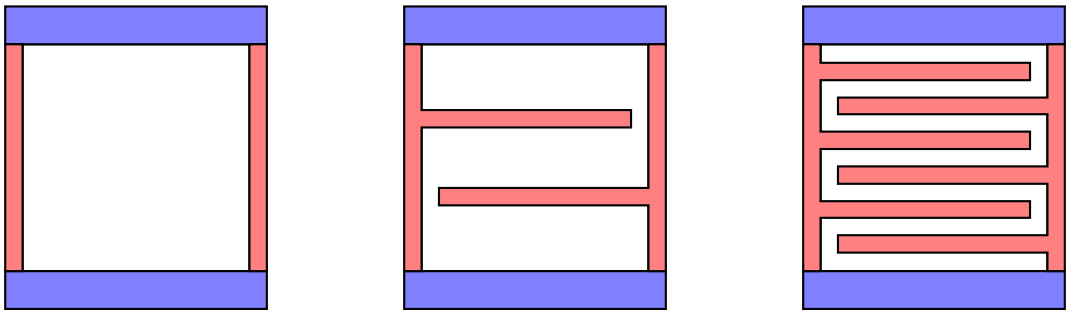

(a) (b) (c)

Figure 3.21 Device designs are shown here in top-down view, with electrodes (S) in blue, bilayers (S′) in white and normal metal patterning (S″) in red. All three designs have rectangular electrodes, but different numbers of partial normal metal bars. Design (a) is a plain device with normal metal side stripes, design (b) is patterned with two additional partial bars and design (c) is patterned with six additional partial bars.

Table 3.5 Key device parameters for three of the TESs tested by our group in Cambridge. All TESs were based on a 40/150 nm Mo/Au bilayer and any normal metal bars were an additional 200 nm thick.

Device number	1	2	3
Design type	(a)	(b)	(c)
Width/μm	60	88	88
Length/μm	62	91	91
R_n/mΩ	81	72	68
T_c/mK	201	195	181

could be supported for these two TESs. This contradicts experimental measurements that show that all three TESs support supercurrents of the order of μA. Additionally, the critical current does not appear to reduce when the number of normal metal bars is increased, which does not agree with my results from Chapter 2.

The reason for this unusually low prediction for I_c for the patterned TESs can be seen in Figure 3.23, which shows the maximum supercurrent as a function of position in the x direction, calculated using the proximity effect model at a temperature of 150 mK. In my modelling, I took the critical current to be the minimum value of this maximum supercurrent. For both TES thin films, the normal metal bars suppress the supercurrent to such an extent that no supercurrent can flow through the bars and the critical current is essentially zero. This shows that in these TES films, the bars are thick enough and wide enough that the supercurrent cannot flow directly through them. The supercurrent in these films therefore follows a meander pattern,

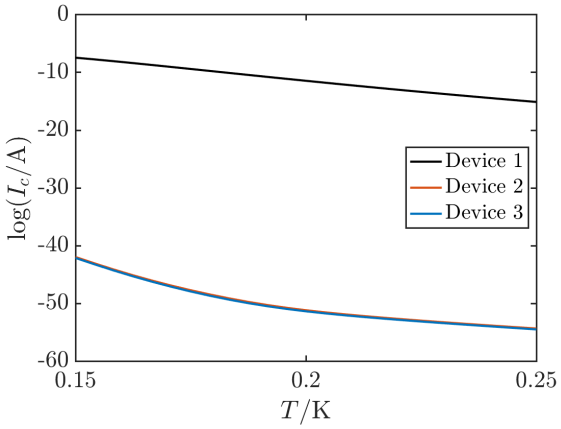

Figure 3.22 Model predictions of $I_c(T)$ for all three devices tested. Device 1 was unpatterned, whilst devices 2 and 3 were patterned with 2 and 6 partial normal metal bars respectively.

as hypothesised by other groups [94]. In order to describe these TES films, a 2D model of current flow would be required.

I therefore focused on applying my model to the plain TES, calculating $R(T, I)$ surfaces and $I(V)$ curves. The $R(T, I)$ surface shows a predicted transition temperature of around 200 mK at the operating current range of 0-5 µA, agreeing well with the measured transition temperature for this device of 201 mK. Using the initial set of parameters, the calculations for $I(V)$ consistently predicted currents that were too high, as seen in Figure 3.24b.

As in the previous section, there was no experimental measurement of the transition temperature of the bilayer, and so a transition temperature was calculated based on giving the correct current for a particular voltage and temperature. The $R(T, I)$ surface and $I(V)$ curves predicted using this updated transition temperature can be seen in Figure 3.25, along with the set of measured $I(V)$ curves for this device. With this updated transition temperature, the prediction for the overall device transition temperature is still of the correct order of magnitude, and the $I(V)$ curves are closer in magnitude to the measured $I(V)$ data and show the expected tracking with temperature. However, the slopes of the $I(V)$ curves are steeper than the model predicts. This could be because the model does not account for the presence of the normal metal side stripes, which produce TES films with steeper transitions.

3.5.2 Conclusions from modelling Cambridge devices

For this set of Mo/Au devices, knowing the exact transition temperature of the bilayer is important in order to make accurate predictions with a proximity effect model. The results for devices with bars show that in order to describe devices with thick normal metal patterning, a 2D model is required to describe the current flow. As for the devices in the previous section, for

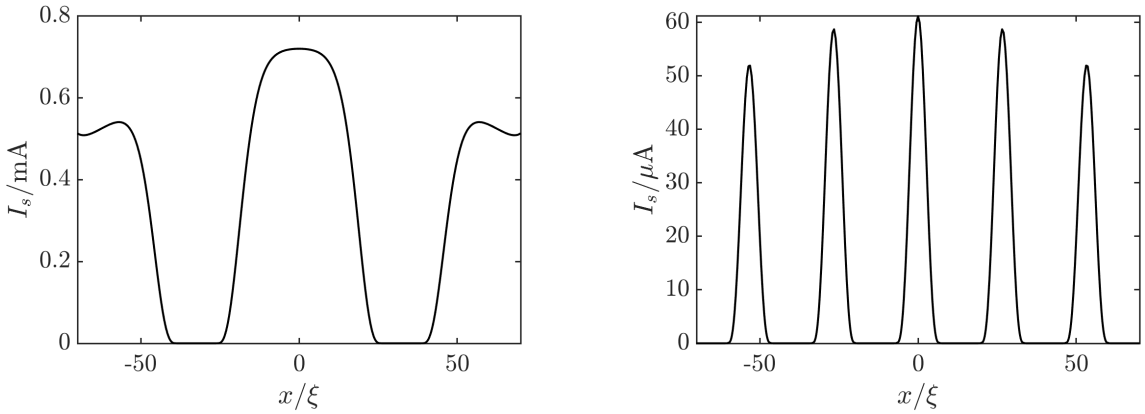

(a) (b)

Figure 3.23 Model predictions of $I_s(x)$ for (a) a TES with two partial normal metal bars and (b) a TES with six partial normal metal bars. For this calculation, T=150 mK.

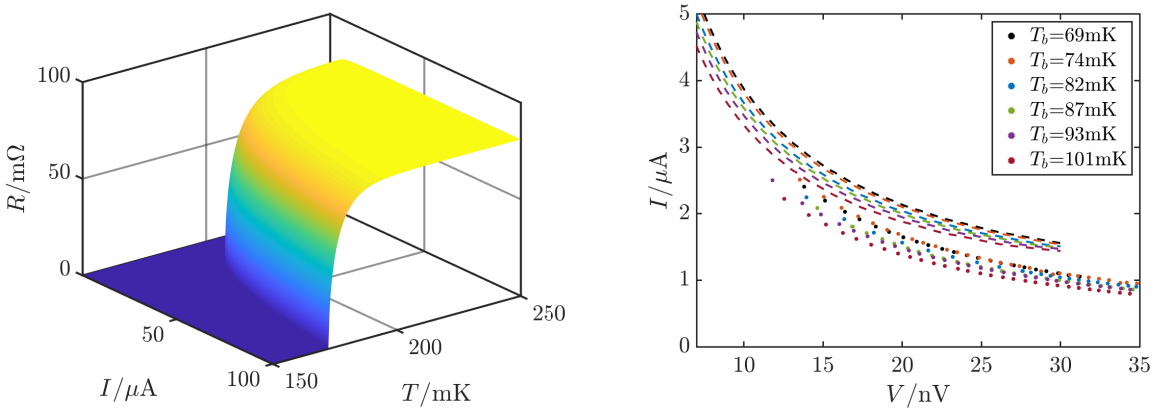

(a) (b)

Figure 3.24 (a) $R(T, I)$ predicted using the proximity effect model and (b) measured (points) and calculated (dashed lines) $I(V)$ curves for the plain TES for a range of bath temperatures.

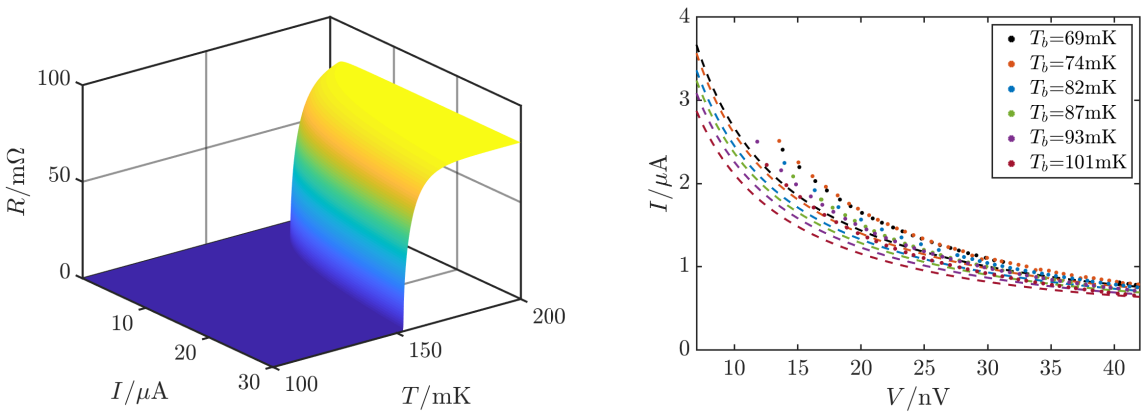

(a) (b)

Figure 3.25 (a) $R(T, I)$ predicted using the proximity effect model and (b) measured (points) and calculated (dashed lines) $I(V)$ curves for the plain TES for a range of bath temperatures.

these Mo/Au devices the model is useful as a tool for predicting general trends rather than exact behaviour.

3.6 Conclusions

I have presented a summary of the TES thin film designs used by different groups, including bilayer-based and alloy-based TESs as well as TESs made from elemental superconductors. I have also given an indication of the potential benefits and drawbacks of some material combinations. In general, these benefits and drawbacks are not sufficiently well known or understood to determine an optimal material combination or thin film geometry.

My proximity effect model has been successfully extended to solve the Usadel equations for real device geometries and material parameters. I have been able to use this model to make predictions of experimental measurements by calculating the $I(V)$ curves for a series of different device designs. My model provided a good account of all of the devices tested, particularly the Ti/Au TESs in Section 3.3, requiring an effective transition temperature to account for the Ti adhesive layer in the normal metal bars. The Mo/Au TESs in Sections 3.4 and 3.5 also required a single parameter, the transition temperature of the bilayer, to be fitted. These Mo/Au TESs display slightly more complex behaviour than Ti/Au TESs, with transitions that are sharper than those predicted by the model.

Ideally this model would not require any fitting or adjustment, in order to predict TES behaviour without actually making the TESs. The model also does not account for the 2D current flow that occurs in the TES films with partial normal metal bars. However, I was still

able to use the model to determine trends in device behaviour for different bilayer geometries, describe observed reductions in transition temperature and sensitivity with increasing numbers of bars and predict increases in transition temperature as bilayer size was reduced.

The overall success of this model provided a good justification for me to proceed in using the model as a predictive tool to design devices. In the next chapter, I will use the model to design a set of Mo/Au TESs for a series of experimental studies.

Chapter 4

Device and measurement system design and implementation

4.1 Introduction

In order to use and test the predictions of my model to investigate experimentally the effects of thin film geometry on TES performance, and to determine whether there is an optimal film geometry for a TES, I needed a set of devices that were all made using the same processing route. These devices should have different bilayer geometries but similar square resistances and thermal conductances. I therefore set out to design a chip containing a series of TESs and a system to test these devices and enable the study of TES magnetic field behaviour. I used the proximity effect model developed in Chapter 2 to help inform device design decisions, the first use of this model for its intended purpose.

In Section 4.2 I describe how the TESs were selected and designed, give an overview of the processing route used in Section 4.3 and explain the creation of the mask used to produce the TESs in Section 4.4. I then show the results of calibration testing in Section 4.5, which contains the results of tests on both calibration structures and unreleased TESs. These results helped me to select the most interesting TESs for study in Chapter 5. Section 4.6 presents the design for a new jig for testing TESs, which allowed me to study magnetic field effects in detail, and I show the results of characterisation of this new test system in Section 4.7, before presenting the final experimental configuration used to test the devices in Section 4.8.

4.2 Selection of device designs

When choosing the devices to study, I looked at data from previous devices made by the group to predict thermal behaviour, as well as using my proximity model from Chapter 2 to predict the transition temperatures of TES thin films of different sizes and with different numbers of bars.

4.2.1 Study of thermal behaviour of previous devices

I needed to ensure that the thermal conductivity G, given by Equation (2.15), and the thermal exponent n in Equation (2.14) were as similar as possible for all of the devices, hence any differences between TESs were due to their geometry and not their thermal behaviour. The group had previously manufactured and tested a number of devices using the same processing routes and silicon wafers that were used to manufacture this set of devices, and so I used these measured values of G and n [2, 12, 16, 17, 83, 121, 136, 137, 168] as a guide to how the two parameters vary with leg dimensions.

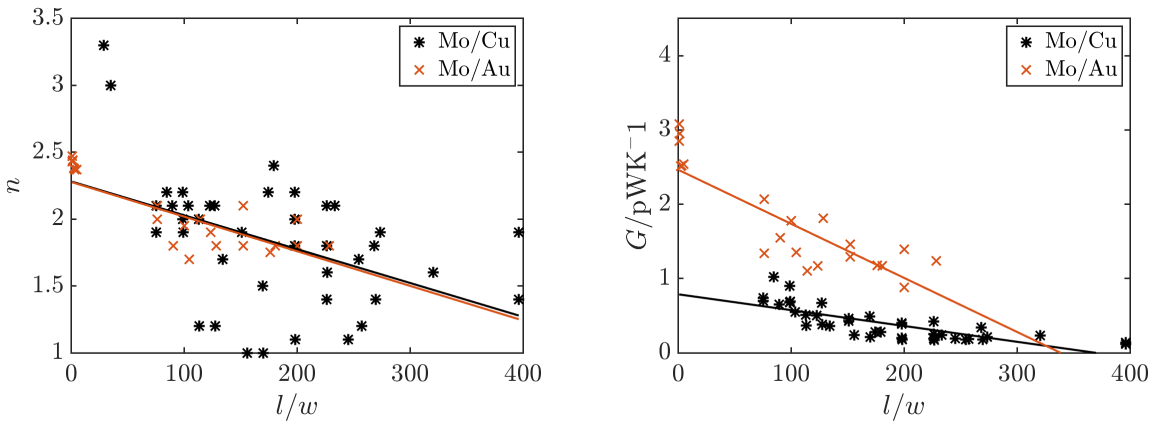

(a) (b)

Figure 4.1 (a) Thermal exponent n and (b) conductivity G as a function of the ratio of TES leg length l to leg width w, for Mo/Au and Mo/Cu devices previously manufactured and tested by the group. For each set of data, a best-fit line of the same colour has been calculated and plotted.

Figure 4.1a shows how the exponent in the power flow equation, n, varies with the length to width (l/w) ratio of the legs for Mo/Au and Mo/Cu devices deposited on Si_xN_y membranes. There is a general reduction in n as the ratio increases for both the Mo/Au devices, and the Mo/Cu devices, reflecting the transition from ballistic to diffusive heat transfer. The effects of the length to width ratio of the legs on the thermal conductivity G are seen in Figure 4.1b. There is a general reduction in G as the ratio increases, as expected, for both the Mo/Cu and

Mo/Au devices. The differences in n and G between the Mo/Cu and Mo/Au devices are likely to be due to the difference in T_c between the two bilayers, resulting in different operating points.

From Equation (2.15), $G \propto T_c^{(n-1)}$, which means that as the transition temperatures are different for each device size, if the leg length is constant then G varies between devices of different sizes. I considered compensating for this by adjusting the leg lengths, but decided against it as the leg length affects other aspects of device behaviour. For example, the mechanism of heat transfer is different in longer legs and shorter legs [135, 136], which has a significant impact on the thermal conductivity of the TES. Making all the legs the same length therefore allowed some standardisation between devices. I set l=50 µm and w=1.41 µm for all of the TESs, with a ratio $l/w \approx 35$, which, from Figure 4.1b, corresponds to $G \approx 2.25\,\mathrm{pWK}^{-1}$. This resulted in devices with slightly different, but comparable values of G, as shown in Section 5.3.2.

4.2.2 Choice of materials

In order to investigate the effects of bilayer geometry, I chose to use the same material combination to make all of the device bilayers. I considered two possible bilayers; Ti/Au and Mo/Au, and carried out simulations for both bilayers to see if there were any significant differences between the two material combinations. The main differences were in device transition temperature, due to the transition temperature of the bilayer and the thicknesses of the gold layer/bars. Mo/Au was eventually selected as the bilayer material composition, as the group has a well-established process route for making Mo/Au devices

4.2.3 Number of bars

I included bilayers with both odd and even numbers of bars, since my field modelling in Section 2.4.2 showed that there are significant differences in the self-field produced by the current in TES thin films with an odd number of bars compared to TES films with an even number of bars. TES films with an odd number of bars have a larger self-field, making them less susceptible to applied magnetic fields. There are no publications that investigate this effect, but in recent years, several groups have designed TES thin films with odd numbers of partial normal metal bars [11, 94, 154, 169].

4.2.4 Aspect ratio

Both square and rectangular bilayers are regularly used to make TESs. The bilayer shape determines the overall resistance of the thin film, which means that a short, wide film may have

a resistance that is too low for stable voltage bias. Since I wanted to be able to compare films of different lengths, there were two options: either to keep the width constant for all film lengths; or to keep the films square so their resistance is the same. The film lengths were chosen to vary by a factor of 20, which would have caused a significant difference in the normal state resistances if the width had been constant. It is difficult to identify a width to produce 100 µm and 5 µm long thin films with suitable resistances. Using square films meant that I could keep the resistance the same between films, whilst also allowing me to probe the effects of normal metal side bars on films of different widths.

4.2.5 Effective width of bilayers

The deposition of normal metal bars (S″) along the sides of a superconducting bilayer (S′) prevents undercutting during processing [153]. These normal metal bars mean that the lateral cross-section of the superconducting component is a S″ – S′ – S″ proximity system, with the normal metal bars acting to reduce superconductivity in the bilayer. For the films investigated, I wanted to make sure that these bars would not result in the complete suppression of superconductivity in the smallest devices.

I simulated cross sections of films based on Ti/Au and Mo/Au bilayers to investigate the effects of normal metal (Au) bars on the variation of superconductivity across the film width. In these simulations, the widths of the side bars were scaled with the overall width of the film: the widest film, with a width of 55 µm, had side bars of width 17 µm, and the narrowest film, with a width of 6 µm, had side bars of width 1.8 µm.

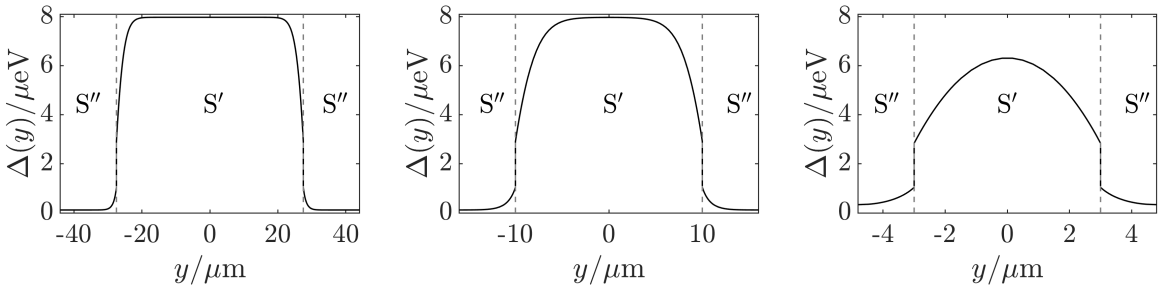

(a) W=55 µm. (b) W=20 µm. (c) W=6 µm.

Figure 4.2 Order parameter $\Delta(y)$ across the width (y) of a Mo/Au thin film of total width W, at a temperature of 0.1 K.

Figure 4.2 shows how the order parameter varies across the width of a Mo/Au thin film, at a temperature of 0.1 K, for three thin films, one of width 55 µm (4.2a), one of width 20 µm (4.2b), and one of width 6 µm (4.2c). Even in the 6 µm wide thin film, the order parameter is

still non-zero across the entire width of the film, indicating that the complete suppression of superconductivity will not occur in TES thin films of this size.

From Figure 4.2c, it can be seen that in the 6 µm wide film the order parameter is constantly changing across the width of the film and never reaches the maximum value of the order parameter obtained in the 55 µm wide film. The region of the film where the order parameter is constant (differences between successive values are less than 0.2 %) can be used to define an effective width of the film, the region where the normal metal side bars do not affect the superconductivity. Figure 4.2b shows the order parameter at this limiting width, of around 20 µm.

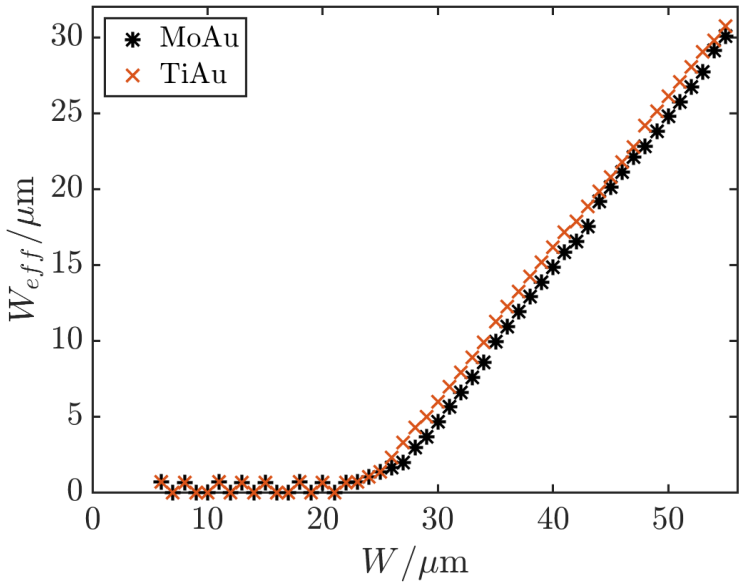

Figure 4.3 Effective width, the width across which the order parameter is constant, as a function of the total bilayer width W for (black asterisks) Mo/Au thin films and (red crosses) Ti/Au thin films, at a temperature of 100 mK.

Figure 4.3 shows how the effective widths of a Mo/Au thin film and a Ti/Au thin film vary with the total bilayer width, at a temperature of 100 mK. For the Mo/Au film, the limiting width looks to be around 20-30 µm, whilst for the Ti/Au film, the limiting width is around 20-25 µm - below this range, the effective width is zero; and above this range, the effective width increases at the same rate as the actual film width. I therefore selected thin film geometries to encompass the three different width regimes - films that had width much less than the limiting width, in which the order parameter is suppressed across the whole film; films of about the limiting width, and films with width much greater than the limiting width.

4.2.6 Device length for Ti/Au bilayers

I simulated thin films based on Ti/Au bilayers, using my model developed in Chapter 2, to investigate the effects of varying the length on $R(T)$ and the transition temperature. I ran two sets of simulations, one for films with three normal metal bars and one for unpatterned films. These were chosen to give the extremes of the transition temperatures for each film size, since the transition temperature is highest for a film with no bars and lowest for a film with the most bars. The range of lengths investigated was based on my results from Section 4.2.5, taking in a range of film sizes, from films where the length and width are much greater than the effective width to films where the length and width are much smaller than the effective width.

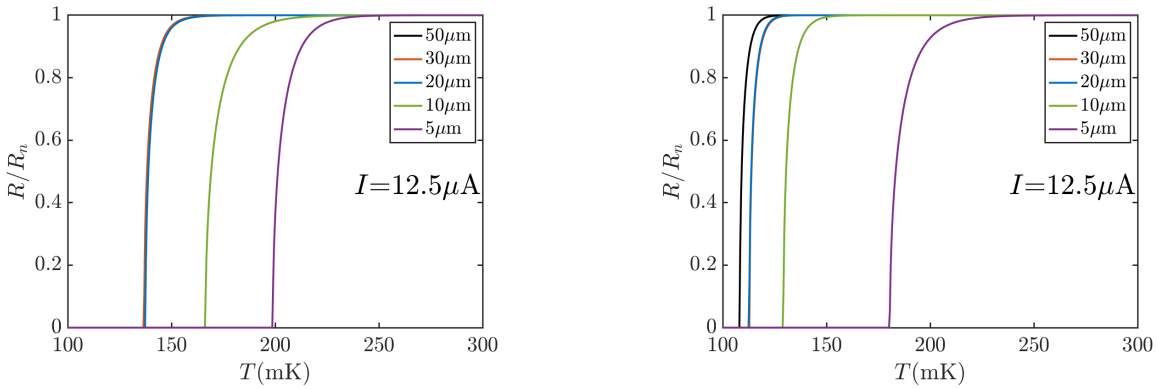

(a) Unpatterned TESs, $N = 0$.

(b) $N = 3$ normal metal stripes.

Figure 4.4 $R(T)$ curves calculated using the proximity effect model, for square Ti/Au bilayers with different side lengths. The two sets of devices shown in (a) and (b) have different bilayer geometries. The calculations were carried out at a TES current of 12.5 µA. I assumed that any stripes were 50 nm thick and were as long as the bilayer was wide. The widths of the stripes were scaled in proportion to the side length of the bilayer.

In Figure 4.4, calculated $R(T)$ curves are shown for square TES bilayers, with side lengths ranging from 5-50 µm. (4.4a) is for bare bilayers; (4.4b) is for bilayers with three normal metal bars. These bars are 50 nm thick, equally spaced and have widths proportional to the size of the bilayer. There is not much difference in transition width or temperature between the 50, 30 and 20 µm films, but there is a significant increase in transition temperature from the 20 µm films to the 10 µm thin films, and a further increase in T_c between the 10 µm thin films and the 5 µm thin films. As can be seen in Figure 4.5, the value of α does not significantly change with the addition of normal metal bars for these smaller thin films. With the exception of the 5 and 10 µm unpatterned thin films, the maximum value of α reduces slightly as the thin film size increases.

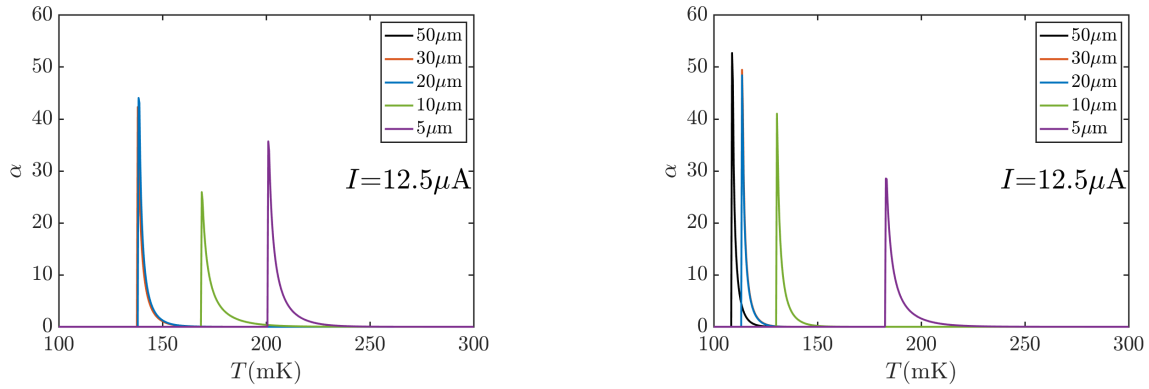

(a) Unpatterned TESs, $N = 0$.

(b) $N = 3$ normal metal stripes.

Figure 4.5 $\alpha(T)$ curves calculated using the proximity effect model, for square Ti/Au bilayers with different side lengths. The two sets of devices shown in (a) and (b) have different bilayer geometries. The calculations were carried out at a TES current of 12.5 µA. I assumed that any stripes were 50 nm thick and were as long as the bilayer was wide. The widths of the stripes were scaled in proportion to the side length of the bilayer.

Table 4.1 Transition temperatures for Ti/Au thin films of a series of different lengths, both with and without stripes.

Device length/µm	T_c for unpatterned TES/mK	T_c for TESs with 3 stripes/mK
50	137	107
30	137	113
20	137	113
10	164	129
5	200	179

Table 4.1 shows the transition temperatures for modelled Ti/Au thin films of different sizes with three normal metal stripes and with no normal metal stripes. Our experimental system is capable of accurately characterising thin films with transition temperatures above 120 mK, meaning that all the thin films simulated have transition temperatures within or very close to our working range. This was a good indication that all of these film sizes could be included in the study with up to three normal metal stripes.

I investigated the relationship between T_c and L in Figure 4.6 for bilayers both with and without normal metal stripes. For a relationship of the form $T_c \propto L^n$, Figure 4.6 shows n = -0.17 for unpatterned bilayers and n = -0.22 for bilayers with normal metal stripes. These values of n are different to the value of n = -2 measured experimentally [1] and the value of n=-0.7 calculated in Chapter 2, due to the difference in material parameters. Previous relationships

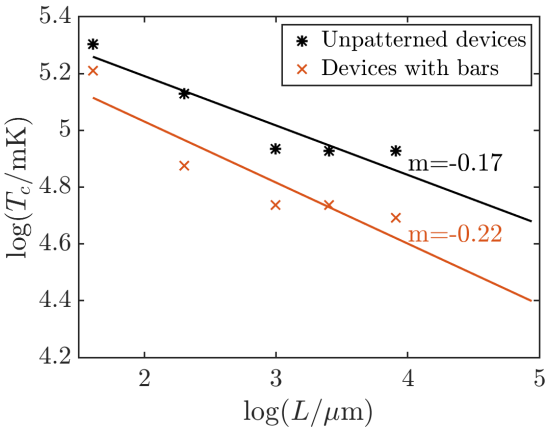

Figure 4.6 T_c as a function of bilayer side length L. For a relationship of the form $T_c \propto L^n$, n = -0.17 for unpatterned bilayers (black asterisks) and n = -0.22 for bilayers with normal metal stripes (red crosses). The solid lines show the fits to the data points of corresponding colour, used to find the values of n. T_c was calculated at a TES current of 12.5 µA.

have been measured and calculated for Mo/Au bilayers whilst these relations are calculated for Ti/Au bilayers.

Table 4.2 Estimates of heat capacity for devices with and without normal metal stripes based on square bilayers with different side lengths. All devices consist of a 17/70 nm Ti/Au bilayer, and any additional Au stripes are 50 nm thick. Any contribution to heat capacity from absorbers is not included.

Side length/µm	C for device without bars/ fJ K^{-1}	C for device with bars/ fJ K^{-1}
50	3.01	3.86
30	1.08	1.39
20	0.48	0.62
10	0.12	0.15
5	0.03	0.04

Table 4.2 displays estimates of the heat capacities of TESs with different square bilayer sizes, with and without normal metal bars. The heat capacity of the largest device is about 100 times that of the smallest, and adding bars increases the heat capacity by about 30 %.

From the heat capacity and the transition temperature, the effect of bilayer size on response time, $\tau_{\text{eff}} \propto C/(G(1+\alpha/n))$, can be predicted. For fast TESs, a small heat capacity and a large value of α are desirable. Comparing the 50 µm bilayer device with the 5 µm bilayer device, the 50 µm bilayer has a value of α about 1.5-2 times larger than the 5 µm bilayer, and a heat capacity approximately 100 times larger. For TESs without absorbers, such as mine, devices with smaller bilayers should therefore be faster, as I keep G and n approximately constant between devices,

and the large reduction in heat capacity compared to the reduction in α shown in Figure 4.5 leads to a decrease in τ_{eff}. These smaller bilayers do not show a significant reduction in α with the addition of normal metal bars, and so adding bars should produce a reduction in excess noise, but will also result in a small reduction in response time. For TES films with thicker bars, this reduction in response time will be more significant so bars may be less desirable.

For devices that will be operated as calorimeters, it is also useful to consider the effect of bilayer size on energy resolution $\Delta E \propto T\sqrt{Ck_{\text{B}}/\alpha}$. For good energy resolution, devices should have low transition temperatures and heat capacities, and high values of α. When operated as calorimeters, TESs typically require an additional absorber, and so the heat capacity C will be dominated by the heat capacity of this absorber, and so will not vary significantly with bilayer size. Therefore, for these devices, the slightly higher α and lower transition temperature of larger bilayers makes larger films more desirable in terms of speed and energy resolution. Although for these larger bilayers, metal bars reduce the value of α by up to an order of magnitude, they have also been shown to reduce excess noise [11]. This phenomenon is not described by my modelling, and so it should be considered whether or not the higher theoretical energy resolution for unpatterned devices is counteracted by the additional excess noise.

When TESs are used for imaging, they are fabricated in arrays to cover the field of view of the instrument. Here a high fill factor is desirable, and so for devices without absorbers, smaller bilayers have the additional advantage of providing better spatial resolution, as they can be packed more closely in arrays.

Finally, smaller films will experience less magnetic flux for a given field, since magnetic flux $\Phi = BA$, where A is the area of the film. This reduced magnetic flux should make smaller TES films less susceptible to applied magnetic fields. It is desirable to create TESs that are less sensitive to applied magnetic fields, since this either allows us to improve the performance of the TESs, or reduce the level of magnetic shielding required.

4.2.7 Device length for Mo/Au bilayers

As discussed in Chapter 3, my proximity effect model does not work well for films with thick normal metal bars, and I will return to this observation later on in this chapter, in Section 4.5.2. I therefore only used my model to examine unpatterned Mo/Au TES films.

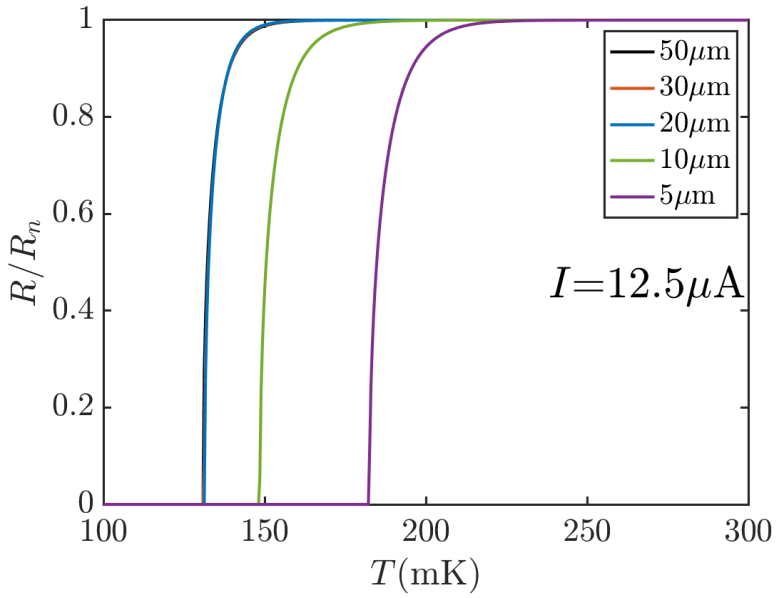

Figure 4.7 $R(T)$ curves calculated using the proximity effect model, for unpatterned square Mo/Au bilayers with different side lengths. The calculations were carried out at a TES current of 12.5 µA.

Figure 4.7 shows $R(T)$ curves for square Mo/Au films of a range of different side lengths. All of the thin films have transition temperatures within the range required for my study. Based on the results of Section 4.2.6, I assume that for films with three full normal metal bars, the transition temperatures will be a few tens of mK lower than for the unpatterned films. There is therefore a concern that these films may have transition temperatures that are lower than the working range of the experiment. Previous experiments suggest that films longer than these with partial normal metal bars have transitions within the working range. I therefore decided to produce bilayers with both partial and full Au bars, since at least some of the bilayers with partial metal bars should have T_c high enough to measure. If both the bilayers with full and partial metal bars have transition temperatures within the working range, this would allow investigation of the differences between the two bar types.

Table 4.3 shows the predicted transition temperatures for these unpatterned devices. As for the Ti/Au devices, there is a significant increase in transition temperature from the 20 µm side length film to the 10 µm thin film, and a further increase in T_c between the 10 µm thin film and

the 5 µm thin film. For these TESs, $T_c \propto L^{-0.14}$, so $n = -0.14$, which does not agree with the value of n = -2 measured experimentally [1].

Table 4.3 Transition temperatures for unpatterned Mo/Au thin films of a series of different lengths.

Device length/µm	T_c for unpatterned TES/mK
50	131
30	131
20	131
10	148
5	182

4.2.8 Conclusions and chosen device geometries

The TES thin film side length of particular interest for my study was 20-30 µm, where from the results of my proximity effect model in Section 4.2.5, the side bars start to have a sizeable impact on the order parameter all the way across the film. I wanted to investigate both above and below this region of interest, starting from a parameter space that has already been explored for reference:

- I designed a wafer containing 6 chips, with 30 released devices and 2 unreleased devices on each chip.
- All unreleased devices have no additional patterning.
- The released TESs have 0-3 normal metal bars.
- Of these 6 chips, 3 chips have devices with partial bars on the thin film (80 % of film width) and 3 have devices with full bars on the film (100 % of film width), as indicated in Figure 4.8.
- The suspended Si_xN_y membrane structures have four legs of length 50 µm, and width 1.41 µm, giving an expected thermal conductance $G \approx$ few pWK^{-1}.
- The wells that were etched are octagonal (with extended regions in the smaller wells to keep the surface area for etch constant), meaning that the legs meet the sides at a 90° angle. This design was selected to improve the etching of the join between the legs and the sides of the well, since acute angles are much harder to etch than right angles. It also reduces stress on the join.
- The width of the Nb electrodes is 10 µm for all TESs, with a 5 µm overlap onto the bilayer.
- The side bars to prevent overetch are 7 µm wide with a 4 µm overlap onto the bilayer.
- The bilayer is made of Mo/Au, with a target $T_c \approx 130 - 140$ mK for the larger films.

The overlaps between the side bars and the bilayer and the electrodes and the bilayer ensured good electrical and thermal conductivity between the layers, as well as allowing for the tolerance in alignment of the layers. These overlaps are indicated in Figure 4.8, which also indicates how the length and width of the bilayer are defined.

Table 4.4 shows the 30 device designs selected for study. The dashed lines indicate the sets of devices with 0, 1, 2 and 3 bars. There are no 5 µm devices with more than one bar as it would not be possible to deposit bars that are narrow enough to fit two or more of them on a single 5 µm film.

Table 4.4 Device parameters for the 30 device designs selected for my study. The dashed lines indicate the sets of devices with 0, 1, 2 and 3 bars. The number in the left hand column is the number used to label the device in processing, to allow easy identification of all the devices. Figure 4.8 shows how the length and width of the TES thin film are defined.

ID number	Side length of bilayer /μm	Number of bars	Bar width/μm	Bar spacing/μm
1	100	0	-	-
2	70	0	-	-
3	50	0	-	-
4	40	0	-	-
5	30	0	-	-
6	20	0	-	-
7	10	0	-	-
8	5	0	-	-
9	100	1	10	45
10	70	1	7	31.5
11	50	1	5	22.5
12	40	1	4	18
13	30	1	3	13.5
14	20	1	2	9
15	10	1	1	4.5
16	5	1	1	2
17	100	2	10	26.7
18	70	2	7	18.7
19	50	2	5	13.3
20	40	2	4	10.7
21	30	2	3	8
22	20	2	2	5.3
23	10	2	1	2.7
24	100	3	10	17.5
25	70	3	7	12.25
26	50	3	5	8.75
27	40	3	4	7
28	30	3	3	5.25
29	20	3	2	3.5
30	10	3	1	1.75

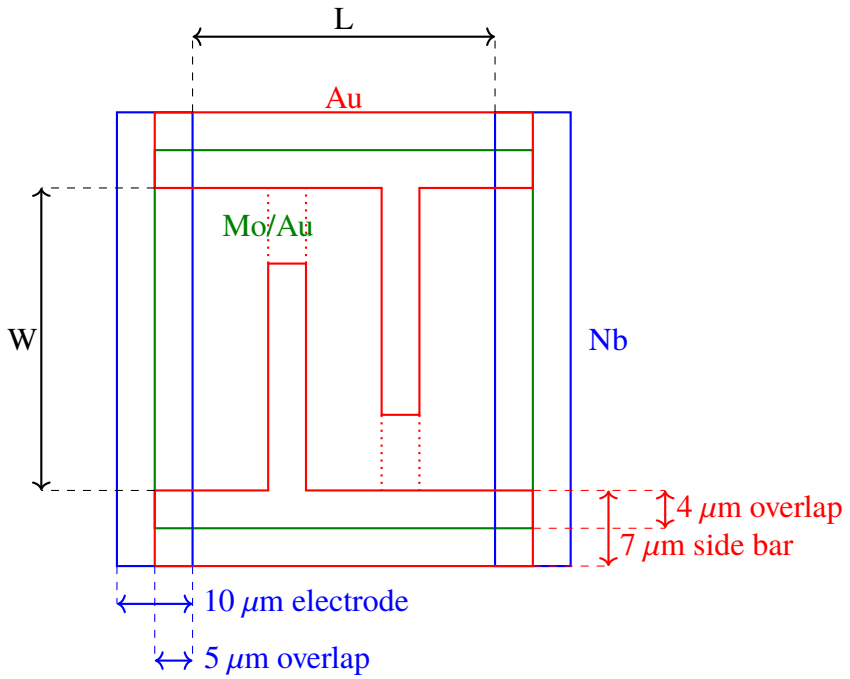

Figure 4.8 Diagram of the superconducting component of a TES, indicating the widths and overlaps of the Au side bars and Nb electrodes, as well as the definitions of the Mo/Au bilayer length L and width W. For all devices designed, the films have $L = W$. The device shown has partial normal metal bars on its thin film; the red dotted lines indicate where the bars will extend for a film with full normal metal bars.

These 30 devices were supplemented by two much larger unreleased TESs linked to the remaining two pairs of pads available on the chip design, as shown in Figure 4.12. The sizes of these unreleased TESs were different on all six chips, and the decision on whether or not to study these devices further was taken based on $R(T)$ measurements made on similar unreleased devices on one of the test chips.

4.3 Overview of device fabrication

In order to produce a mask design for a TES chip, it is important to understand the processes involved. Fabrication of my devices was however carried out by other members of the Quantum Sensors group, who have considerable processing experience.

The processing route used to produce the Mo/Au TESs is similar to routes used previously by the group to make Mo/Au devices for other projects [153]. We started with a silicon wafer coated with 50 nm of SiO_2 and 200 nm of Si_xN_y on both sides, as seen in the first diagram of Figure 4.9. The SiO_2 acts as an etch stop and the Si_xN_y will form the supporting membranes. These coatings were selectively removed using a reactive ion etch (RIE) to define the supporting membrane for the TESs (diagram 2), and on the underside of the wafer to define the undersides of the wells (diagram 3). Mo/Au bilayers of thickness 40/120 nm were deposited and wet-etched to form the TES bilayer (diagram 4), then a gold thermalisation layer of thickness 200 nm was deposited and patterned by lift-off on the underside of the wafer (diagram 5). Further deposition and lift-off steps were used to form the 200 nm thick Au bars on the bilayers (diagram 6) and the 200 nm thick Nb wiring (diagram 7). Finally the wafer was bonded onto a carrier wafer using crystal bond and deep reactive ion etching (DRIE) was used to define the wells from the backside (diagram 8). Two further wafers were fabricated, one with a 40/140 nm Mo/Au bilayer to give a set of devices of lower transition temperature, and one without the final DRIE step to provide devices for early transition temperature tests.

4.4 Mask design

I used Klayout [170] to produce a mask design for a wafer containing six large chips, each of which contained a set of 32 devices as described in Section 4.2.8. Of these six chips, three contained TESs with partial bars on the bilayers and three contained TESs with stripes on the bilayers. This redundancy meant that even if some devices had been damaged during processing, I would have had backup devices to replace them. I based the wiring and layout on an existing mask design by the group to make the chips compatible with our electronics and wiring.

To ensure a good yield on devices of a variety of different film sizes, I designed the wells to all have the same cross-sectional area. DRIE is known to be faster for larger feature sizes so this ensured a uniform etch rate across all the wells. Images of the mask for the largest and smallest devices can be seen in Figure 4.10. The minimum feature size was determined by the processing methods available and the smallest single feature is a 1 µm wide bar on a 5 µm wide TES film.

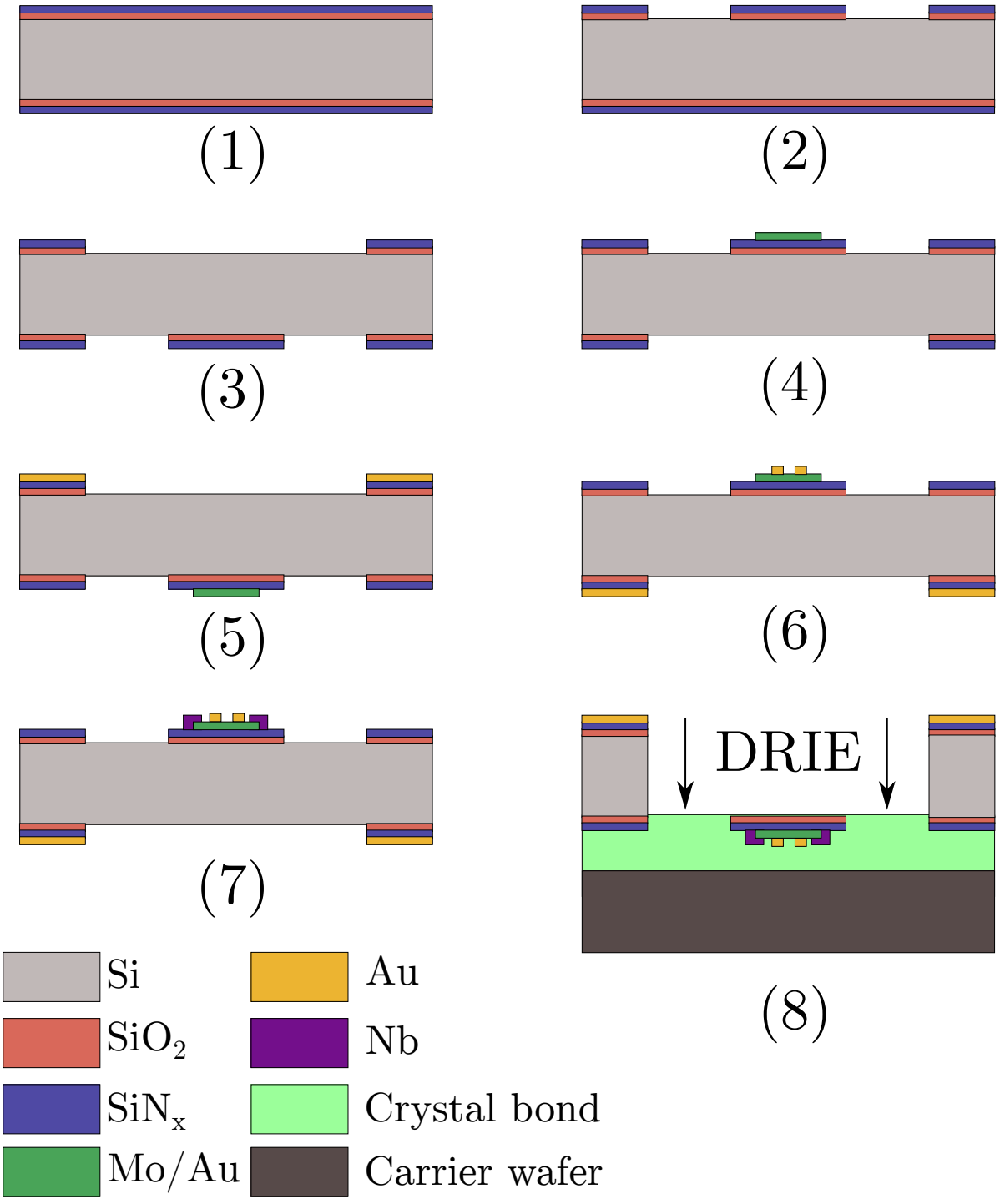

Figure 4.9 Processing route used to produce our devices. A silicon wafer (1) is patterned using RIE (2), (3), before TES bilayers are deposited (4), an Au thermalisation layer is added on the underside (5) and the bilayers are patterned (6). Finally the Nb wiring is added (7) and the TES wells are defined using DRIE (8).

In order to produce designs for all 30 TESs with the correct overlaps, bilayer sizes and well depths, I made use of the macro functionality of Klayout, writing Python-based code to automatically generate the TES designs and scale the etch wells, membranes and bilayers appropriately.

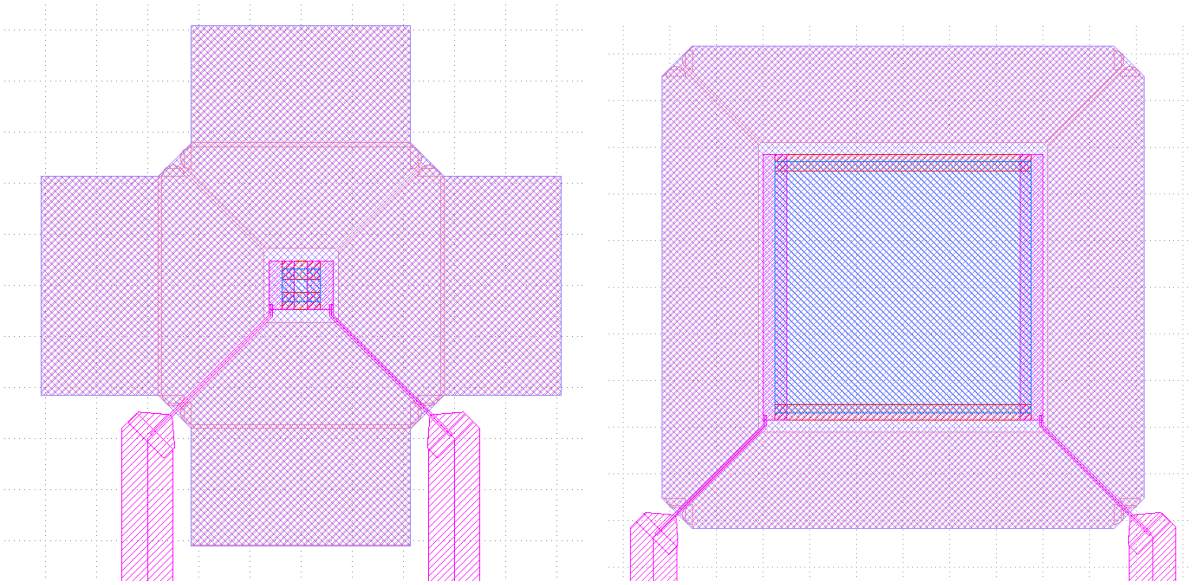

(a) L=5 µm. (b) L=100 µm.

Figure 4.10 Mask designs for (a) the smallest unpatterned device made and (b) the largest unpatterned device made. The bright pink regions show the niobium wiring, the blue regions are the Mo/Au thin film of side length L and the dark pink regions indicate where the substrate will be removed to produce membrane-suspended devices.

Several aspects of the mask were designed to optimise the yield of devices, as seen in Figure 4.11. The ends of the Si_xN_y legs were rounded off to reduce stress on the corners and ensure there are no sharp corners, thereby preventing cracking. The legs were attached at right angles to the surrounding membrane, rather than at acute angles, making them easier to etch as well as reducing the stress on the join. I also connected the main niobium wiring structure to the wires running down to the TES leads using a taper in the wiring, to reduce the stress on the connection and prevent damage during liftoff.

The mask design for a single chip, featuring 32 devices, can be seen in Figure 4.12. The light blue represents the Au thermalisation layer on the back of the chip, which improved the thermal contact between the chip and the box, and the pink regions show the niobium wiring. As for previous TES mask designs by the group, the wires were kept close together to minimise flux loops, and the devices were all grounded during manufacture to prevent static buildup. The grounding was removed in the final processing step. The border around the outside was removed in the DRIE processing step, with only two small gaps in the border connecting the

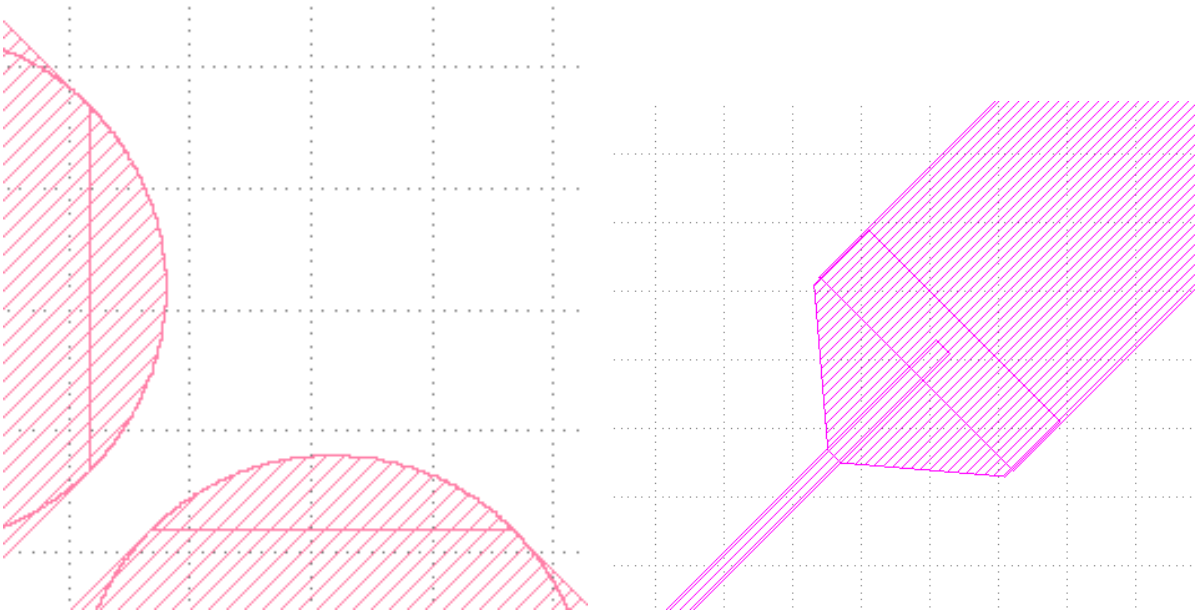

(a) (b)

Figure 4.11 Features designed to improve device yield. (a) Rounded corners on the legs supporting the TES membrane to ensure there were no sharp corners to launch cracks and (b) tapered niobium wiring. In (a), the shaded region indicates where the membrane was etched away to define the leg, whilst in (b), the shaded region indicates where Nb was deposited to form the wiring.

chip to the rest of the wafer, which allowed the chip to be 'broken out' using tweezers. The TESs occupy a small region in the centre of the chip, in order to prevent any damage to the devices when the chip is picked up. All of the TESs and their corresponding pads are labelled, to make it easy to identify the pads that connect to a given device.

The full wafer mask design can be seen in Figure 4.13, with a grounding ring around the outside, six main chips in the centre and six smaller test chips to the outside. Dicing marks were included to allow the chips to be diced out if the main chips were made with unreleased devices, which required the DRIE and RIE processing steps, normally used to release the chips, to be omitted. Each test chip featured twice, once on the left side of the mask and once on the right side. The alignment marks were required to line up the different mask layers.

4.4.1 Mask polarity and alignment marks

Each layer in a fabrication process has a mask for the patterning of the photo-resist by optical lithography. In order to align the different layers, each mask has an alignment mark on it that allows it to be lined up with alignment features already present on the wafer. The mark required

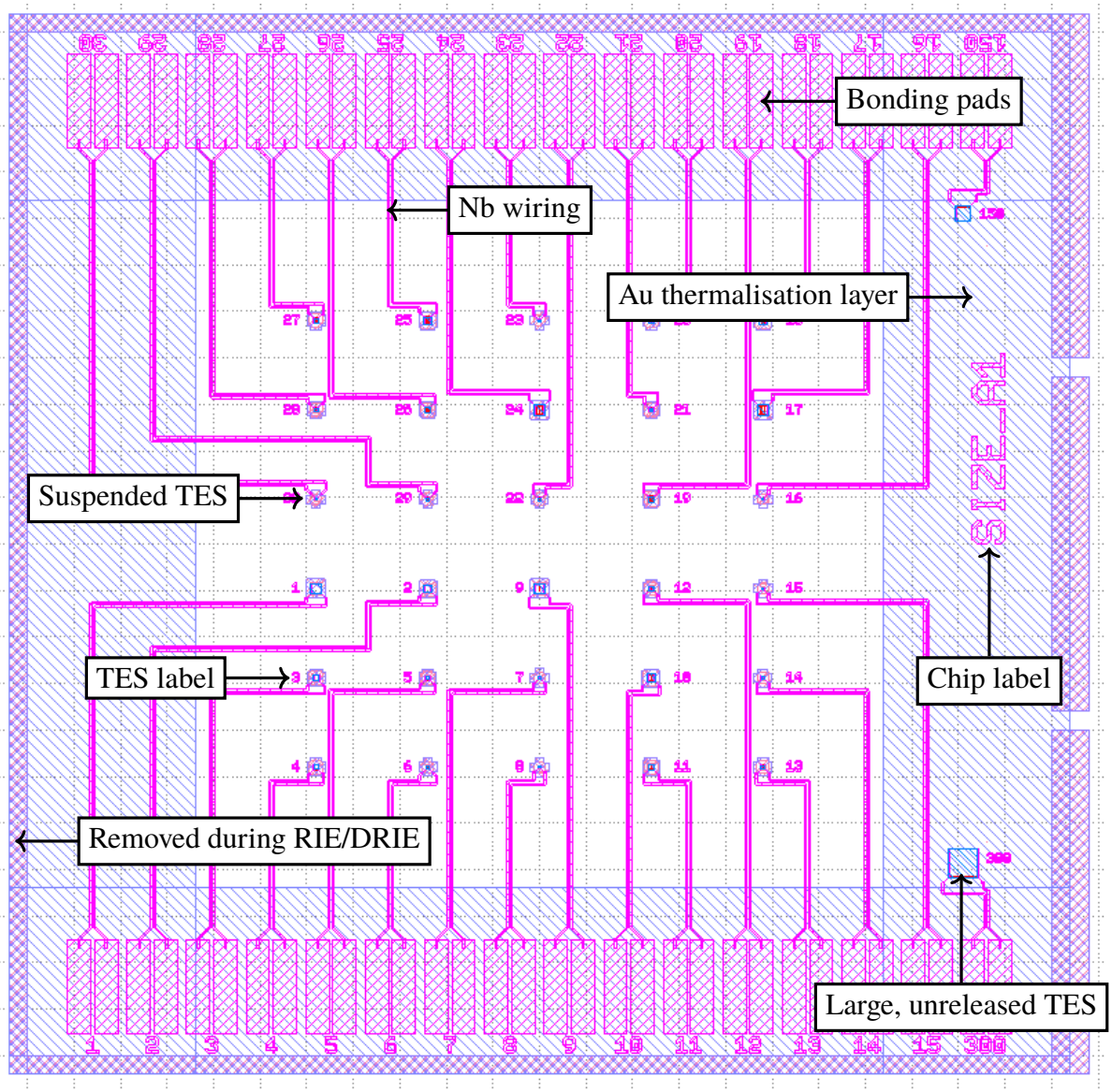

Figure 4.12 Design for one of the six main device chips from the mask, with the key features labelled. The TESs were all connected to bonding pads by niobium wiring; all TESs had a label next to them to show the set of pads they were connected to. 'Large' TESs had a bilayer side length greater than 100 µm. The Au thermalisation layer on the back of the chip ensures good thermal contact between the chip and the enclosing box.

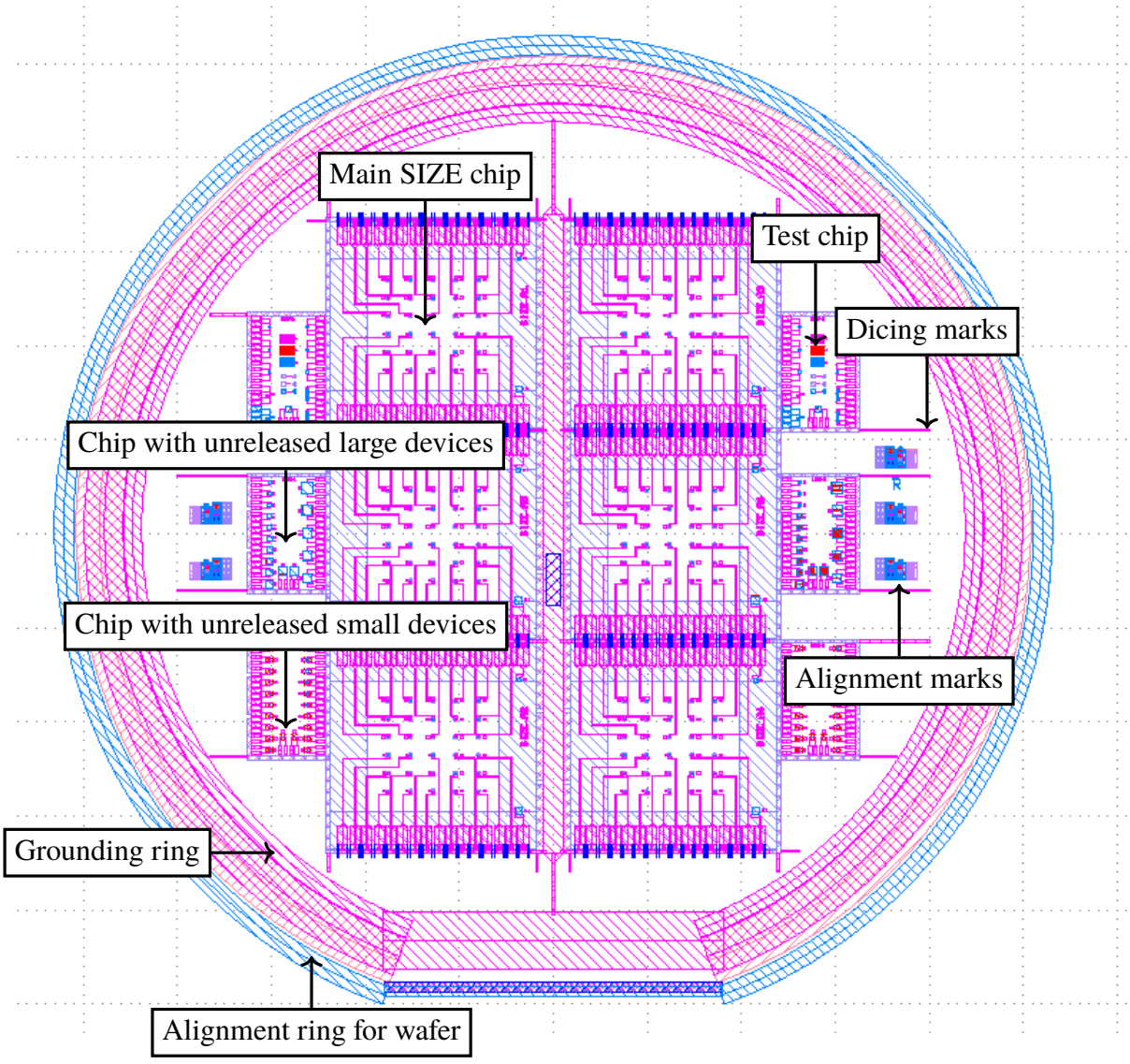

Figure 4.13 Full mask design, featuring six main (SIZE) chips and six smaller chips: two test chips for calibration measurements, and four chips with unreleased devices. Key features have been labelled, including the alignment marks for the different mask layers and the grounding ring to prevent devices being damaged by static build up during processing. The dicing marks were included to allow the chips to be diced out if the DRIE processing step was omitted, to produce the main chips with unreleased devices.

depends on whether the mask for that layer is positive or negative (its polarity). The polarity of the mask in turn depends on the polarity of the processing step. For example, an etch has a different polarity to a lift-off, although both remove material. Lift-off steps remove material where there is a layer of photoresist, whereas etches remove material where the photoresist has been removed by exposure. The first layer to be deposited is aligned to the wafer itself.

Figure 4.14 shows one set of the alignment marks used. Each alignment mark had three different features, to remove any rotation. The DRIE mask layer required larger alignment marks, on the far right of the figure. The TES bilayer mask had a different polarity to the other masks, resulting in its alignment marks (second from left at the bottom) differing in appearance.

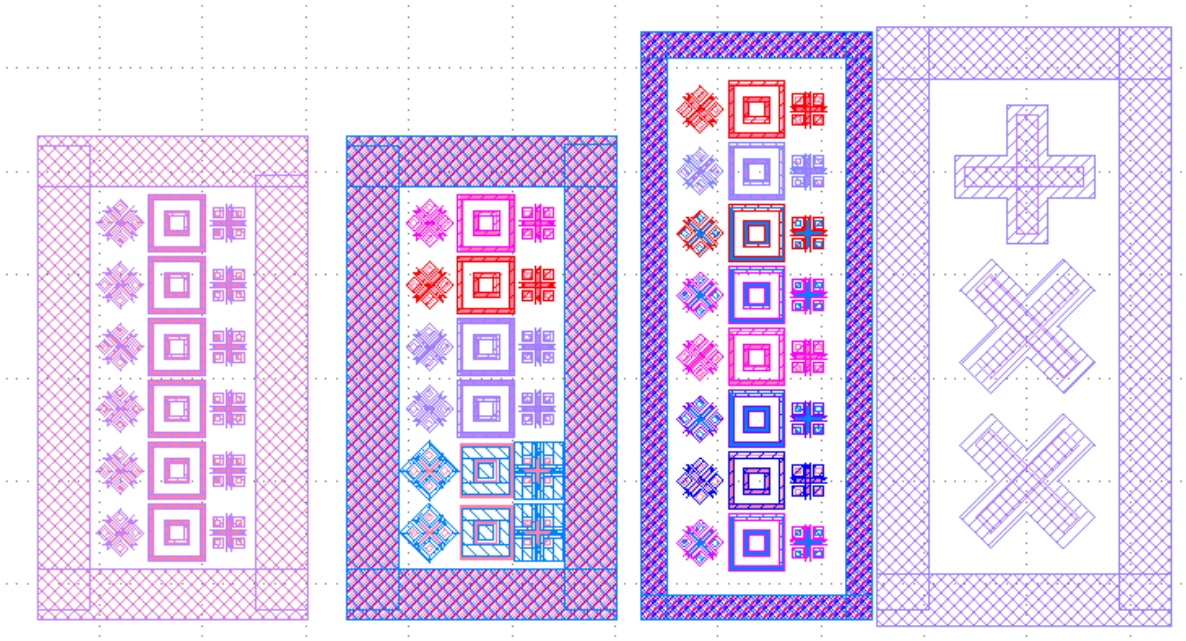

Figure 4.14 Alignment marks used to line up different layers on the front and back of the wafer. There were different sets of alignment marks for the layers on the front and back of the wafer. The larger alignment marks on the right hand side were for the DRIE etching mask. The TES bilayer mask had a different polarity to the other masks, resulting in its alignment marks (in the rectangle second from left, at the bottom) being different in appearance.

4.5 Calibration structures and unreleased chips

The mask featured six smaller chips, of which two contained calibration structures for post-processing checks; two contained unreleased TESs of the same size as the 30 main devices; and two contained unreleased TESs that were much larger than the 30 main devices.

4.5.1 Calibration structures

The chips with calibration structures on served two purposes: firstly, to ensure that all of the processing steps were successful; and secondly, to allow parameters such as T_c and $R_{interface}$ to be measured.

Verifiction of processing

The following processing checks were carried out:

- Etch uniformity check: the entire well was etched with no topside patterning. Three different structures were created: one covered with metal, one with the SiO_2 and Si_xN_y removed, and one with the SiO_2 and Si_xN_y present. This allowed the uniformity of the membrane etch to be examined.
- Thickness check: parallel bars were deposited for thickness tests using the Dectak machine.

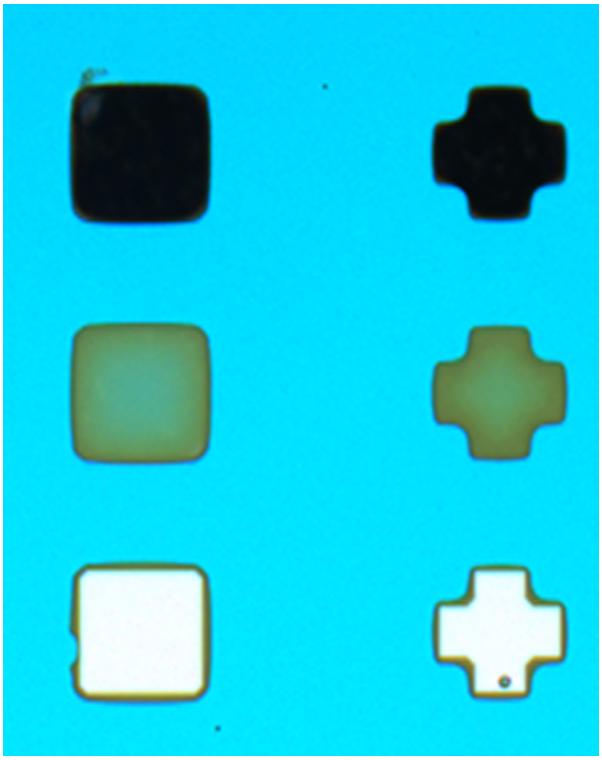

Figure 4.15 Etch uniformity test features following processing, as viewed through a microscope at a magnification of 20. The Si_xN_y layer in the top row of wells was completely removed prior to DRIE; in the middle row this layer was left and in the bottom row a layer of Nb was added to the wells prior to DRIE.

Figure 4.15 shows the etch uniformity test features viewed at a magnification of 20, following the DRIE processing step. The top row of wells have had the SiO_2 and Si_xN_y removed and have therefore been etched completely using DRIE, as the etch region is completely dark with no residual membrane. The middle row, which have not had the SiO_2 and Si_xN_y removed, still have a layer of Si_xN_y and the bottom row, which have been coated in Nb, have layers of both Si_xN_y and Nb, as the etch region is bright white and shiny due to the presence of Nb. This shows that the DRIE step has fully defined the suspended membrane structures, whilst leaving the superconducting component and supporting membrane intact.

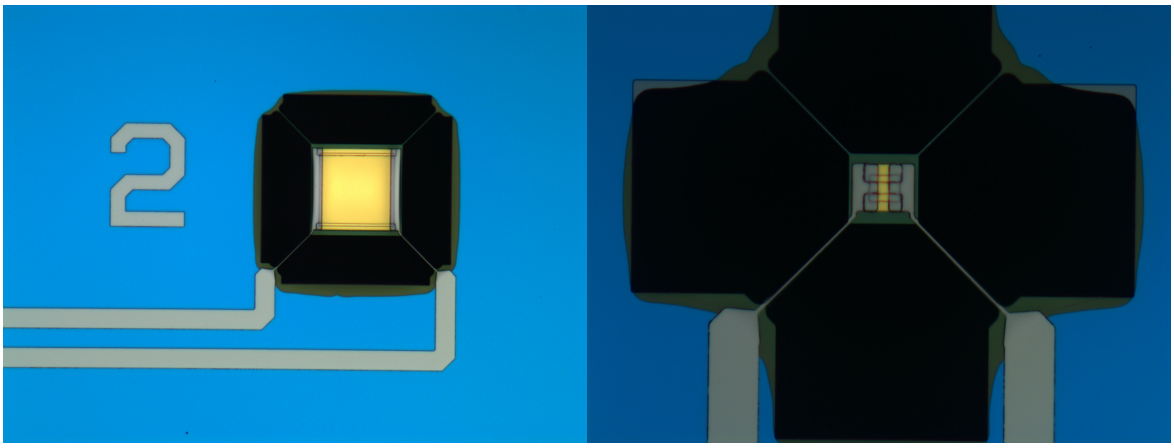

(a) L=70 µm. (b) L=5 µm.

Figure 4.16 Two of the unpatterned Mo/Au TESs, with different bilayer side lengths L, on the chip A1. Images taken during a final visual inspection of the devices.

Visual checks of the devices were also carried out to check the quality of the wiring, the overlap between the bilayer and the Au side bars and wiring and the structural integrity of the supporting Si_xN_y legs. Figure 4.16 shows images of two of the devices taken during this final inspection. Figure 4.16a shows the device with a unpatterned 70 µm film at a magnification of 20; Figure 4.16b shows the device with a unpatterned 5 µm film at a magnification of 50. The photos show that both devices have all four supporting legs intact, good overlap between the wiring and the bilayer, and no obvious defects in the wiring.

Calibration of transition temperatures and interface resistance

The following processing checks were carried out:

- Transition temperature check: samples made made entirely of one film, including the contact pads, were deposited. $R(T)$ for these samples was measured to determine the transition temperature of the film. Measurements of the transition temperature for all

the materials used are required to determine accurate transition temperatures for use in modelling, since transition temperatures in the literature are given for the bulk material, and the transition temperature of a thin film will differ from these values.

- Interface resistance check: a series of alternating Mo/Au and Nb films, consisting of a large number of material interfaces were deposited. The resistance of the structure was then measured. This was used to calculate the resistance of a single material interface, required as an input to the proximity effect model.

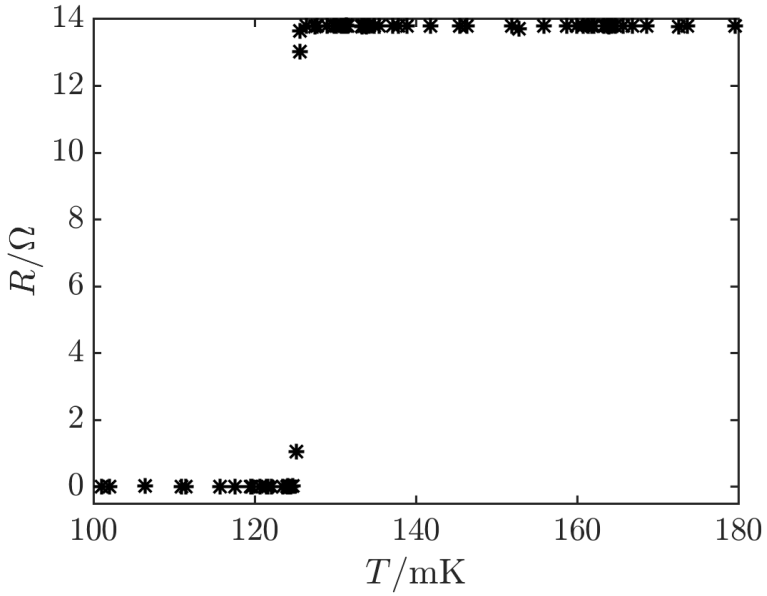

Figure 4.17 $R(T)$ for a transition temperature test structure made from a Mo/Au bilayer of thickness 40/120 nm.

Figure 4.17 shows how the resistance of a Mo/Au sample of thickness 40/120 nm varies with temperature. There is a sharp transition from the superconducting state to the normal state, showing a transition temperature of 125 mK for the bilayer. This T_c is slightly higher than the target transition temperature of 100 mK but still well within the target range.

Figure 4.18 shows the variation of the resistance of a Nb sample of thickness 200 nm with temperature. As for the Mo/Au sample, there is a sharp transition from the superconducting state to the normal state, showing a transition temperature of 7.5 K for the Nb sample. This is typical for the Nb films deposited by the group.

From Figure 4.19, I obtain an upper bound on the transition temperature of the normal metal bar sections. A sample consisting of 40/340 nm Mo/Au has a transition temperature below 90.5 mK. In order to further investigate the transition temperature of the normal metal bar section, a fridge with a lower base temperature would be required.

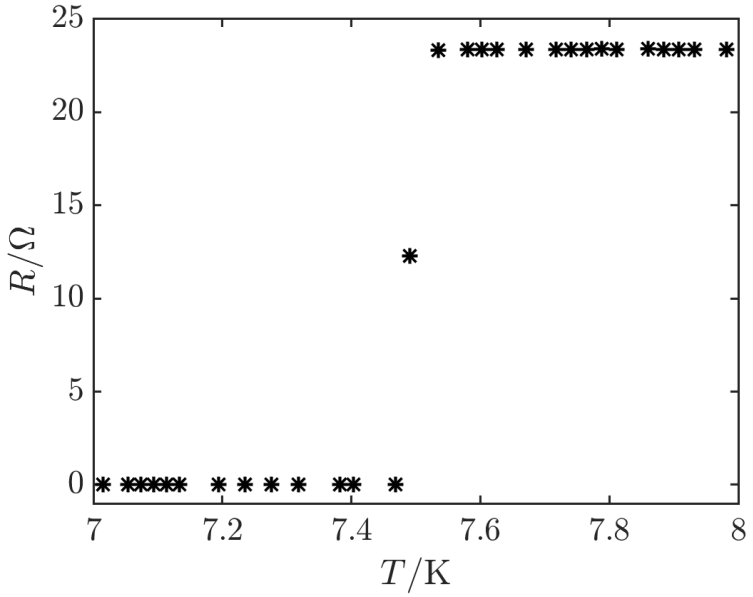

Figure 4.18 $R(T)$ for a transition temperature test feature made from Nb of thickness 200 nm,

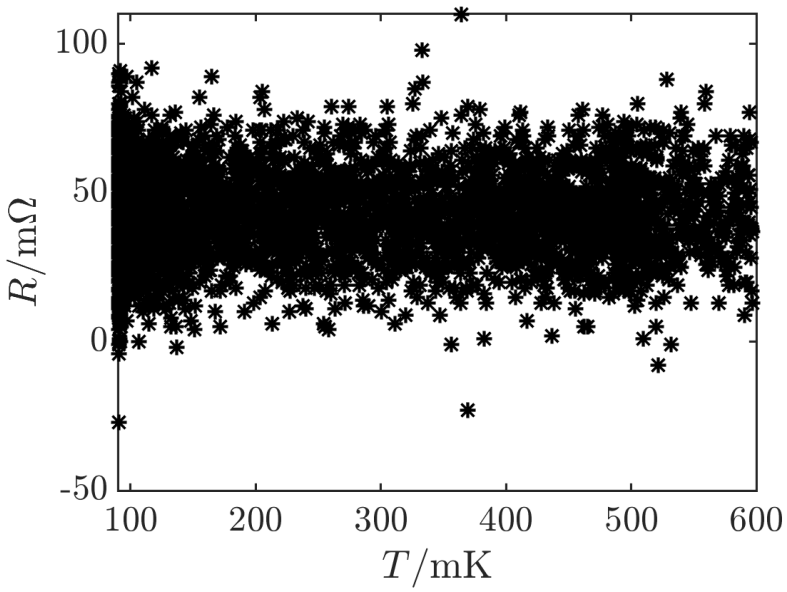

Figure 4.19 $R(T)$ for the transition temperature test structure made from a Mo/Au bilayer with additional Au of the same thickness as the normal metal bars, meaning that the bilayer is 40/320 nm Mo/Au.

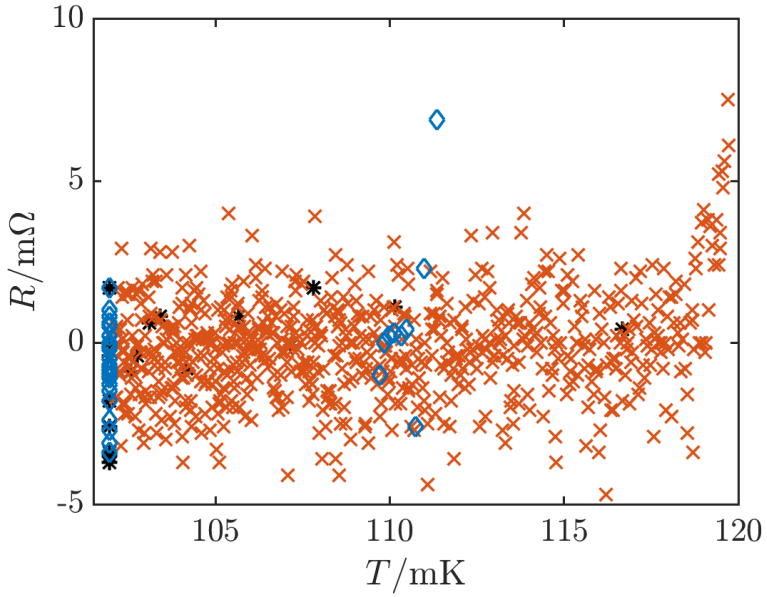

Figure 4.20 $R(T)$ measurements of the interface resistance test structure, consisting of 24 interfaces, taken for two different test devices (black asterisks and red crosses), with additional datapoints from repeated measurements shown as blue diamonds.

Figure 4.20 shows several different measurements of the interface resistance as a function of temperature. Even combining multiple material interfaces, the overall resistance is too small to be measured. This allows an upper bound on the resistance of the Nb - Mo/Au interface to be calculated, based on the accuracy to which the resistance of the interface can be measured. For the two devices, the mean and standard deviation of the resistance measured are -0.9 ± 2 mΩ and -0.5 ± 1 mΩ. In theory, the maximal value of the resistance of these 24-boundary test devices could therefore be 2 mΩ. Taking this value as an upper bound, an upper value of the boundary resistance parameter γ can be obtained, using

$$\gamma = \frac{R_{\text{interface}} A_{\text{interface}} \sigma}{\xi}, \tag{4.1}$$

where $R_{\text{interface}}$ is the (measured) interface resistance for a single interface, $A_{\text{interface}}$ is the interface area, σ is the conductivity and ξ is the coherence length. The maximal possible resistance of a single interface is 83 μΩ, giving an upper bound on γ of 21.5.

4.5.2 $R(T)$ measurements of unreleased devices

Two of the smaller chips contained TESs that were much larger than those on the main chips, with side lengths of up to 550 μm. Because these TESs were deposited directly onto the substrate

with no thermal isolation, as well as allowing the transition temperatures of larger TESs to be investigated, they also could have be used as a useful diagnostic had there been any serious processing defects.

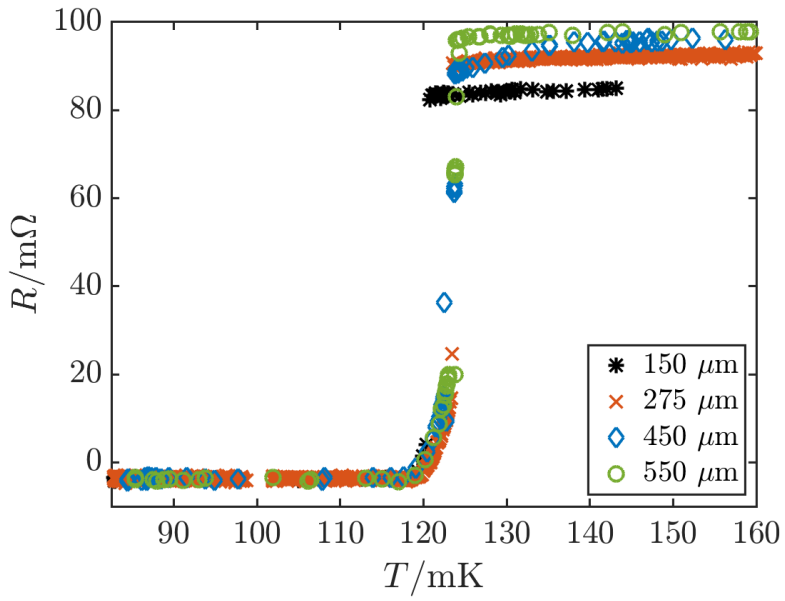

Figure 4.21 Resistance as a function of temperature for a series of four unreleased TESs of different bilayer side lengths: 150 µm (black asterisks), 275 µm (red crosses), 450 µm (blue diamonds) and 550 µm (green circles).

Figure 4.21 shows how the resistance varies as a function of temperature for four large unpatterned TESs of different bilayer side lengths: 150 µm (black asterisks), 275 µm (red crosses), 450 µm (blue diamonds) and 550 µm (green circles). The transition temperatures for all of the devices are all very similar, close to 120 mK, and the normal state resistance increases with increasing device size. This indicates at these length scales, the proximity effect from the Nb electrodes is the same for all of the thin films and doesn't significantly affect the transition temperature. The transitions are also sharp and well defined, with no anomalous features or steps that would indicate phase slip. Based on this, I decided not to include the devices with large thin film areas on the main chips in my investigations.

The test chips also contained two series of TESs, all with 100 µm side length bilayers but different numbers of normal metal features. These features differed between the two sets, with one set having full width bars (stripes) and the other set having partial width bars. Measuring the variation of resistance with temperature for these devices allowed me to examine the effects of the bars on the transition temperature, the normal state resistance and the residual resistance

in the superconducting state. This was the first systematic comparison of full width and partial width bars.

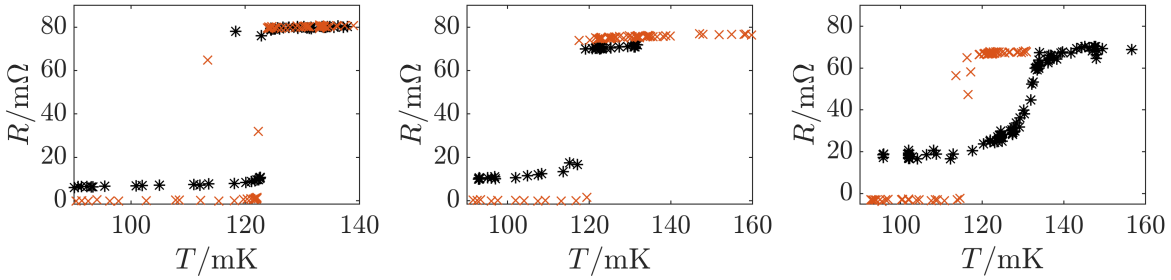

(a) $N = 1$. (b) $N = 2$. (c) $N = 3$.

Figure 4.22 $R(T)$ for unreleased devices with N full normal metal bars (black asterisks) or partial normal metal bars (red crosses). All of the devices have thin films of side length 100 µm, and all bars are 10 µm wide.

Figure 4.22 shows $R(T)$ for unreleased devices with one to three partial or full normal metal bars on their bilayers. From these, it can be seen that as the number of normal bars increases, there is a general reduction in the transition temperature, defined here as the lowest temperature at which the resistance increases from its minimum value, for both the devices with full bars and partial bars. This agrees with the results of my fundamental model in Chapter 2, which showed that the larger the number of regions with bars, the lower the transition temperature. Other groups have also observed the same effect for devices with partial metal bars [87].

Additionally, from Figure 4.22, for the devices with full normal metal bars the residual resistance in the superconducting state is observed to increase as the number of bars increases. This suggests that the bars do not superconduct at the typical operating temperature of these devices. This phenomenon was also observed by Sadleir et al. [87] for a 4 µm thick Au absorber spanning the whole width of a TES bilayer. Figure 4.23 shows the effect of the bars on the transition temperature and residual resistance in greater detail. Figure 4.23a shows the variation of the transition temperature with the number of normal metal bars on a 100 µm side length TES bilayer, for both full and partial bars. This reduction is of the order of 2 mK for each additional metal bar. Figure 4.23b shows the increase in the residual resistance of the TESs with full metal bars as the number of full metal bars is increased, along with a linear fit to this relationship. For the numbers of bars studied, the increase in resistance with each bar is approximately the same.

This observation of non-zero residual resistance for full normal metal bars agrees with the observation for NIST devices [94] that partial metal bars force current to flow in a meander pattern at bias points below 40 % of the normal state resistance, then as the temperature increases, the supercurrent passes directly through the bars with a reduction in maximum

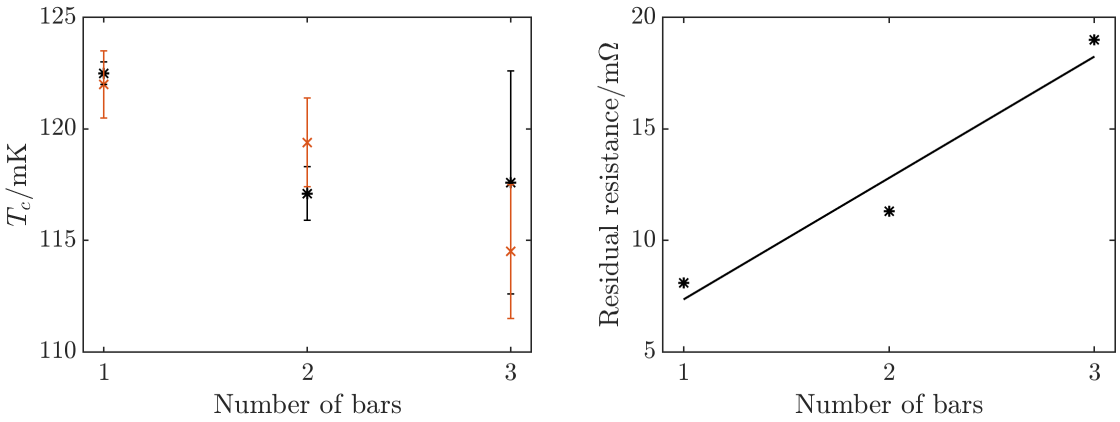

Figure 4.23 (a) Transition temperature as a function of the number of normal metal bars on a 100 µm long TES bilayer, for devices with bars spanning the full width of the film (black asterisks) and devices with bars spanning 80 % of the width of the film (red crosses). (b) Residual resistance of the TES as a function of the number of full bars on the bilayer (black asterisks) along with a linear fit to the residual resistance.

supercurrent. This also explains why devices made by our group, with much thicker metal bars, are not well described by my proximity effect model, which assumes that supercurrent passes directly through the bars for all points in the transition. However, in Chapter 3, I showed that my model gave a good account of devices made by SRON [4]. The reason for this can be seen by looking at Figure 4.24, which shows the different thicknesses of the bilayers and normal metal bars used by different groups to make TESs. SRON's bilayers have much thinner metal bars relative to the overall bilayer thickness, and so will provide much less suppression of the supercurrent than the metal bars on our bilayers and the NIST bilayers. Table 4.5 quantifies this, showing that the additional gold bars on the SRON bilayers are just over 50 % of the bilayer thickness. The thickness of the normal metal bars relative to the bilayer is therefore crucial in determining whether the supercurrent follows a meandering path or flows straight across the film at low bias points. There is a thin layer of Ti in between the bilayer and the bar in the SRON device for adhesion, which could also affect the path taken by the supercurrent.

I used a simple model to calculate the expected residual resistance of the normal metal bars, based on the parallel configuration of resistors shown in Figure 4.25. Each layer in Figure 4.24 is approximated by a resistor, of resistance $R = \rho l / A$, where ρ is the resistivity of the metal, l the width of the bar and A its cross-sectional area. This gives an expected resistance of 3.4 mΩ for a single bar. Accounting for the gold side bars used to prevent overetch, and the variation of the resistance of the gold with its thickness, the expected resistance is 3.3 mΩ per bar. From

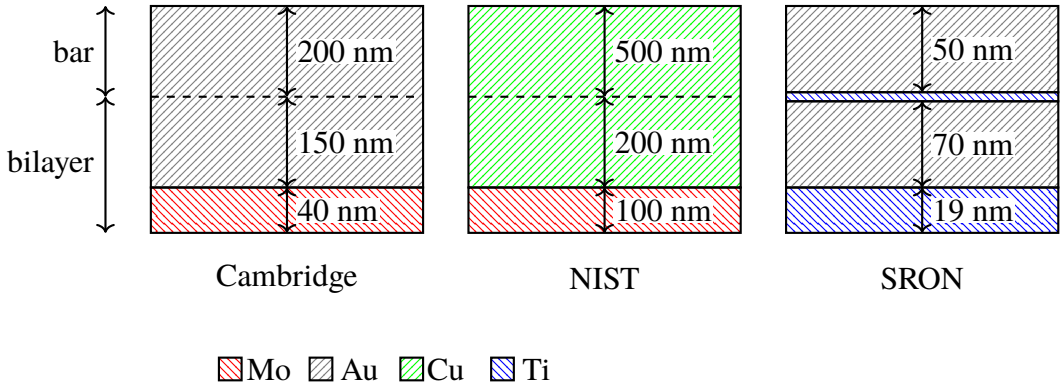

Figure 4.24 Bilayer layups used by our group (Cambridge), researchers at the National Institute of Standards and Technology (NIST) [94] and researchers at the Netherlands Space Agency (SRON) [4], showing the thicknesses of the metal bars compared to the rest of the bilayer.

Table 4.5 Thickness of the normal metal bars as a percentage of the thickness of the Au layer and the total thickness of the bilayer, for the different layups used by our group (Cambridge), researchers at the National Institute of Standards and Technology (NIST) and researchers at the Netherlands Space Agency (SRON).

	Cambridge	NIST [94]	SRON [4]
Thickness of bars relative to thickness of Au / %	133	250	71
Thickness of bars relative to total bilayer thickness / %	105	167	56

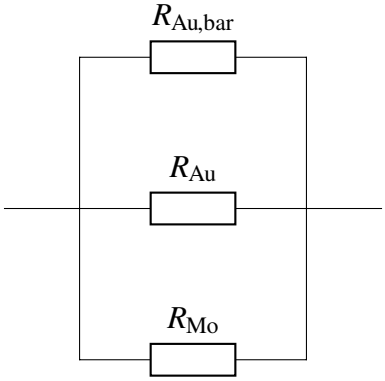

Figure 4.25 Resistance model used to calculate the expected residual resistance of the normal metal bars. Each layer in Figure 4.24 is approximated by a resistor, of resistance $R = \rho l / A$.

Figure 4.23, the residual resistance per bar is about 7.5 mΩ, twice the predicted value. The additional measured resistance may be due to spreading resistance in the bars.

4.6 Design of TES box and test fixtures

Since I wanted to test the response of a detector to an applied magnetic field in any direction, I needed to develop a box design that would allow a uniform field to be applied to detectors in any direction, with adjustable magnitude. It is also important to shield the readout systems from the magnetic field applied to the detectors, as any stray magnetic field may interfere with their operation. To assist with this, I kept the coils small and close to the TESs.

To allow adjustment of the magnitude and direction of the magnetic field, I used pairs of current-carrying coils to produce the field, using the Biot Savart law given by Equation (2.38) to calculate the expected field for different coil configurations. As long as the current through the coils is constant, the field produced is directly proportional to the current through the coils, and so the field could be changed in a predictable way by adjusting the current.

The best way to produce a uniform magnetic field throughout the detectors is to use a pair of Helmholtz coils, where the coils are separated by a distance equal to their radius. I wrote Python code to model the magnetic fields produced by coils, using finite element analysis. Figure 4.26a shows my simulation results for the magnetic field strength (shading) and direction (white arrows) around a pair of coils in the Helmholtz configuration. This configuration produces a very uniform field across the chip, which will occupy the region indicated by the red line. However, this configuration does not lend itself to being extended to three pairs of coils, as the coils would have to be interleaved and this would almost certainly affect their operation. I came up with a viable alternative, using three pairs of coils separated by a distance equal to their diameter. The field produced by such a configuration is shown in my results in Figure 4.26b. A chip in the box still experiences a relatively uniform field, but the field further out from the central region is less uniform than when the coils are in the Helmholtz configuration.

Figure 4.27 shows the field direction and magnitude in and around the region the detector chip occupies. The image in Figure 4.27a shows the magnetic field strength (shading) and direction (black arrows) in the central region where detector chips are mounted. A chip occupies the region shown by the red line, but the devices only occupy the central region, indicated by the black line. The field strength across the devices is very uniform, with deviations of the order of 2-3 %. The field direction is also uniform to a good degree. The image in Figure 4.27b shows the percentage deviations of the field strength from the central magnetic field strength. Across a square region of 11 mm side length, the magnetic field varies by a maximum of about 15 % from the field in the centre.

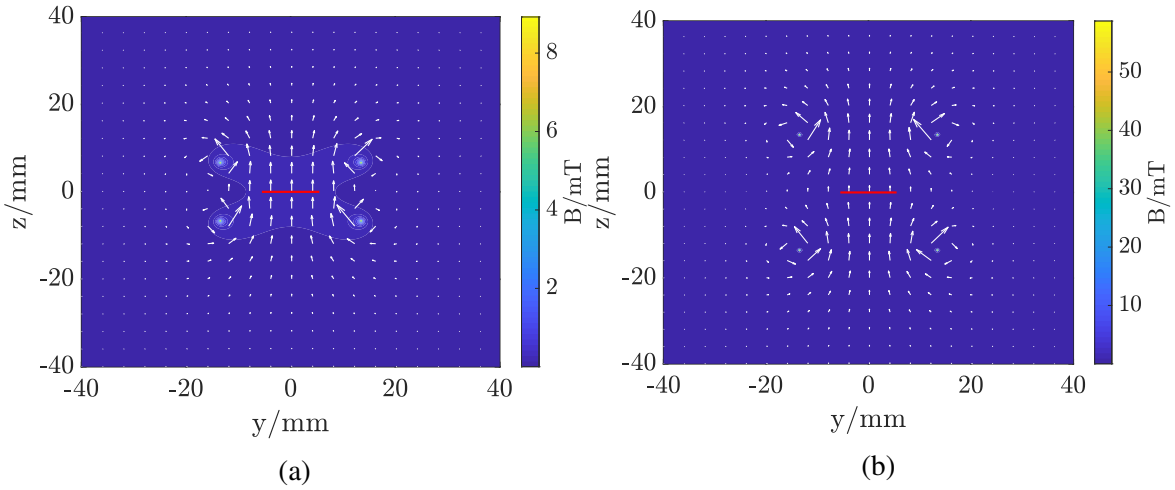

Figure 4.26 (a) Magnetic field around a pair of coils in the Helmholtz configuration. The shading corresponds to the magnetic field strength, and the field lines are shown in white. The red line at the centre of the figure indicates the size of the detector chip that will be tested. (b) Magnetic field around a pair of coils with the same radius but double the coil separation.

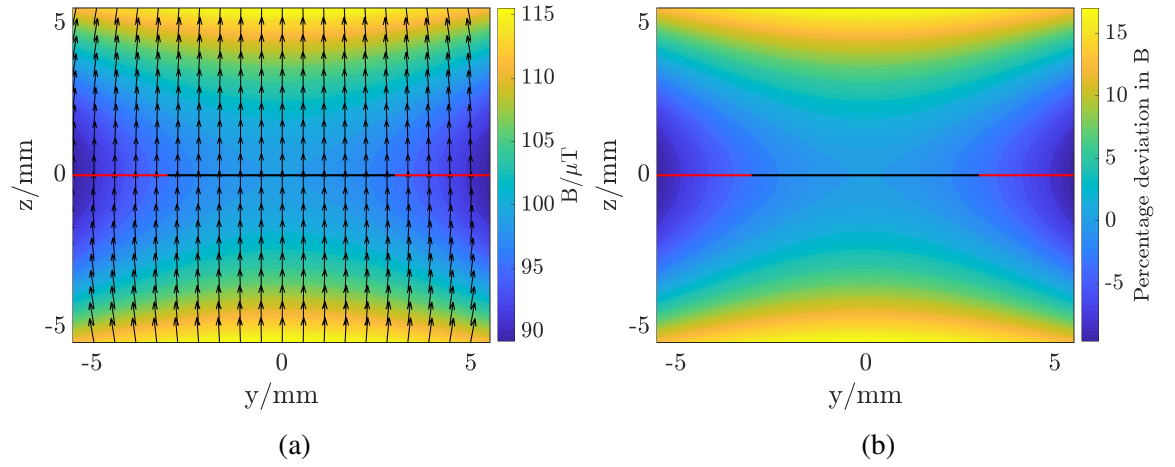

Figure 4.27 (a) Magnetic field across the width of the detector chip. The region occupied by the chip is indicated by the red line, but the TESs only occupy the central region shown by the black line. The overall field strength is indicated by the shading and the black lines show the direction of the magnetic field. The field across the chip is relatively uniform, with deviations of the order of 2-3 %. (b) shows the percentage deviations in magnetic field from the field at the centre of the chip.

Working with other members of the group, I produced several conceptual designs for the box, with the final design shown in Figure 4.28. In this design, each pair of coils has a current flowing through it, controlled by a current drive at room temperature. The coils are made of superconducting wire in order to minimise the dissipative heating. The Superconducting Quantum Interference Devices (SQUIDs) and the rest of the readout electronics are shielded by a superconducting niobium box, shown in green, from the field produced by the magnetic coils. The box is in two halves to allow for easy rewiring of the detector chip without requiring the box to be fully taken apart.

4.7 Characterisation of the magnetic field

The fridge configuration used for field characterisation is shown in Figure 4.29. When the box was used for characterising detectors, the devices were mounted in the centre, in the square seen in the exploded view of the box in Figure 4.29a. The Hall probe was therefore also mounted in this region. I defined a coordinate system so that the TES detectors were orientated with their thin films in the $x-y$ plane, with current flowing in the x direction. The coils were attached to the sides of the box and the box was then mounted on the 2 K stage of a Pulse Tube Cooler (PTC), as shown in Figure 4.29b. The current through the coils was controlled by a current drive at room temperature. The current drive allowed adjustment of the current through each pair of coils individually, allowing the magnitudes of the x, y and z magnetic fields to be set separately. I refer to the $x/y/z$ coils as the pair of coils that produce a field principally along the $x/y/z$ axis.

As the TESs to be tested are based on films whose thickness is very much smaller than their length and width, and since magnetic flux is directly proportional to projected area, the TESs should be most sensitive to fields in the z direction, as the projected area and hence the magnetic flux were much larger than in the x or y directions.

Figure 4.30 shows the Hall probe mounted inside the box, set up to detect fields in the z direction. The three orientations of the Hall probe during calibration testing are indicated in Figure 4.31. When set up to record fields in the z direction, the probe can be mounted with its active area in the same place as the detectors, but when recording fields in the x and y directions the active area of the probe is centred 3 mm above the plane where the detectors will be mounted. The measured field is therefore reduced by about 5-10 %, based on Figure 4.27.

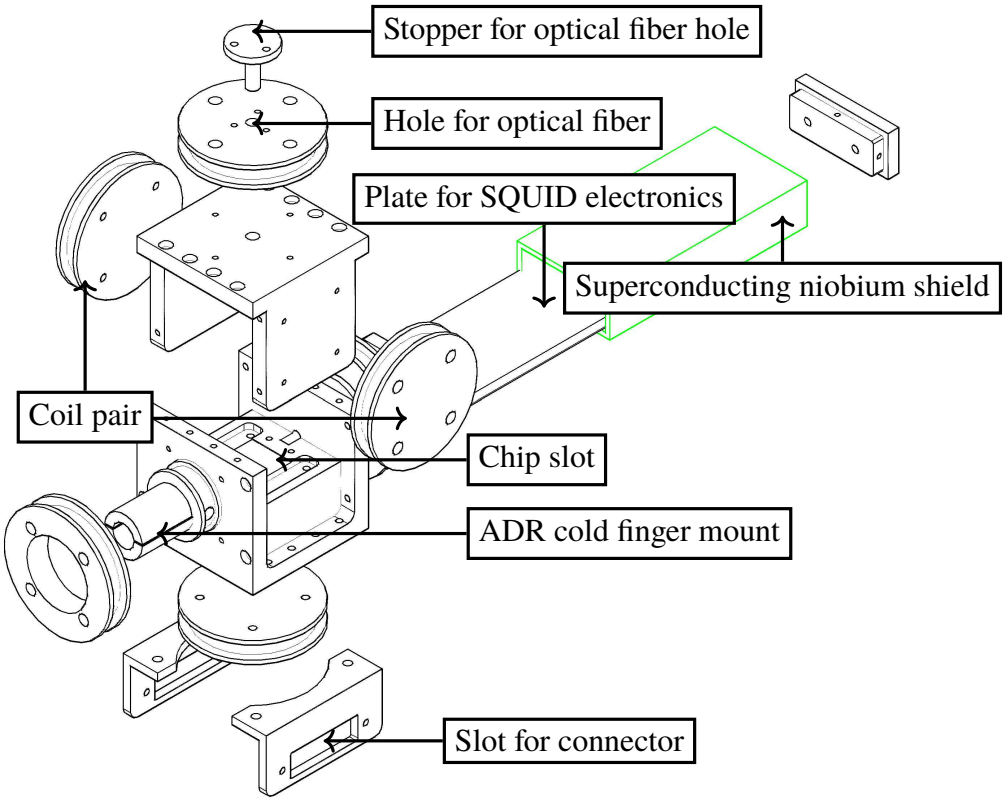

Figure 4.28 Design for the box to investigate the effects of magnetic field on the detectors, with all the key features labelled. The box where the devices sit is to the left of the figure; the devices lie in the square region in the centre labelled 'chip slot'. This box has two halves that slot together to form a cubic container. The six coils on the sides of the box produce the magnetic fields. The current through each pair of coils is controlled separately via a current drive at room temperature. The SQUIDs are mounted outside the box, inside a superconducting shield to ensure that their operation is not disrupted by the magnetic field produced by the coils. An optical fiber hole and stopper are included so that the box can be used for optical testing in the future.

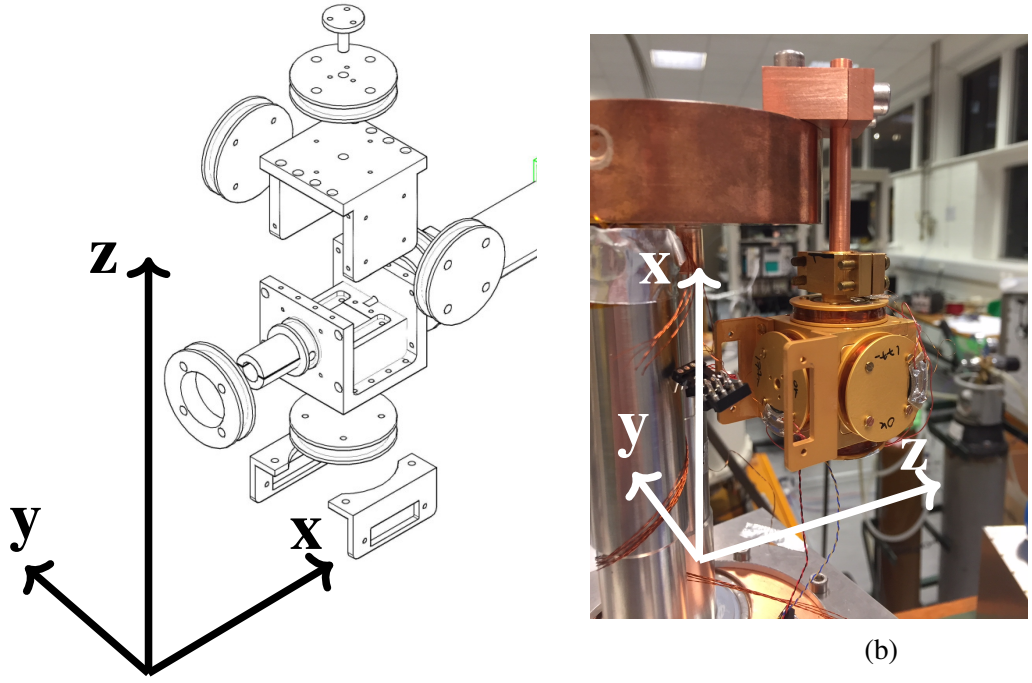

(a) (b)

Figure 4.29 Experimental configuration used to test the Hall magnetic probe. The exploded image of the box from Figure 4.28 is shown in (a), with the axis directions indicated. The Nb shield containing the SQUIDs was not attached for this testing phase. The Hall probe is mounted in the square region in the centre, where the detector chip will sit during testing. The box containing the probe is attached to the 2 K stage of a pulse tube cooler (PTC), as shown in the photograph in (b).

4.7.1 Characterisation of fields using semiconductor Hall probe

The Hall probe used for the initial magnetic field characterisation was the cryogenic Hall effect sensor HGCT-3020 made by Lake Shore Cryotronics [171], a diagram of which is shown in Figure 4.32. These sensors may be susceptible to a phenomenon known as the planar Hall effect, resulting in non-zero magnetic fields being measured when a magnetic field is applied in line with the sensor, when the probe should be measuring zero field. Lake Shore Cryotronics have recently developed a probe that does not exhibit this effect, and I collaborated with them to carry out the first cryogenic tests of this probe by repeating some of the magnetic field tests, as described in Section 4.7.2.

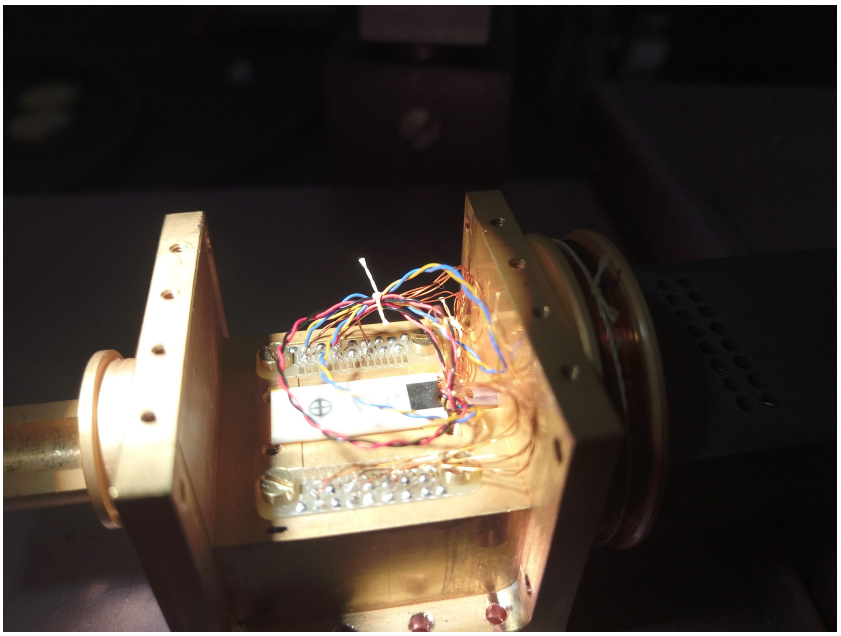

Figure 4.30 Open box, showing the Hall probe mounted to detect fields in the z direction.

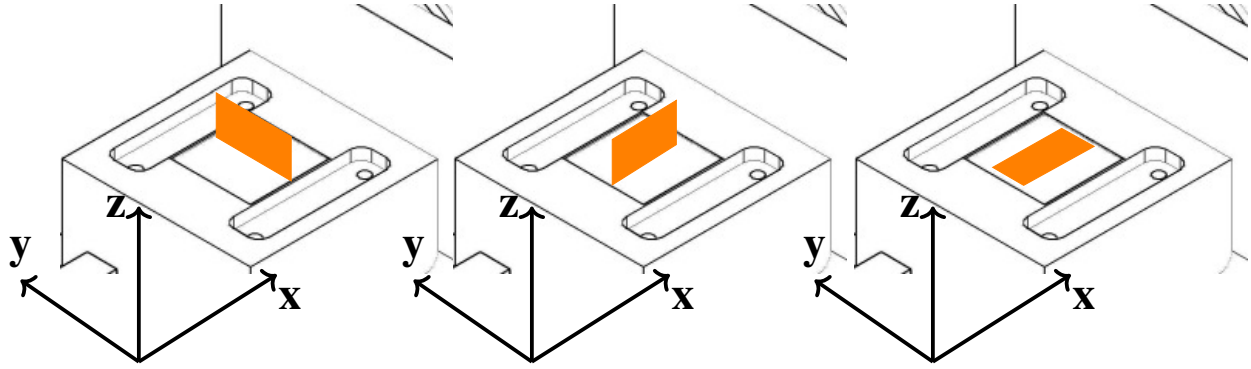

(a) x (b) y (c) z

Figure 4.31 All three orientations in which the Hall probe (represented by the orange rectangle) was mounted in the chip slot for calibration testing, to measure fields in the (a) x, (b) y and (c) z directions. When the probe was mounted to monitor fields in the x and y directions, its active area was raised above the plane of the devices and hence the centre of the coils by about 3 mm.

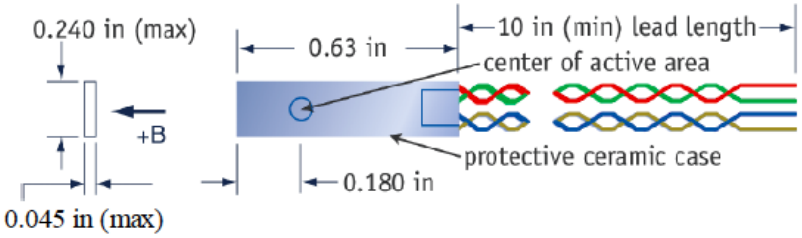

Figure 4.32 Dimensions of the semiconductor Hall probe used for magnetic field characterisation, a transverse cryogenic Hall effect sensor made by Lake Shore Cryotronics. The circle indicates the active area of the probe. The image is taken from the application note for the sensor [171].

Calibration of magnetic fields

The current through each pair of coils should be directly proportional to the magnetic field produced by that coil pair, as predicted by Equation 2.38, i.e.

$$B_\mathrm{a} = k_\mathrm{a} I_\mathrm{a} \tag{4.2}$$

where $a = x, y, z$, but the constant of proportionality k may be different for different pairs of coils. I therefore carried out experiments to determine the values of the constants of proportionality $k_{x,y,z}$. For each pair of coils, the current was swept up and down to check for any hysteretic behaviour.

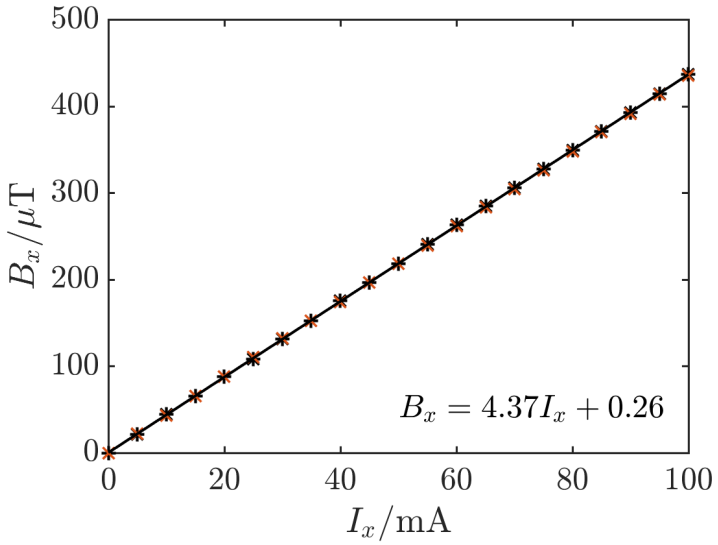

Figure 4.33 Magnetic field produced by the x-coil pair, when the current in the coils is swept from 0-100 mA (black asterisks) and from 100-0 mA (red crosses). The black line shows a linear fit to the data with gradient 4.37. The full equation of this best fit line is on the graph.

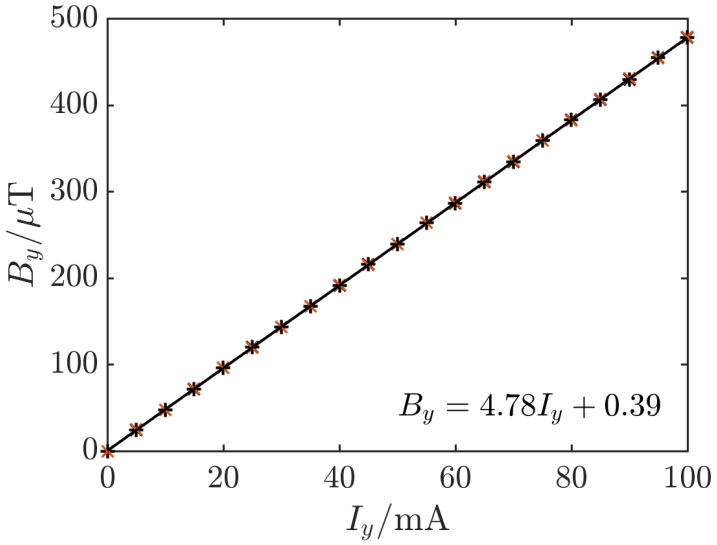

Figure 4.34 Magnetic field produced by the y-coil pair, when the current in the coils is swept from 0-100 mA (black asterisks) and from 100-0 mA (red crosses). The black line shows a linear fit to the data with gradient 4.78. The full equation of this best fit line is on the graph.

Figures 4.33 to 4.35 show the changes in the measured magnetic field when the current in the x, y and z directions is increased, when the Hall probe is set up to detect the fields in these directions. In all three directions, the constant of proportionality between the field and the current is between 4.4-5.0 μT mA^{-1}. As discussed in Section 4.7, the fields in the x and y directions are likely to be reduced by around 10-15 % due to the Hall probe not being exactly in the plane where the TESs will lie, and so the value of k_z gives the best indication of the value of k_a. I therefore set k_a=5 μT mA^{-1} for $a = x, y, z$, consistent with the results for all three pairs of coils. The system does not show any evidence of hysteresis or heating, even at maximum field, and the fields produced are highly reproducible.

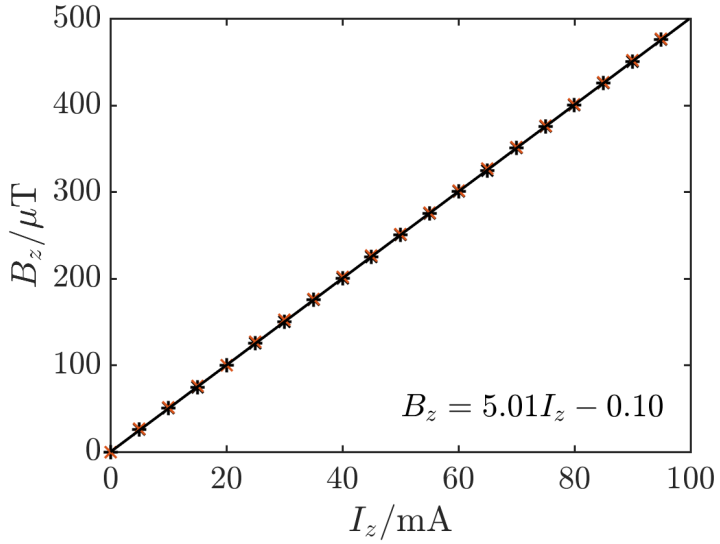

Figure 4.35 Magnetic field produced by the z-coil pair, when the current in the coils is swept from 0-100 mA (black asterisks) and from 100-0 mA (red crosses). The black line shows a linear fit to the data with gradient 5.01. The full equation of this best fit line is on the graph.

Stability measurements

I wanted to know the accuracy to which the magnetic field can be determined given the stability of the system, and therefore I needed to carry out measurements to determine the magnitude of the system fluctuations, as measured by taking the standard deviation of a number of measurements of magnetic field at constant coil current. Table 4.6 shows the fluctuations measured in the magnetic field with no current, with average times of 5s and 10s, and with a current of 5 mA through the coil pair aligned with the Hall probe. From this, as the magnitudes of the fluctuations in the field are the same with and without a current through the coils, any fluctuations produced by the coils themselves cannot be detected using the HGCT-3020 probe. Figure 4.36 shows two of the measurements of the fluctuations at zero magnetic field: the red cross points were taken with double the hold and sample times of the black asterisk points. The other two sets of points were taken with a different Hall probe, as discussed in Section 4.7.2.

Table 4.6 Standard deviations σ_{B_i}, in μT, of the magnetic field measurements taken with the Hall probe aligned in the x, y and z directions. Additional measurements were carried out to investigate the effects of doubling the averaging time and having a non-zero current in the coil pair aligned with the probe.

	σ_{B_x}/μT	σ_{B_y}/μT	σ_{B_z}/μT
Fluctuation in B with no current/μT	0.5	0.4	0.2
Fluctuation with double the averaging time/μT	0.4	0.2	0.5
Fluctuation with 5 mA through coil pair aligned with probe/μT	0.4	0.4	0.3

Magnitude of parallel magnetic fields

From Section 4.6, the magnetic fields produced by each coil pair are not perfectly uniform, since the coils are not in the Helmholtz configuration. In addition to the magnetic field in the direction of interest, each pair of coils produces a smaller magnetic field in the two perpendicular directions. From Figure 4.27, this deviation is of the order of 1 %. From the measurements shown in Figures 4.33 to 4.35, a 1 % deviation from the vertical would be measured as a maximum field of about 5 μT at a current of 100 mA. If the field at 100 mA is higher than 5 μT then this is likely to be due to the planar Hall effect.

From Figure 4.37, as the maximum fields measured are as high as 20 μT, this cannot be explained purely by the non-uniformity of the magnetic field. This suggests there is a non-zero contribution from the planar Hall effect, as will be discussed in the next section.

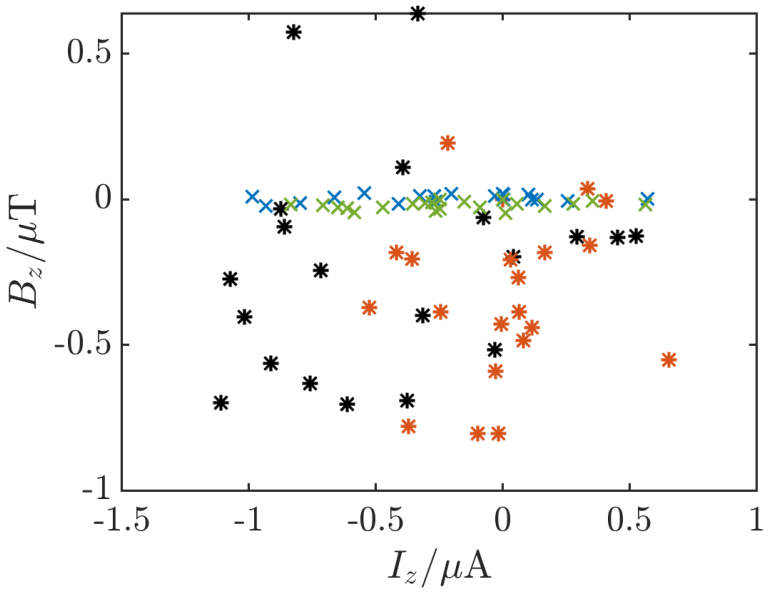

Figure 4.36 Fluctuations measured with a target current of 0 µT through the coils. Asterisks indicate data taken with the semiconductor Hall probe, with settling and averaging times of 5 s (black) and 10 s (red). Crosses indicate data taken with the 2D electron gas Hall probe, with settling and averaging times of 5 s (blue) and 10 s (green).

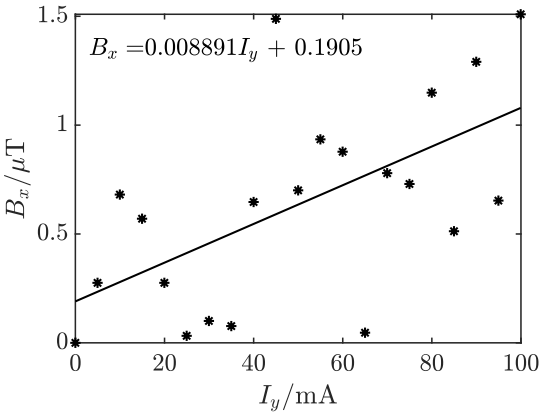

(a) Probe set to measure B_x, I_y varied.

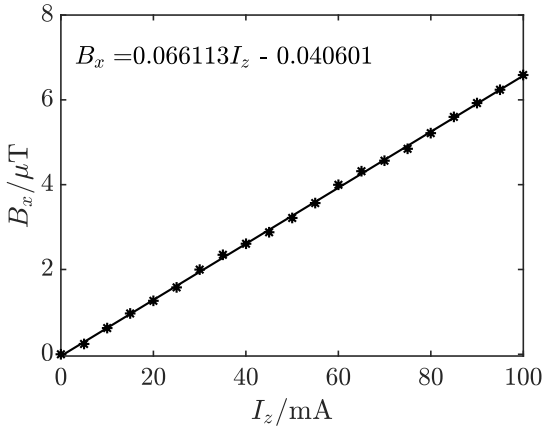

(b) Probe set to measure B_x, I_z varied.

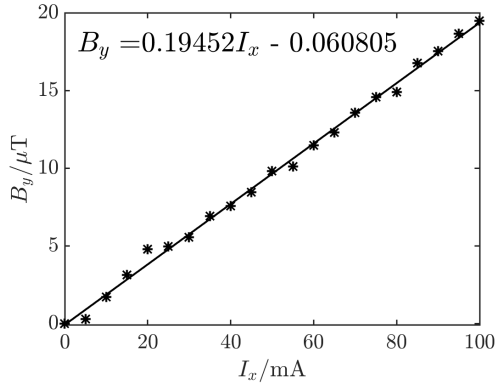

(c) Probe set to measure B_y, I_x varied.

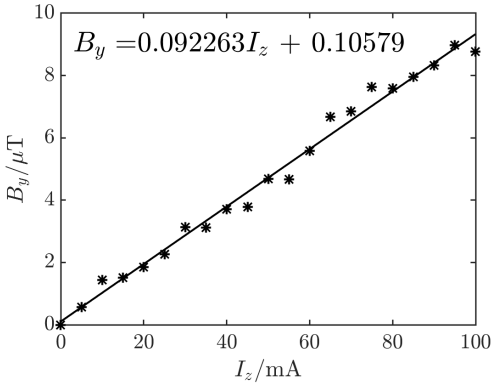

(d) Probe set to measure B_y, I_z varied.

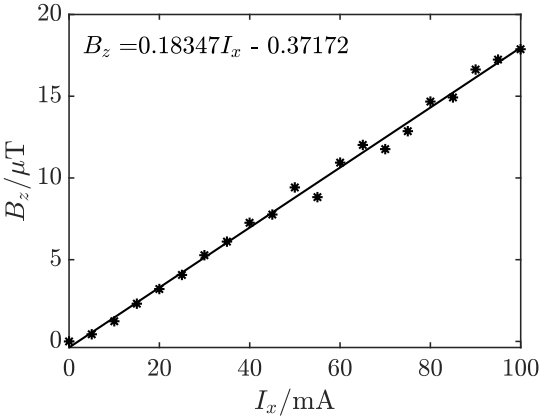

(e) Probe set to measure B_z, I_x varied..

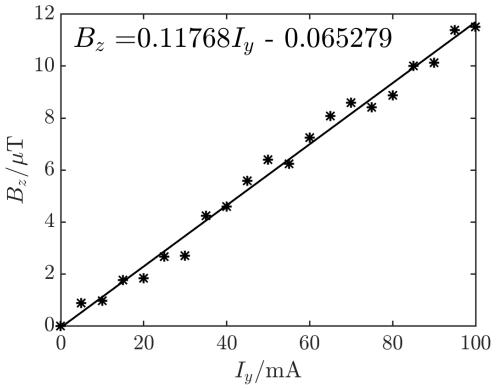

(f) Probe set to measure B_z, I_y varied.

Figure 4.37 Magnetic field measured for applied currents through each coil pair not orientated in the same direction as the Hall probe.

4.7.2 Test of 2D electron gas Hall probe

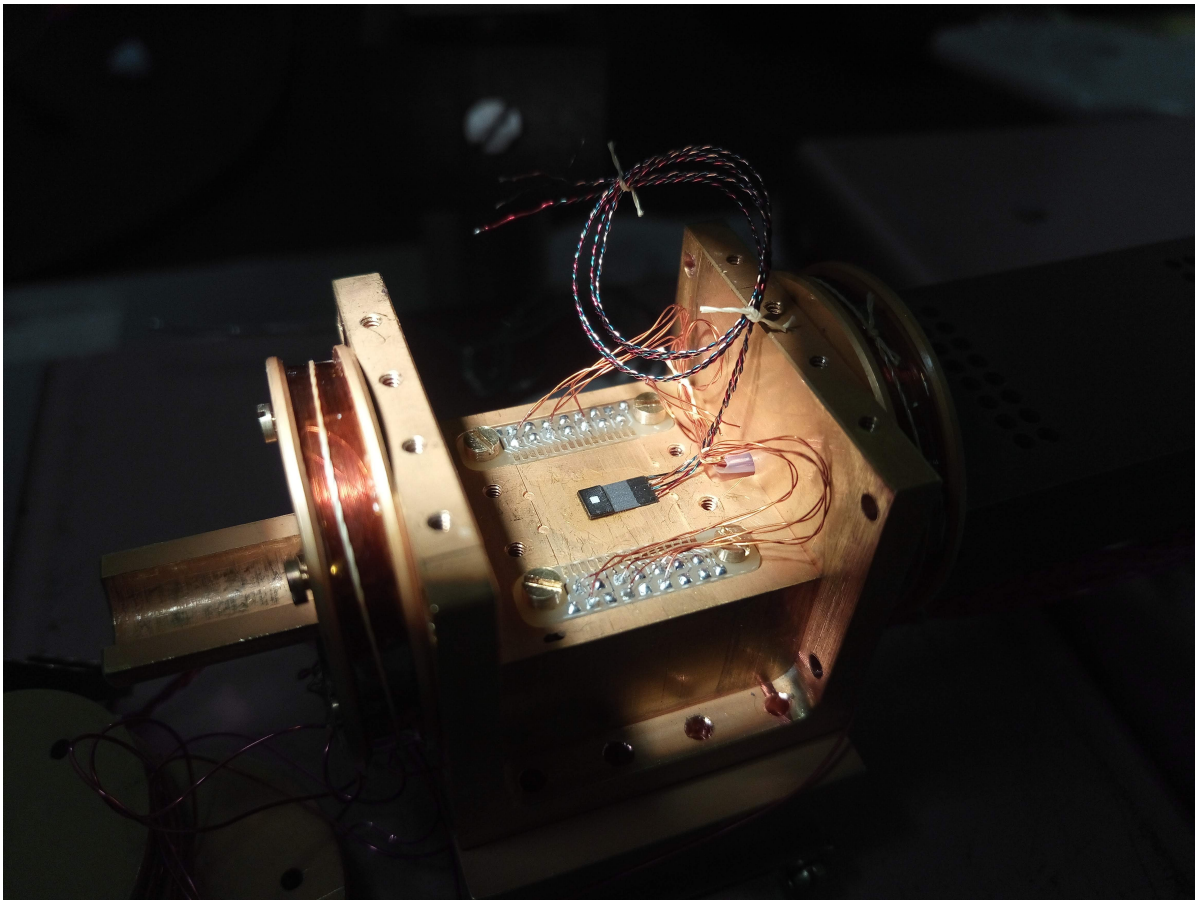

Figure 4.38 2D electron gas Hall probe mounted in the box for calibration measurements. One of the superconducting coils is clearly visible to the left of the picture. The Hall probe is mounted to detect magnetic fields in the z direction.

Lake Shore Cryotronics are developing a new probe that has a smaller active area and a much thinner profile than the HGCT-3020, achieved by using a 2D electron gas as the Hall effect material. One of the main advantages of this probe is that since it is effectively 2D, it will not experience the planar Hall effect. Lake Shore provided with me one of these probes to test, after I reported the large planar Hall effect observed using the HGCT-3020. The new probe requires a F71 Teslameter to read out instead of the 475 DSP Gaussmeter that I had previously used. I used this probe to repeat some of my calibration measurements and compared my results with those obtained using the semiconductor Hall probe. My results are reported in a case study available for download on the manufacturer's website [172].

The new 2DEG probe is able to operate down to much lower temperatures, since an electron gas does not freeze out at 50 mK. When mounted in the appropriate cooling system, we were

able to operate the probe at 300 mK, allowing in-situ calibration of the magnetic field system. Although heating from the sensor prevented operation below this temperature, this technology shows excellent potential for the development of active shielding systems in the future.

Calibration of magnetic fields

The probe worked well at a temperature of 2 K. The calibration measurements showed the same constant of proportionality between magnetic field and current through the z axis coils as the HGCT probe, as shown in Figure 4.39.

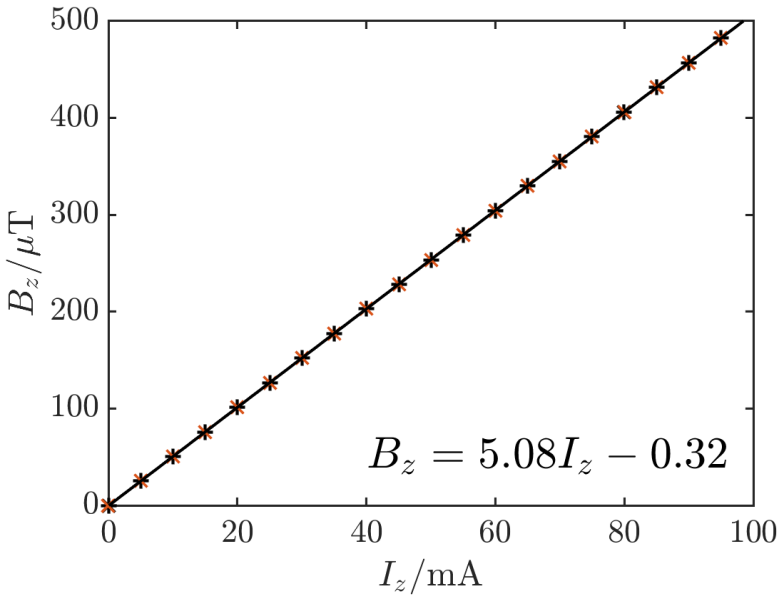

Figure 4.39 Magnetic field produced by the z-coil pair, as measured by the 2D electron gas Hall probe, when the current in the coils is swept from 0-100 mA (black asterisks) and from 100-0 mA (red crosses). The black line shows a linear fit to the data with gradient 5.08. The full equation of this best fit line is on the graph.

Stability measurements

The measured magnetic field fluctuations were much smaller with the probe based on the 2D electron gas, as shown in Figure 4.36 and Table 4.7. The averaging time does not appear to significantly impact the measured fluctuations for both sets of data, suggesting that intrinsic fluctuations of the magnetic field occur on noise scales exceeding the 5-second integration time.

Table 4.7 Standard deviations σ_{B_z}, in μT, of the magnetic field measurements taken when the two different Hall probes were set up to detect fields in the z direction. Additional measurements were carried out to investigate the effects of doubling the averaging time and having a non-zero current in the coil pair aligned with the probe.

	HGCT-3020	2DEG
Fluctuation in B with no current/μT	0.2	0.01
Fluctuation with double the averaging time/μT	0.5	0.01
Fluctuation with 5 mA through coil pair aligned with probe/μT	0.3	0.02

Measurements of parallel magnetic fields

Figure 4.40 shows the field measured by the Hall probe in the z direction in response to applied fields in the x and y directions with both the 2D electron gas Hall probe and the semiconductor Hall probe. The magnitude of the response of the 2D electron gas Hall probe (red crosses) was reduced significantly compared to the response of the semiconductor Hall probe (black asterisks). There was still some response to applied fields in the x direction as the Hall probe is a couple of millmetres off-centre in the x direction, due to the size of the recessed region for mounting devices. From Figure 4.27, this can result in a measured field of about 5 μT at a current of 100 mA. As seen in Figure 4.40, the magnetic field measured in the x direction at a current of 100 mA was about 4.5 μT agreeing well with my simulations and showing that the planar Hall effect had been eliminated. I estimated the magnitude of the planar Hall effect experienced by the semiconductor probe as the difference between the measurements with the two different probes, shown in Figure 4.41. The planar Hall effect results in a spurious magnetic field reading of up to 15 μT and increases linearly as a function of current through the coils producing the magnetic field.

4.7.3 Spherical scanning

When characterising detectors, it is valuable to be able to investigate the device response to magnetic fields in all directions, to find the magnetic field directions that are of most concern. This information will inform design decisions when developing magnetic shielding for instruments. I set the magnitude of the magnetic field and swept its direction in order to investigate the directional response of the HGCT semiconductor probe.

The method I used to sweep the magnetic field required some consideration. I wanted to use the magnetic field to define a sphere of fixed radius, which can be parameterised in terms of two angles, the azimuthal (ϕ) and polar (θ) angles. However, moving in constant increments of ϕ and θ will oversample the poles of the sphere relative to the rest of the surface. I therefore set

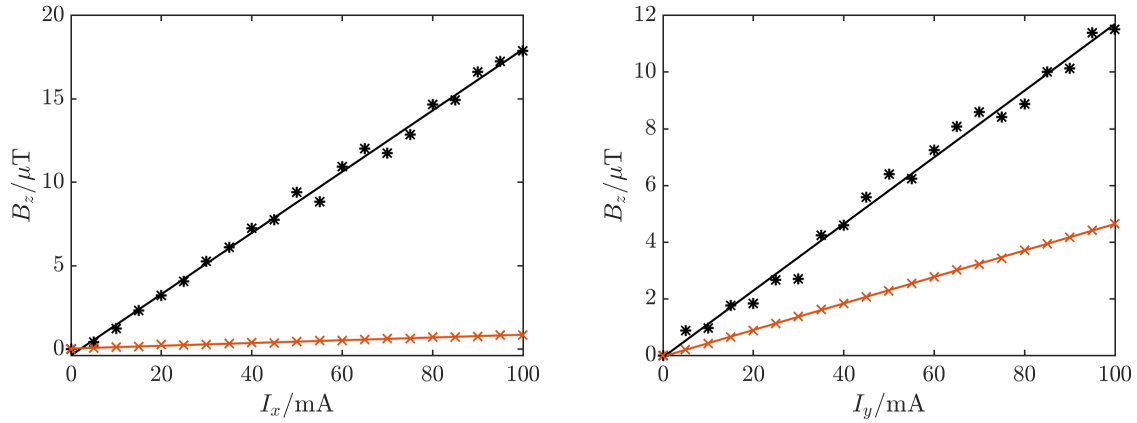

(a) I_x varied. (b) I_y varied.

Figure 4.40 Magnetic field measured as a function of current through the (a) x and (b) y coil pairs when the Hall probe is mounted to detect fields in the z direction. The black asterisks show data using a 2D electron gas Hall probe; the red crosses show data from a semiconductor Hall probe. The solid lines of the corresponding colour show linear fits to the two data sets.

the increment of ϕ and the area element and used these to calculate the required increments of polar angle θ. The sampling produced by this method is shown in Figure 4.42a. The path the scan takes is shown in Figure 4.42b - I fix the value of ϕ, vary θ, then increment ϕ and repeat the process.

The voltage across a device of interest can be expressed as a Taylor series expansion,

$$V = f(|\mathbf{B}|_0, \theta, \phi) + \frac{\partial f(|\mathbf{B}|_0, \theta, \phi)}{\partial |\mathbf{B}|}|\mathbf{B}| + \frac{\partial^2 f(|\mathbf{B}|_0, \theta, \phi)}{\partial |\mathbf{B}|^2}\frac{|\mathbf{B}|^2}{2} + \ldots \tag{4.3}$$

in which we want to find the linear response to a magnetic field, $\frac{\partial f(|\mathbf{B}|_0, \theta, \phi)}{\partial |\mathbf{B}|}$, but in which there may be higher order terms. Each of these terms can be expanded using spherical harmonics.

Expanding the response in a spherical harmonic basis

The experimental procedure gives four parameters for each time point: three expressing the direction of the field and one expressing its magnitude. Using these, it is possible to plot the points on the surface of the response, but there is not any information about the functional form of the surface. There is insufficient time to take enough data points for interpolation to produce a smooth surface, and so the full response surface cannot be plotted directly from the experimental data. I therefore used a spherical harmonic basis to get information about the functional form of the response surface, allowing me to plot it. The spherical harmonic basis has three additional advantages for my work: firstly, the shape of the expected response

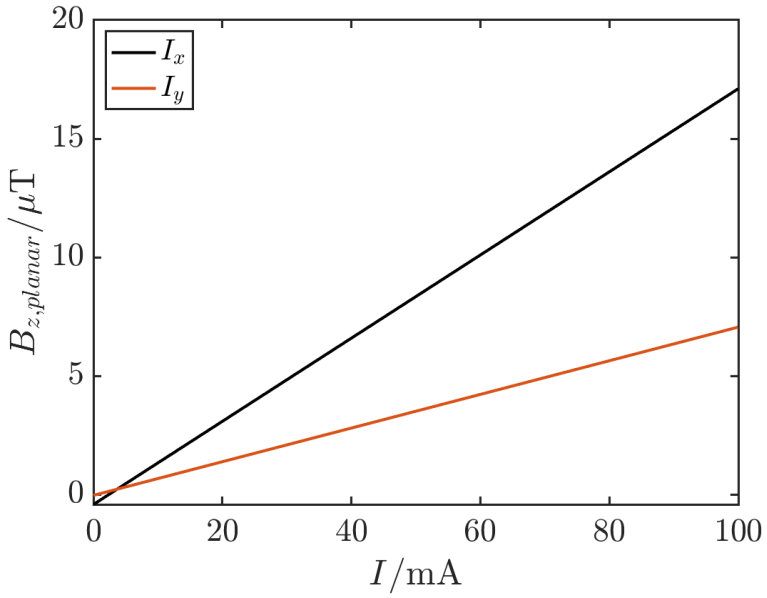

Figure 4.41 Magnetic field attributable to the planar Hall effect, calculated using the best fit lines, as a function of current in (black) the x coil pair and (red) the y coil pair.

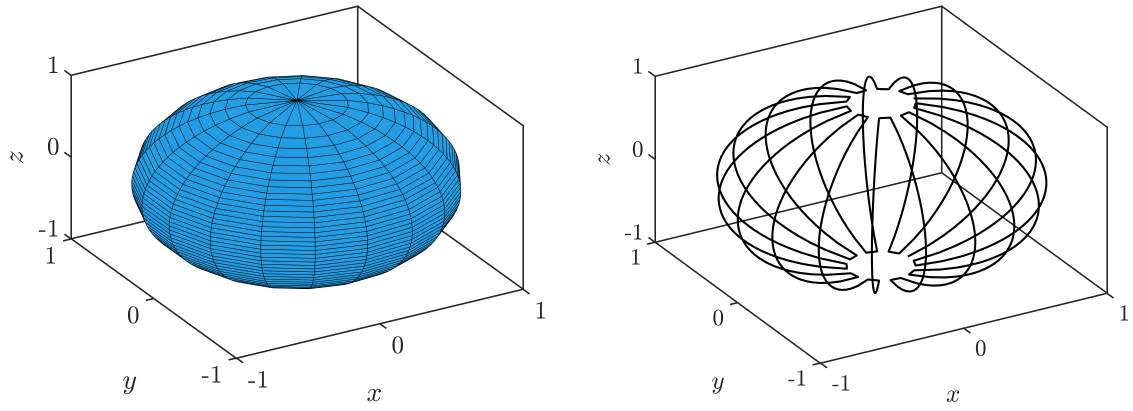

Figure 4.42 Strategy for scanning the magnetic field over the surface of a sphere, allowing examination of the response of devices to fields in all directions. The surface of the sphere was divided up into sections of equal area, as shown in (a). Each section is defined by two angles, its azimuthal angle and its polar angle. The azimuthal angle is fixed and the polar angle is scanned over an arc of the sphere. This process is repeated until all of the desired values of azimuthal and polar angles are covered. The path the scan takes is shown in (b).

of the Hall probe matches the first order spherical harmonics; secondly, both my spherical measurements and the spherical harmonics have a preferred axis; and finally, the spherical harmonic coefficients allowed me to characterise a surface using only a few parameters.

The response (D) of a device to a magnetic field can be expressed using spherical harmonics as basis functions,

$$D = \sum_{l=0}^{3} \sum_{m=-l}^{l} N(l,m) Y_l^m \tag{4.4}$$

where Y_l^m are the real spherical harmonic basis functions and $N(l,m)$ are the spherical harmonic coefficients. The spherical harmonics are already an orthogonal basis so components can be extracted by integrating the product of the device response with each spherical harmonic,

$$N(l,m) = \sum_{\theta,\phi} D \times Y_l^m dA(\theta,\phi), \tag{4.5}$$

This integration step is further simplified by the fact that as my scanning strategy divides the surface of the sphere into sections of equal area, Equation (4.5) becomes

$$N(l,m) = \sum D \times Y_l^m dA. \tag{4.6}$$

To test this procedure I applied it to two of the spherical harmonic basis functions themselves, as seen in Figures 4.43 and 4.44. The procedure works as expected, giving $N(l,m) = 1$ for the spherical harmonic basis function used and $N(l,m) = 0$ for all other spherical harmonic basis functions.

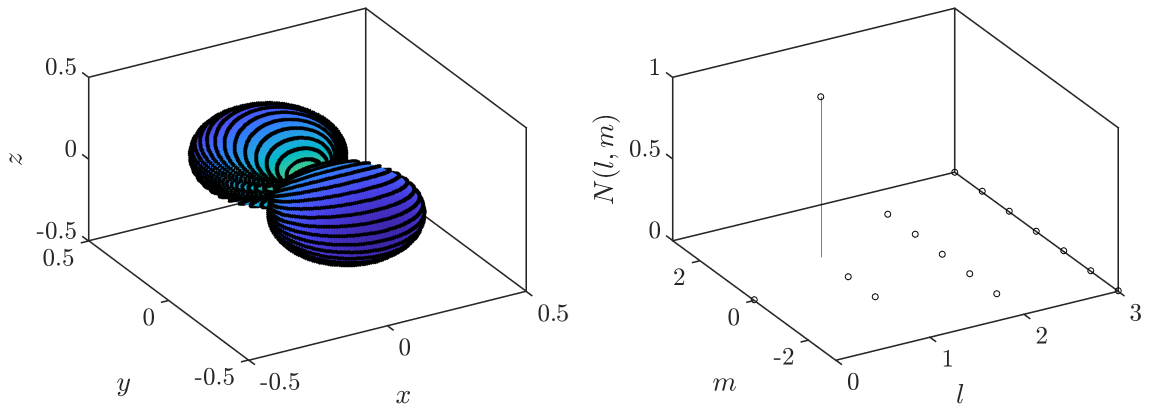

(a) (b)

Figure 4.43 (a) Real part of the spherical harmonic Y_1^{-1} (black asterisks) and the calculated surface using the spherical harmonic basis functions. The shading corresponds to the magnitude. (b) Coefficients $N(l,m)$ from equation (4.4) for the calculated surface.

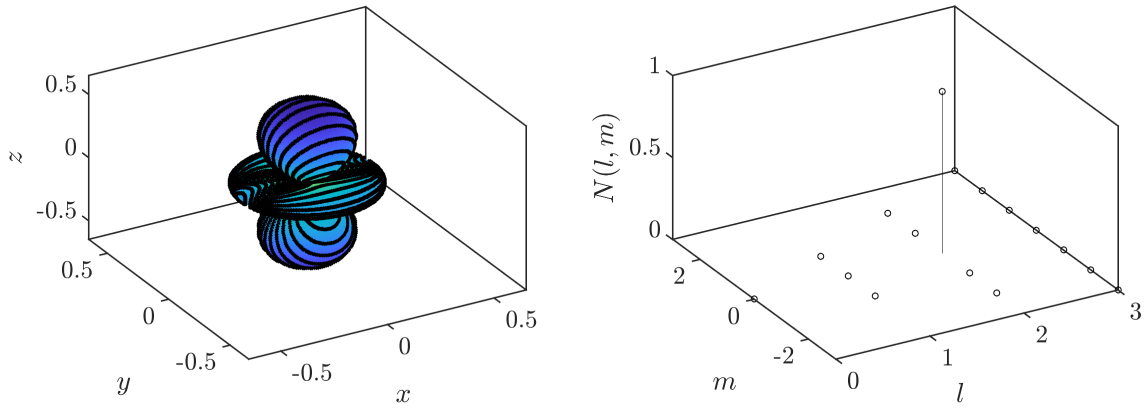

(a) (b)

Figure 4.44 (a) Real part of the spherical harmonic Y_2^0 (black asterisks) and the calculated surface using the spherical harmonic basis functions. The shading corresponds to the magnitude. (b) Coefficients $N(l, m)$ from equation (4.4) for the calculated surface.

I used this procedure to calculate the spherical harmonic components of the experimental data obtained. I carried out several checks to ensure that the resulting sum of spherical harmonics was a good representation of the data, as shown in Figure 4.45. Figure 4.45a shows a slice through the response surface in the $x - z$ plane. The data is shown as black asterisks, the first order spherical harmonic, which goes as $\cos\theta$, scaled to fit the data, is shown as red crosses, and the full spherical harmonic sum is shown as blue diamonds. As the response is expected to vary as $\cos\theta$, the first order spherical harmonic is a good approximation to the data, but the spherical harmonic sum provides some higher order corrections, likely to be due to small deviations of the experimental arrangement from the ideal, such as the presence of mixed media, stray fields, and slight misalignments in orientation. Figure 4.45b shows the direction of the field scaled by the response of the Hall probe, as measured experimentally (black points) and calculated using the spherical harmonic basis (multicoloured surface). The calculated surface is a good representation of the experimental data.

The response surface is well described by the first order spherical harmonic, as shown by Figure 4.46a, which shows the coefficients $N(l, m)$ in the spherical harmonic decomposition. The first order coefficient provides the largest contribution to the spherical harmonic sum. The response surface as calculated using the spherical harmonic sum is shown in Figure 4.46b. As expected the response varies as $\cos\theta$, with maximal response when the field is entirely in the z direction, as this is the direction in which the Hall probe is orientated.

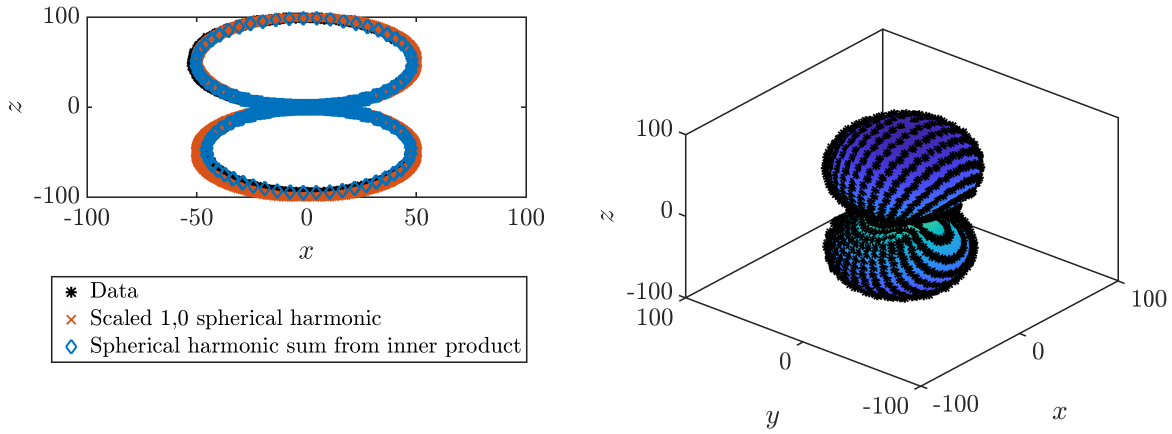

(a) (b)

Figure 4.45 (a) A slice in the $x-z$ plane shows the data (black asterisks), a scaled first order spherical harmonic (red crosses) and the calculated spherical harmonic sum (blue diamonds). (b) The direction of the field scaled by the response of the Hall probe, as measured experimentally (black asterisks) and as expressed in a spherical harmonic basis (multicoloured surface). The shading corresponds to the magnitude of the response of the Hall probe.

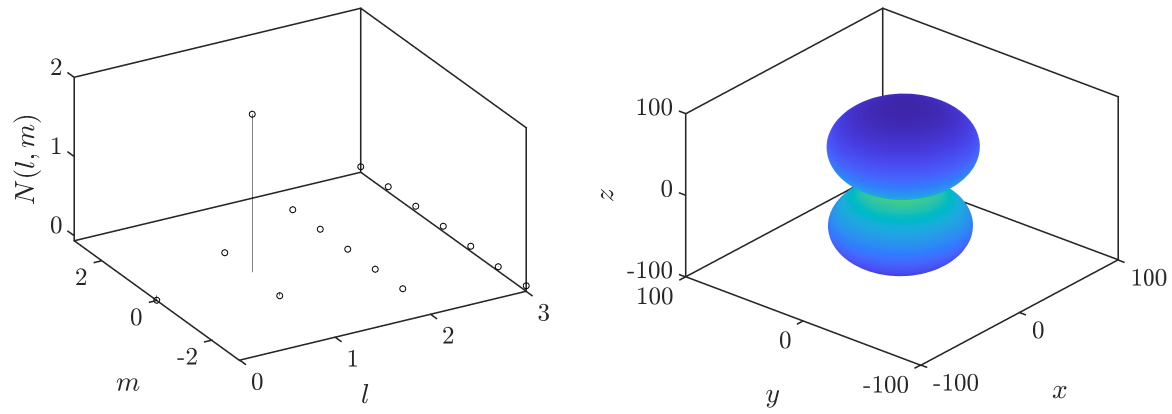

(a) (b)

Figure 4.46 (a) Coefficients $N(l,m)$ from Equation (4.4) for the spherical harmonic decomposition. (b) Direction of the field scaled by the response of the Hall probe, using the spherical harmonic basis to obtain a smooth surface. The shading corresponds to the magnitude of the response of the Hall probe.

4.7.4 Spherical scanning with 2D Electron Gas probe

I repeated the spherical scan using the 2D electron gas Hall probe, as shown in Figure 4.47. These scans were carried out for target magnetic fields of 100 µT (Figure 4.47a) and 200 µT (Figure 4.47b). The results showed that varying the magnitude of the target magnetic field does not change the shape of the response.

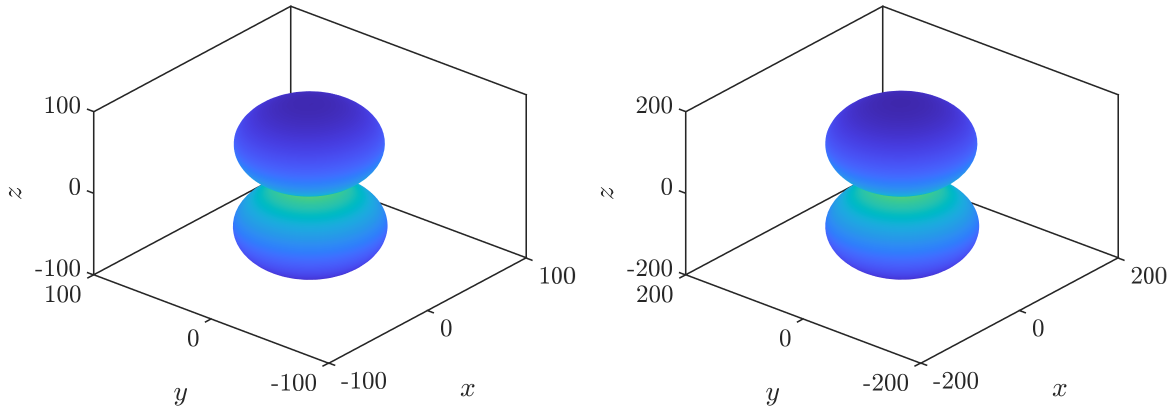

Figure 4.47 Direction of the field scaled by the response of the Hall probe, for a target magnetic field of (a) 100 µT and (b) 200 µT. The shading corresponds to the magnitude of the response of the Hall probe. In (a), the largest spherical harmonic coefficient for the surface is N(1,0)=0.2; the next largest is N(0,0)=0.003. In (b), the largest spherical harmonic coefficient for the surface is N(1,0)=0.4; the next largest is N(1,1)=0.004.

4.8 Description of measurement system

Both the SQUIDs and the TESs were cooled to a very low temperature, in order to minimise the noise of the system. The SQUIDs were surrounded by a niobium shield, to prevent their operation being affected by the 3-axis magnetic field coil system. Figure 4.48a shows the location of this shield relative to the box - it was mounted next to one of the coils, directly opposite the mount onto the refrigerator.

Characterisation of the TESs was carried out over a temperature range of 60-250 mK, allowing measurements close to the transition temperature of even the highest T_c device as well as measurements well below the transition temperature of all the devices. Cooling was achieved using a four-stage Closed-Cycle Adiabatic Demagnetisation Refrigerator (CC-ADR). The four stages are at 45 K, 4 K, 1 K and 60-70 mK (the exact temperature depends on the thermal load provided by the TES box). A Pulse-Tube Cooler (PTC) was used to maintain the temperature

of the 4 K stage, whilst the ADR was used to cool the 1 K and 60-70 mK stages below this temperature. Figure 4.48b shows the TES box mounted on the lowest temperature stage of the ADR. The TESs were read out using SQUIDs to track the current through the TES, by measuring the magnetic field of an inductor in series with the TES. The SQUIDs were provided by PTB [173].

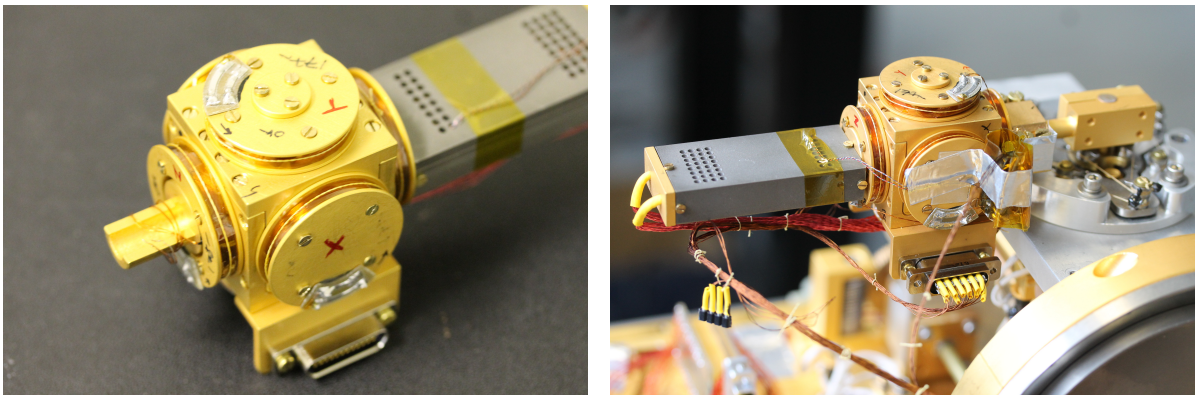

(a) (b)

Figure 4.48 (a) Fully assembled TES box prior to mounting on the ADR. The SQUIDs are in the Nb magnetic shield to the right of the image. (b) TES box mounted on the lowest temperature stage of an ADR, with the wiring connected.

Keeping the SQUIDs close to the TESs was essential to maintain good thermal contact between the 60-70 mK stage, the SQUID chip and the TES chip. Figure 4.49 shows the three SQUID chips used for readout. Figure 4.49a shows the SQUIDs before clamping; Figure 4.49b shows the SQUIDs clamped to the mount.

Although the SQUIDs were shielded, there was no external magnetic shield around the TESs, to enable measurements of field sensitivity without the distortions in field generated by magnetic shielding. For zero-field measurements, I used the 3-axis coil system to cancel out the Earth's magnetic field.

As the 2D Electron Gas Hall probe is theoretically capable of being operated at 50 mK, it was mounted just above the TES array in the TES box, as shown in Figure 4.50a, to give a means of checking the magnetic field calibration in-situ.

Each TES was connected to two pads at the edge of the chip, via Nb wiring. These pads were then connected to fan out boards by wire bonding, allowing more room for the wiring to the readout electronics to be soldered on. This can be seen in Figure 4.50b.

The circuit used for the readout of the TESs is shown in Figure 4.51. In the TES bias circuit to the left of the figure, the TES is kept under voltage bias by the use of a small bias resistor R_B, with resistance of $\approx 1\,\text{m}\Omega$. The large load resistor R_L, with a resistance of the order of tens

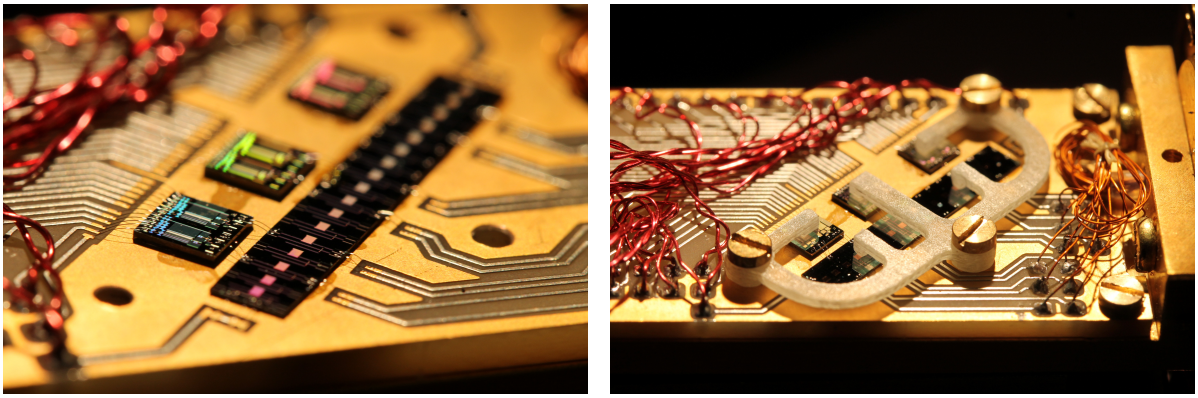

(a) (b)

Figure 4.49 (a) SQUID chips used for readout. Each chip contains two SQUID channels. One of the main differences between the SQUIDs was the parameter M_{ratio}, defined as the ratio of M_{in} to M_{F} from Figure 4.51. Two of the chips contained SQUIDs previously used by the group, with $M_{\text{ratio}} = 7.73$. The third chip contained two new SQUIDs, with a much higher M_{ratio}. (b) The SQUIDs clamped in place on the mount, prior to its insertion into the magnetic shield.

(a) (b)

Figure 4.50 (a) Inside the TES box, showing the 2D Electron Gas Hall probe mounted just above the TES array. (b) A close up view of the inside of the TES box - the pads on the chip are connected to fan out boards, seen here at the top left and bottom right of the image. These fan out boards are then wired to the readout system.

of kΩ, provides a constant current source. There is some stray resistance in the circuit, in the soldered joints and contacts, represented as a single resistor R_S. The value of this resistance is measured for each individual TES and then compensated for in the analysis of the data.

To the right of the figure is the SQUID component of the readout circuit. The first stage SQUID, SQ1, can be used to determine the current through the TES by measuring the magnetic field in the inductor L_{in}, via the mutual inductance M_{in}. The SQUID series array (SSA) consists of many SQUIDs in series, providing a higher impedance to allow a wider bandwidth and simpler room temperature electronics [174]. Here it is represented as a single equivalent SQUID. Both SQ1 and the SSA are current biased to ensure good sensitivity, via the voltages V_I and V_{IFX} respectively. There are two feedback circuits, one for SQ1 and one for the SSA, both containing the same feedback resistance R_{fb}. These feedback circuits allow the output voltage V_B to be linearised with respect to the current in the feedback circuit, via the mutual inductances M_F and M_{FX}. The currents in the feedback circuits are set via the voltages V_F and V_{FX}. The feedback circuit for the SSA is used before measurements are taken, in order to determine the bias voltages V_{FX} and V_{IFX} that allow SQ1 to have the greatest responsivity. The feedback circuit for SQ1 is needed to linearise V_B with respect to I_{TES} and is used to lock both SQUIDs and take measurements. All of the voltages are controlled at room temperature using a custom-made set of electronics. Overall the effect of the SQUID readout circuit was to act as both a low noise current to voltage converter and an amplifier with sufficient gain and output impedance to allow the signal to be passed through a room temperature pre-amplifier.

I recorded the voltage applied across the TES bias circuit V_A and the voltage produced at the output of the operational amplifier V_B, passing both voltages through a series of filters and an analogue to digital converter. Data was taken using a data acquisition card in a PC, with a series of custom-made LabView virtual instruments used to process and record the data.

The output voltage V_B can be related to the current through the TES I_{TES} by

$$I_{TES} = \frac{V_B - y_{off}}{M_{ratio} R_{fb}}, \tag{4.7}$$

where y_{off} is the voltage offset in the measurement of V_B, determined by the bias point of the SQUIDs, and M_{ratio} is the ratio of M_{in} to M_F.

Once I_{TES} is known, the bias voltage across the TES can be calculated, assuming the inductor L_{in} has no resistance, as

$$V_{TES} = \frac{R_B(2V_A - x_{off}) - I_{TES}(R_L R_S + R_S R_B + R_B R_L)}{R_L + R_B}, \tag{4.8}$$

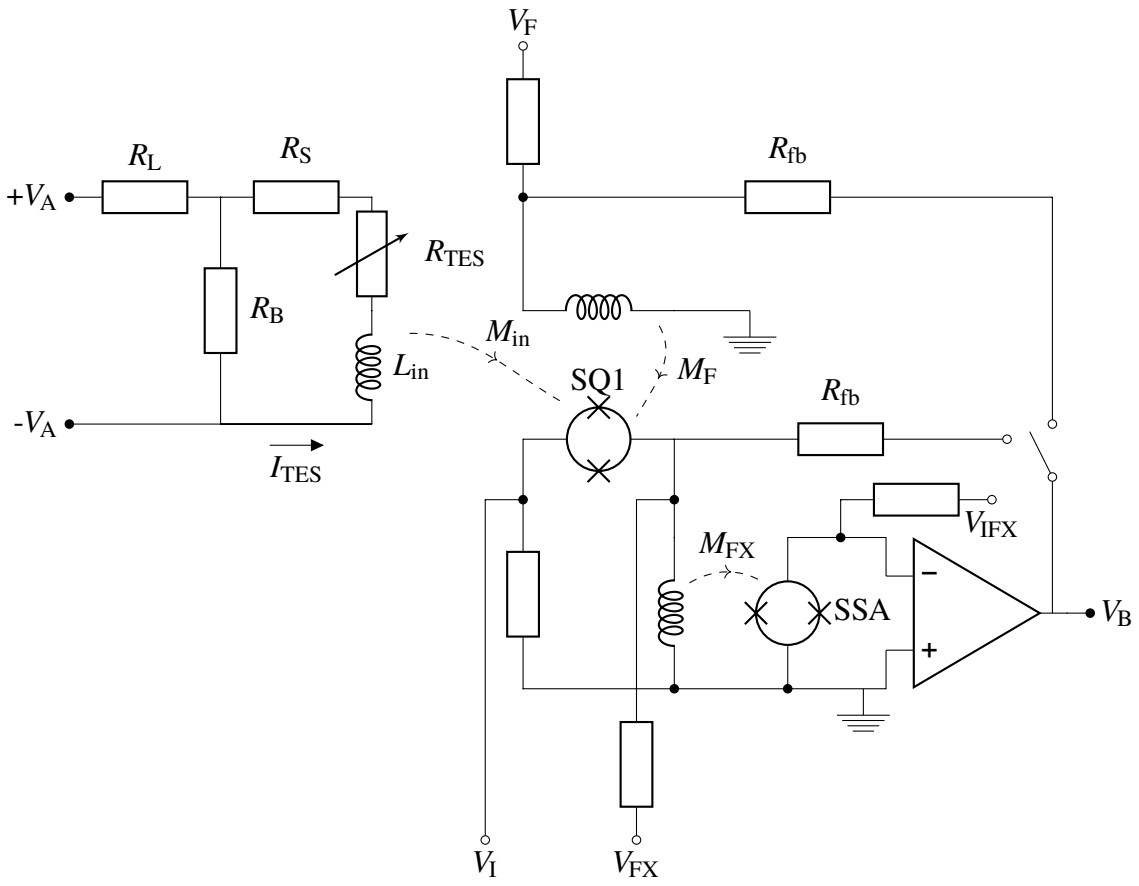

Figure 4.51 Readout circuit used to test the TESs. The dashed arrows represent the mutual inductances between the SQUIDs and the inductors. The labels next to the terminals indicate the voltages. The total voltage applied across the terminals of the circuit containing the TES is $2V_A$. SQ1 indicates the first stage SQUID whilst SSA indicates the SQUID series array.

where x_{off} is the voltage offset in the measurement of V_A, due to filters in the bias and readout circuits and the data acquisition card.

The stray resistance R_S is calculated from the requirement that the gradient of the graph of V_{TES} against I_{TES} must be zero when the TES is superconducting. The offsets x_{off} and y_{off} can be determined using the requirement that the normal state resistance is invariant under a reversal of the polarity of V_{TES}. At a temperature close to T_c, a double-sided $I(V)$ curve was measured, and used to plot a $R - V$ curve. The values of x_{off} and y_{off} are the values for which this $R - V$ curve and its reflection in the R axis most closely coincide at the limits of the voltage range. I assumed that R_{TES} at maximum V_{TES} lies on this curve for all of the other bath temperatures.

With this measurement system, I was able to test the TES chip at a base temperature of 63 mK, with 30 minutes of hold time at base temperature, 2 hours of hold time at 90 mK and

over 8 hours of possible measurement time for the highest T_c devices. The results of these tests will be reported in the next chapter.

4.9 Conclusions

This chapter describes the design of a set of TESs to enable a systematic study of the effects of bilayer geometry, standardising other parameters such as shape and thermal conductivity. The use of the proximity effect model developed in Chapter 2 enabled me to carry out preliminary studies of the TES designs and select devices which would have transitions in the temperature range accessible using our ADR. I created a mask for a wafer containing six TES chips, creating macros in Klayout to automatically generate appropriately scaled TES designs. As the mask design features a range of geometries, the mask could be re-used for future investigations by the group, for example to test new material combinations.

The results of the calibration testing provided realistic parameters for input into my proximity effect model, whilst putting limits on other parameters such as γ_B. $R(T)$ measurements on unreleased TESs led to two key observations - the invariance of T_c with bilayer side length for large TESs and the presence of a residual resistance in TESs with normal metal bars across the full film width. This residual resistance shows that supercurrent cannot flow directly through thick normal metal bars, which provides an explanation as to why the proximity effect model does not give a good account of TES bilayers with thick bars, supporting the observations in Section 3.5.

The new jig design allows the effects of magnetic field on TESs to be studied, by enabling a uniform magnetic field to be applied in any direction. This allows measurements of the directional magnetic field dependence to be carried out, something that has not been done before for TESs. This is important for my measurements in Chapter 6 and will also be a useful resource for the group going forward, particularly since it was designed with a standard chip size in mind. The semiconductor Hall probe tests of this jig allowed me to calculate the constant of proportionality between the current and field, as well as showing the directional response of the probe had the expected form and that the off-axis fields were within the range expected for a probe susceptible to the planar Hall effect. The fields produced by the jig are very stable, with any fluctuations being smaller than the error of the Hall probe. The Hall probe testing with the 2DEX probe verified the results of the calibration testing, providing results that were more accurate and free from the planar Hall effect. Such a probe could be implemented in future active shielding systems for TESs, as it is able to operate at much lower temperatures than semiconductor probes.

When the ADR was configured as described in this chapter, the TESs reached a minimum temperature of less than $T_c/2$ for the majority of the TES designs, with excellent hold time at 90 mK.

Chapter 5

Experimental study of bilayer geometry

5.1 Introduction

This chapter describes the experimental study of a series of TESs with systematically varying bilayer geometries, to investigate whether there is an optimal bilayer geometry and to test the predictions made in Chapter 4. Section 5.2 explains how sets of TESs were selected for study, and in Section 5.3, I present the results of experimental measurements, showing the effects of bilayer geometry on transition temperature, response time, thermal properties, noise, electrothermal parameters and transition sharpness. I utilise these measurements to examine whether there is a bilayer configuration that optimises all of these performance parameters.

In Section 2.4.3, I calculated the self-field for films with different arrangements of partial bars, and observed that devices with an odd number of bars have a larger self-field than devices with an even number of bars, and that unpatterned devices have a significantly smaller self-field than patterned devices. I examine whether trends in device behaviour are linked to differences in self-field, looking for differences in behaviour between TESs with odd and even numbers of bars.

5.2 Order for device measurement

As described in Section 4.2.7, two different types of chip design were available for measurement. One had devices patterned with normal metal bars, extending across 80 % of the bilayer width, and one had devices patterned with normal metal stripes, extending across the full bilayer width. From the results of Section 4.5.2, the regions with normal metal bars do not superconduct, so the devices with full width stripes would not be able to support supercurrent flow through the

bilayer. A chip with partial normal metal bars was selected for investigation, ensuring that supercurrent is able to flow through the bilayers.

Table 5.1 shows the order in which devices were tested, with dashed lines to show which devices were tested in each cooldown. The investigations carried out in each cool down were as follows:

1. Effect of bilayer size on TES performance and magnetic field dependence.

2. Effect of number of bars on TES performance and magnetic field dependence for devices with larger (40 µm square) films, plus feasibility testing on a device with a 5 µm side length bilayer with a single metal bar.

3. Effect of number of bars on TES performance and magnetic field dependence for devices with smaller (10-20 µm square) bilayers.

The investigation into the magnetic field dependence of these devices will be presented in Chapter 6.

Table 5.1 Order for testing devices, with dashed lines to indicate divisions between batches. The chip tested was SIZE-1, a chip on which the normal metal bars extend across 80 % of the bilayer width.

ID number	L /µm	Number of bars	Bar width/µm	Bar spacing/µm	SQUID channel
4	40	0	-	-	3
5	30	0	-	-	4
7	10	0	-	-	5
8	5	0	-	-	6
2	70	0	-	-	5
12	40	1	4	18	3
16	5	1	1	2	4
20	40	2	4	10.7	2
27	40	3	4	7	6
6	20	0	-	-	2
15	10	1	1	4.5	3
22	20	2	2	5.3	4
23	10	2	1	2.7	5
30	10	3	1	1.75	6

5.3 TES measurements

For each device, I carried out the following set of measurements to investigate the effects of bilayer geometry on TES properties. In most measurements, the external magnetic field was cancelled by using the new magnetic field system to generate an opposing field.

- $I_c(T)$ - double-sided $I(V)$ curves were recorded for a series of temperatures and used to determine the critical current as a function of temperature. This gives a measure of transition sharpness.
- $I(V)$ curves as a function of temperature - from these measurements T_c, K and n were calculated, to investigate whether n and K vary between the TESs and to study trends in T_c for the different bilayer geometries.
- Circuit impedance - the TES impedance was calculated from the measured circuit impedance and used to determine α and β for the devices under test.
- Risetimes - the response time of a TES determines how long it must be left to settle before measurements can be recorded. The current response to a step in voltage was recorded at or around base temperature for all of the devices to calculate this response time.
- Noise - noise spectra were taken to investigate differences in noise between the TES designs.

5.3.1 $I_c(T)$

Figure 5.1 shows how the critical current varies as a function of temperature for all of the unpatterned TESs. The larger devices all display transitions of approximately the same width, with a slightly wider transition for the device with a 20 µm side length film. The devices with 10 µm side length and 5 µm side length bilayers show much wider transitions. This broadening in $I_c(T)$ for smaller bilayer sizes was also observed by Smith et al. [14], and suggests a change to a different behaviour regime. This is supported by the modelling in Section 4.2.7, which showed that devices with bilayer side lengths less than 20 µm have broader transitions and higher transition temperatures. For these smaller devices, the proximity effect from the Nb electrodes has a significant influence on the full bilayer length.

Figure 5.2 shows the effect of adding bars on the shape of $I_c(T)$. For the TESs with 40 µm side length films shown in Figure 5.2a, adding any number of bars to the film broadens the transition, attributable to the increase in self-field, but there is very little difference in shape between patterned TESs of the same bilayer size, suggesting the variation in self-field due to

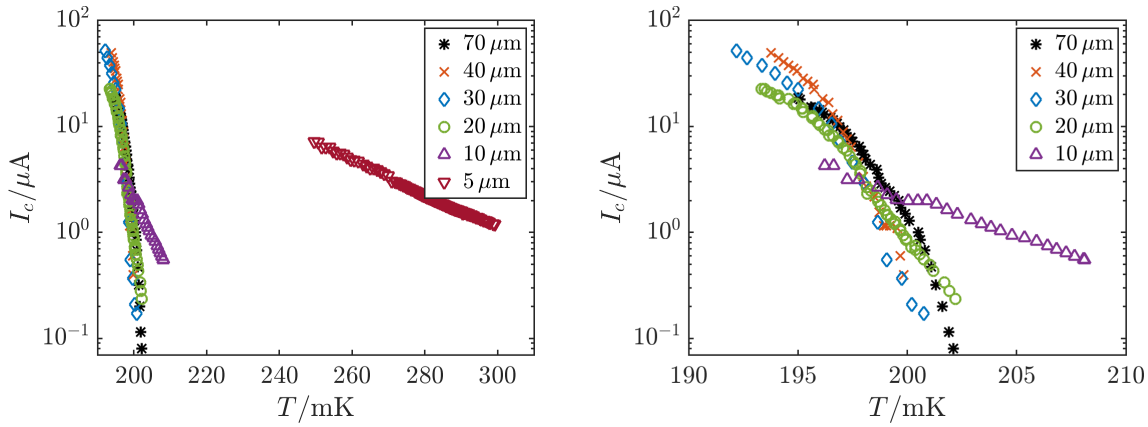

Figure 5.1 $I_c(T)$, measured with the Earth's magnetic field cancelled, for a series of unpatterned devices with bilayer side lengths ranging from (a) 70 µm to 5 µm. In (b) $I_c(T)$ for the device with the smallest (5 µm) bilayer side length has been omitted to allow trends in the data for the other devices to be observed.

the different numbers of bars is not significant. Figure 5.2b shows that adding two bars to a TES with a 20 µm side length bilayer broadens the width of the superconducting transition, supporting the observation from Figure 5.2a that the addition of bars widens the transition. For the smaller 10 µm side length and 5 µm side length TES bilayer sizes, there is less of an effect on transition width when normal bars are added, as shown in Figures 5.2c and 5.2d, although here, the devices where the films are patterned with an even number of normal bars exhibit slightly sharper transitions than the devices where the films are patterned with an odd number of bars, suggesting a possible self-field effect.

5.3.2 $I(V)$ curves

$I(V)$ curves were measured for all TESs by biasing the device in its normal state, locking the SQUIDs, then reducing the voltage V_A and measuring V_B, where V_A and V_B are related to V_{TES} and I_{TES} as shown in Figure 4.51 and described in Section 4.8.

Figure 5.3 shows (a) the $I(V)$ curves and (b) the $P(V)$ curves as a function of temperature for the device with a 70 µm side length unpatterned bilayer. Measurements at low temperatures are shown in light blue, whilst measurements close to T_c are shown in dark blue. All of the $I(V)$ curves show one single, smooth transition from the normal state to the superconducting state as the voltage is reduced, with no evidence of multiple transitions. The $P(V)$ curves all show relatively flat power plateaus, although as there is a slight slope I used a resistance-based method to find $P(T)$.

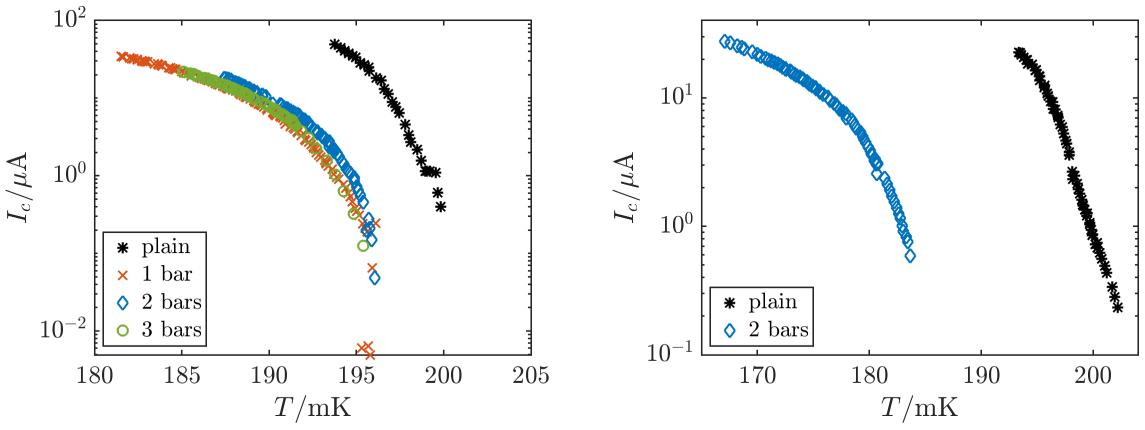

(a) 40 µm.

(b) 20 µm.

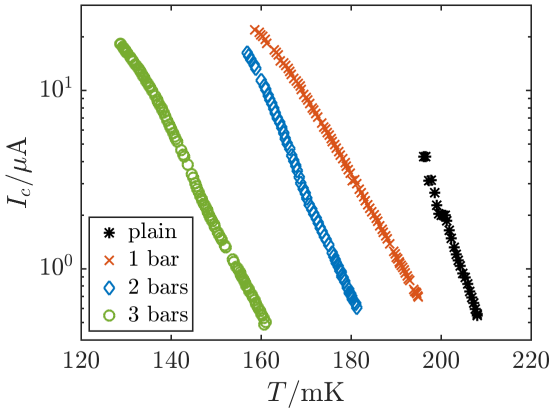

(c) 10 µm.

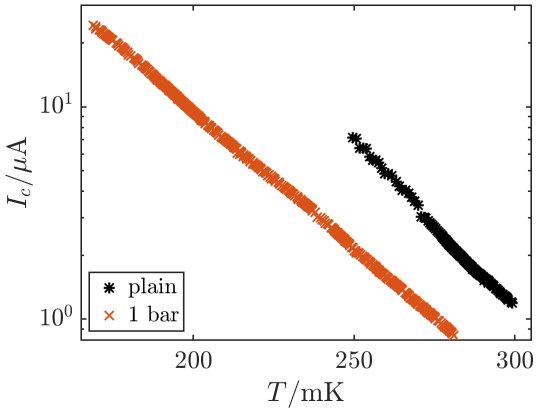

(d) 5 µm.

Figure 5.2 $I_c(T)$ with number of bars for devices with square bilayers of different side lengths.

$P(R)$ was calculated as shown in Figure 5.4a, and used to read off values of P at a constant value of R for the different temperatures. For fixed R,

$$P(T_b) = K(T_c^n - T_b^n), \tag{5.1}$$

where n and K are the thermal constant and constant of proportionality, defined in Section 2.2.2. By fitting this function to the $P(T_b)$ data, values of K, n and T_c were determined for each device. G was then calculated using Equation (2.15).

Figure 5.5a shows T_c as a function of $1/L$, with the points to the left of the figure corresponding to the devices with larger film areas. Increasing the size of the TES bilayer and adding partial normal metal bars to this bilayer both reduce T_c. The effect of adding bars is greater for the smaller bilayers. The trends in T_c for the devices with 10 µm side length bilayers do not appear to link to any variations in self-field, as the transition temperature reduces as

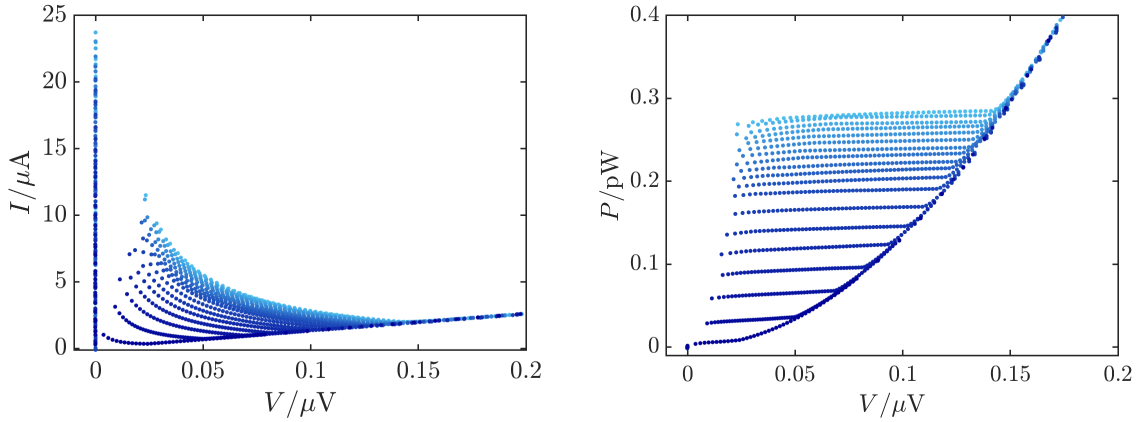

(a) (b)

Figure 5.3 (a) $I(V)$ curves and (b) $P(V)$ curves as a function of temperature for the TES with a 70 µm side length unpatterned bilayer. Measurements at low temperatures are shown in light blue, whilst measurements close to T_c are shown in dark blue.

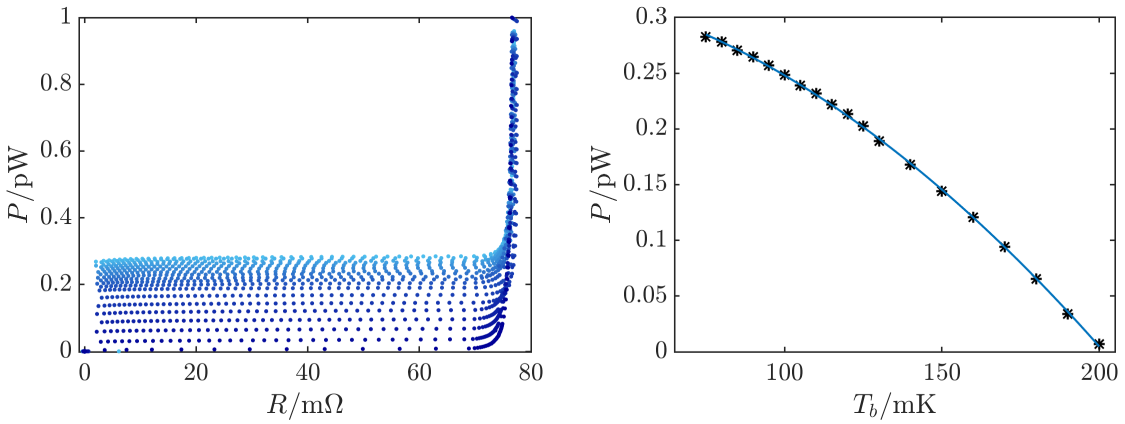

(a) (b)

Figure 5.4 (a) $P(R)$ as a function of temperature for the TES with a 70 µm side length bilayer. Measurements at low temperatures are shown in light blue, whilst measurements close to T_c are shown in dark blue. (b) $P(T_b)$ measured (black asterisks) and fitted using the power flow equation (blue line) with the Earth's field cancelled. From the fit to the power flow equation, G = 3.2 pW K^{-1}, n = 1.94 and T_c = 201.5 mK.

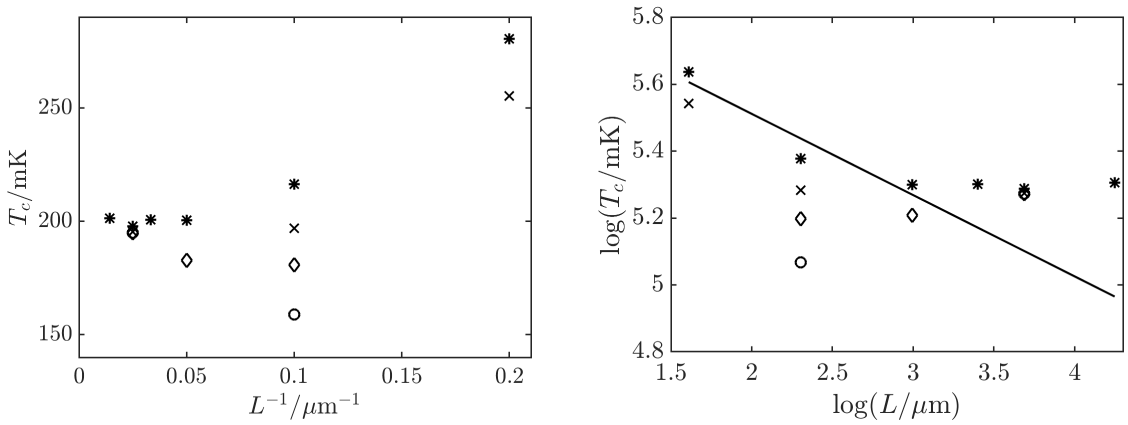

(a) (b)

Figure 5.5 T_c with (a) $1/L$ and (b) $\log(T_c)$ against $\log(L)$ to determine n in the relationship $T_c \propto L^n$. Asterisks correspond to devices with no bars, crosses to devices with one bar, diamonds to devices with two bars and circles to devices with three bars. The solid line in (b) shows a linear fit for the points corresponding to the three smallest unpatterned devices, which has gradient $n = -0.2$.

the number of bars is increased, regardless of whether the number of bars is odd or even. For the TESs with 40 µm side length bilayers, T_c for the device with two bars is nearly the same as T_c for the device with three bars, but the variations in T_c are so small that they cannot be definitively attributed to changes in self-field.

In Figure 5.5b, $\log(T_c)$ is plotted against $\log(L)$, so a linear fit can be used to determine the n in the relationship $T_c \propto L^n$. As before, the asterisks correspond to devices with no bars, the crosses to devices with one bar, the diamonds to devices with two bars and the circles to devices with three bars. For this set of TESs, the largest devices show minimal variation in T_c with L, whilst the transition temperatures of the three smallest devices show $n = -0.2$. This is lower than both the value of $n = -0.7$ determined in Section 2.3, using the proximity effect model with generalised TES parameters, and the value of $n = -2$ measured experimentally by Sadleir et al. for square Mo/Au bilayers [1]. However, it is consistent with my proximity effect model simulations for this set of devices in Section 4.2.7, where for the three smallest devices, $n = -0.2$.

Comparing the experimental measurements of T_c in Figure 5.5a with the predicted values in Table 4.3 from Section 4.2.7, the proximity effect modelling gives a good account of the measured trends in T_c. As observed experimentally, the devices with bilayer side lengths greater than 20 µm side length were predicted to have similar transition temperatures and the two devices with the smallest bilayers were predicted to have much higher transition temperatures. From Figure 4.7, the two smallest TESs were expected to display broader transitions, which

was also observed experimentally. Simulations for the patterned TES bilayers were not carried out, since the proximity effect model does not give a good account of TES thin films with bars of the thicknesses used in this set of devices, as discussed in Sections 3.5 and 4.5.2.

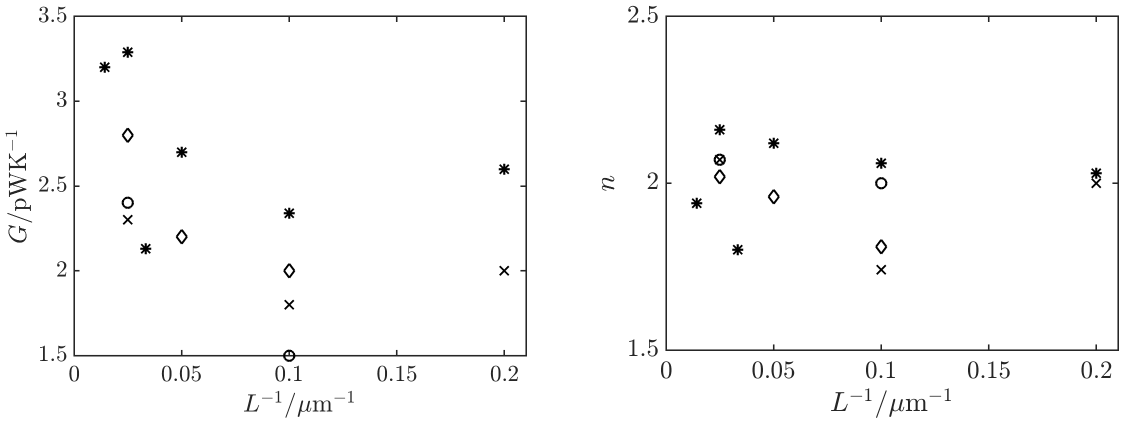

(a) (b)

Figure 5.6 (a) G and (b) n with inverse side length. Asterisks correspond to devices with no bars, crosses to devices with one bar, diamonds to devices with two bars and circles to devices with three bars.

Figure 5.6 shows the values of (a) G and (b) n for all of the devices tested, as a function of inverse side length. The asterisks represent unpatterned devices, the crosses show devices with one bar, the diamonds show devices with two bars and the circles show devices with three bars. The devices were designed to all have the same values of G and n, and the thermal exponent n remains close to 2 for the majority of the TESs, indicative of diffusive scattering in a narrow leg [175]. This demonstrates that the thermal transport mechanisms are the same for all of the TESs, as required for a study of the effects of bilayer geometry. However, G does vary between the different devices, which could be an artefact of the way the experiment was conducted or a result of the device design. There is a reduction in G as bilayer size increases, and a reduction in G when bars are added, suggesting that the change in thermal conductivity could be linked to changes in bilayer geometry.

In Figure 5.7, R_n is shown as a function of inverse side length for all of the devices tested. As the bilayer size is reduced, R_n also reduces. Although, from Section 4.2.4, the use of square bilayers means that all of the TESs should have the same normal state resistance, the normal metal side bars of fixed width provide a lower resistance in parallel with the thin film. As the size of the bilayer reduces, the length of the normal metal side bars reduces and their resistance becomes even lower, resulting in a reduction in R_n as bilayer size decreases. The predicted normal state resistance, based on the parallel combination of the resistances of the TES thin

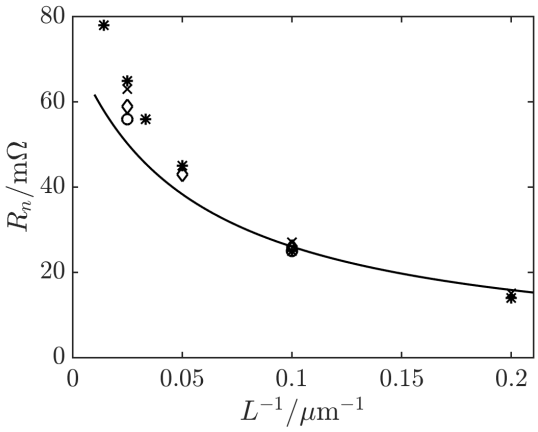

Figure 5.7 R_n with inverse side length. Asterisks correspond to devices with no bars, crosses to devices with one bar, diamonds to devices with two bars and circles to devices with three bars. The solid line shows the prediction for the normal state resistance based on the parallel combination of the resistances of the TES thin film and the two full-length normal metal side bars.

film and the bars, gives a good account of the measured normal state resistance, as shown by the solid line on Figure 5.7. Additionally, R_n is reduced as more normal metal patterning is added. As the bars on the larger devices occupy a larger surface area, they produce a greater reduction in R_n than the bars on the smaller devices. Trends in device behaviour may therefore be influenced by the variation in normal state resistance between devices.

5.3.3 α and β

Circuit impedance was measured by applying a DC voltage plus a white noise source [16, 176], The small signal electrothermal parameters α and β can be estimated from measurements of the circuit impedance. Using the analysis of Irwin and Hilton [18], the circuit impedance measured is

$$Z_\mathrm{tot} = R_\mathrm{S} + R_\mathrm{B} + 2\pi i f L + Z_\mathrm{TES}(f), \tag{5.2}$$

where the TES impedance Z_TES is given by

$$Z_\mathrm{TES}(f) = R_0(1+\beta) + R_0 \frac{\mathscr{L}_I}{1-\mathscr{L}_I} \frac{(2+\beta)}{(1+i2\pi f\tau)}, \tag{5.3}$$

with R_0 the resistance at the bias point and $\mathscr{L}_I$ the loop gain. A sample measurement of Z_TES can be seen in Figure 5.8, for an unpatterned TES with a 70 µm side length thin film. In the

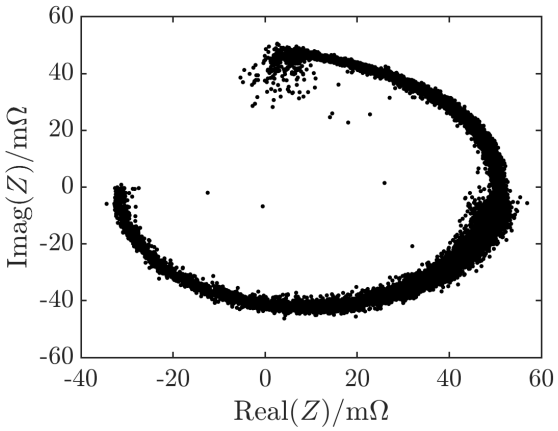

Figure 5.8 Real and imaginary parts of the TES impedance, calculated from measurements of the circuit impedance. This measurement was carried out for an unpatterned TES with a 70 µm side length thin film, at a temperature of 120 mK.

limit of high frequencies, Equation (5.3) becomes

$$Z_{\mathrm{TES}} = R_0(1+\beta), \tag{5.4}$$

allowing β to be determined. Conversely, as $f \to 0$, Equation (5.3) becomes

$$Z_{\mathrm{TES}} = R_0(1+\beta) + R_0(2+\beta)\frac{\mathscr{L}_I}{1-\mathscr{L}_I}, \tag{5.5}$$

from which the loop gain and hence $\alpha = \mathscr{L}_I GT/P_{J0}$ can be estimated.

Table 5.2 shows the values of α and β measured for all of the devices at zero field, as well as the value of α/β. The values of α and β are displayed in Figures 5.9a and 5.9b respectively, as a function of inverse bilayer length, with the points to the left of the figure corresponding to the devices with larger film areas. The asterisks represent unpatterned TESs, whilst the crosses, diamonds and circles show TESs with bilayers that have one, two and three partial normal metal bars. In general, as bilayer side length decreases, α decreases and β increases. The values of α for the TESs with 40 µm side length bilayers appear to be influenced by the variations in self-field, with sharper transitions for devices with even numbers of bars. The patterned devices with 10 µm side length bilayers show significant deviations from the general trends in α and β, possibly due to the interplay between the larger proximity effect from the electrodes in these smaller devices and the self-field effects produced by the patterning.

As mentioned in Chapter 2, other groups have measured the α/β ratio to be in the range 10-200 [16, 97], and the results for the devices with larger bilayers are consistent with this

Table 5.2 α and β for all of the TES geometries tested. All measurements were taken at zero field and at a temperature of 120 mK.

Device side length/μm	Bars	α	β	α/β
70	0	27.4	0.1	250
40	0	23.1	0.4	64
40	1	15.8	0.2	100
40	2	24.2	1.4	17
40	3	17.3	0.3	63
30	0	27.4	0.5	60
20	0	19.3	1.1	18
20	2	16.4	0.7	25
10	0	14.6	3.5	4
10	1	47.2	5.3	9
10	2	72.9	7.1	10
10	3	10.3	13.6	1
5	0	11.4	13.2	1
5	1	10.9	17.1	1

observation. For the devices with 10 μm side length and 5 μm side length bilayers, the α/β ratio is lower than previously measured, due to the broader transitions displayed by these devices.

5.3.4 Risetimes

The TES current response to a step in voltage at time $t = 0$ is determined by two time constants: the electrical time constant $\tau_{\text{elec.}} = L/R$, where L is the input impedance to the SQUID and R is the TES resistance; and the electrothermal feedback time constant τ, a measure of the TES response speed. Typically, $\tau_{\text{elec.}} \ll \tau$, so the response curve consists of a sharp drop in current with time constant $\tau_{\text{elec.}}$ and then a slower rise in current with time constant τ. When characterising the TESs, I wanted to ensure that the devices were given enough time to settle before measurements were taken, and so needed to determine the value of τ for each device. In order to do this, I fitted the rise in current with an exponential function, with an offset to account for the electrical response,

$$I(t) = b - a\exp(-t/\tau), \tag{5.6}$$

where τ is the device response time. Figure 5.10 shows the TES response to a single step voltage pulse (in black) and the fit using Equation (5.6), with $\tau = 0.64$ ms. The response was measured

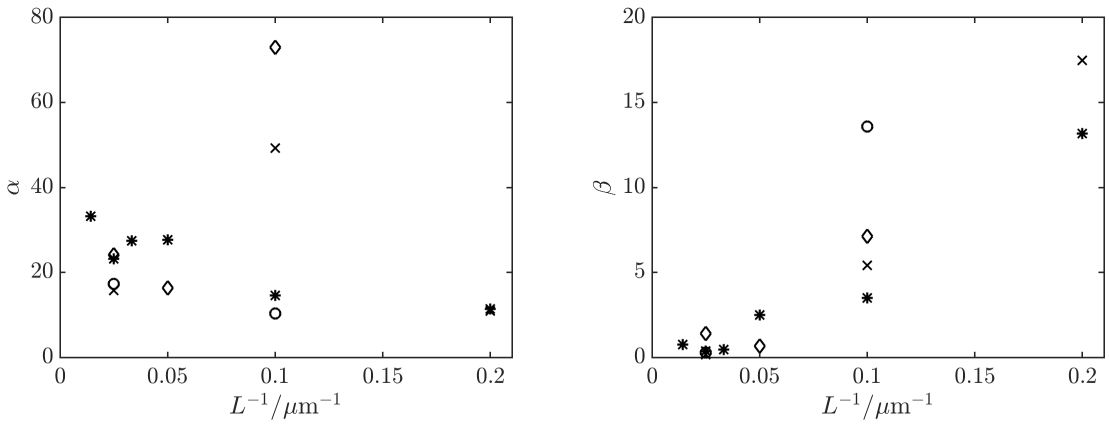

Figure 5.9 (a) α and (b) β as a function of $1/L$, measured at zero field. Asterisks correspond to devices with no bars, crosses to devices with one bar, diamonds to devices with two bars and circles to devices with three bars.

at the base temperature of the fridge, 66 mK, and at a bias voltage of 0.338 µV, corresponding to a bias point of 30 % R_n. It can be seen that Equation (5.6) is a good fit to the response curve.

This fitting procedure was repeated for all of the devices tested to measure their response times. In Figure 5.11, the values of τ for all of the devices under test can be seen as a function of inverse side length, with the points corresponding to the devices with the largest bilayers on the left of the figure and those corresponding to the devices with the smallest bilayers on the right. The asterisks indicate the response times for the unpatterned devices, the crosses correspond to devices patterned with a single bar, the diamonds show the response times for devices with two bars and the circles the response times for devices with three bars. For the unpatterned TESs, the response time initially decreases as the bilayer size is reduced, to a size of 20 µm side length, then increases. Adding bars to a bilayer of any size reduces the device response time. The larger the number of bars, the slower the device, due to the increase in heat capacity with the addition of successive bars. As for the transition temperature measurements, here there does not appear to be a significant difference between devices with odd and even bars, with the total number of bars having a greater influence on response time.

All of the TESs tested have reasonably fast response times of around 0.1-0.7 ms, typical for devices with no absorbers attached. For characterisation of these TESs, I therefore allowed at least 2 ms settling time for each measurement, to ensure that measurements were not obscured by the transient device response.

Figure 5.12 shows the current responses of a series of unpatterned TESs with different sized bilayers to a step in voltage at time $t = 0$, with all the device responses normalised to their final

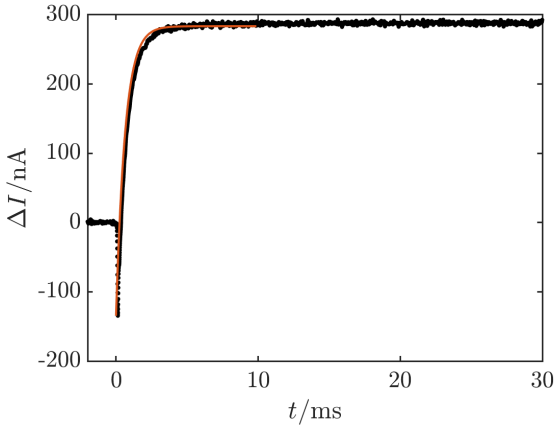

Figure 5.10 Current response to a step in voltage at $t = 0$ for the device with a unpatterned 70 µm side length bilayer (black points), taken at a temperature of 66 mK and a bias of 30 % R_n. The red line shows the exponential fit used to determine the device response time in Equation 5.6, $\tau = 0.64$ ms.

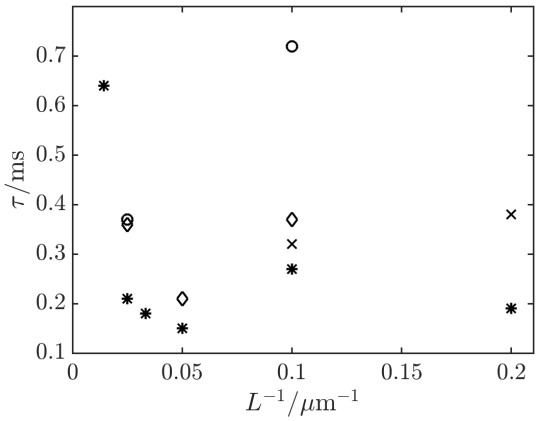

Figure 5.11 τ, the TES response time, with inverse side length. Asterisks correspond to devices with no bars, crosses to devices with one bar, diamonds to devices with two bars and circles to devices with three bars.

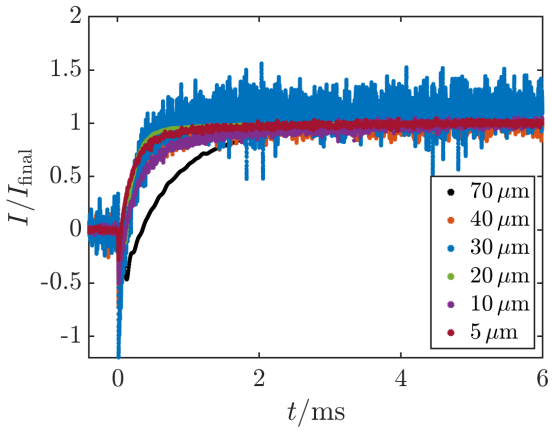

Figure 5.12 Current response to a step in voltage at $t = 0$ for a series of unpatterned TESs of different bilayer side lengths L, normalised to the final amplitude.

amplitudes. From this, the device with the largest bilayer is about three times slower than the device with the smallest bilayer. Four of the devices were tested using a 5 dB filter to attenuate the voltage step applied to the TES, which adds to the noise in the measurement; the risetimes for the devices with the 70 µm side length and 20 µm side length bilayers were taken without filtering so exhibit less noise.

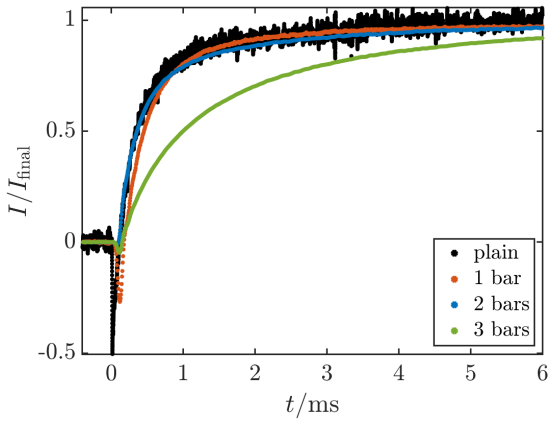

Figure 5.13 Current response to a step in voltage at $t = 0$ for the devices with 10 µm side length bilayers and differing numbers of normal metal bars, normalised to the final amplitude.

Figure 5.13 shows the current responses of a series of TESs with the same size bilayers and differing numbers of normal metal bars to a step in voltage applied at $t = 0$. All of the device responses are normalised to their final amplitudes. This figure demonstrates the effect of adding normal metal bars on response time: as more bars are added, the response time is increased. In this case the device patterned with three normal metal bars is about three times slower than the

unpatterned device. The TESs with smaller bilayers are slowed down to a greater degree by the addition of bars.

5.3.5 Noise

All noise spectra were taken with the ADR magnet unplugged and the AVS unplugged to minimise the sources of noise in the system. As this meant that the exact temperature of each measurement could not be recorded, all measurements were taken shortly after demagnetisation, when the fridge was stable at a base temperature of 63-67 mK. The exact base temperature achieved depended on the conditions of each cooldown. To achieve the best possible noise performance, the electronics of the magnetic test system had to be unplugged, which meant that for some of these measurements it was not possible to cancel out external magnetic fields.

To accurately compare the noise performance of the TESs, spectra for the TESs should be taken under very similar conditions. However, due to external influences, the quality of the noise spectra was variable, with spectra showing high $1/f$ noise on some days and large amounts of 50 Hz pickup on other days. Where possible, sets of spectra were taken on the same day in order to compensate for this.

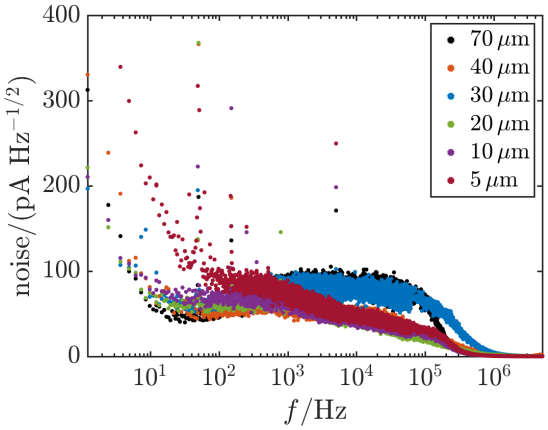

Figure 5.14 Noise spectra for a series of unpatterned TESs with bilayer side lengths ranging from 70 µm to 5 µm, taken without cancelling the Earth's magnetic field. The temperature is 63-67 mK and the bias voltage is set to a bias point of 30 % R_n for all the TESs except the device with the smallest bilayer area, which is at a bias point of 40 % R_n.

Figure 5.14 shows the noise as a function of frequency for a series of unpatterned TESs with different bilayer side lengths, taken without using the coils to cancel the Earth's magnetic field to achieve optimal noise performance of the system. All of these spectra were taken at the base temperature of the fridge, around 63-67 mK. The TESs were all biased at 30 % R_n, except for the device with the smallest bilayer, which was not stable at this bias point, as its resistance is too close to the bias resistance of 1.45 mΩ. As the bilayer size is reduced, the noise increases, especially at low frequencies. The noise is especially high for the device with the smallest (5 µm side length) bilayer.

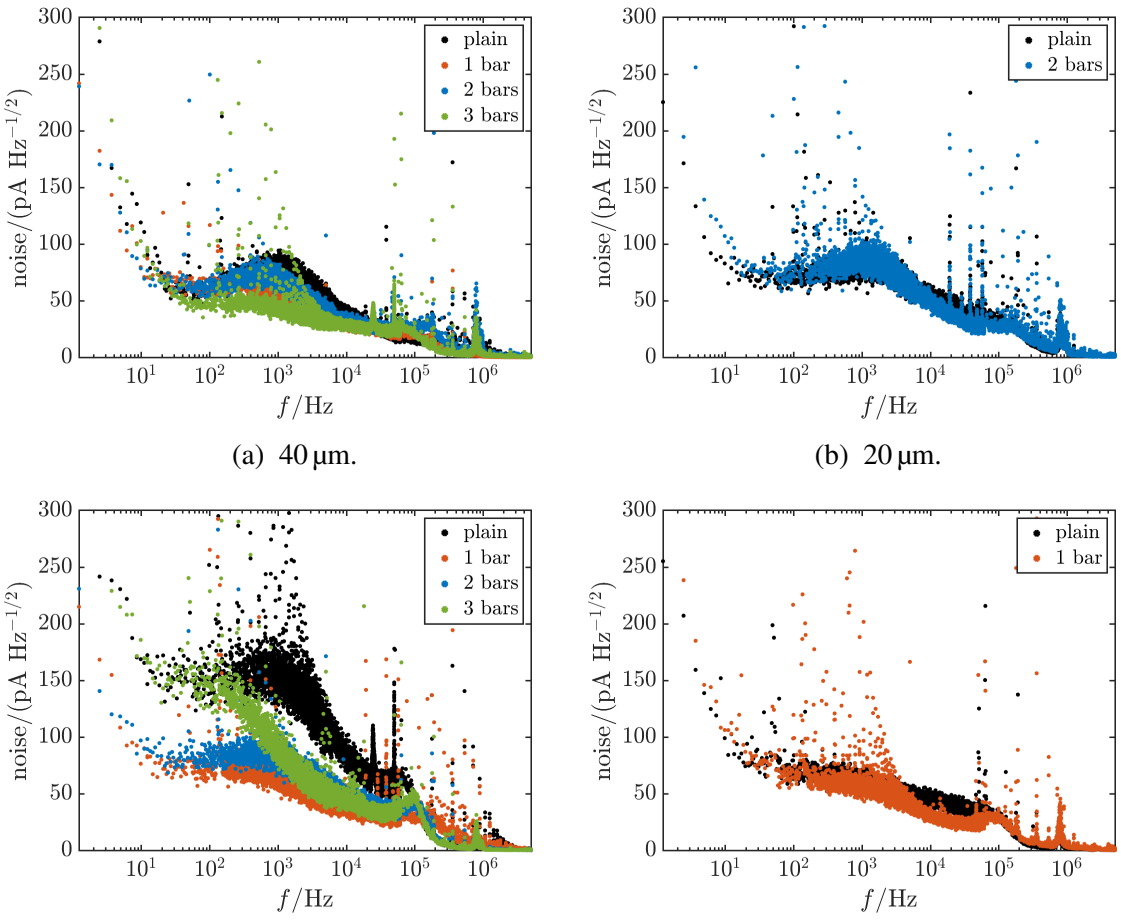

(a) 40 µm. (b) 20 µm.

(c) 10 µm. (d) 5 µm.

Figure 5.15 Noise spectra for four TES bilayer sizes with number of bars N, taken with the Earth's magnetic field cancelled so the overall field was zero, at a temperature of around 65 mK. All devices except the TESs with the smallest bilayer size were biased at 30 % R_n; the devices with the smallest bilayers (5 µm side length) were biased at 40 % R_n.

Figure 5.15 shows noise spectra for four bilayer side lengths, with the 3-axis coil system used to cancel the Earth's magnetic field. For each side length, the noise spectrum for a unpatterned

device is shown along with the noise spectra for TESs of the same bilayer side length with one or more partial normal metal bars. All of the devices were biased at 30 % R_n, with the exception of the two devices with 5 µm bilayers, which were biased at 40 % R_n. All measurements were taken at a temperature of around 65 mK. In all of the field-cancelled spectra, the noise peaks at high frequency are due to noise from the three-axis coil system and its wiring.

In Figure 5.15a, the $1/f$ noise is unchanged by the addition of the normal metal bars, but the presence of the bars acts to suppress the excess noise peak at around 1 kHz. This agrees with the observations of Ullom et al. [11] and Smith et al. [86, 97]. This suppression of the excess noise peak appears to be greater for devices with an odd number of bars than for devices with an even number of bars, something that is also seen in Figure 5.15b, in which there is little to no suppression of the peak with the addition of two partial normal metal bars. This implies that the self-field of the device influences the noise that is generated, as from the modelling in Section 2.4.3, the thin films with an odd number of partial bars have a larger self-field. The excess noise peak may be related to magnetic effects.

For the two devices with the smallest bilayers, the noise behaviour does not follow the same trends with the addition of partial normal metal bars. Figure 5.15c shows the noise spectra for a series of TESs with 10 µm side length bilayers and varying numbers of normal metal bars. The noise is highest for the unpatterned device, as expected, and is suppressed by the presence of metal bars. However, the $1/f$ noise and phonon noise in the device with three normal metal bars are both higher than in the devices with one and two bars, due to the low bias current for this device. For the smallest bilayer size, the addition of a single partial bar has little effect on the noise spectrum, as seen in Figure 5.15d.

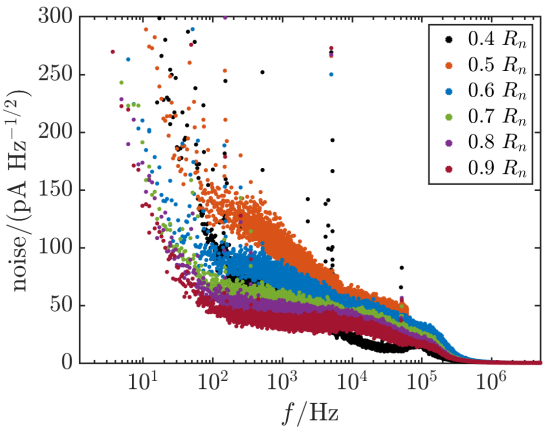

Figure 5.16 Noise spectra for the smallest unpatterned TES, with a 5 µm side length bilayer, as a function of bias point.

Figure 5.16 shows the effect of varying the bias point on the noise behaviour of the TES with a unpatterned 5 µm side length bilayer. In general, as the bias point increases, all types of noise are reduced, but the device responsivity will also be reduced. Since the devices with the smallest bilayers already have broader transitions, as shown in Section 5.3.1, making them intrinsically less responsive, it is not feasible to move their operating point to a higher bias voltage in order to improve the noise performance.

5.4 Conclusions

A summary of the effects of varying the TES bilayer size and number of partial normal metal bars is shown in Table 5.3. Desirable effects have been highlighted in blue, whilst undesirable effects are shown in red. Both larger and smaller bilayers show advantages and disadvantages. It should be noted that although the larger devices have slightly longer response times, all of the TESs have comparably fast response times compared to devices with absorbers.

Table 5.3 Effects of bilayer geometry on key device performance metrics. Desirable effects are highlighted in blue; undesirable effects are highlighted in red. Any numerical changes refer to the difference between the extremes of the bilayer geometries, unless otherwise stated.

Parameter	Effect of decreasing bilayer size	Effect of adding bars to 40 µm side length device	Effect of adding bars to 10 µm side length device
T_c	Increases by a factor of 1.4	No noticeable effect	Decreases by a factor of 1.4
Transition width	Broadens	Broadens when one bar added, then no further variation	No obvious trend
Heat capacity	Decreases	Increases	Increases
Noise	Increases by a factor of up to 3, especially $1/f$ noise	Suppression of excess noise by a factor of 2	Some suppression of excess noise
τ	Faster (by a factor of 4) response until 20 µm, then response gets slower by a factor of 2	Slower (by a factor of 2) response for 2+ bars	Slower (by a factor of up to 3) response, especially for 3 bars
R_n	Decreases by a factor of 4	Slightly decreases	Slightly decreases
G	Decreases by a factor of up to 1.4	Decreases by a factor of up to 1.4	Decreases by a factor of 1.6
n	No obvious trend	Slight general decrease	No obvious trend

All of the devices tested, with a wide range of sizes and geometries, displayed very good performance. In particular, the success of the smallest devices, with 5 µm side lengths, is surprising given the substantial influence of the proximity effect in this device, as seen in the modelling in Sections 4.2.5 and 4.2.7.

The TESs with smaller bilayers have faster response times and lower heat capacities than the TESs with larger bilayers, but also display higher noise and broader transitions. Although there is no bilayer design that optimises all of the parameters, devices with 20 µm side length bilayers were found to give a good compromise between low noise, fast response and reasonable transition temperature. Referring to the results of the proximity effect model in Figures 4.2

and 4.7, 20 µm bilayer side length TESs are a limiting size where the proximity effect from the normal metal side bars only just influences the full device width, and the proximity effect from the superconducting electrodes does not produce a significant increase in transition temperature, unlike the 10 µm and 5 µm bilayer side length TESs.

For larger devices, adding bars slows down the device due to the increase in heat capacity, but for smaller devices, the addition of bars appears to improve the device sensitivity. Other groups are now designing rectangular TESs, which are narrow to reduce phase slip and heat capacity, but long in order to improve the noise performance and device stability [177].

Some device properties show significant variations depending on whether the TES bilayer has an odd or even number of partial normal metal bars, supporting the hypothesis that some of the effects of partial bars can be attributed to the self-field produced by the current flow around the bars. From the results of Section 2.4.3, devices with an odd number of bars have a larger self-field than devices with even numbers of bars. In particular, large devices with even numbers of bars have sharper transitions than devices with odd numbers of bars, but a higher excess noise peak. Both transition sharpness and excess noise may therefore be linked to magnetic field phenomena.

Chapter 6

Experimental study of magnetic field dependence

6.1 Introduction

I present the results of a systematic study of the effects of bilayer geometry on magnetic field dependence. Having developed a new magnetic field test system, as described in Chapter 4, I used this new system to carry out an investigation into the magnetic field dependence of Mo/Au TESs with different bilayer sizes and varying numbers of normal metal bars. The new system allowed both the magnitude and the direction of the applied field to be varied, allowing me to carry out the first ever measurements of TES directional magnetic field dependence. To describe the direction of the applied field, I used the co-ordinate system described in Section 4.7, in which the TES detectors have their thin films in the $x-y$ plane, current flows in the x direction and the z direction is perpendicular to the plane of the film. Most measurements focused on applied fields in the z direction, as the magnetic flux in this direction is maximal so these fields should theoretically have the greatest impact on TES performance.

Section 6.2 describes the results of the tests I carried out to ensure the SQUIDs used were not affected by the new experimental configuration. In Section 6.3, I present the results of my investigation into magnetic field dependence, showing the effects of magnetic fields on critical current, transition temperature, response time, thermal properties, noise, electrothermal parameters and bias point. These results are vital in informing the design of TESs with low magnetic field dependence. I compare my measurements for different bilayer geometries, investigating the effects of bilayer size and patterning with normal metal bars, to examine whether there is an optimal bilayer configuration for minimal magnetic field dependence.

As in the investigation of bilayer geometry in Chapter 5, I study whether any trends in magnetic field behaviour can be attributed to the self-field of the devices, comparing devices with odd and even numbers of partial normal metal bars. This follows on from the modelling in Section 2.4.3, which indicated that bilayers with odd numbers of partial bars have a larger self-field than bilayers with even numbers of partial bars. The greater self-field of the devices with odd numbers of bars may provide reduced magnetic field dependence, as larger applied fields are required to cancel the effects of the self-field and change device behaviour. In Chapter 5, I observed that TESs with even numbers of bars had sharper transitions but higher excess noise than TESs with odd numbers of bars.

6.2 Testing SQUIDs

In order to test the effectiveness of the magnetic shielding on the SQUIDs, I studied two SQUID channels when the connection between the first stage SQUID and the TES was shorted. Channel A had its connection to the TES shorted next to the TES, and so the only input to the SQUID was the current through the stray resistance in the readout circuit. Channel B had its connection to the first stage SQUID shorted next to the SQUID bonding pads, and so there was no resistance across the input to the SQUID.

The first stage SQUID on Channel B showed high sensitivity to magnetic field, as the SQUID was connected to a superconducting loop. This meant that when the magnetic field was varied, there were large changes in current, as the superconducting loop expels magnetic field. The input circuit to the SQUID was behaving as a highly sensitive magnetometer. This magnetometer was so sensitive that the low-frequency magnetic field fluctuations coming from the pulse tube magnetic cooler were visible on the SQUID trace. These are not visible when the SQUID is connected to a resistive element, meaning that it was not possible to lock the SQUID and so no measurements of current could be taken. For SQUID testing, some resistive input is therefore required. However, observations of this sensitive SQUID magnetometer gave valuable insights into possible sources of stray field in the experimental system, showing that there was a very small variation in background field due to the operation of the pulse tube cooler despite the niobium shield surrounding the SQUIDs.

As the first stage SQUID on Channel A was shorted next to the TES, the SQUID was connected to a much larger wire loop that had a stray resistance of about 4 mΩ. This meant that there was a resistive input to the SQUID, making it less sensitive to magnetic fields and meaning that current measurements could be taken. Firstly, the current through the SQUID was recorded as the fields in the x, y and z directions were varied, to investigate the magnitude of this variation relative to the TES currents to be measured. Figure 6.1 shows how the current

measured by the SQUID varied as a function of the field applied in the z direction. The SQUID showed large drifts in current at an applied field of about 80 µT, corresponding to a coil current of 16 mA. This drift was reproducible when fields were applied using the y and z coils but was not reproduced when the x coils were used. There was also a 'cooldown' period between drift events. It was determined that these events were caused by the SQUID wiring being heated by the currents through the coil wiring, as both the SQUID wiring and the coil wiring were in the same bundle of wires going to the cold stage. The heating effect occured when the currents were large enough to drive the coil wiring normal. This effect was only exhibited by the y and z coils as the resistance of these sets of wires was 100 Ω, whereas the low resistance x coil wiring had a resistance of only 10 Ω, causing much less heating.

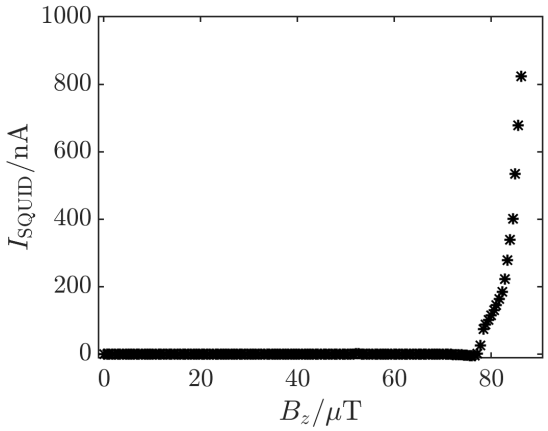

Figure 6.1 I_{SQUID} as a function of increasing magnetic field in the z direction. I_{SQUID} is defined as the current measured by a SQUID when its the connection to the TES was shorted next to the TES, meaning that the only input to the SQUID was the stray resistance in the readout circuit.

This heating issue was resolved by using low resistance wiring for all of the coils. Once the low resistance wiring was used, the SQUID response was similar to that shown in Figure 6.2. This figure displays the current measured by the SQUID as a function of field when the currents through the coils were kept below 10 mA, corresponding to an applied field of 50 µT. Here the heating effects were not displayed and the variation in the measured current was lower than 30 nA in all directions. Since the TES current variations being measured were of the order of tenths of µA, the change in current due to the effect of the magnetic field on the SQUIDs was not significant compared to the change in magnitude of the TES current, showing that the shielding around the SQUIDs was sufficient.

The SQUID shielding in the z direction provided a greater reduction in field dependence than that in the x and y directions, due to the design of the box. In the z direction, the coils were further away from the SQUIDs and the SQUIDs were protected by the niobium shield. In

the y direction, the coils were closer to the SQUIDs but the SQUIDs were still protected by the niobium shield. In the x direction, the coils were closer to the SQUIDs and the SQUIDs were not protected by the niobium shield.

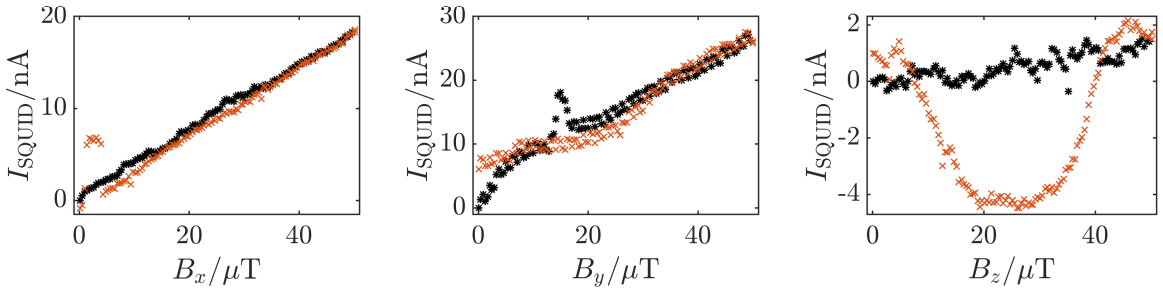

Figure 6.2 I_{SQUID} when the magnetic fields in the (a) x, (b) y and (c) z directions were cycled between 0-50 µT. Black asterisks show data taken when the field was increased, whilst red crosses show data taken when the field was decreased. I_{SQUID} is defined as the current measured by a SQUID when its connection to the TES was shorted next to the TES, meaning that the only input to the SQUID was the stray resistance in the readout circuit.

In order to assess the sources of the noise in the experimental system and provide a reference spectrum for noise measurements of TESs, a noise spectrum was measured with the TES shorted and this is presented in Figure 6.3. The spectrum obtained is similar to a TES noise spectrum but without the TES Johnson noise or excess noise. The roll-off feature at 1 kHz can be attributed to the SQUID bandwidth, and the roll off at 1 MHz is due to filtering. $1/f$ noise can be seen below 10 Hz, and the mains peak and one of its harmonics are visible at 50 Hz and 100 Hz.

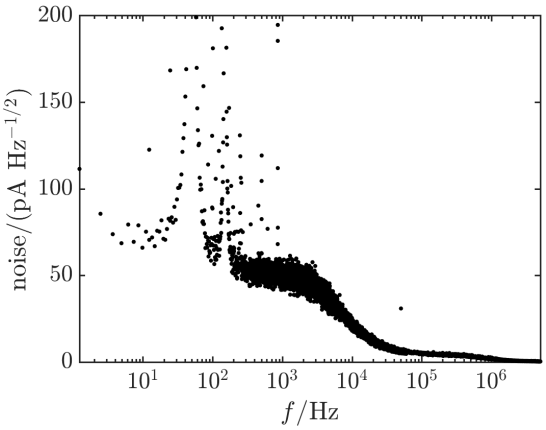

Figure 6.3 Noise spectrum of a SQUID when its connection to the TES was shorted next to the TES, meaning that the only input to the SQUID was the stray resistance in the readout circuit.

Five SQUID channels were available for testing. The first stage SQUID on one channel showed 'switching' behaviour, where the flux-voltage curve abruptly changes phase whenever the magnetic field is altered. This switching behaviour meant that this SQUID could not be used to monitor continuously varying magnetic fields, and so $I(B_{x,y,z})$ and directional dependence measurements could not be taken.

6.3 TES measurements

The set of devices tested is given in Table 5.1. For each device, I carried out the following set of measurements to investigate the magnetic field dependence:

- $I_c(B_z)$ - at a temperature close to T_c, double-sided $I(V)$ curves were measured for a series of field values and used to determine the critical current at each field value. The applied magnetic field was varied from 0-100 μT in the z direction. These measurements were compared to model predictions and results from other groups, in addition to being used to compare the different devices.

- $I(V)$ curves as a function of temperature - one set of measurements was carried out without cancelling external magnetic field, and a second set was carried out with field cancellation. This showed the impact of applied magnetic fields on T_c, K and n.

- $T_c(B_z)$ - $I(V)$ curves were measured as a function of temperature for different values of B_z, and T_c, K and n were calculated for each field value, allowing trends in T_c as a function of magnetic field to be observed.

- $I(B_{x,y,z})$ - TESs were biased in the transition and the magnitude of the applied magnetic field was varied using the new magnetic field system. These measurements were carried out for both parallel and perpendicular applied fields. From this, regions of interest were identified and the magnetic field sensitivity of the different devices was calculated.

- Directional dependence - full spherical sweeps were carried out with a target field of 20 μT, measuring the current through the TES as a function of field direction. From this, the field directions that the TESs are most sensitive to were determined, providing valuable information for use when designing magnetic shielding.

- Impedance(B_z) - device impedance was measured as a function of applied perpendicular field and used to determine α and β for the devices under test, to investigate how magnetic field strength affects these electrothermal parameters.

- Risetimes - the field in the z direction was varied to study whether the magnitude of the applied magnetic field significantly alters the device response time.
- Noise - spectra were taken as a function of field strength in the z direction to investigate the effect of magnetic field magnitude on device noise, with a particular focus on the excess noise feature.

6.3.1 Critical current as a function of magnetic field

The variation of the critical current through a TES as a function of magnetic field provides valuable insights into the magnetic field dependence of the device, as well as into the effects of magnetic field on properties such as the superconducting phase difference across the device. I measured $I_c(B_z)$ by using the 3-axis coil system to vary the **B** field in the z direction. For each field value, I_c was determined from the first onset of resistance for both positive and negative bias directions when the voltage was swept symmetrically about $V = 0$. The voltage sweep was carried out at a rate of 0.3 Hz to avoid thermal hysteresis, as in the study carried out by Smith et al. [97].

Fitting oscillations in I_c

For all of the devices, although there are oscillations in I_c, the critical current does not reach zero, a result that is not predicted by my model in Chapter 2, which assumes $I_c = 0$ when $\Phi = n\Phi_0$ for integer n. This suggests additional field effects caused by phenomena I have not included in my model, such as phase-slip. It also implies that magnetic field behaviour across the TESs may not be uniform. The absence of zeros in the critical current explains the observation in Section 2.4.2 that, despite some groups making devices where the surrounding wiring produces fluxes larger than Φ_0, no one has reported TESs that do not superconduct due to the fields from the wiring. For fields of this magnitude, there is no magnetic field that makes $I_c = 0$, and so it is not possible for any fields produced by current flow in the wiring to entirely suppress the flow of supercurrent. My observations agree with the results obtained by several other groups [97, 98, 123]: Smith et al. account for this effect in their model by introducing linear current- and temperature-dependent offsets in the magnetic field, to take the self-field into account.

Our current understanding of microscopic modelling is therefore unable to fully describe the $I_c(B_z)$ behaviour of a TES. However, it is still valuable to be able to describe the frequency of oscillations in I_c, as this is closely related to the flux threading the TES bilayer, from which an effective area can be defined. When designing devices, a small effective area, corresponding to a low flux threading the TES for a given field, is desirable. The effective areas for different

bilayer geometries can be compared to identify the geometries which are least affected by magnetic fields. Knowing the location of maxima and minima in I_c is also important, in order to ensure that the TES is operating as close as possible to its maximum value of I_c.

I fit a model which predicts $I_c = 0$ when $\Phi = n\Phi_0$ to the main peak of the $I_c(B_z)$ curve, in order to describe the oscillations, but not the zeros, in I_c. The model assumes uniform supercurrent density across the sample in the y direction, which is a reasonable assumption for the devices with larger bilayers but not for the devices with smaller bilayers, due to the inverse proximity effect from the normal metal side bars, as discussed in Section 4.2.5. The critical current is expected to depend on the magnitude of the applied magnetic field according to [98]

$$I_c = I_{c,0} \left| \mathrm{sinc}\left(\frac{\pi\Phi_z}{\Phi_0}\right)\right|, \tag{6.1}$$

where the magnetic flux $\Phi_z = B_z A$. For these measurements, the oscillations in I_c should display relatively little skew, as the measurements were taken close to T_c, and from the left inset of Figure 2.11, the closer a TES is to its transition temperature, the smaller the skew in its current-phase profile.

From Figures 6.6 and 6.8, using the true area A in this calculation does not give good agreement with the period of the data. This suggests that the magnetic flux does not thread the full area of the TES bilayer [99, 138]. I therefore calculated an effective area A_{eff} to obtain the best fit to the oscillations, assuming that the intrinsic device behaviour is the same as the flux varies.

From the effective area, an effective length can be defined in two different ways, depending on the assumptions that are made about the flux threading the TES:

1. $A_{\mathrm{eff}} = W L_{\mathrm{eff}}$, where W is the true width of the bilayer and L_{eff} is an effective length. This assumes that the main factor preventing flux threading is the superconducting proximity effect from the electrodes, reducing the effective length of the TES but not its width.

2. $A_{\mathrm{eff}} = L_{\mathrm{eff}}^2$, where L_{eff} is an effective side length for the square TES bilayer. This assumes that the main factor preventing flux threading is non-uniformity in current across the bilayer, and that in normal operation, some regions of a TES will be superconducting, preventing magnetic flux threading the whole bilayer.

In both cases, L_{eff} is a geometric measure, related to the bilayer dimensions rather than the path taken by the current. In this study, I take the first definition of effective length, assuming that the superconducting proximity effect from the electrodes is preventing flux threading the full bilayer area.

Measurements of $I_c(B_z)$

Figure 6.4 shows I_c as a function of flux for a series of unpatterned devices of different bilayer areas, with each set of measurements taken just below the transition temperature of the TES under test. For each device, the flux was calculated using the effective area that gives the best fit to the oscillations in I_c. The model given by Equation (6.1) is shown by the black line. The smaller devices show behaviour that is closer to the predictions of this equation, suggesting that despite the inverse proximity effect from the normal metal side bars, supercurrent flow is relatively uniform across these devices. The minima in I_c for the devices with smaller bilayers are much closer to zero, and as the bilayer size increases, the minima in I_c move to higher values of current. For these larger devices, the field behaviour is asymmetric about $\Phi = 0$, which is indicative of hysteresis. This hysteresis could be occurring in the devices themselves or could indicate nearby structures which are magnetised and demagnetised. Hysteresis within the device is indicative of non-uniform behaviour across the TES, possibly due to the presence of magnetic field vortices and edge effects, suggesting that the current flow across large devices may be non-uniform. Although care was taken in the design of the system to avoid the presence of any magnetisable materials that could produce magnetic field distortions, if the hysteresis is due to external influences this emphasises the need for extreme care to avoid any use of magnetisable materials when designing TES systems.

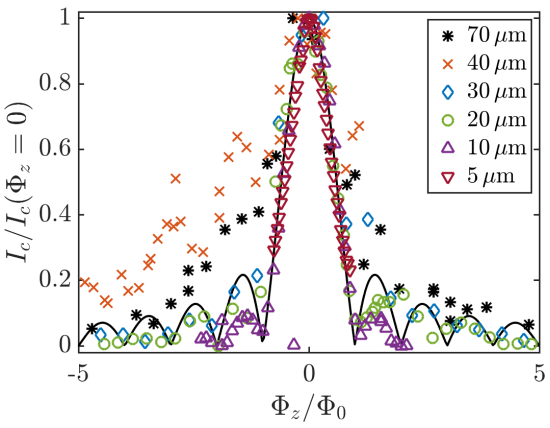

Figure 6.4 Critical current as a function of magnetic flux, calculated using the effective area that gives the best fit to the oscillations in I_c, for all of the unpatterned devices tested. Each set of measurements was taken just below the transition temperature of the TES under test. All data sets have been normalised to I_c at zero flux. The solid black line shows the prediction of Equation (6.1).

In Figure 6.5, the devices with 40 µm side length bilayers are compared to show the effects of adding bars to devices with larger bilayers. The addition of partial normal metal bars drastically

alters the form of I_c, broadening the central maximum and producing TESs with critical currents that are much less sensitive to applied magnetic fields. There is no clear difference between devices with odd and even numbers of partial bars.

Figure 6.6a shows the measured $I_c(B_z)$ for the TES with an unpatterned 40 µm side length bilayer (black asterisks), along with two predictions of $I_c(B_z)$ given by Equation (6.1). The dashed line shows the prediction using the area based on the actual bilayer length of 40 µm, whilst the solid black line shows the prediction for $I_c(B_z)$ using an effective area based on a bilayer with width 40 µm and an effective length of 6.7 µm. The 3-4 oscillations closest to $\Delta B_z = 0$ are described well by the solid line, but the oscillation period increases as the magnitude of ΔB_z increases.

The measured $I_c(B_z)$ for the TES with a 40 µm side length bilayer patterned with three partial bars is shown as black asterisks in Figure 6.6b, along with two predictions of $I_c(B_z)$ given by Equation (6.1). The dashed line shows the prediction using the area based on the actual bilayer length of 40 µm, whilst the solid black line shows the prediction for $I_c(B_z)$ using an effective area based on a bilayer with width 40 µm and an effective length of 1.5 µm. In this case, the central maximum used for the fitting has been taken as the region in between the two small drops in I_c in the central plateau. When an effective area is used, the model describes the period of the slight oscillations in the central maximum but does not show the drop off at higher fields. For this patterned device, Equation (6.1) does not give a good account of the magnitude of $I_c(B_z)$. Based on the form of the data in Figure 6.6b, it could be considered as the sum of three separate sinc functions. However, attempts to fit a sum of sinc functions to this data did not show good agreement with the shape of the broad central plateau or the drop off at the edge of this plateau.

Figure 6.7 shows $I_c(\Phi_z)$ for the series of devices with 10 µm side length bilayers, demonstrating the effect of adding bars to these small devices. Here there is a significant difference between the devices with odd numbers of bars, which show a minimum I_c of around 30-40 % $I_c(B_z = 0)$, and the devices with an even number of bars, which show a minimum I_c of around 5-10 % $I_c(B_z = 0)$. All of the devices, especially the devices with an even number of bars, have oscillations that are well described by Equation (6.1), as shown in Figure 6.8.

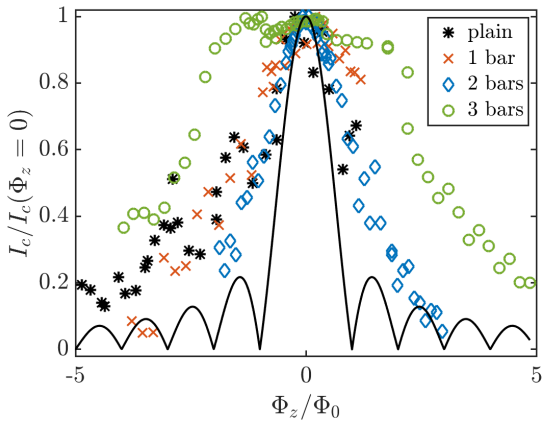

Figure 6.5 Critical current as a function of magnetic flux through the bilayer for a series of devices with 40 µm side length bilayers, patterned with different numbers of normal metal bars. All data sets have been normalised to I_c at zero flux, and each set of measurements was taken just below the transition temperature of the TES under test. The solid black line shows the prediction of Equation (6.1).

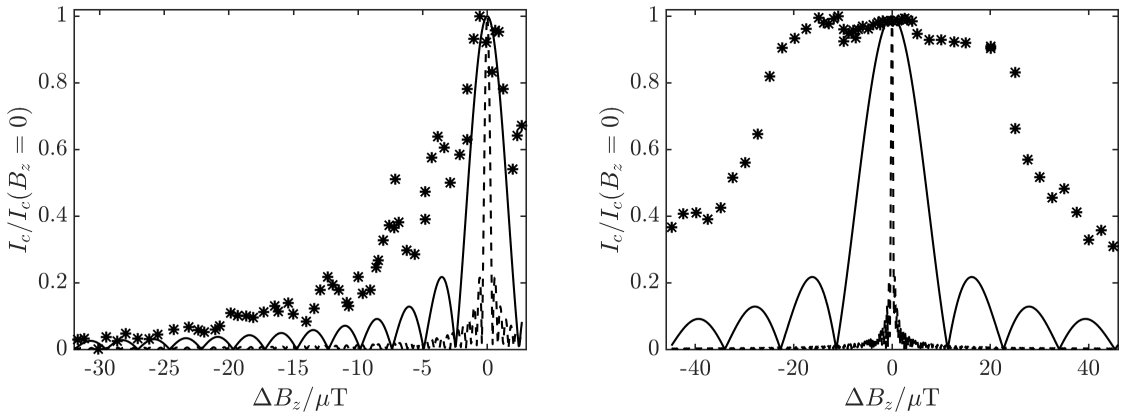

(a) Unpatterned bilayer, T_b=194.8 mK, L_{eff}=30 µm. (b) Three partial bars, T_b=187 mK, L_{eff}=7.5 µm.

Figure 6.6 Critical current as a function of applied magnetic field for two TESs with 40 µm side length bilayers, one unpatterned and one patterned with three partial bars. The dashed line shows the predicted dependence given by Equation (6.1) with the actual bilayer side length of 40 µm, whilst the solid line shows the prediction with an effective bilayer side length L_{eff}, calculated from the effective area used to fit the period of the oscillations for that particular device. Both data sets have been normalised to I_c at zero flux, and each set of measurements was taken just below the transition temperature of the TES under test.

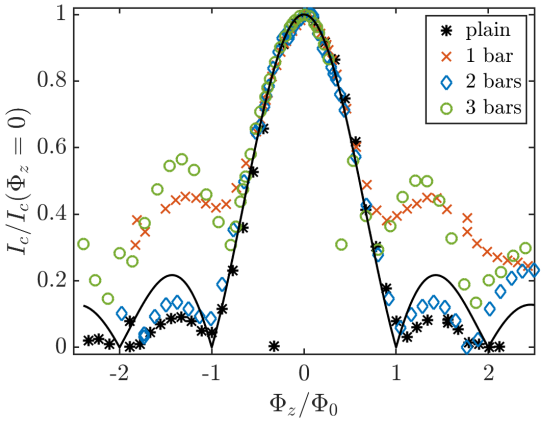

Figure 6.7 Critical current as a function of magnetic flux through the bilayer for a series of devices with 10 µm side length bilayers, patterned with different numbers of normal metal bars. All data sets have been normalised to I_c at zero field, and each set of measurements was taken just below the transition temperature of the TES under test. The solid line shows the prediction of Equation (6.1).

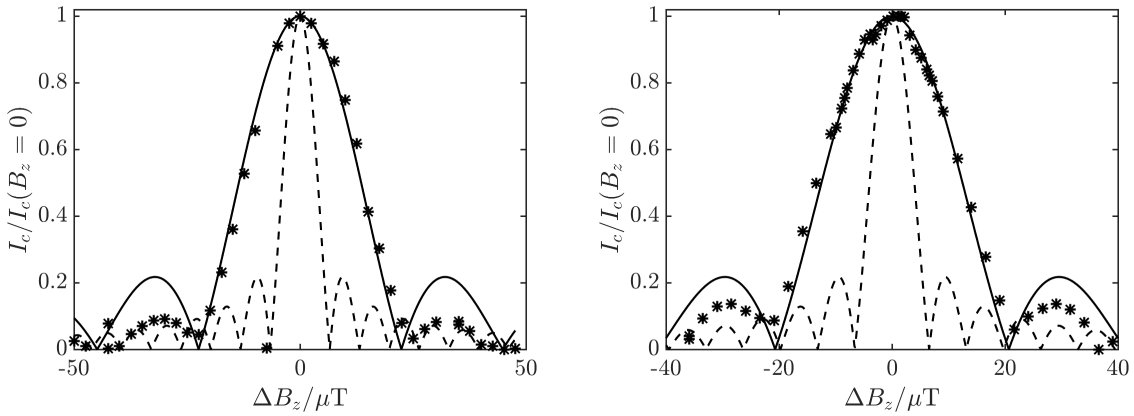

(a) Unpatterned bilayer, T_b=202 mK, L_{eff}=9.5 µm. (b) Two partial bars, T_b=160 mK,L_{eff}=10 µm.

Figure 6.8 Critical current as a function of applied magnetic field for two TESs with 10 µm side length bilayers, one unpatterned and one patterned with two partial bars. The dashed line shows the predicted dependence given by Equation (6.1) with the actual bilayer side length of 10 µm, whilst the solid line shows the prediction with an effective bilayer side length L_{eff}, calculated from the effective area used to fit the period of the oscillations for that particular device. Both data sets have been normalised to I_c at zero flux, and each set of measurements was taken just below the transition temperature of the TES under test.

Effective bilayer length

Table 6.1 shows the effective bilayer length that gives the best fit to the oscillations in I_c with applied field for each device. The effective length is then plotted against the actual length in Figure 6.9. The solid black line shows the case when the effective length and the actual length are the same, when the magnetic flux threads the whole area of the bilayer. The effective lengths of the bilayers of the unpatterned devices are shown as black asterisks, those for the devices with a single metal bar are shown as crosses, whilst those for devices with two partial bars are shown as diamonds and those for devices with three metal bars are shown as circles. In all cases, the effective length is smaller than the actual length, indicating that flux does not thread the full bilayer area. As the actual length decreases, the effective length approaches the actual length, with the two being most similar for the TESs with 5 µm side length bilayers. This shows that for these small devices, despite the Au side bars being comparable in width to the bilayer width, the supercurrent flow across the bilayer is very uniform. This is likely to be due to the large proximity effect from the metal electrodes, coupled with the relatively small area which means the magnetic flux is lower. The larger devices have effective lengths that are much smaller than their actual lengths, indicating non-uniform supercurrent flow. For the patterned devices with the larger 40 µm side length bilayers, the effective thin film length is very different to the actual length, suggesting that the presence of the normal metal bars significantly affects the weak link behaviour of the TES, potentially due to the larger self-field of these devices. However, for the devices with smaller bilayers, the addition of normal metal patterning appears to improve the agreement with the model. Since these results suggest that across 5x5 µm^2 regions of the bilayer, the supercurrent flow is close to uniform, it may be possible to model the thin film as a network of small, uniform supercurrent regions, as in the work of Yan et al. [89].

Table 6.1 Effective bilayer lengths for all of the TESs, calculated from the effective area that gives the best fit of Equation (6.1) to the oscillations in $I_c(B_z)$. In this calculation, it is assumed that flux threads the full bilayer width W, so $A_{\text{eff}} = WL_{\text{eff}}$.

Actual length, L/µm	Effective length, L_{eff}/µm			
	unpatterned	1 bar	2 bars	3 bars
70	3.6	-	-	-
40	6.7	1.6	0.8	1.5
30	4.2	-	-	-
20	4.1	-	9.9	-
10	2.9	2.9	3.2	3.5
5	2.1	3.6	-	-

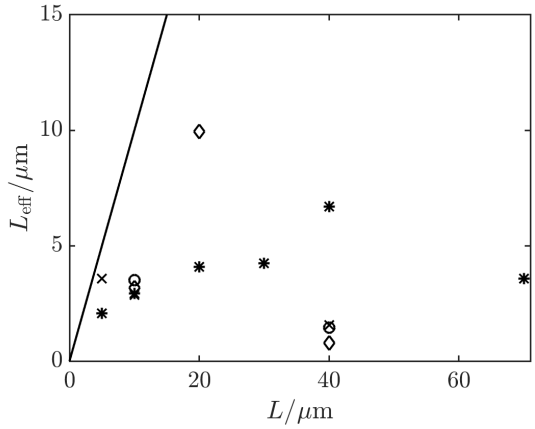

Figure 6.9 L_{eff} as a function of actual bilayer side length L. The solid black line indicates when the two lengths are the same. Points corresponding to unpatterned TESs are shown as black asterisks, whilst points for devices with one, two and three partial normal metal bars are shown as crosses, diamonds and circles respectively.

6.3.2 $I(V)$ curves

Sets of $I(V)$ curves were taken both with and without the external magnetic field cancelled, allowing the effect of this external magnetic field on the transition temperature and thermal conductance to be investigated. Figure 6.10 shows $P(T)$ for the TESs with 70 µm side length bilayers both at zero field (black asterisks fitted with a blue line) and at the external field (black asterisks fitted with a red line). In the presence of the external magnetic field, the measured transition temperature was reduced from 201.5 mK to 196.2 mK, indicating a change in TES behaviour with applied field. This agrees with the predictions of the microscopic model in Figure 2.10a, which shows that magnetic flux reduces T_{c}. The measured G appeared to be reduced by 0.1 pW K^{-1}, from 3.2 pW K^{-1} to 3.1 pW K^{-1}, whilst the measured n appeared to be reduced by 0.03 from 1.94 to 1.91. This could be a physical change, but is more likely to be another manifestation of the change in TES behaviour.

Figure 6.11 shows the values of (a) G and (b) n for all of the devices tested, as a function of inverse bilayer side length. The black points were measured with the external magnetic field cancelled, whilst the red points were measured without field cancellation. The asterisks represent unpatterned devices, the crosses show devices with one bar, the diamonds show devices with two bars and the circles show devices with three bars. The values of G and n were changed by the application of the external magnetic field, but did not systematically increase or decrease. For the majority of the devices, G decreased slightly in the presence of this magnetic field, whilst n remained close to 2 for the majority of the TESs, indicative of diffusive scattering in a narrow leg [175].

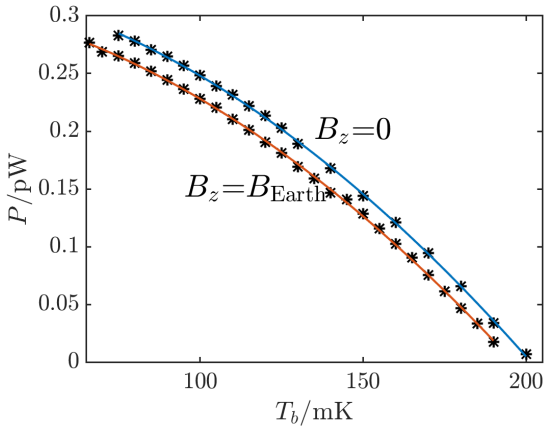

Figure 6.10 $P(T_\text{b})$ curves measured and fitted using the power flow equation without cancelling the external magnetic field (black asterisks fitted with a red line) and cancelling the external field (black asterisks fitted with a blue line). When the external magnetic field was not cancelled, G = 3.1 pW K^{-1}, n = 1.91 and T_c = 196.2 mK. When the external magnetic field was cancelled, G = 3.2 pW K^{-1}, n = 1.94 and T_c = 201.5 mK.

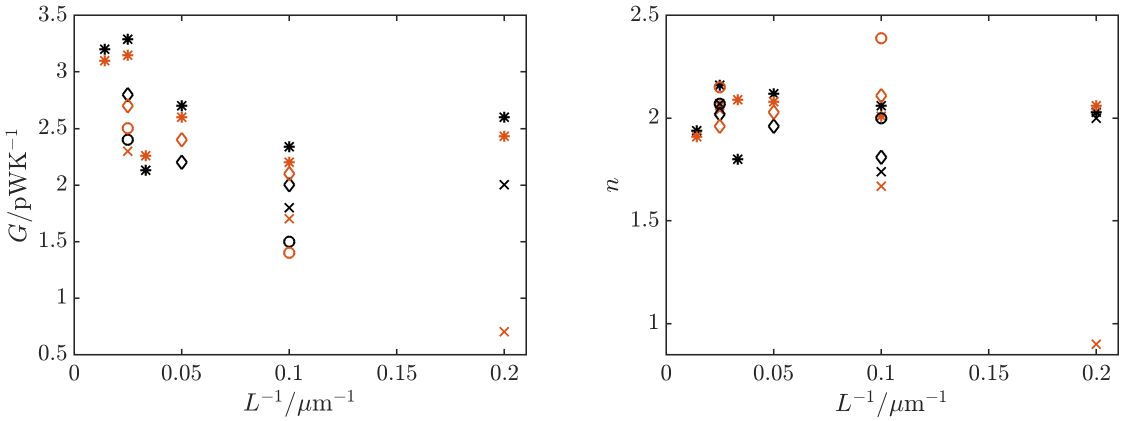

(a) (b)

Figure 6.11 (a) G and (b) n with inverse side length, with the external magnetic field cancelled (black points) and without the external magnetic field cancelled (red points). Asterisks correspond to devices with no bars, crosses to devices with one bar, diamonds to devices with two bars and circles to devices with three bars.

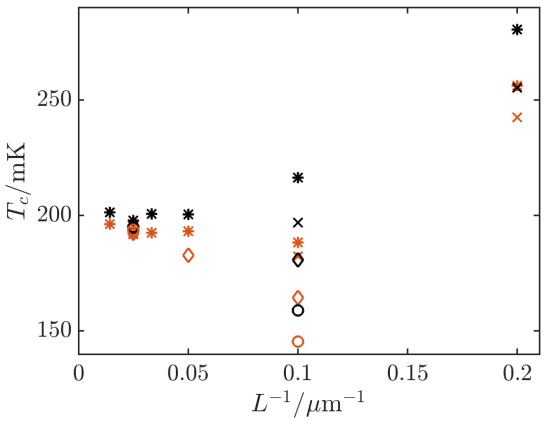

Figure 6.12 T_c as a function of $1/L$, with the external magnetic field cancelled (black points) and without the external magnetic field cancelled (red points). Asterisks correspond to devices with no bars, crosses to devices with one bar, diamonds to devices with two bars and circles to devices with three bars.

Figure 6.12 shows T_c as a function of $1/L$. The asterisks correspond to devices with no bars, the crosses to devices with one bar, the diamonds to devices with two bars and the circles to devices with three bars. Points taken with the external field cancelled are shown in black whilst points taken without field cancellation are shown in red. In general, the presence of a magnetic field suppressed the measured T_c. There is no clear difference between devices with odd and even numbers of bars, with the changes in T_c being approximately the same magnitude for all devices of a particular bilayer size.

6.3.3 T_c as a function of applied magnetic field

The results of Section 6.3.2 demonstrate that an applied magnetic field in the z direction significantly changes the transition temperature of a TES. To further investigate this effect, $I(V)$ curves were measured for a series of different temperatures and applied fields, and then used to calculate $P(T_b)$ curves as a function of field. These $P(T_b)$ curves are shown in Figure 6.13a, for a device with an unpatterned 70 µm side length bilayer. Assuming n and G did not vary significantly with field, the $P(T_b)$ curves were fitted using Equation (5.1), to determine $T_c(B_z)$.

$T_c(B_z)$ was then fitted with an equation either of the linear form

$$T_c = a_1 B_z + a_2, \tag{6.2}$$

where a_j are fitting parameters, as shown in Figure 6.13b, or of the polynomial form

$$T_c = d_1(1 - (B_z/d_2)^{d_3}), \tag{6.3}$$

where d_j are fitting parameters. These fits were carried out to allow prediction of $T_c(B_z)$ when required, for example in Section 6.3.4 to predict changes in magnitude of I_{TES} with applied field.

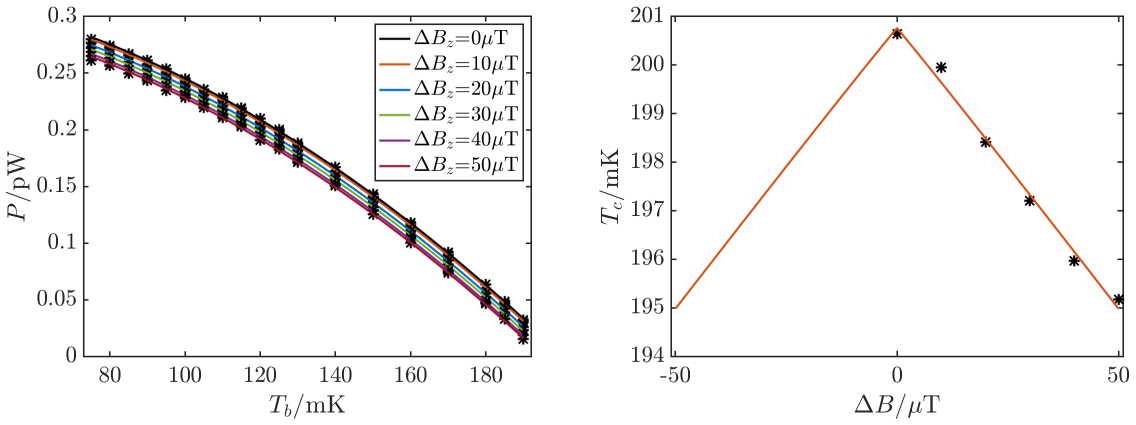

(a) (b)

Figure 6.13 (a) $P(T_b)$ curves for the device with an unpatterned 70 µm side length bilayer, for magnetic fields from 0-50 µT, fitted using the power flow equation with G = 3.2 pW K^{-1}, n = 1.94. (b) T_c as a function of applied magnetic field for the same device. Black asterisks show the data points and the red line is the fit obtained using Equation (6.3). The values of T_c were determined from fits to the $P(T_b)$ curves in (a). In both plots, the external field has been measured and cancelled using the active shielding provided by the magnetic field test system.

Figure 6.14 shows $T_c(B_z)$ for all of the unpatterned devices tested, normalised to the transition temperature at zero field. I would expect the devices with the smallest bilayers to display the least variation in T_c, as their areas are much smaller and so for a given magnetic field, the flux through a TES with a small bilayer is significantly less than that through a TES with a large bilayer. Instead, the devices with smaller bilayers show the largest variation in T_c with applied magnetic fields, despite the lower magnetic flux. In particular, the transition temperature of the device with the 10 µm side length bilayer varies by up to about 13 % for applied fields of around 40 µT, which is about three times the variation displayed by the devices with larger bilayers. From Section 6.3.1, the devices that show the largest percentage variations in $T_c(B_z)$ show the smallest variations in $I_c(B_z)$, and so the variation in transition temperature is not reflected in the change in critical current, as might have been expected. The variation in $T_c(B_z)$ does not seem to be entirely linear, and there are certain magnetic fields that produce

more suppression of T_c. For example, the T_c of the device with the 10 µm side length bilayer is suppressed more than expected at fields of 20 µT and 40 µT.

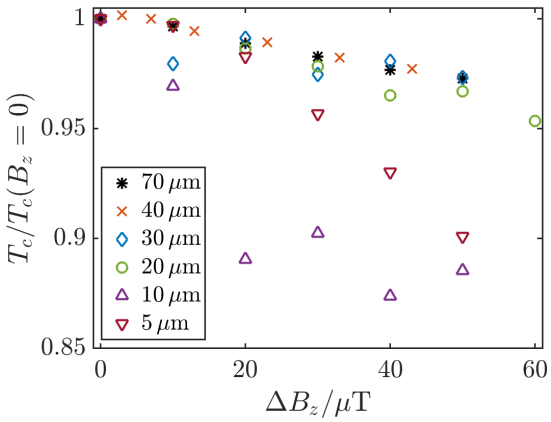

Figure 6.14 $T_c(B_z)$ for a series of unpatterned devices with bilayer side lengths ranging from 70 µm to 5 µm.

Figure 6.15 shows $T_c(B_z)$ for a series of devices with 40 µm side length bilayers: one unpatterned and three with numbers of partial normal metal bars ranging from 1 to 3. In general, as the number of normal metal bars on the bilayer is increased, the variation of T_c with field is reduced, although the device with a single normal metal bar shows similar variation in $T_c(B_z)$ to the unpatterned device. There is no clear divide between devices with odd and even numbers of partial bars.

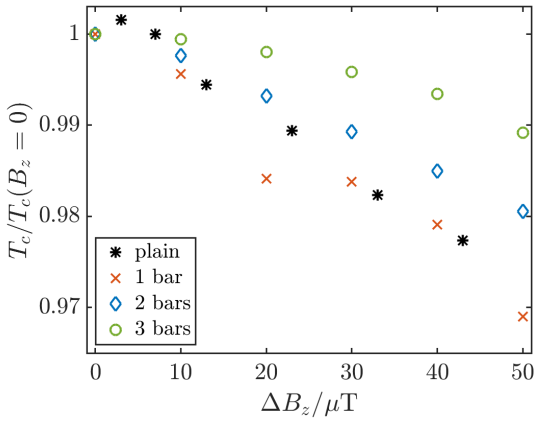

Figure 6.15 $T_c(B_z)$ for four devices of bilayer side length 40 µm, with numbers of bars ranging from 0 to 3.

Figure 6.16 shows $T_c(B_z)$ for a series of devices with smaller, 10 µm side length, bilayers, again with one unpatterned and three with numbers of partial normal metal bars ranging from 1

to 3. The addition of normal metal bars again reduces the variation in the measured T_c with field, although the effect of increasing the number of normal metal bars is less obvious. However, all the devices show oscillations in $T_c(B_z)$ as B_z increases, with dips and peaks at the same field values. Again, there is no obvious difference between devices with odd and even numbers of partial bars.

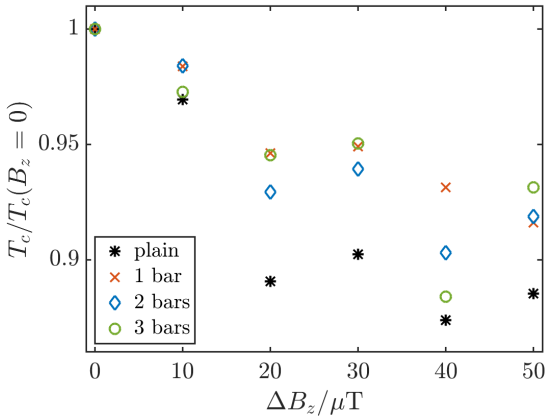

Figure 6.16 $T_c(B_z)$ for four devices of bilayer side length 10 µm, with numbers of bars ranging from 0 to 3.

For the devices with the very smallest bilayer size, T_c varies more for a device with a single normal metal bar than for a unpatterned device, as shown in Figure 6.17, despite the larger self-field of the TES with the metal bar. Unlike the devices with 10 µm side length bilayers, there are no oscillations in $T_c(B_z)$ as B_z increases.

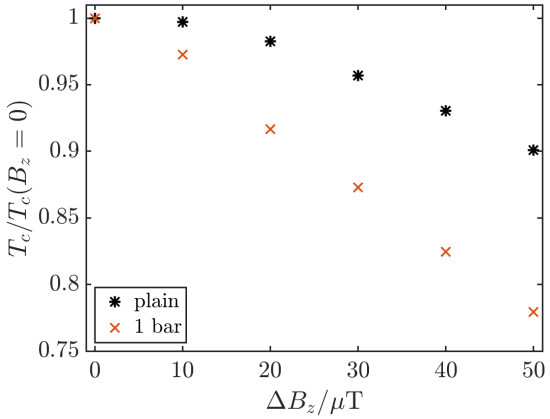

Figure 6.17 $T_c(B_z)$ for two devices with bilayer side length 5 µm, one with no bars and one with a single partial metal bar.

6.3.4 Current and resistance as a function of field

For these measurements, the TES was biased at around 0.5 R_n with no applied field and the magnetic field was cycled between no applied field and an applied field of 100 µT using the 3-axis coil system, whilst the current through the TES was recorded continuously. This was carried out for fields applied in the x, y and z directions. These current measurements can be used to calculate the variations in the bias point with field for applied fields in the z direction. I would expect no significant variation of the current for applied fields in the x direction, as this is the direction in which the current is flowing, and very little variation for fields in the y direction, as the projected area in this direction is much smaller than the projected area in the z direction.

Fields applied in the plane of the thin film

Figures 6.18 to 6.20 show the variation of the TES current for applied fields in the x and y directions, for unpatterned devices with a variety of bilayer sizes, as well as for TESs with bilayer side lengths of 40 µm and 10 µm and different numbers of partial normal metal bars. Referring back to Figure 6.2, roughly 20-30 nA of the variation in I_{TES} can be attributed to the effect of the magnetic field on the SQUIDs, and so even accounting for this there is still a significant change in I_{TES} due to the effect of the applied magnetic field on the TESs.

For the unpatterned devices, Figure 6.18 shows that I_{TES} increased in magnitude with some oscillations when applied fields in both the x and y directions were increased. This increase in magnitude was similar for the applied fields in the x and y directions. The exception was the device with an unpatterned 10 µm side length bilayer, which showed clear oscillations but no increase in magnitude of I with increasing field. The TESs with larger bilayers show smaller changes in I_{TES} for small changes in applied field, but the size of the bilayer does not appear to influence ΔI_{TES} for large changes in applied field.

Figure 6.19 shows $\Delta I_{TES}(B_x)$ and $\Delta I_{TES}(B_y)$ for devices with bilayer side length 40 µm and different numbers of partial bars. In general, the addition of bars, and especially odd numbers of bars, reduced the sensitivity of I_{TES} to applied fields in both the x and y directions. However, the device with a 40 µm side length bilayer with two partial metal bars showed a slightly larger change in bias current, relative to the unpatterned device, when a field was applied in the y direction.

The effect of adding bars to TESs of bilayers of side length 10 µm on $\Delta I_{TES}(B_x)$ and $\Delta I_{TES}(B_y)$ is presented in Figure 6.20. Like the unpatterned device, the device with an even number of bars appeared to be relatively insensitive to applied fields in the x direction, as it exhibited clear oscillations but no significant increase in the overall magnitude of ΔI_{TES} as B_x was increased. For applied fields in the y direction, as the number of bars was increased the

field dependence was increased, even at very small applied magnetic fields. This shows that although bars may reduce the dependence to magnetic fields in the z direction, they may not reduce dependence to fields in all directions, which is why a consideration of the full directional dependence on magnetic fields is important.

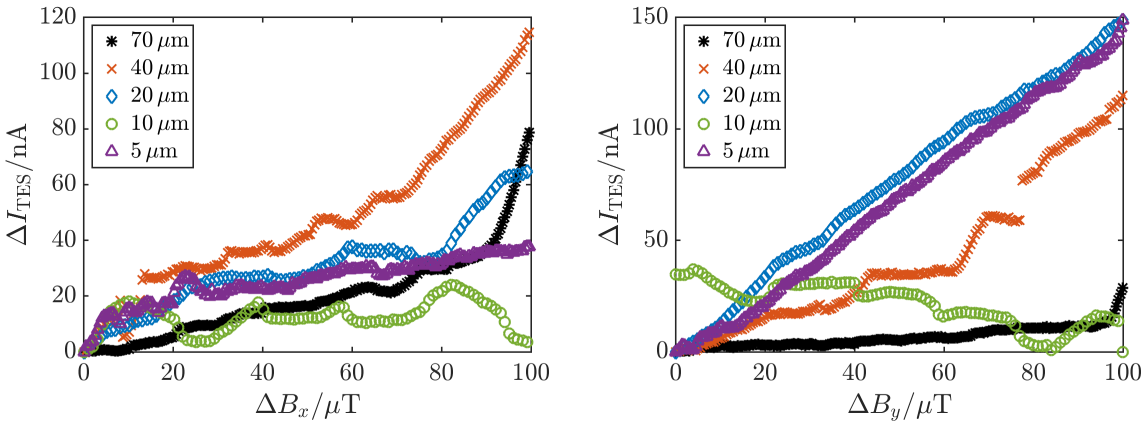

(a) (b)

Figure 6.18 Change in TES current when the field applied in the (a) x direction or (b) y direction was increased from 0 to 100 μT, for a series of unpatterned devices of different bilayer sizes.

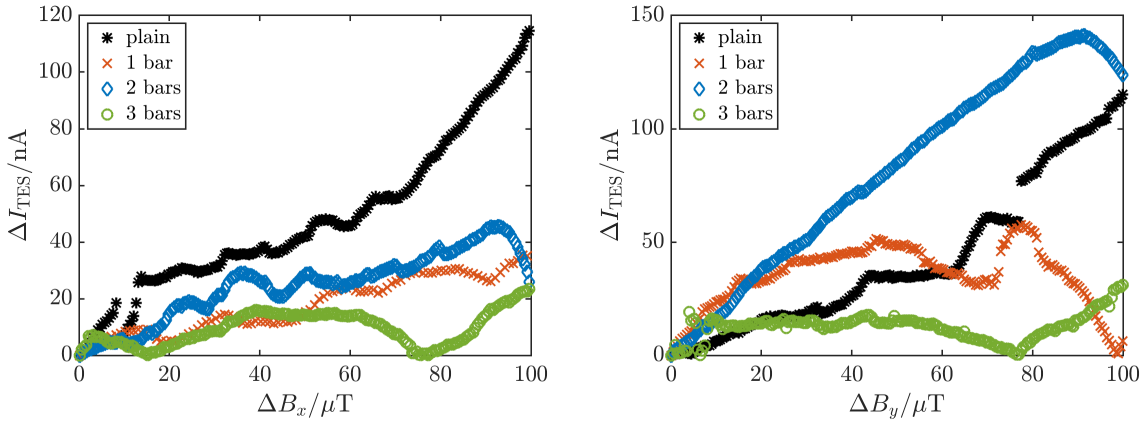

(a) (b)

Figure 6.19 Change in TES current when the field applied in the (a) x direction or (b) y direction was increased from 0 to 100 μT, for a series of TESs of bilayer side length 40 μm and varying numbers of normal metal bars.

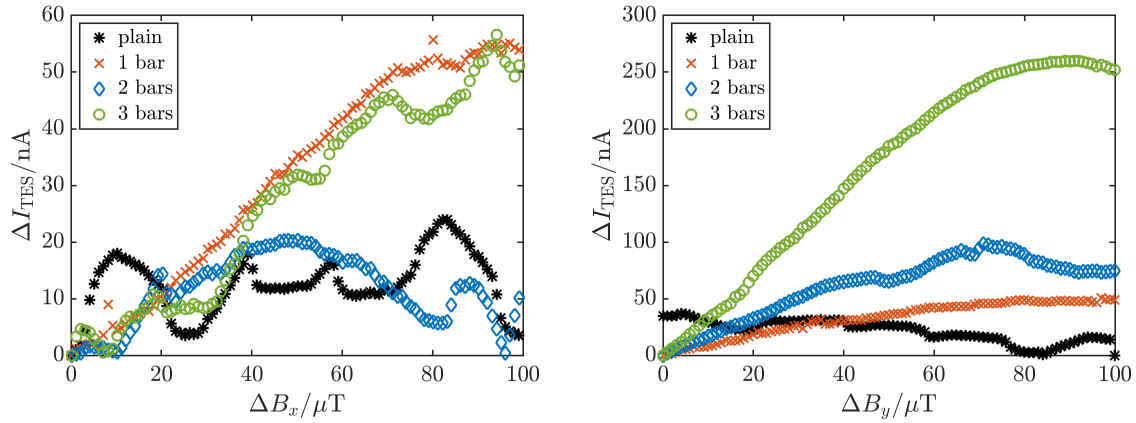

Figure 6.20 Change in TES current when the field applied in the (a) x direction or (b) y direction was increased from 0 to 100 µT, for a series of TESs with bilayer side length 10 µm and varying numbers of normal metal bars.

Fields applied perpendicular to the plane of the thin film

Figures 6.21 to 6.23 show the effects of applying fields in the z direction, the direction in which the TES is most sensitive to applied fields. The measured changes in current were of the order of µA, compared to the changes of the order of nA that were observed for applied fields in the x and y directions. For all three figures, the plot on the left hand side shows the variation in I_{TES} relative to I_{TES} at zero field (plotted as points), along with a prediction for the expected change in magnitude of I_{TES} based on the variation of transition temperature described in Section 6.3.3 (shown as a solid line of the same colour). The right hand side shows how the bias point, expressed as a fraction of the normal state resistance, changes with applied field.

Figure 6.21 shows the effects of bilayer size on both $I(B_z)$ and $R_0(B_z)$ for unpatterned devices. The devices with the largest bilayers were the least sensitive to applied fields, as they exhibited the smallest changes in both I_{TES} and bias point for an applied field of fixed magnitude in the z direction. All devices displayed oscillations in I_{TES}, and as for the critical current measurements in Section 6.3.1, the devices with the smallest bilayers had the largest periods of oscillation. Unlike the critical current results, the devices with the smallest bilayers showed the largest changes in magnitude of both I_{TES} and bias point, which appears to be due to the large changes in T_{c} with field measured in Section 6.3.3, as the prediction for ΔI_{TES} based on $T_{\mathrm{c}}(B_z)$ gives a good account of the magnitude of the change in I_{TES} for all bilayer areas. From Figure 6.21b, none of the TESs become fully normal ($R = R_{\mathrm{n}}$) at the minima of the oscillations in I_{TES}. This is consistent with the observation in Section 6.3.1 that the TES critical current is not zero at the minima of $I_{\mathrm{c}}(B_z)$.

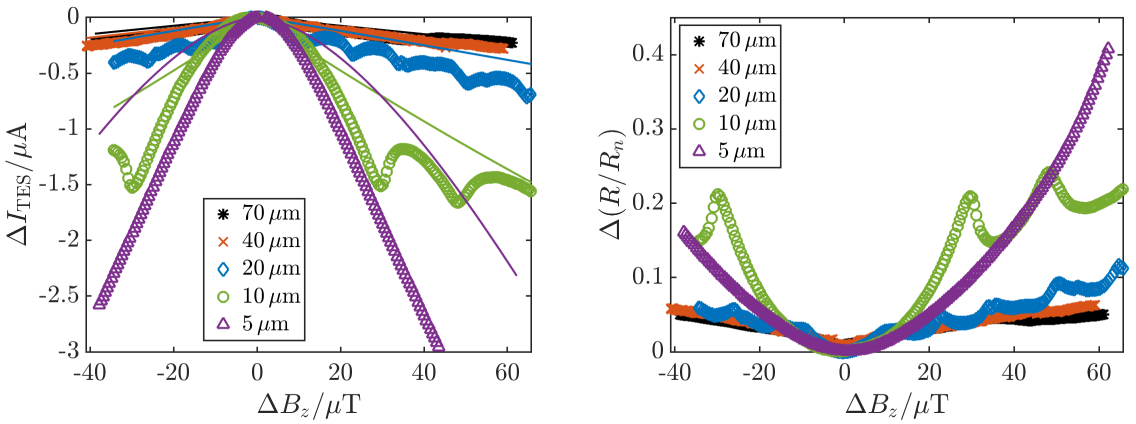

(a) (b)

Figure 6.21 (a) Change in TES current relative to the current measured at zero field, and (b) TES bias point when the applied field in the z direction was increased from 0 to 100 µT, for a series of unpatterned devices with different bilayer areas. The solid lines of the corresponding colour in (a) show the prediction for the expected change in magnitude of I_{TES} based on the variation of T_{c} with field measured in Section 6.3.3. In both plots, the external field has been measured and cancelled using the active shielding provided by the magnetic field test system.

Figure 6.22 shows $I_{\mathrm{TES}}(B_z)$ and the change in bias point with B_z for a series of TESs with bilayer side length 40 µm and 0-3 partial normal metal bars. Oscillations in I_{TES} were displayed by all of the devices. The period of these oscillations is 2-3 µT. As the number of bars on the bilayer increased, the magnitude of the change in I_{TES} for a fixed magnetic field was reduced, agreeing with the trends followed by I_{c} and T_{c}. In general, the devices with odd numbers of bars displayed the smallest changes in I_{TES}. All four TESs exhibited only minor variations in bias point, of the order of 5 % or less, with applied field. The features at around -5 µT and 45 µT for the unpatterned device are indicative of phase slip behaviour - the current decreases abruptly, then jumps to a higher value. This behaviour was reproduced at approximately the same values of field when this measurement was repeated.

In Figure 6.23, $I_{\mathrm{TES}}(B_z)$ and the change in bias point with B_z are presented for a series of devices with bilayers of 10 µm side length and 0-3 partial normal metal bars. The prediction based on the variation of T_{c} with field is shown by the solid lines. The oscillations in I_{TES} have roughly the same magnitude for all of the devices, which is not a result that is predicted by the variation of T_{c} with field. The first minima in I_{TES} of the devices with even numbers of bars appear to be lower than those for the devices with odd numbers of bars. All of the devices show large variations in bias point, of the order of at least 20 % across the range of applied fields tested, which is consistent with the large changes in $T_{\mathrm{c}}(B_z)$ exhibited by the devices with small bilayers. The oscillations in I_{TES} were of roughly the same magnitude for all of the devices,

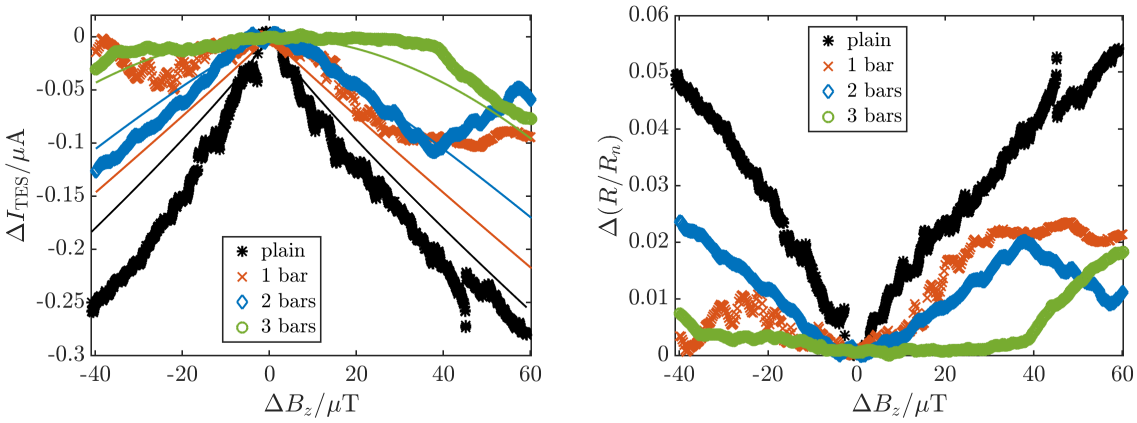

Figure 6.22 (a) Change in TES current relative to the current measured at zero field, and (b) TES bias point when the applied field in the z direction was increased from 0 to 100 µT, for a series of devices with bilayer side length 40 µm and different numbers of partial normal metal bars. The solid lines of the corresponding colour in (a) show the prediction for the expected change in magnitude of I_{TES} based on the variation of T_{c} with field measured in Section 6.3.3. In both plots, the external field has been measured and cancelled using the active shielding provided by the magnetic field test system.

which is not a result that was predicted by the variation of T_{c} with field. These two observations are reminiscent of the behaviour of $I_{\mathrm{c}}(B_z)$ in Section 6.3.1.

Some of the TESs displayed significant differences between the current measured when the field was increased from zero to 100 µT and the current measured when the field was decreased from 100 µT to zero, whilst other TESs displayed very little difference. In general, the devices with larger bilayers showed this hysteresis in measured current, an example of which is presented in Figure 6.24. The current as a function of field is shown for the device with the 70 µm side length bilayer when fields are applied in the x, y and z directions. The black asterisks show the current measured when the field was increased; the red crosses show the current measured when the field was decreased. In all cases, both the shape and the magnitude of the measured current differed significantly between the increasing field and decreasing field cases. Figure 6.24c shows asymmetric hysteresis, which may be due to increased current heating at positive fields, due to the current required to cancel out the external magnetic field.

The devices with smaller bilayer areas showed little to no hysteresis, as shown in Figure 6.25. Here, the current as a function of field is shown for the device with the 20 µm side length bilayer for applied magnetic fields in the x, y and z directions. Again, the black asterisks show the current measured when the field was increased; the red crosses show the current measured when the field was decreased. For this device, there was little to no difference in shape and

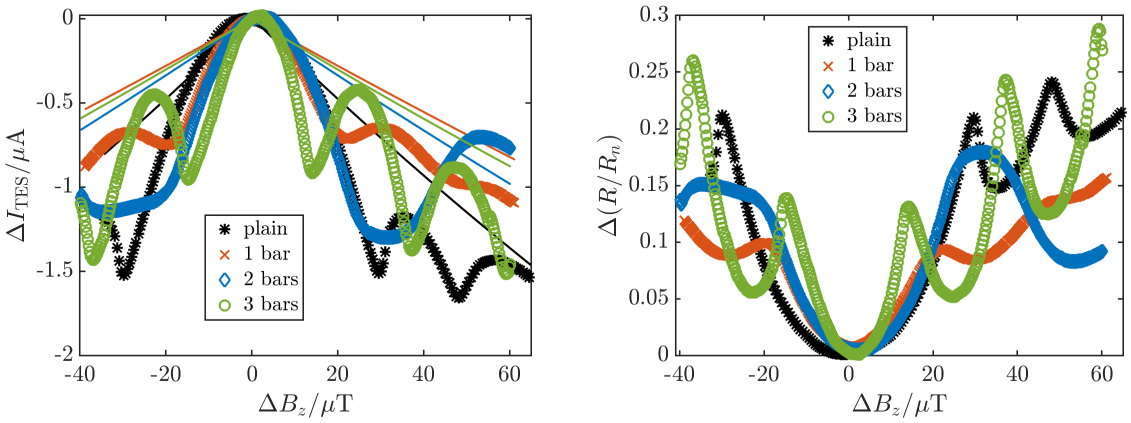

(a) (b)

Figure 6.23 (a) Change in TES current relative to the current measured at zero field, and (b) TES bias point when the applied field in the z direction was increased from 0 to 100 µT, for a series of devices with bilayer side length 10 µm and different numbers of partial normal metal bars. The solid lines of the corresponding colour in (a) show the prediction for the expected change in magnitude of I_{TES} based on the variation of T_{c} with field measured in Section 6.3.3. In both plots, the external field has been measured and cancelled using the active shielding provided by the magnetic field test system.

magnitude between the increasing and decreasing field cases. Some of this hysteresis, especially for applied fields in the z direction, may be due to the fact that TESs with smaller bilayers show a greater ΔI when a field is applied in the z direction, and so are less sensitive to small fluctuations in overall I. However, this does not explain the significant differences in the degree of hysteresis in the x and y directions. The hysteresis may be linked to the larger magnetic flux for longer, wider bilayers when fields are applied in the x and y directions.

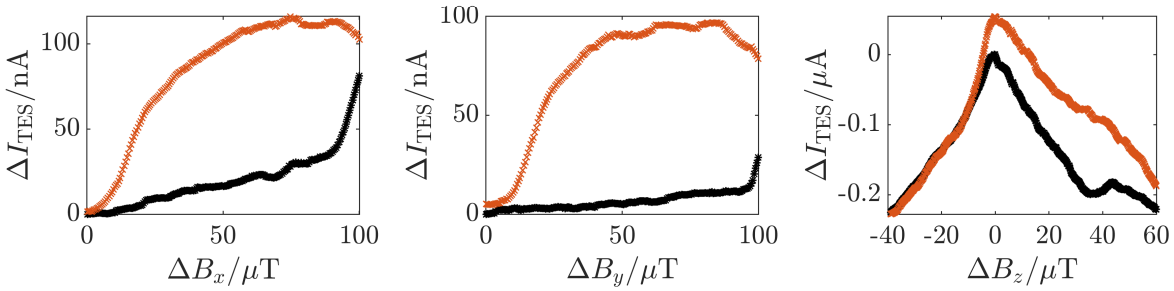

(a) (b) (c)

Figure 6.24 Current through the TES as a function of field for the device with the unpatterned 70 µm side length bilayer, for applied fields in (a) the x direction, (b) the y direction and (c) the z direction, measured relative to the current at zero field. The black points show data taken when the field was increased; the red points show the data taken when the field was decreased.

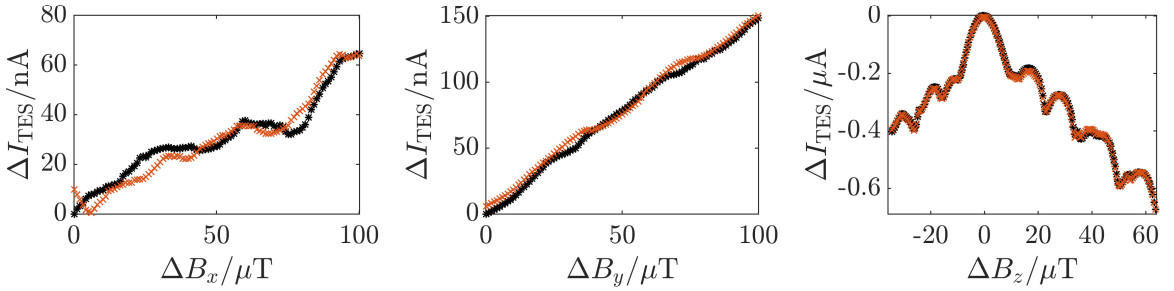

(a) (b) (c)

Figure 6.25 Current through the TES as a function of field for the device with the unpatterned 20 µm side length bilayer, for applied fields in (a) the x direction, (b) the y direction and (c) the z direction, measured relative to the current at zero field. The black points show data taken when the field was increased; the red points show the data taken when the field was decreased.

6.3.5 Spherical scans

From Section 6.3.4, TESs are sensitive to in-plane fields as well as out-of-plane fields. As discussed in Section 4.7.3, knowledge of the field directions that have the largest impact on device behaviour is therefore hugely beneficial when designing magnetic shielding. I therefore developed a system to allow the first ever measurements of directional TES response, and present these measurements in this section. In these scans, I fixed the magnitude of the magnetic field and swept its direction to investigate the directional response of the TES. For each scan, I plotted the direction of the applied field scaled by the change in bias current of the TES. Figures 6.26 to 6.29 show the resulting change in current when a field of a fixed magnitude is applied to the TES and its direction is varied. As expected, the TESs were almost always most sensitive to applied fields in the z direction, generally showing maximal response when the field was in this direction.

Figure 6.26 shows the directional response to an applied field of 20 µT for four unpatterned TESs of different bilayer side lengths: (a) 70 µm, (b) 40 µm, (c) 20 µm and (d) 5 µm. In all four scans, there are clear lobes along the z axis and the maximal response is for applied fields in the z direction. The TESs with smaller bilayers displayed a greater change in current, as observed in Section 6.3.4. The device with the unpatterned 20 µm side length bilayer has lobes that are not perfectly spherical, instead displaying visible oscillations. None of the TESs showed zero change in current for any of the magnetic field directions, but there was definitely a minimum in response when fields were applied in the $x - y$ plane.

The results in Figures 6.26 to 6.29 can be compared to predictions using the model described in Section 2.4.1. Although this model predicts changes in critical current with field rather than current, Sections 6.3.1 and 6.3.4 show that both I_{TES} and I_{c} exhibit a similar shape close to zero field, especially for small devices, and so the model predictions can be used to estimate general trends in I_{TES}.

Model results are shown in Figure 6.27 for (a) a TES with an unpatterned 20 µm side length bilayer and (b) a TES with an unpatterned 10 µm side length bilayer. The model gives a good account of the behaviour of the TES with the smaller bilayer, although predicts zero change in current for applied fields in the $x - y$ plane. It also predicts the oscillations for the devices with larger bilayer areas, and as bilayer size increases, these oscillations decrease in magnitude, explaining why no oscillations are visible for the devices with 70 µm side length and 40 µm side length bilayers. However, the model response for the device with the 20 µm side length bilayer has a more spherical envelope than the measured response, which shows a clearly double-lobed envelope.

Figure 6.28 shows the measured directional response to an applied field of 20 µT for a series of devices with 40 µm side length bilayers and $N = 0 - 3$. The addition of bars, especially odd

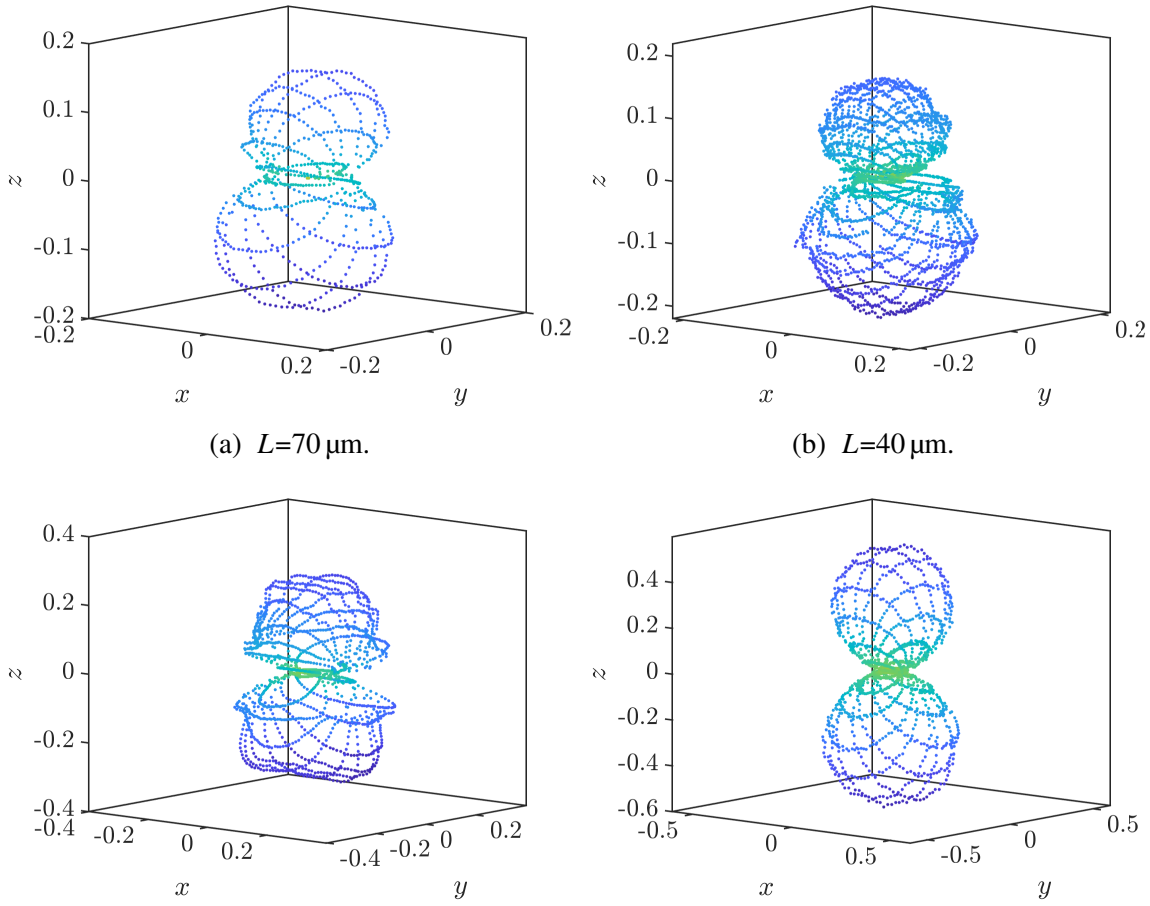

(a) L=70 µm. (b) L=40 µm.

(c) L=20 µm. (d) L=5 µm.

Figure 6.26 Direction of the applied field scaled by the current response of the TES (in µA), with a field magnitude of 20 µT, for four unpatterned devices with different bilayer side lengths, L. These scans were taken at a temperature of 90 mK and a bias point of 50 % R_n. The colours of the points correspond to the magnitude of the current response.

numbers of bars, to the TES bilayer produced response surfaces that no longer display a lobed shape. The overall magnitude of the response decreased, which is consistent with the results of Section 6.3.4. The device with a bilayer featuring a single partial bar showed clear oscillations in the response surface, but these were less visible for the other three TESs.

Figure 6.29 shows the directional response to an applied field of magnitude 20 µT for a series of TESs with bilayer side length 10 µm and 0-3 partial normal metal bars. All four devices display clear lobed response surfaces, with spherical lobes that showed no obvious oscillations. The device with three normal metal bars no longer had its maximal response for applied fields in the z direction, because the first minima in its $I(B_z)$ dependence were within

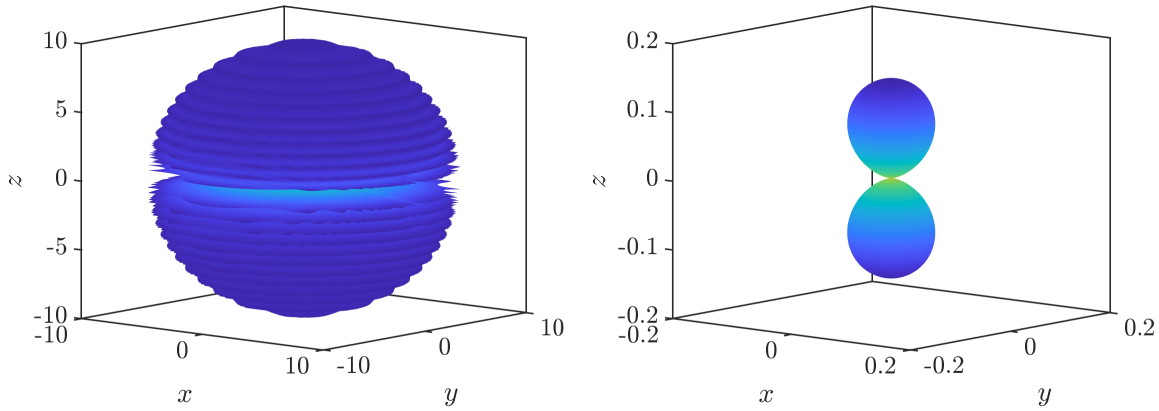

(a) L=20 µm. (b) L=10 µm.

Figure 6.27 Direction of the applied field scaled by the change in critical current of the TES (in µA), as calculated using a model of device magnetic field response, for two unpatterned devices with different bilayer areas. In both cases, the magnetic field changes were centred exactly about the external field. The shading corresponds to the magnitude of the change in current.

the ± 20 µT range of the scan. There is no clear difference in behaviour between devices with odd and even numbers of bars.

The asymmetry in lobe size in some of the scans was caused by the TES not being exactly at zero field, as shown by Figure 6.30. This figure shows simulations of device response for a small constant field offset of 0.3 µT and a large constant field offset of 1.5 µT. In the small offset case, the offset produced two lobes of different shapes and sizes, whilst in the large offset case, the response looked nearly spherical. These scans are therefore also a useful diagnostic tool for determining whether or not a TES is operating under zero-field conditions.

Spherical harmonic expansion

When designing magnetic shielding to reduce the fields experienced by TESs, it is beneficial to quantify the field components that a TES is most and least sensitive to. As in Section 4.7.3, I wrote software to calculate the spherical harmonic expansion of the response surface. This could be then compared to the spherical harmonic expansion of the field inside a given shielding design, to quantify how effective the shield is for reducing the magnetic fields that have the greatest impact on TES performance.

Taking the data from an unpatterned device with a 10 µm side length bilayer, I expressed the response surface in a spherical harmonic basis, as in Figure 6.31. Figure 6.31a shows the experimentally measured response (black asterisks) as well as the response surface calculated using the spherical harmonic decomposition (multicoloured surface). The response surface is

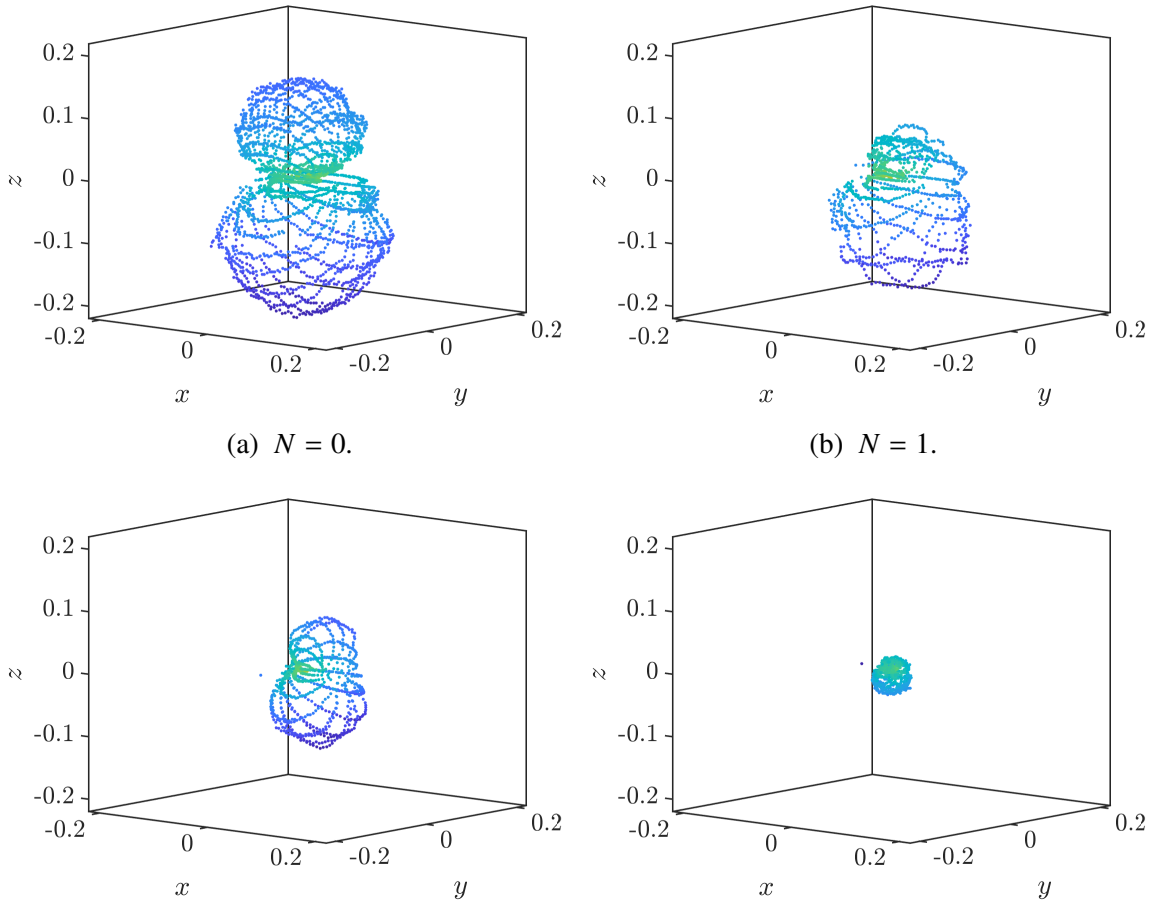

(a) $N = 0$. (b) $N = 1$.

(c) $N = 2$. (d) $N = 3$.

Figure 6.28 Direction of the applied field scaled by the current response of the TES (in µA) with a field of magnitude 20 µT, for four TESs with bilayer side length 40 µm and different numbers of partial bars, N. These scans were taken at a temperature of 90 mK and a bias point of 50 % R_n. The colours of the points correspond to the magnitude of the current response.

not perfectly described by the spherical harmonic expansion, due to the slight asymmetry in the response surface due to imperfect cancellation of the external magnetic field, as demonstrated in Figure 6.30. Figure 6.31b shows the components of the spherical harmonic decomposition, with positive components in black and negative components in red. Unlike the spherical harmonic decomposition of the Hall probe response surface, the TES response surface is described by a zeroth order spherical term with two higher order components subtracted off.

Figure 6.32 explores this in more detail. It shows a slice through the response surface in the $y - z$ plane (black asterisks), along with a first order spherical harmonic scaled to the overall z dimension of this slice (red crosses) and the full spherical harmonic expansion (blue diamonds). The response surface is not well described by the scaled first order spherical harmonic, showing

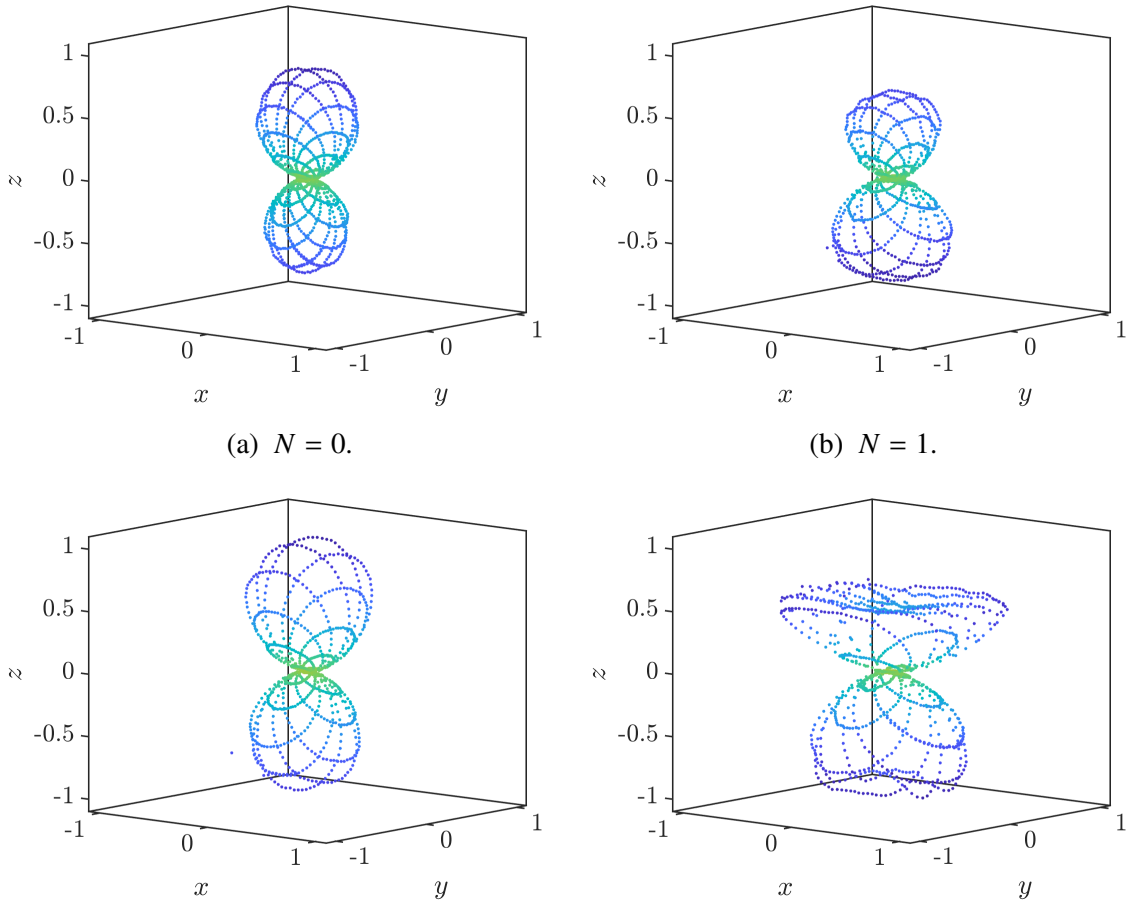

(a) $N = 0$. (b) $N = 1$.

(c) $N = 2$. (d) $N = 3$.

Figure 6.29 Direction of the applied field scaled by the current response of the TES (in μA) with a field of magnitude 20 μT, for four TESs with bilayer side length 10 μm and different numbers of partial bars, N. These scans were taken at a temperature of 90 mK and a bias point of 50 % R_n. The colours of the points correspond to the magnitude of the current response.

that unlike a Hall probe, the TES is sensitive to applied fields in all directions, and so the response doesn't vary as $\cos\theta$, where θ is the angle between the normal to the TES and the direction of the applied field. The discrepancy between the scaled first order spherical harmonic and the measured response could be attributed to the slight offset in background field, due to imperfect cancellation of the external magnetic field. However, even in the absence of a constant field offset, the response surface would still not be described well by a first order spherical harmonic, since from Figure 6.32, the scaled first order spherical harmonic is wider in the y direction than either lobe of the measured response. Subtracting off the current offset caused by the field offset will make the larger lobe narrower in the y direction and the smaller lobe wider, without changing the overall height in the z dimension, so if the measured response

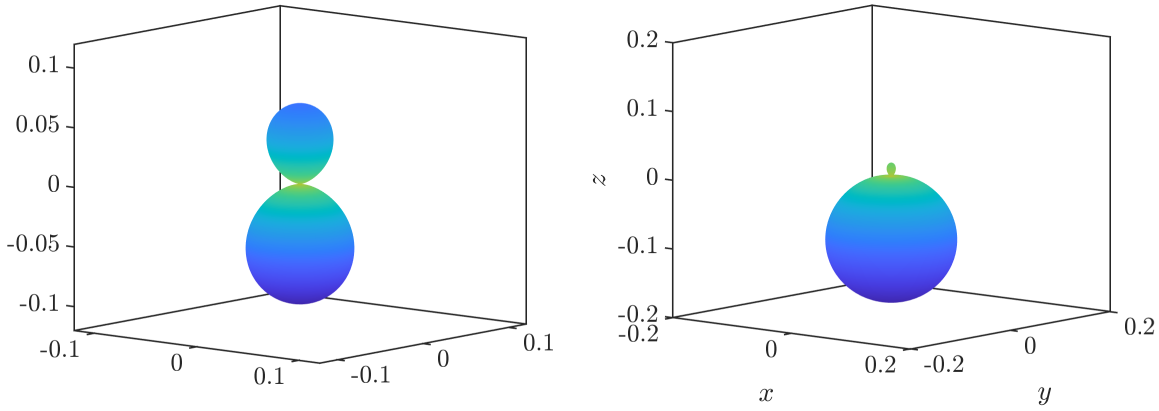

(a) B_{offset}=0.3 µT. (b) B_{offset}=1.5 µT.

Figure 6.30 Direction of the applied field scaled by the current response to the TES (in µA), as calculated using a model of device magnetic field response, for a device with an unpatterned 5 µm side length bilayer. (a) shows the case where there was a small, constant field offset; (b) shows the case where there was a large, constant field offset. The surfaces are coloured according to the magnitude of the current response.

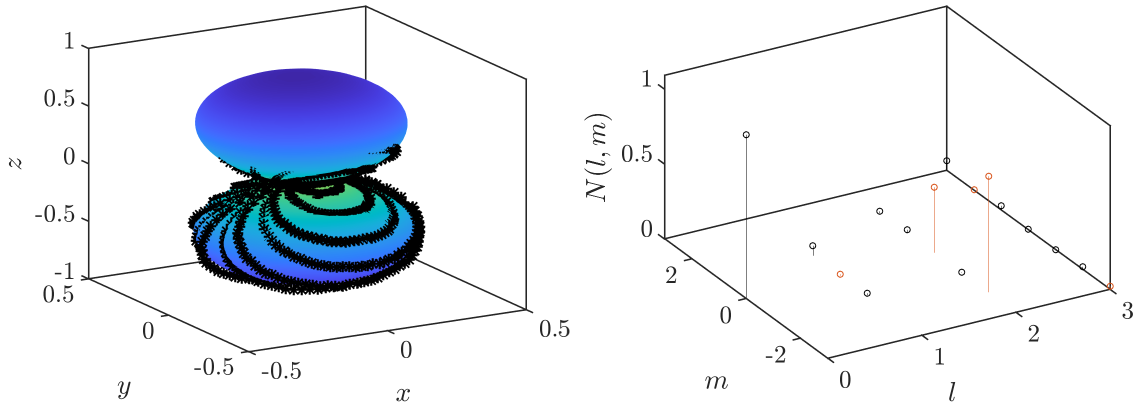

(a) (b)

Figure 6.31 (a) Direction of the field scaled by the current response of the TES (in µA), as measured experimentally (black asterisks) and as expressed in a spherical harmonic basis (multicoloured surface). The surface is coloured according to the magnitude of the current response. (b) Coefficients $N(l, m)$ from Equation (4.4) for the spherical harmonic decomposition. Black points show positive coefficients, whilst red points indicate negative coefficients.

surface could be described purely by a first order spherical harmonic, the larger lobe should be wider than the scaled first order spherical harmonic.

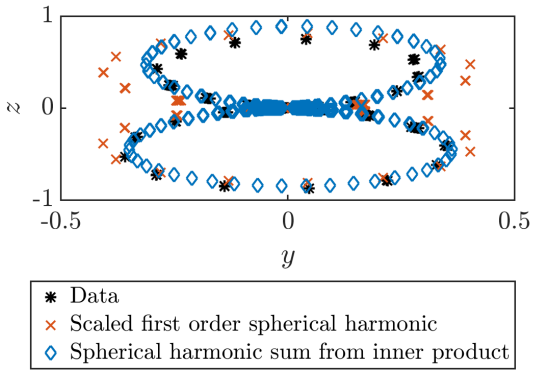

Figure 6.32 A slice in the $x - z$ plane shows the TES response in μA (black asterisks), a first order spherical harmonic scaled to the overall $z-$height of the slice(red crosses) and the calculated spherical harmonic decomposition (blue diamonds).

6.3.6 α and β

Figures 6.33 to 6.36 show α and β as a function of B_z, for several subsets of the TESs tested. Figure 6.33 displays $\alpha(B_z)$ and $\beta(B_z)$ for all of the unpatterned devices measured, with bilayer side lengths ranging from 70 µm to 5 µm. For all devices, both α and β generally decreased as the applied field was increased, with evidence of oscillatory behaviour as observed by Smith et al. [97]. The overall magnitude of the change in α with applied field was similar for all bilayer sizes, whilst the devices with smaller bilayers showed larger changes in β than the devices with larger bilayers.

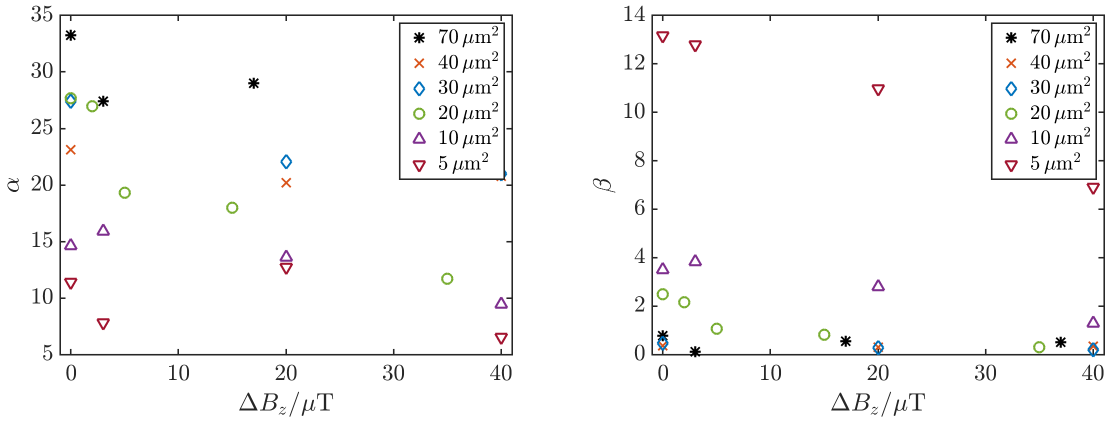

(a) (b)

Figure 6.33 (a) $\alpha(B_z)$ and (b) $\beta(B_z)$ for a series of unpatterned devices with bilayer side lengths ranging from 70 µm to 5 µm.

In Figure 6.34, $\alpha(B_z)$ and $\beta(B_z)$ are displayed for four TESs of bilayer side length 40 µm and numbers of partial metal bars ranging from 0-3. There is a divide in behaviour between the devices with odd numbers of bars and devices with even numbers of bars, with α and β generally lower for devices with odd numbers of bars. There is less evidence of oscillatory behaviour for these devices with larger bilayers, and the addition of partial normal metal bars does not reduce the overall variation in α or β.

Figure 6.35 shows α and β as a function of B_z for four TESs with bilayer side length 10 µm and 0-3 partial normal metal bars. Here there is less of a divide in behaviour between devices with odd and even numbers of bars compared to the devices with 40 µm side length bilayers, and more evidence of oscillatory behaviour, especially for the devices with bars. This suggests that the applied field had more of an effect on the devices with bars, contradicting the results from Section 6.3.4. For these devices, the presence of patterning generally increased α and β, implying that normal metal bars produce more sensitive devices. In particular, the

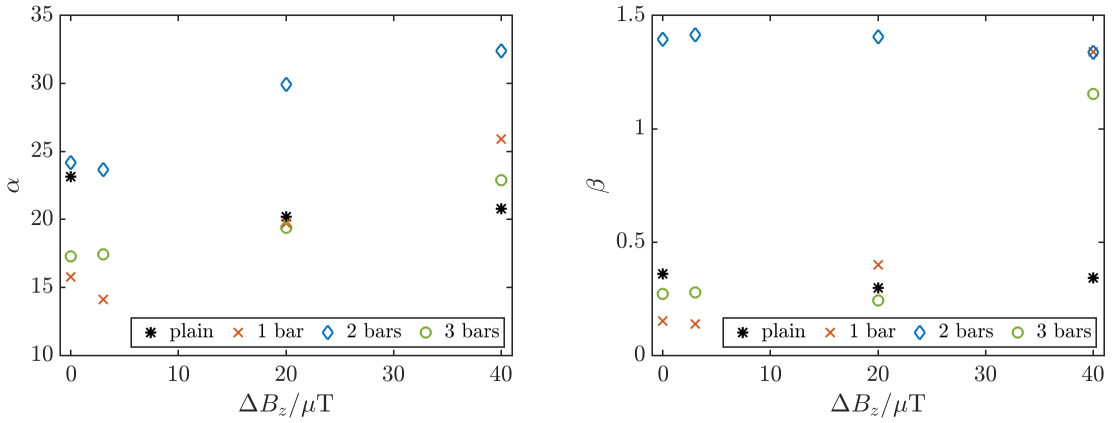

(a) (b)

Figure 6.34 (a) $\alpha(B_z)$ and (b) $\beta(B_z)$ for a series of devices with bilayer side length 40 µm and $N = 0 - 3$ partial normal metal bars.

TES patterned with two normal metal bars displayed a high value of β for all magnetic fields, suggesting that the self-field of the device may have an impact on the value of β.

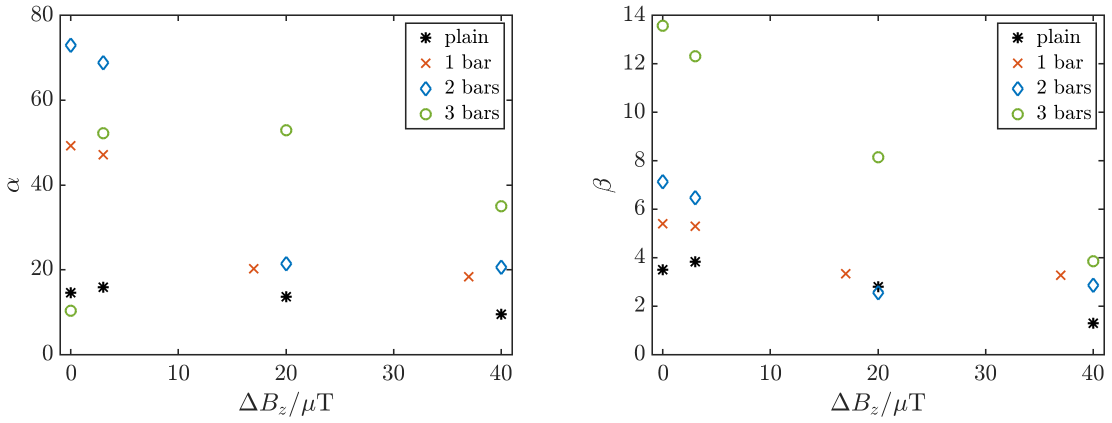

(a) (b)

Figure 6.35 (a) $\alpha(B_z)$ and (b) $\beta(B_z)$ for a series of devices with bilayer side length 10 µm and $N = 0 - 3$ partial normal metal bars.

$\alpha(B_z)$ and $\beta(B_z)$ are displayed in Figure 6.36 for the two TESs with the smallest bilayer side length, 5 µm. One bilayer was unpatterned whilst the other had a single 1 µm wide partial metal bar. β decreased with increasing field for both TESs, with no evidence of oscillatory behaviour, whilst α decreased with field for the device with one bar but displayed oscillations for the device without bars. The change in β observed for the unpatterned device is smaller than that for the patterned device, agreeing with the results of Figure 6.35.

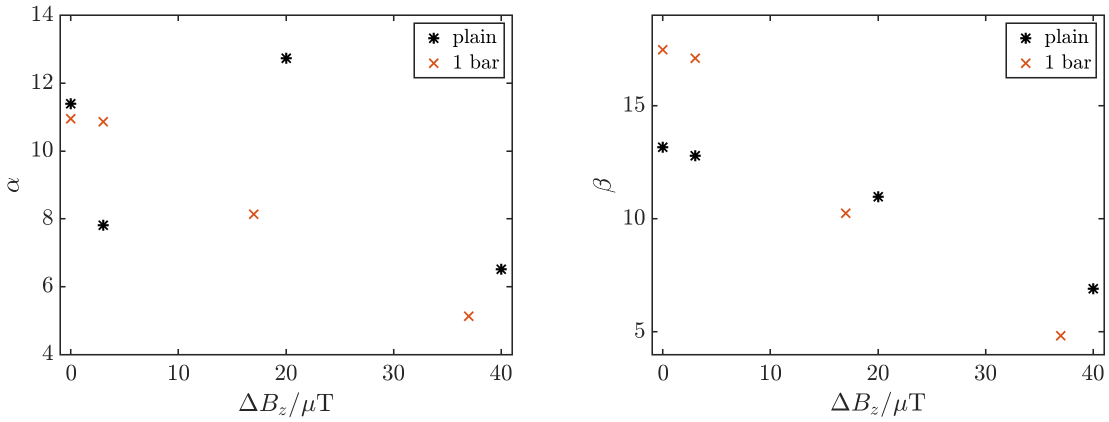

(a) (b)

Figure 6.36 (a) $\alpha(B_z)$ and (b) $\beta(B_z)$ for two devices with bilayer side length 5 µm, one unpatterned and one with a single partial normal metal bar.

6.3.7 Risetimes

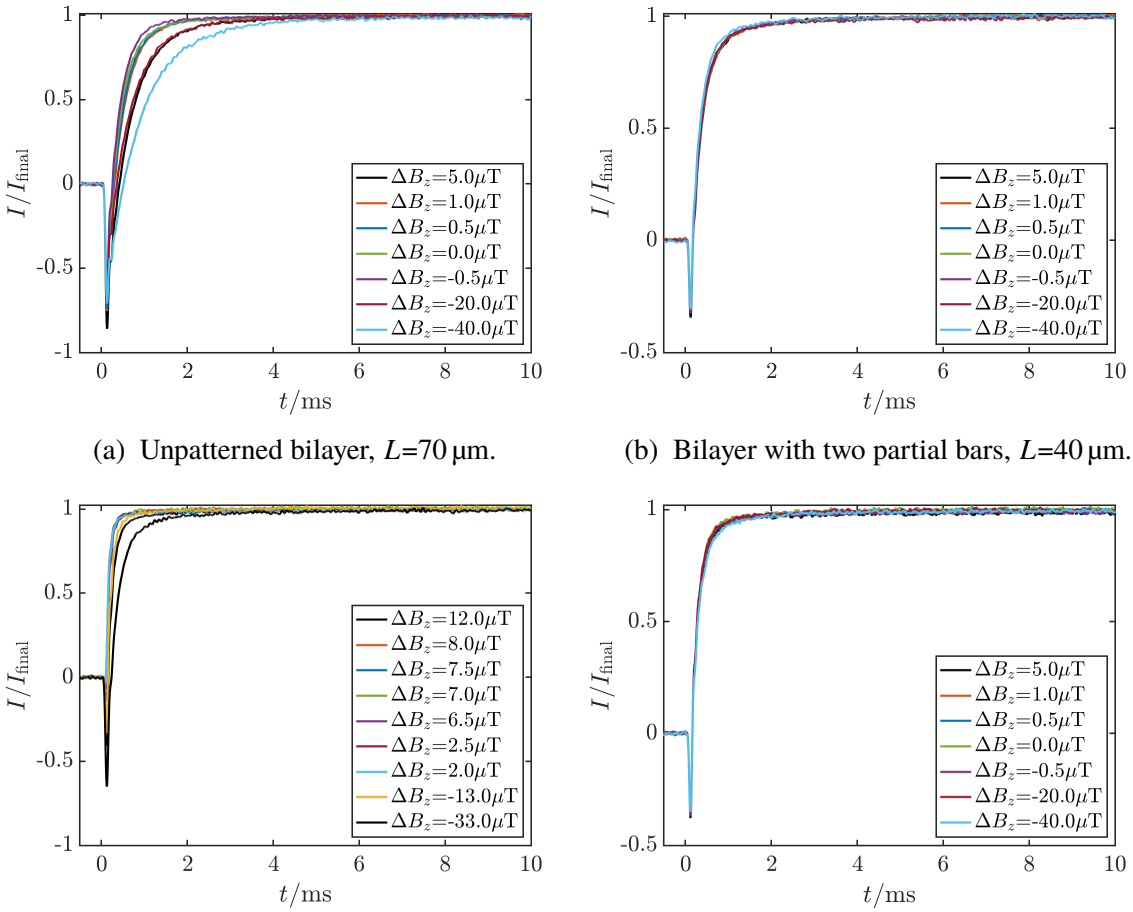

(a) Unpatterned bilayer, L=70 µm.

(b) Bilayer with two partial bars, L=40 µm.

(c) Unpatterned bilayer, L=20 µm.

(d) Bilayer with two partial bars, L=20 µm.

Figure 6.37 Risetimes measured at several different fields for four devices. All the risetimes were taken at a temperature of 120 mK and a bias point of 50 % R_{n}, with no attenuation, and have been normalised to the final response amplitude.

When carrying out magnetic field scans, it is important to make sure that the applied magnetic field does not affect the device response time. Figure 6.37 shows risetimes as a function of field for four different devices: two unpatterned, and two with two partial normal metal bars. The two unpatterned devices had bilayers of side length 70 µm and 20 µm, and both showed a reduction in response time for applied fields above a few µT. The two devices with bars had bilayers of side length 40 µm and 20 µm, and neither device showed any significant reduction in response time with applied field. This suggests that the addition of normal metal bars produces devices whose speed is minimally affected by the presence of magnetic fields. I

allowed a settling time of at least 5 ms for field measurements on the device with the largest bilayer, and 2 ms on all the other devices.

6.3.8 Noise

Applied magnetic fields have been observed by other groups to reduce the magnitude of the 'excess noise' feature in the noise spectrum of some TESs at about 1 kHz [11]. The presence of normal metal bars also reduces this excess noise [97], which may be caused by the self-field produced by meander current flow in these patterned devices. I investigate whether devices with bars have noise spectra that are less influenced by magnetic fields. In all of the spectra in this section, the noise peaks at high frequency are due to noise from the three-axis coil system and its wiring. The spectra for some devices show a clear, high 50 Hz peak. There was no passive shielding of the devices, in order to prevent field distortions and ensure applied fields were uniform, so electromagnetic interference effects were inevitable.

Figure 6.38 shows the noise spectra as a function of field for four TESs with bilayer side length 40 µm and 0-3 partial normal metal bars. At the external magnetic field of around 40 µT, all TESs had noise spectra at approximately the 50 $pAHz^{-1}$ level at a frequency of 10 Hz, indicating similar levels of $1/f$ noise for all devices. The contribution from the Johnson noise can be seen at higher frequencies of around 10 kHz - 100 kHz. As expected, the excess noise feature, seen in the frequency range 0.1-1 kHz at zero applied field, was highest for the unpatterned TES, and showed the largest degree of suppression under an applied magnetic field, from Figure 6.38a. The excess noise peak was higher for the device with two partial bars, shown in Figure 6.38c, and exhibited greater suppression with applied field. Some suppression of an excess noise peak was exhibited by the device with a single metal bar in Figure 6.38b, whilst Figure 6.38d shows that the device with three partial normal metal bars underwent very little change in its noise spectrum when magnetic fields were applied. This difference in behaviour between the device with an even number of bars and the devices with odd numbers of bars agrees with the observations in other sections, such as Sections 5.3.5 and 5.3.1.

For the series of four TES with bilayer side length 10 µm in Figure 6.39, the trends in noise with applied field are less obvious. The unpatterned device showed the largest noise and the largest excess noise peak, from Figure 6.39a. It took a larger applied magnetic field to suppress this peak, with a field of about 20 µT having no real effect on the excess noise. For the device with two partial normal metal bars, the spectra in Figure 6.39c show more evidence of an excess noise peak at zero field compared to the devices with one and three partial bars. However, the devices with one and three bars showed more variation in low frequency noise. The spectra for the device with one partial bar, shown in Figure 6.39b, exhibited variations in $1/f$ noise with field, with a minimum at an applied field of 20 µT rather than 40 µT. The same variation was

visible in the low-frequency phonon noise. The device with three partial normal metal bars also showed significant variation in both the $1/f$ noise and phonon noise, this time with a minimum at 40 µT. The spectra for this device are presented in Figure 6.39d.

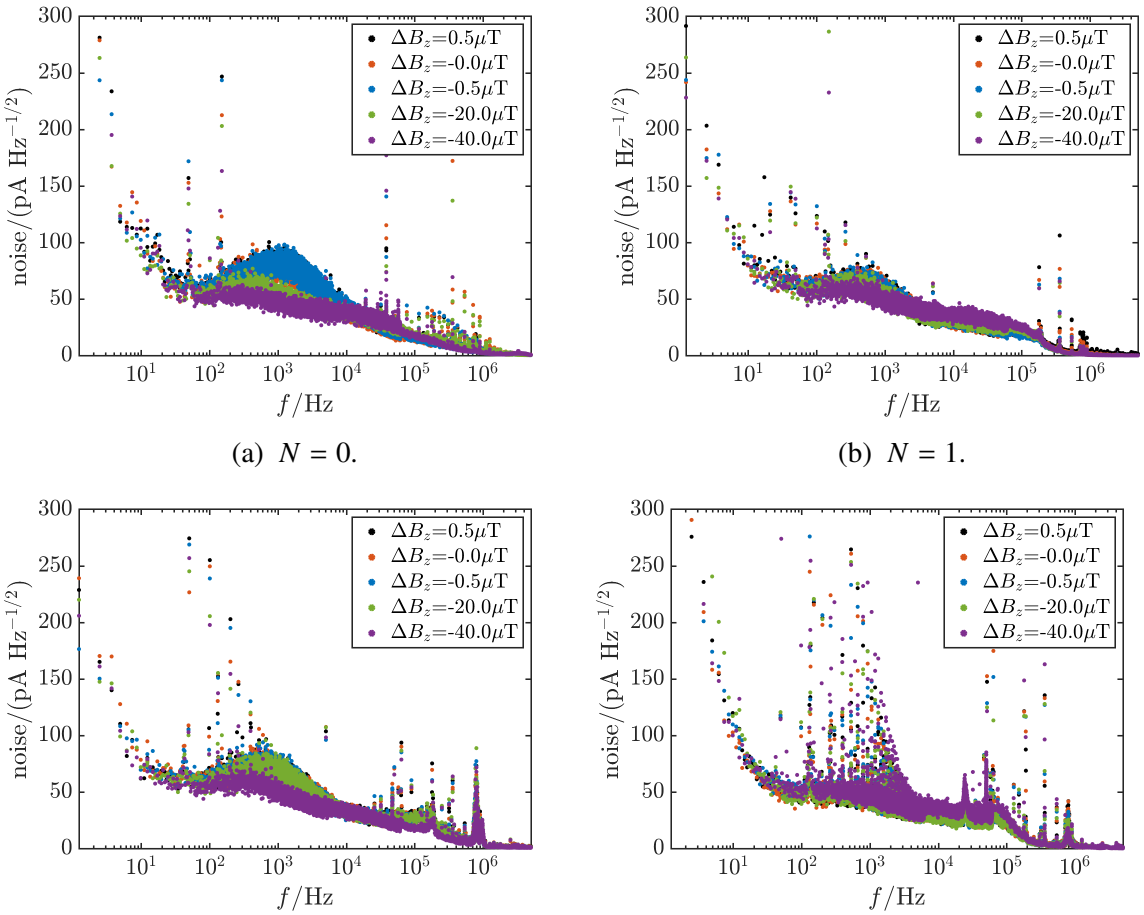

(a) $N = 0$. (b) $N = 1$.

(c) $N = 2$. (d) $N = 3$.

Figure 6.38 Noise as a function of frequency, for a series of different magnetic fields, for four TESs with bilayer side length 40 µm and varying numbers of partial bars N. All spectra were taken at a bias point of 30 % R_n and at the base temperature of around 65 mK.

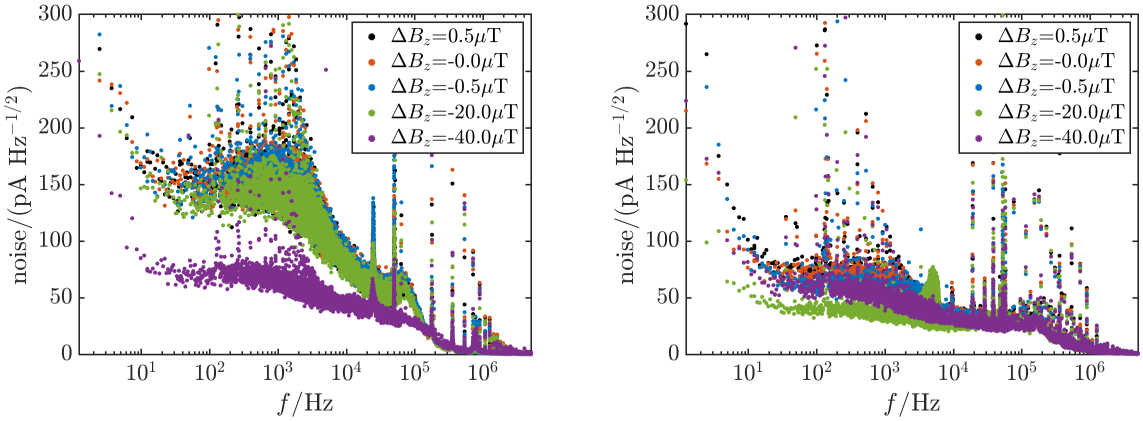

(a) $N = 0$.

(b) $N = 1$.

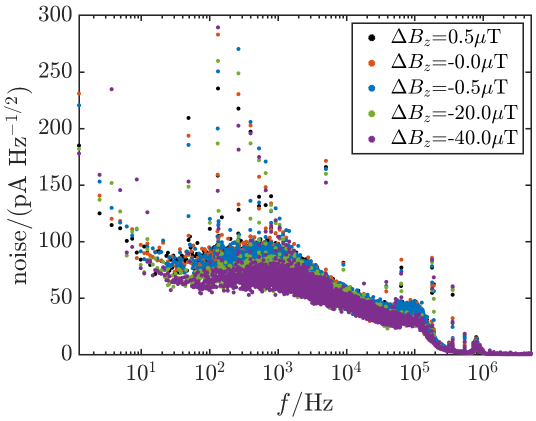

(c) $N = 2$.

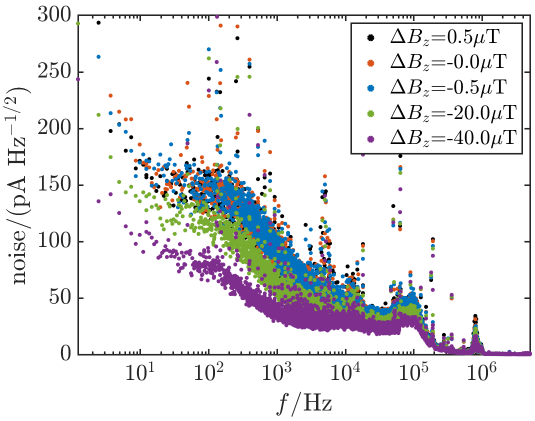

(d) $N = 3$.

Figure 6.39 Noise as a function of frequency, for a series of different magnetic fields, for four TESs with bilayer side length 10 µm and varying numbers of partial normal metal bars N. All spectra were taken at a bias point of 30 % R_n and at the base temperature of around 65 mK.

6.4 Conclusions

This is the first systematic study of the effects of bilayer geometry on magnetic field dependence, allowing me to fully investigate which geometries produce TESs with the greatest insensitivity to applied fields. Unexpectedly, the devices with the smallest bilayers, and hence the least magnetic flux for a given field strength, showed the largest changes in magnitude of I_{TES}, bias point and T_{c} with field, but the smallest changes in I_{c}. I_{c} is measured at zero bias voltage, whilst all of the other measurements are carried out under voltage bias, and so there is a change in behaviour depending on whether or not TESs are operated under voltage bias. Since TESs are voltage biased under normal operating conditions, measurements taken under voltage bias are more reflective of the expected device behaviour.

An updated summary, including magnetic field dependence, of the effects of varying the bilayer size and number of partial normal metal bars can be shown in Table 6.2. Desirable effects have been highlighted in blue, whilst undesirable effects are shown in red. Both larger and smaller bilayer areas have advantages and disadvantages. Although the devices with larger bilayers have slightly longer response times, all of the TESs have comparably fast response times compared to devices with absorbers.

One of the goals of this thesis was to investigate whether there is an optimal bilayer geometry for a TES, and investigate design trade offs. Although TESs with smaller bilayer areas showed the greatest variation in bias current with applied field, these TESs also displayed behaviour that was more consistent with our current understanding of how TESs work, with no features that indicate phase slip behaviour. On the other hand, the TESs with larger bilayer areas showed lower noise and sharper transitions, as well as less variation in bias point when magnetic fields were applied, meaning these devices had greater sensitivity and lower magnetic field dependence. Although there was no bilayer design that optimises all of the parameters, devices with 20 µm side length bilayers were found to give a good compromise between low noise, fast response and reasonable transition temperature. The benefit of normal metal patterning is less apparent, as adding bars tended to considerably reduce the magnetic field dependence and excess noise of the TESs, but also broadens the transition width and makes the device behaviour less predictable.

Some device properties showed significant variations depending on whether the bilayer had an odd or even number of partial normal metal bars, which will affect the self-field of the device, as seen in Section 2.4.3. Bilayers with odd numbers of partial normal metal bars produced slower TESs that were less sensitive to magnetic fields. These differences were particularly pronounced for devices with larger bilayer areas. There is a trade off between speed and insensitivity to field effects.

Table 6.2 Effect of bilayer geometry on key device performance metrics. Desirable effects are highlighted in blue; undesirable effects are highlighted in red. Any numerical changes refer to the difference between the extremes of the bilayer geometries/applied fields, unless otherwise stated.

Parameter	Effect of decreasing bilayer size	Effect of adding bars to 40 µm side length device	Effect of adding bars to 10 µm side length device
T_c	Increases by a factor of 1.4	No noticeable effect	Decreases by a factor of 1.4
ΔT_c when field of 40 µT applied	More effect. 13 % reduction for 10 µm side length device compared to 3 % reduction for 70 µm side length device	Less effect. Less than 1 % reduction compared to 3 % reduction	Less effect. 8 % reduction compared to 13 % reduction
Transition width	Broadens	Broadens when one bar added, then no further variation	No obvious trend
ΔR_0 when field of 40 µT applied	More effect. 15 % change compared to 5 % change	Less effect. Less than 1 % change compared to 5 % change	No noticeable effect
Heat capacity	Decreases	Increases	Increases
Noise	Increases by a factor of up to 3, especially $1/f$ noise	Suppression of excess noise by a factor of 2	Some suppression of excess noise
τ	Faster (by a factor of 4) response until 20 µm, then response gets slower by a factor of 2	Slower (by a factor of 2) response for 2+ bars	Slower (by a factor of up to 3) response, especially for 3 bars
$\Delta\tau$ when field of 40 µT applied	Less effect.	Less effect. No change in τ with field for patterned device	Less effect. No change in τ with field for patterned device
Agreement with models	Better agreement	Less agreement	No noticeable effect
R_n	Decreases by a factor of 4	Slightly decreases	Slightly decreases
G	Decreases by a factor of up to 1.4	Decreases by a factor of up to 1.4	Decreases by a factor of 1.6
n	No obvious trend	Slight general decrease	No obvious trend

Minima and maxima were observed in the TES current as the magnetic field was varied, but the TESs did not become fully normal, although their bias point was altered. This contradicts the assumption made in my proximity effect model that TESs become normal when an integer number of magnetic flux quanta pass through the bilayer, implying that other phenomena, such as the self-field effects of the bilayer, have a significant influence on device behaviour. It also explains the observation in Section 2.4.2 that despite the magnetic field produced by the surrounding wiring producing a large enough flux to drive TESs normal, no group has reported TESs that do not superconduct as a result of the effect of the wiring.

In this chapter, I also presented the first measurements of the directional field dependence of TESs, which give valuable insights into the magnetic field directions that have the greatest impact on TES behaviour. These measurements could be used to test the effectiveness of passive magnetic shielding or active magnetic field cancellation, as clear asymmetries in the TES response surface are visible for stray fields of less than 1 μT. I carried out a decomposition of the field response surface in a spherical harmonic basis, which could be used to compare the shielding requirements of a TES to the reduction in field produced by a particular shield design. The representation in a spherical harmonic basis showed that TESs are sensitive to in-plane as well as out-of-plane fields.

All the measurements in this chapter show that applied magnetic fields have a significant impact on TES performance, reducing transition temperature, device sensitivity and critical current. It is therefore desirable to operate TESs within a magnetic shield to reduce the field experienced by the sensors, and I will investigate a possible magnetic shield design in the next chapter.

Chapter 7

On-chip shielding of Mo/Au TESs

7.1 Introduction

Magnetic fields significantly alter TES performance, especially when normal to the plane of the device. In order to achieve good performance, TESs must be shielded from magnetic fields during operation. This is typically carried out using large and bulky passive magnetic shields, significantly increasing the mass of the TES instrument. In this chapter, I carry out the very first experimental and theoretical investigations of a new shielding concept. I present a design for a thin-film planar magnetic shield that is lithographically integrated very close to the detectors, to attenuate the perpendicular magnetic field component without a large increase in instrument mass. If such an on-chip shield could provide a significant reduction in field, thereby reducing the sensitivity of the TESs to external magnetic fields, it would relax the shielding requirements for the TES instrument. This would in turn allow a reduction of the total mass and volume of the instrument and would make it easier to stay within assembly constraints.

This on-chip, thin-film magnetic shield would be similar to the backing plates used for infra-red TESs, which provide an impedance-matched backstop to improve the absorption of the incident radiation. This design allows the shield to be positioned within tens of microns of the TES. As well as providing magnetic shielding, this on-chip shield must also be designed to have minimal impact on other aspects of TES performance, such as device noise and response time. The design considerations depend on the wavelength of interest: for example, when detecting infra-red radiation, the shielding must be integrated with the reflective backstop. The shield should have a low surface impedance so that it acts as a mirror, and the distance between the TES and the shield should be chosen to maximise the absorption efficiency.

Firstly, I describe the models that I used to inform the design of the on-chip shield. I present a model using the method of image dipoles to estimate the shielding factors for two different designs in Section 7.2. In Section 7.3, I then describe the selection of the materials that could

be used to make an on-chip shield, using a transmission line model to calculate the expected infra-red reflection coefficients for potential material combinations. This enables me to select materials that would provide good absorber matching for TESs that will be used to detect infra-red radiation, in order to produce an on-chip shield that can also act as a reflective backstop. In Section 7.4 I describe the production of an on-chip shield, detailing the development of a mask and the process route used. Finally, in Section 7.5 I present the results of a series of experiments to characterise the magnetic field behaviour of TESs with on-chip shielding, allowing me to determine the experimental reduction in field that is possible using this new shielding concept.

7.2 Modelling of on-chip shielding

In order to model the effects of an on-chip shield, the method of image dipoles was used. This is analogous to the method of image charges in electrostatics, as shown in Table 7.1.

Table 7.1 Comparison between the method of image charges used in electrostatics and the method of image dipoles used to model the effects of an on-chip shield.

Method of image charges	**Method of image dipoles**
Used to model an electrostatic charge near an infinite conducting plane	Used to model a magnetic dipole near an infinite superconducting plane
Tangential component of electric field is zero at the plane	Normal component of magnetic field is zero at the plane
Conducting plane is modelled by an image charge of opposite sign	Superconducting plane is modelled by an image dipole with its component normal to the plane reversed

The on-chip shield was modelled as an infinite superconducting plane, neglecting edge effects. For this to be a reasonable assumption, I therefore wanted to ensure that the shield extends well past the area of the TES bilayer.

In order to use the method of image dipoles, all field sources must be represented as dipoles. The field produced by a dipole is given by

$$\mathbf{B}(\mathbf{r}) = \frac{\mu_0}{4\pi}\left[\frac{3\mathbf{r}(\mathbf{m}\cdot\mathbf{r})}{r^5} - \frac{\mathbf{m}}{r^3}\right], \tag{7.1}$$

where $\mathbf{m}$ is the magnetisation of the dipole and $\mathbf{r}$ is the displacement vector between the dipole and the point where the field is being calculated.

There are two potential sources of magnetic fields: stray fields from external sources, and fields produced by current flow within the TES. In this modelling work, I neglect the fields

due to the TES bias currents and focus on the shielding of external magnetic fields. I use a magnetic dipole to represent each external magnetic field source. This allows straightforward modelling and can be easily generalised to include as many external field sources as required.

I applied this model to describe the specific case of the near-uniform field produced by the magnetic field test system, as described in Section 4.6. I used a single equivalent dipole to model the field, and calculated the field at the TES bilayer to assess the uniformity, in order to ensure that this model produced an appropriate approximation to the field from the coils.

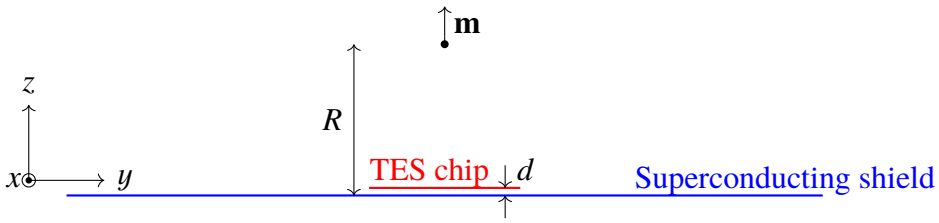

Figure 7.1 Configuration of the model used to assess the uniformity of the field produced by a dipole to see whether it gives an accurate representation of the field generated by the superconducting coils in my test system. $\mathbf{m} = (0, 0, m)$= (0,0,1 $\times$ 10^{-13}) Am^2 is the magnetic moment of the model dipole, R = 13.5 mm is the distance between the model dipole and the superconducting shield, and d is the distance between the TES bilayer and the shield. In this first model the effects of the superconducting shield are not included. The coordinate system used is indicated to the left of the figure.

Figure 7.1 shows the configuration used to ensure the model dipole representing the superconducting coils produces a uniform field of the correct magnitude. The distance between the model dipole and the superconducting plane R is set to the distance between the coil and the TES bilayer, and then the value of the magnetisation m is adjusted so the field at the TES bilayer is of the order of tens of μT. The field is calculated over the 5.5 mm square region of the chip occupied by the TESs.

The field produced by this model dipole is reasonably uniform, as shown in Figure 7.2. The arrows representing field direction in Figure 7.2a are all entirely in the z direction, whilst the field magnitude in the z direction varies in the region occupied by the TESs, as seen in Figure 7.2b. The field value of about 50 μT is typical of the fields produced by the superconducting coils, and so I conclude that using this model dipole to represent the uniform field from the coils is a good approximation.

Next, I modelled the field experienced by the TESs when a superconducting shield is placed behind the TES wafer. Figure 7.3 shows the configuration of the model including the effects of the superconducting on-chip shield. The image dipole representing the superconducting shield has magnetic moment $-\mathbf{m} = (0, 0, -m)$.

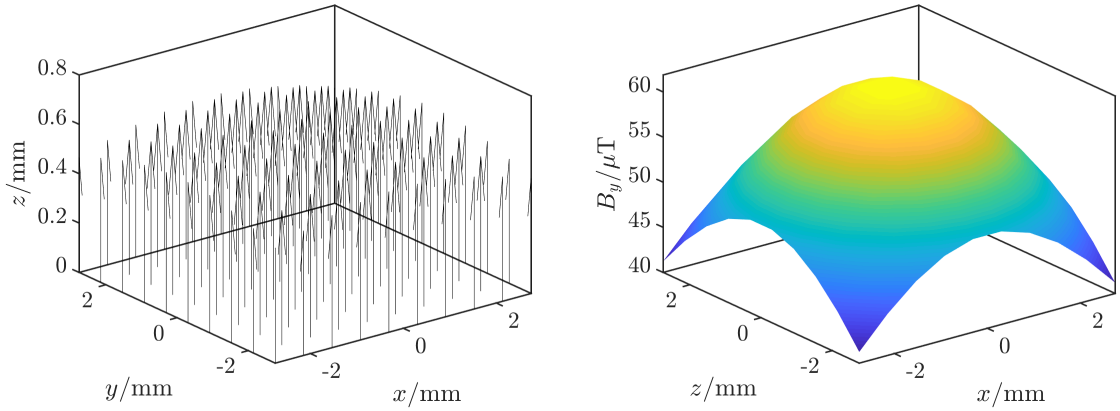

(a) (b)

Figure 7.2 Magnetic field produced by a dipole of magnetisation $(0,0,1 \times 10^{-13})$ Am^2 a distance R = 13.5 mm above the backing plate in the z direction. (a) shows the direction of the field and (b) shows the magnitude of its z component. The calculation was carried out over the central region of the chip, which is the region occupied by the TESs.

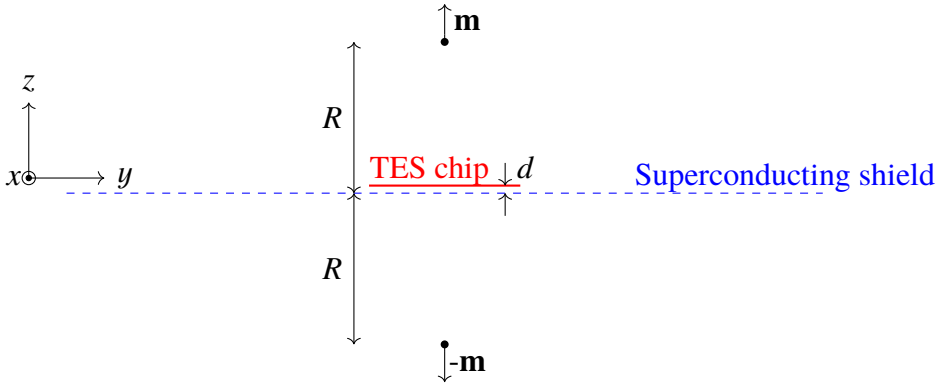

Figure 7.3 Configuration of the model used to examine the effectiveness of a superconducting on-chip shield at reducing the field experienced by the TESs. The field-generating coils are modelled by a dipole of magnetic moment $\mathbf{m} = (0, 0, m) = (0,0,1 \times 10^{-13})$ Am^2, whilst the image dipole representing the superconducting on-chip shield has magnetic moment $-\mathbf{m} = (0, 0, -m) = (0,0,-1 \times 10^{-13})$ Am^2. R = 13.5 mm is the distance between the model/image dipole and the superconducting plane, and d is the distance between the TES bilayer and the superconducting plane. The coordinate system used is indicated to the left of the figure.

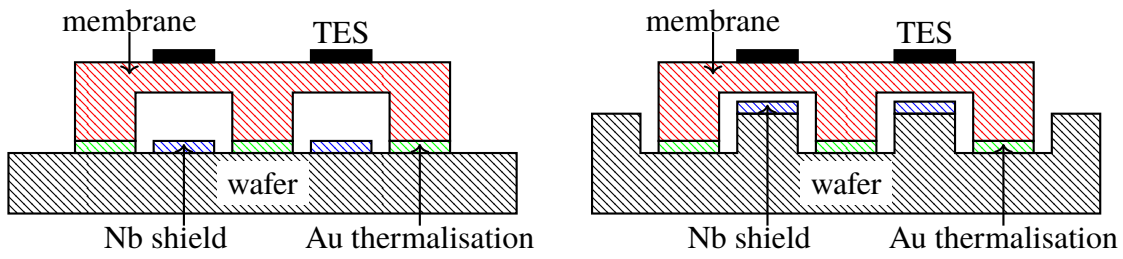

Figure 7.4 Two possible designs for an on-chip shield for membrane-suspended TESs. The TES chip has a Au thermalisation layer on the base of the membrane. (a) shows a design using a Si wafer, where the Nb shields are deposited onto the wafer and patterned using lithography. The typical shield-TES distance is of the order of 225 µm. (b) shows a design using a silicon-on-insulator (SOI) wafer, where the Nb shields are deposited onto the wafer and patterned using lithography. A top-down DRIE etch is then used to remove the remaining silicon. The typical shield-TES distance is of the order of 21 µm.

Two possible designs for an on-chip shield for membrane-suspended TESs were considered, as shown in Figure 7.4. For unreleased TESs, the on-chip shield would need to be placed below the silicon wafer. Figure 7.4a shows the design using a unpatterned silicon wafer, where Nb shields are deposited on the wafer and patterned using lithography. The typical shield-TES distance is of the order of 225 µm. Figure 7.4b shows the design using a silicon-on-insulator (SOI) wafer. In this case, the Nb shields are again deposited and patterned using lithography. However, since the SOI wafer consists of a layer of Si on top of a SiO_2 etch stop, the silicon can be etched away to leave raised pillars. Three SOI wafers were easily available, giving possible TES - shield separations of 10 µm, 21 µm and 35 µm. The wafer giving a TES - shield separation of 21 µm was selected, giving a compromise between a small TES - shield separation and a low risk of collision between the TES and the shield in mounting and alignment. The TESs are raised by 500 µm due to the underlying wafer, and so the fan-out boards must be raised by the same height to allow easy wiring.

Figure 7.5 shows the magnetic field across the TESs using the shield design in Figure 7.4a, where the TES - shield separation is 225 µm. The presence of the superconducting shield reduces the field to 10 % of its original value, as shown in Figure 7.5b. The z magnetic field strength becomes more similar to the x and y magnetic field strength, as shown in the left hand plot, where the arrows showing field direction no longer point uniformly in the z direction. Figure 7.6 shows the magnetic field using the shield design in Figure 7.4b, where the TES - shield separation is 21 µm. Here the superconducting shield reduces the magnetic field to 1 % of its original value. This is an encouraging result as it shows that high levels of shielding are in principle possible with this on-chip shield design, and that experimental measurements

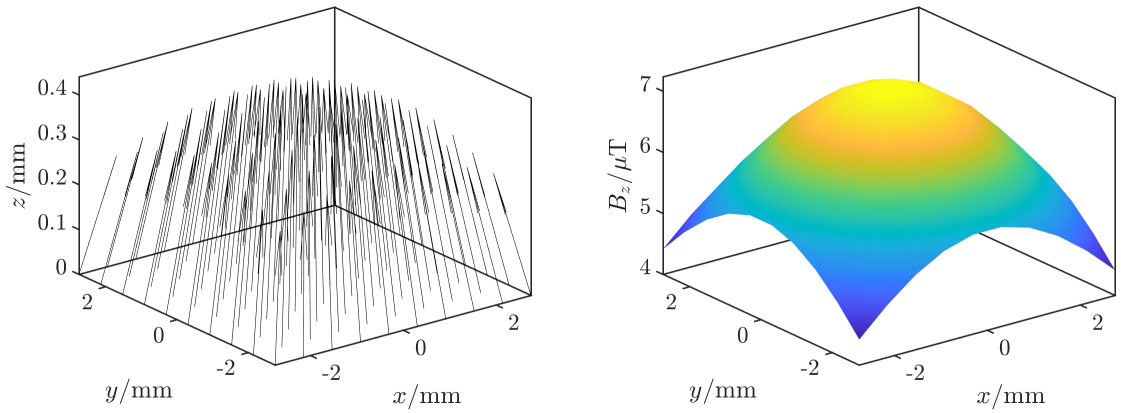

(a) (b)

Figure 7.5 Magnetic field produced by a dipole of magnetisation $(0,0,1 \times 10^{-13})$ Am^2 a distance 13.5 mm above the backing plate in the z direction, and an image dipole of magnetisation $(0,0,\text{-}1 \times 10^{-13})$ Am^2 a distance R=13.5 mm below the backing plate, representing the backing plate being made of a superconducting material. (a) shows the direction of the field and (b) shows the magnitude of its z component. The TES - backing plate separation d=225 µm. The calculation was carried out over the central region of the chip, which is the region occupied by the TESs.

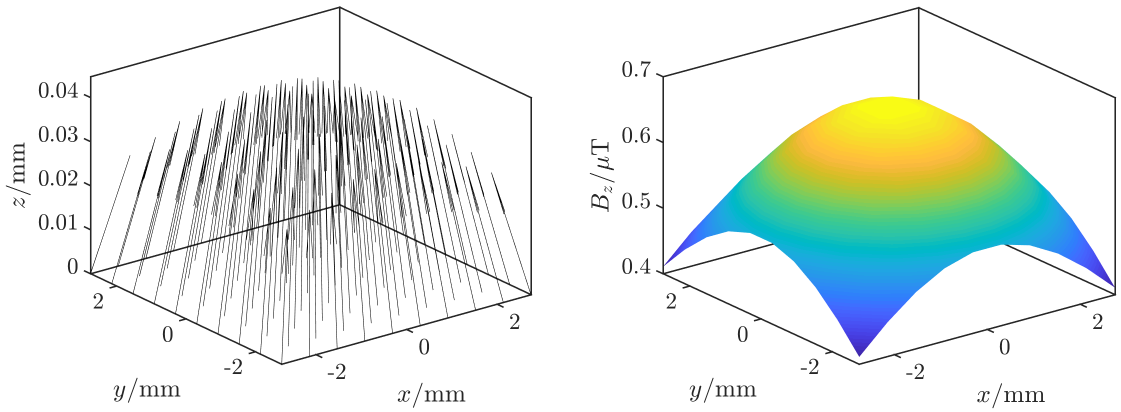

(a) (b)

Figure 7.6 Magnetic field produced by a dipole of magnetisation $(0,0,1 \times 10^{-13})$ Am^2 a distance 13.5 mm above the backing plate in the z direction, and an image dipole of magnetisation $(0,0,\text{-}1 \times 10^{-13})$ Am^2 a distance R=13.5 mm below the backing plate, representing the backing plate being made of a superconducting material. (a) shows the direction of the field and (b) shows the magnitude of its z component. The TES - backing plate separation d=21 µm. The calculation was carried out over the central region of the chip, which is the region occupied by the TESs.

should be carried out to determine the level of shielding the can be achieved in practice. For the experimental study, the design using a SOI wafer, was used to make the backing plates, as it has the potential to demonstrate a very significant reduction in perpendicular field.

7.3 Selection of materials for on-chip shielding

The material combination for a good on-chip shield should have two main properties:

1. No (or low) magnetic flux threading, for effective magnetic shielding.

2. No effect on the primary behaviour of the TES, meaning that the detector can still couple to the wavelength it is trying to detect. For example, at infra-red wavelengths, the material combination should have high reflectance of the radiation of the wavelengths of interest, allowing the shield to also act as a reflective backstop for the incident radiation.

The first property means that using a superconductor or high-permeability metal is desirable. The superconductor should be operating well below its critical field and its transition temperature. Two superconductors were considered: aluminium and niobium. Aluminium is a type-I superconductor with a critical field of the order of hundreds of mT [178], well above the maximum field used in these studies. As its transition temperature is 1.2 K, it will be a superconductor at the operating temperature of the TESs. Niobium also meets these specifications as it is a type-II superconductor with a lower critical field of the order of hundreds of mT [179], and a transition temperature above 7.5 K.

It may be desirable to use a multilayered shield to optimise performance. To prevent trapped flux, a high-permeability metal could be layered with a superconductor, adding a thin layer of gold for oxidation protection. To enhance the reflection coefficient of the on-chip shield and improve its impedance-matching, layers of high-reflectivity metal could be added to increase the reflection coefficient.

7.3.1 Model of reflection coefficient of possible on-chip shield designs

A good reflective backstop should have a power reflection coefficient with magnitude close to 1, so nearly all of the incident power is reflected back towards the TES. To calculate the reflection coefficient Γ of the shield, I used a transfer matrix approach [180]. This approach meant that I could combine the transfer matrices for multiple individual film layers to investigate multilayered shields as well as single-layer shields.

Figure 7.7 shows the configuration used for the calculation of the transfer matrix linking the fields at point z_1 to the point z_2, through a single film layer of uniform conductance. The

basis is chosen so that the electric field is in the x direction and the magnetic field is in the y direction. I assume the substrate is silicon, which has impedance $Z_{\mathrm{Si}} = \sqrt{\mu/\epsilon} \approx 0.29 Z_0$ [117], and that this substrate is sufficiently thick that there is no reflected wave. Therefore, on the lower side of the film, E_1/H_1 is known and is equal to Z_{Si}.

On the surface of the film, $E_2 = E_i + E_r$ and $H_2 = (E_i - E_r)/\mu_0$. Additionally, $E_r = \Gamma E_i$, where Γ is the reflection coefficient. The ratio of E_2 and H_2 gives me an expression containing Γ,

$$\frac{E_2}{H_2} = \frac{E_i + E_r}{\frac{E_i - E_r}{Z_0}} = \frac{1+\Gamma}{\frac{1-\Gamma}{Z_0}}, \tag{7.2}$$

which can be rearranged for Γ,

$$\Gamma = \frac{E_2/H_2 - Z_0}{E_2/H_2 + Z_0}. \tag{7.3}$$

Once the ratio E_2/H_2 is known, then Γ can be calculated.

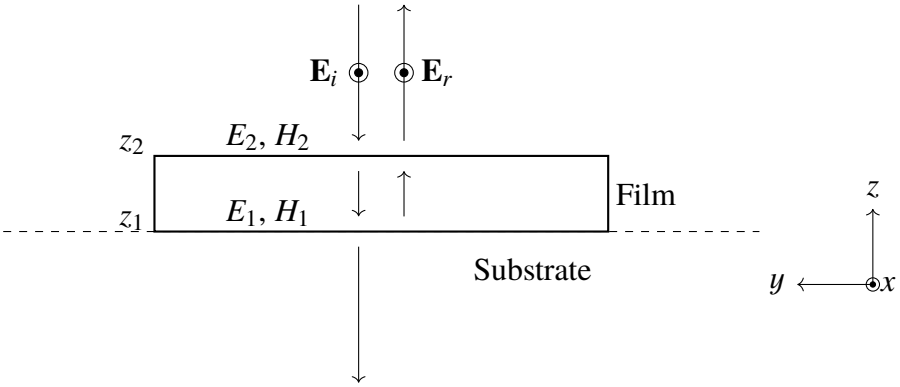

Figure 7.7 Configuration assumed for the calculation of the transfer matrix for a single layer of the film, located between z_2 and z_1. The fields $\mathbf{E}_a = (E_{x,a}, 0, 0)$ and $\mathbf{H}_a = (0, H_{y,a}, 0)$. The impedance at z_1 is assumed to be $E_1/H_1 = Z_{\mathrm{Si}}$, and so if the transfer matrix linking E_1 and H_1 to E_2 and H_2 is known, $Z = E_2/H_2$ and hence the reflection coefficient $\Gamma = (Z - Z_0)/(Z + Z_0)$ can be calculated.

For a multilayered structure, the transfer matrices can be combined to represent transmission through the full structure,

$$\begin{pmatrix} E_2 \\ H_2 \end{pmatrix} = \left[\prod_{\text{all layers,a}} \mathbf{M}_a \right] \begin{pmatrix} E_1 \\ H_1 \end{pmatrix}. \tag{7.4}$$

where $\mathbf{M}_a$ is the transfer matrix for propagation through a single layer a of the shield.

The calculation of the transfer matrices starts with the following Maxwell equations, using the shorthand ∂_t to represent $\partial/\partial t$,

$$\nabla \times \mathbf{E} = -\mu \partial_t \mathbf{H} \tag{7.5}$$

$$\nabla \times \mathbf{H} = \mathbf{J} + \epsilon \partial_t \mathbf{E}, \tag{7.6}$$

where $\mathbf{J} = \sigma \mathbf{E}$. Assuming $\mathbf{H}$ and $\mathbf{E}$ exhibit an $e^{i\omega t}$ time dependence,

$$\nabla \times \mathbf{E} = -i\omega\mu \mathbf{H} \tag{7.7}$$

$$\nabla \times \mathbf{H} = \sigma \mathbf{E} + i\omega\epsilon \mathbf{E}. \tag{7.8}$$

Given that $\mathbf{E}_a = (E_{x,a}, 0, 0)$ and $\mathbf{H}_a = (0, H_{y,a}, 0)$, and that fields are assumed to only vary in the z direction, the only non-zero terms are the x-component of $\mathbf{E}$, the y-component of $\mathbf{H}$, and their partial derivatives with respect to z. The equations (7.7) therefore simplify to give

$$\partial_z E_{x,a} = -i\omega\mu H_{y,a} \tag{7.9}$$

$$\partial_z H_{y,a} = -(\sigma + i\omega\epsilon) E_{x,a}, \tag{7.10}$$

expressed in matrix form as

$$\partial_z \begin{pmatrix} E_{x,a} \\ H_{y,a} \end{pmatrix} = \begin{pmatrix} 0 & i\omega\mu \\ \sigma + i\omega\epsilon & 0 \end{pmatrix} \begin{pmatrix} E_{x,a} \\ H_{y,a} \end{pmatrix}. \tag{7.11}$$

For the matrix $\mathbf{A} = \begin{pmatrix} 0 & i\omega\mu \\ \sigma + i\omega\epsilon & 0 \end{pmatrix}$, the eigenvalues λ_i and corresponding eigenvectors $\mathbf{u}_i$ are

$$\lambda_1 = \gamma, \qquad \mathbf{u}_1 \propto \begin{pmatrix} \eta \\ 1 \end{pmatrix} \tag{7.12}$$

and

$$\lambda_2 = -\gamma, \qquad \mathbf{u}_2 \propto \begin{pmatrix} -\eta \\ 1 \end{pmatrix}, \tag{7.13}$$

where $\gamma^2 = i\omega\mu(\sigma + i\omega\epsilon)$ and $\eta = i\omega\mu/\gamma$.

For a pure dielectric, $\sigma = 0$ and $\gamma = i\omega c$, where $c = 1/\sqrt{\mu\epsilon}$ is the speed of light. In this limit, $\eta = \sqrt{\mu/\epsilon}$ as expected.

Transforming to the eigenvector basis,

$$\begin{pmatrix} E_{x,a} \\ H_{y,a} \end{pmatrix} = \begin{pmatrix} \eta & -\eta \\ 1 & 1 \end{pmatrix} \begin{pmatrix} u_1 \\ u_2 \end{pmatrix}, \tag{7.14}$$

inverting this gives

$$\begin{pmatrix} u_1 \\ u_2 \end{pmatrix} = \frac{1}{2\eta} \begin{pmatrix} 1 & \eta \\ -1 & \eta \end{pmatrix} \begin{pmatrix} E_{x,a} \\ H_{y,a} \end{pmatrix} \tag{7.15}$$

and overall

$$\frac{1}{2\eta} \begin{pmatrix} 1 & \eta \\ -1 & \eta \end{pmatrix} \mathbf{A} \begin{pmatrix} \eta & -\eta \\ 1 & 1 \end{pmatrix} = \begin{pmatrix} \gamma & 0 \\ 0 & -\gamma \end{pmatrix}. \tag{7.16}$$

Equation (7.11) is transformed to

$$\partial_z u_1 = -\gamma u_1 \tag{7.17}$$

$$\partial_z u_2 = \gamma u_2. \tag{7.18}$$

Solving these,

$$\ln u_1(z_2) - \ln u_1(z_1) = -\gamma(z_2 - z_1) \tag{7.19}$$

and hence

$$u_1(z_2) = \mathrm{e}^{-\gamma(z_2 - z_1)} u_1(z_1). \tag{7.20}$$

Rotating the basis back,

$$\begin{pmatrix} E_x(z_2) \\ H_y(z_2) \end{pmatrix} = \begin{pmatrix} \eta & -\eta \\ 1 & 1 \end{pmatrix} \begin{pmatrix} \mathrm{e}^{-\gamma(z_2 - z_1)} & 0 \\ 0 & \mathrm{e}^{\gamma(z_2 - z_1)} \end{pmatrix} \frac{1}{2\eta} \begin{pmatrix} 1 & \eta \\ -1 & \eta \end{pmatrix} \begin{pmatrix} E_x(z_1) \\ H_y(z_1) \end{pmatrix}. \tag{7.21}$$

Defining $\Delta = z_2 - z_1$,

$$\begin{pmatrix} E_x(z_2) \\ H_y(z_2) \end{pmatrix} = \begin{pmatrix} \cosh(\gamma\Delta) & -\eta \sinh(\gamma\Delta) \\ -\sinh(\gamma\Delta)/\eta & \cosh(\gamma\Delta) \end{pmatrix} \begin{pmatrix} E_x(z_1) \\ H_y(z_1) \end{pmatrix}, \tag{7.22}$$

so the transfer matrix required for Equation (7.4) is

$$\mathbf{M}_a = \begin{pmatrix} \cosh(\gamma\Delta) & -\eta \sinh(\gamma\Delta) \\ -\sinh(\gamma\Delta)/\eta & \cosh(\gamma\Delta) \end{pmatrix}. \tag{7.23}$$

Using the overall transfer matrix, built up from the product of the individual transfer matrices for each layer, the reflection coefficient can be calculated for a given film configuration. Figure 7.8 shows the reflection coefficients as a function of layer thickness, calculated for infra-red

radiation of wavelength 3 µm, for three possible shield configurations - the black line is for pure Nb, the red line is for pure Al and the blue line is for a multilayered structure of SiO_2 with 150 nm Au on top and 150 nm Nb underneath, to investigate whether there are any significant improvements in the reflection coefficient for such a structure.

All material combinations give very good reflection coefficients, close to the target value of -1, especially for thicknesses larger than 50 nm. Initially, for simplicity of manufacture, I therefore decided to use a pure superconductor. Since the system used for testing is held at 4 K using a pulse tube cooler and an adiabatic demagnetisation refrigerator is used to cycle down to 60 mK, the Al shield would pass through its resistive transition on each cycle, changing the magnetic field conditions. To avoid this, pure Nb was used to make the shield, as its T_c is well above the base temperature of the pulse tube cooler, and Nb will remain superconducting throughout thermal cycling. A thickness of 300 nm was used to ensure the film was much thicker than the penetration depth of the material.

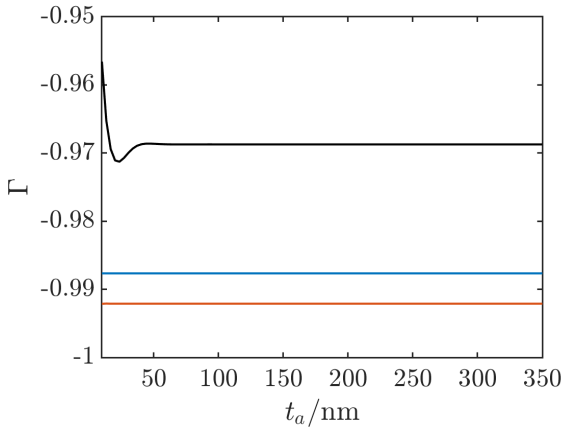

Figure 7.8 Reflection coefficient Γ as a function of thickness for different shield material combinations: pure Nb (black), pure Al (red), and a multilayered structure of SiO_2 with 150 nm Au on top and 150 nm Nb underneath (blue). All calculations were carried out for radiation of wavelength 3 µm. Data on material conductivities collected by the Quantum Sensors Group.

7.4 Design of on-chip shield

The processing route used had two steps - firstly, a 300 nm thick layer of niobium was deposited and patterned by lift off, and secondly, a layer of photoresist was deposited and DRIE was used from the top side to remove the remaining material.

I designed the mask for the processing using KLayout, adapting my Python code described in Section 4.4 to automatically generate and scale pillar designs. The SOI wafer used was 4" in

diameter, allowing the manufacture of 30 different chips with a variety of pillar designs. The two basic designs used are shown in Figure 7.9, with design (a) featuring pillars the same shape as the well, reduced by a scaling factor, and design (b) featuring diamond-shaped pillars. In total, five types of chip were made, with six copies of each chip, labelled as follows:

1. Pillar same shape as well, dimensions reduced to 70 % of the full well size. Minimum 20 µm spacing between the pillar and the side of the well.

2. Pillar same shape as well, dimensions reduced to 50 % of the full well size. Minimum 40 µm spacing between the pillar and the side of the well.

3. Diamond pillar, dimensions reduced to 80 % of the full well size. Minimum 12 µm spacing between the pillar and the side of the well.

4. Diamond pillar, dimensions reduced to 70 % of the full well size. Minimum 20 µm spacing between the pillar and the side of the well.

5. Diamond pillar, dimensions reduced to 50 % of the full well size. Minimum 40 µm spacing between the pillar and the side of the well.

The smaller pillars are less risky to align, since a larger alignment error is needed for the pillar to knock the edge of the TES chip. The larger pillars are riskier to align but will provide more effective shielding, and so a chip with larger pillars was tested first, with the chips with smaller pillars as backup.

Two chip designs are shown in Figure 7.10, (a) with type 1 pillars and (b) with type 3 pillars. The top-down DRIE step meant that labelling the individual chips was not possible, and so instead a pillar was deliberately omitted from the second row to allow the different types of chip to be distinguished. Chips of type 1 had the first pillar omitted, chips of type 2 had the second pillar omitted and so on. In addition to this, a grid system was used to label the chips, as shown in the full mask design in Figure 7.11. In this figure, the white regions were removed in the DRIE step, and the black dicing marks allowed the chips to be diced out.

Figure 7.12 shows a type 1 backing plate post-processing, with the deliberately omitted pillar in the second row. Apart from these, the yield of the pillars was 100 % for all of the backing plates. Following cleaning, a mounting test was carried out using a spare TES chip and a spare backing plate, to ensure that there was good clearance between the TES and the top of the niobium as well as reasonable separation between the pillar and the edge of the well. Figure 7.13 shows a close up of one of the TESs used for the mounting test. The silver-grey region behind the TES is the Nb shielding layer on top of the pillar. There is some residue left on the niobium, visible as black features, which was not removed by cleaning with acetone. Normally such a residue would be removed by ultrasonic cleaning, but in order to ensure a high yield of

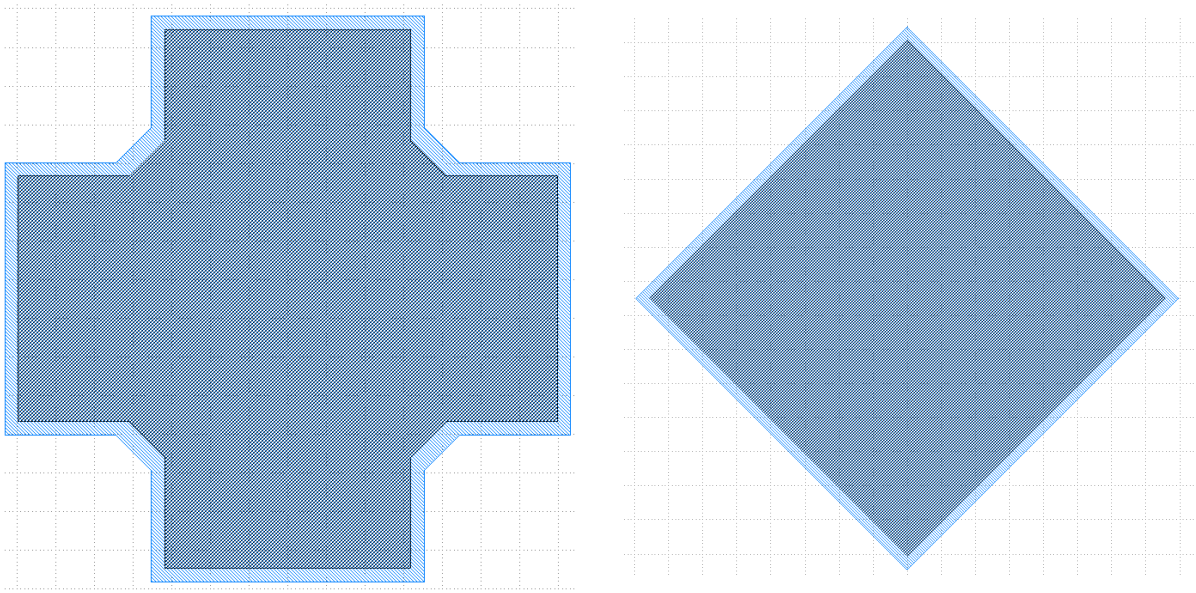

(a) (b)

Figure 7.9 Two types of pillar designs used for the raised on-chip shield. In (a) the pillar is of type 1, the same shape as the well, reduced to 70 % of the full well size. In (b) the pillar is of type 3, diamond-shaped and reduced to 80 % of the full well size. The dark blue region indicates where Nb was deposited; the light blue region shows where resist was patterned prior to DRIE.

pillars, this processing step was omitted for this chip. The pillar is not perfectly central in the well because in order to image the TES, the backing plate and TES chip had to be taken out of the jig used for alignment. Even without the jig for alignment, the shielding layer still covers the whole area of the TES.

7.5 TES measurements

Key magnetic field measurements from Section 6.3 were repeated for four TESs. The devices chosen were a TES with an unpatterned 40 µm side length bilayer, a TES with an unpatterned 10 µm side length bilayer, a TES with a bilayer of area 10 µm side length and three partial normal metal bars and a TES with an unpatterned 5 µm side length bilayer. This set of TESs meant that the effect of on-chip shielding on devices with a range of different bilayer geometries could be studied.

Although not shown in the following figures, the coil current required to achieve zero perpendicular field was twice as large for the shielded TESs compared to that for the unshielded TESs, indicating a larger background field. This is likely to be due to trapped flux in the Nb

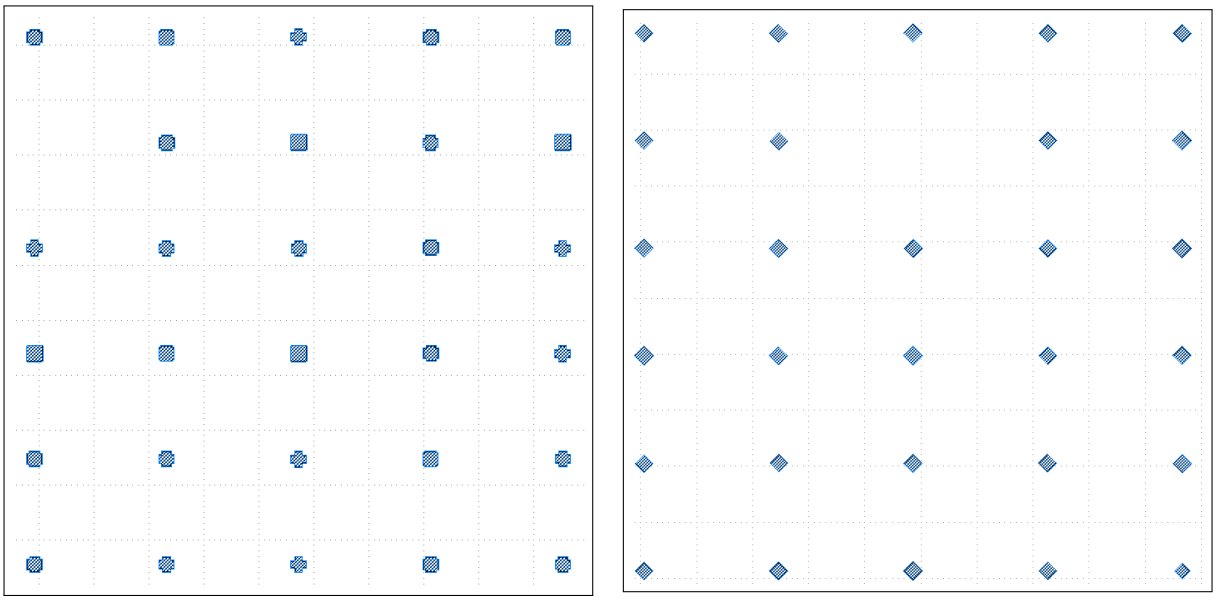

(a) Type 1 chip.

(b) Type 3 chip.

Figure 7.10 Central regions of two chip designs, using the pillar designs from Figure 7.9. Since the top-down DRIE removed any labelling, a pillar was deliberately omitted from the second row, to allow the different types of chip to be distinguished. Chips of type 1 had the first pillar omitted, chips of type 2 had the second pillar omitted and so on. No devices on the second row were required for the tests described in this thesis.

shielding [181, 182], since the system did not allow cooling under zero-field conditions, a theory that is supported by the fact that the field required to cancel the Earth's field was approximately doubled. For a thin film cooling through its transition temperature, with no magnetic shielding, the flux focuses into arrays [183] which are pinned in thin films. All of these measurements showed good reproducibility, confirming that any trapped flux in the Nb shielding must be pinned and immobile.

As it is not possible to remove trapped flux, for this system, there are two possible solutions:

- Making the on-chip shield using a superconductor/μ metal bilayer or trilayer would provide shielding for the superconductor, ensuring it was being cooled under zero-field conditions. This would work for any system.

- Making the on-chip shield out of a lower-T_c superconductor such as Al would allow the magnetic shielding provided by the magnetic coil system to be used to prevent trapped flux. This would only work for my test system, as most TES instruments do not feature the same magnetic coil system.

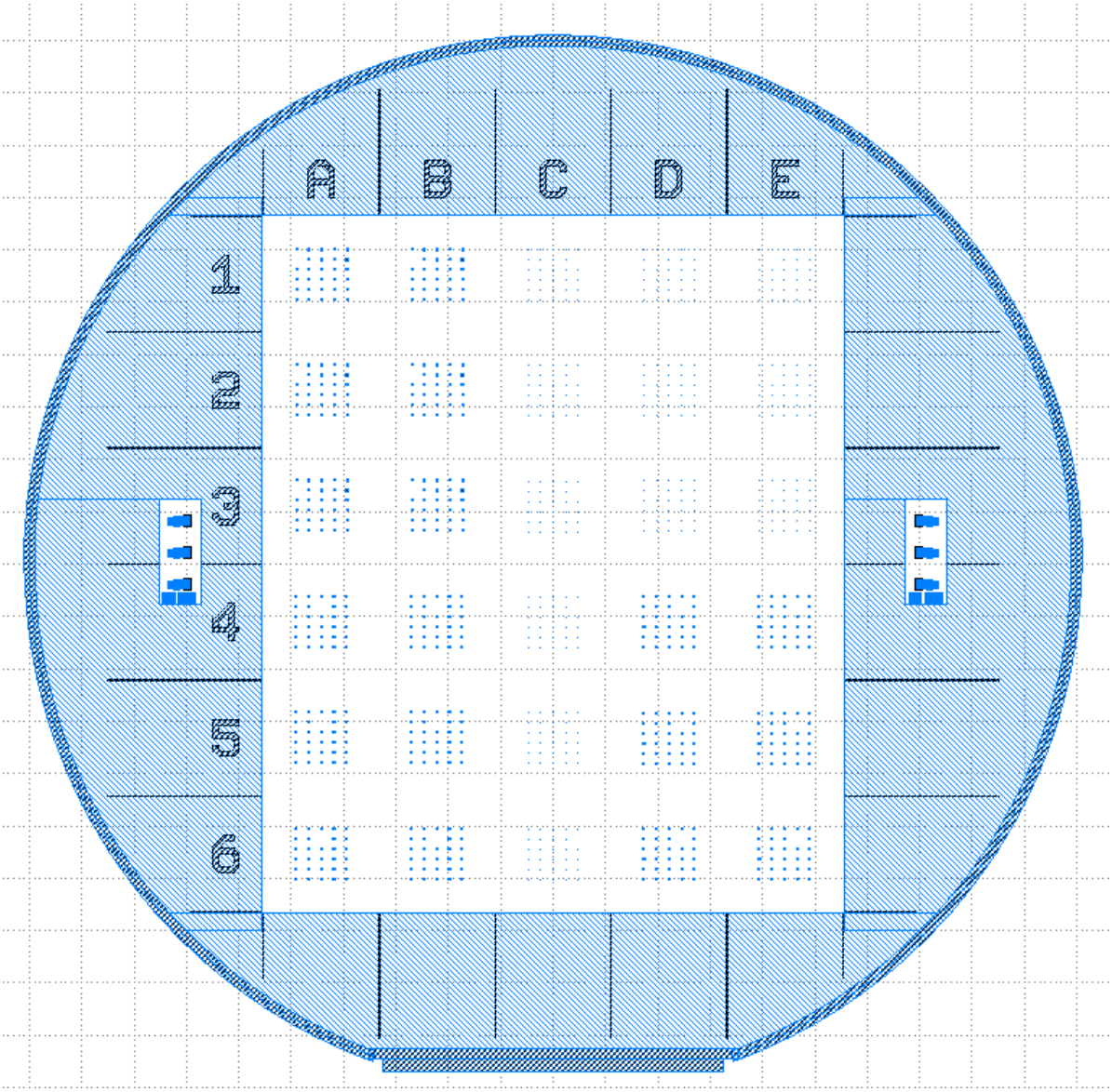

Figure 7.11 Full mask design used for the manufacture of the backing plates, showing the grid system used to label the chips and the dicing marks (in black). The white regions were removed in the final DRIE step. The dicing marks are all at least 1 mm long and set back from the edge of the large DRIE well by 100 µm.

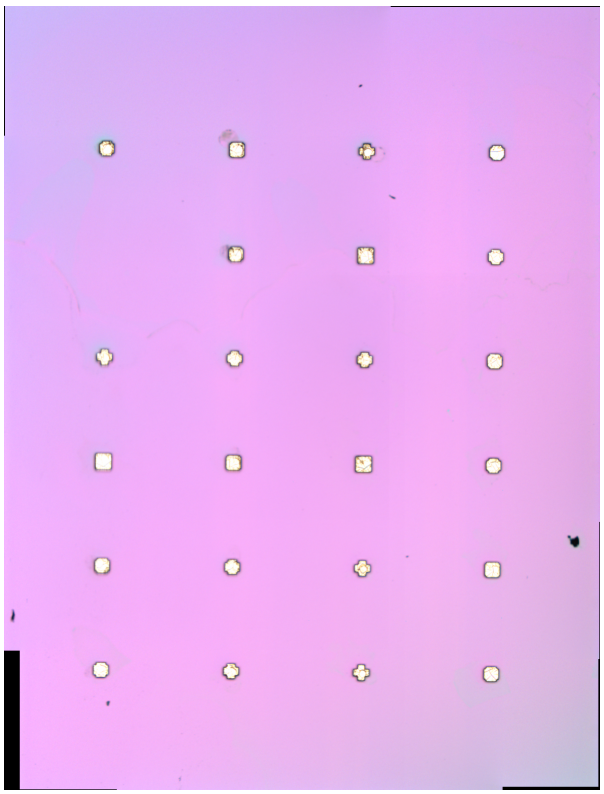

Figure 7.12 Image of the central region of an on-chip shield with type 1 pillars post-processing. The pink unfocused region is the silicon wafer; the bright white regions are the pillars.

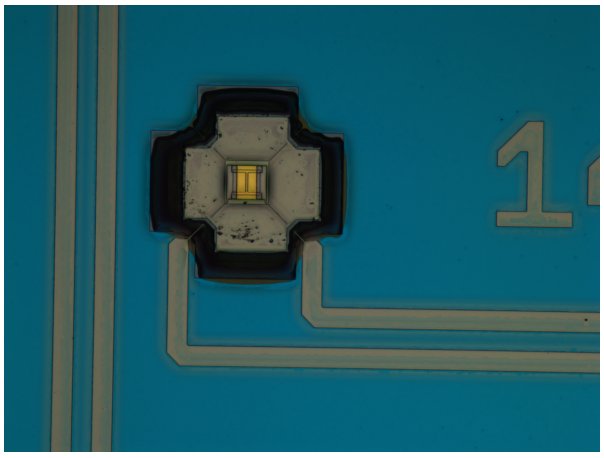

Figure 7.13 Membrane-suspended TES with silver Nb on-chip shield visible underneath. The black region is the well.

7.5.1 $I_c(B_z)$

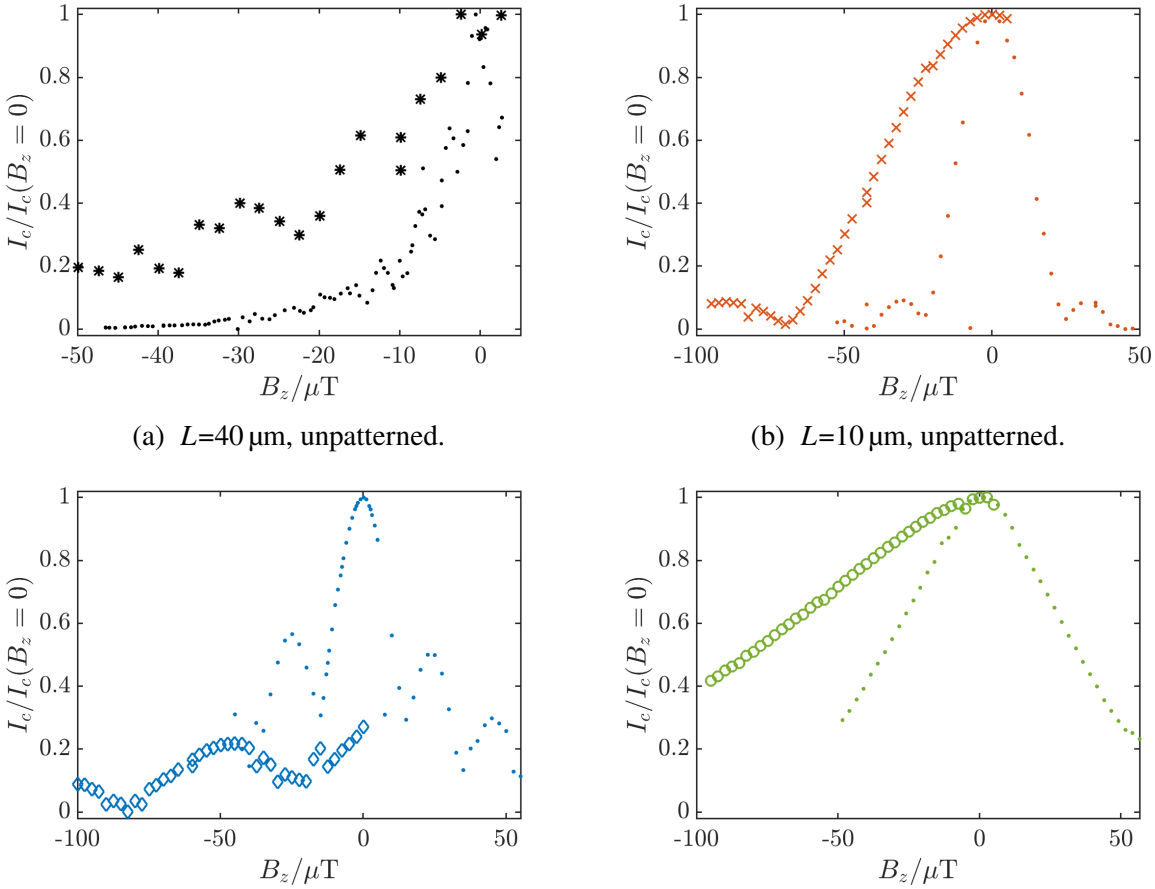

(a) L=40 µm, unpatterned.

(b) L=10 µm, unpatterned.

(c) L=10 µm, three normal metal bars.

(d) L=5 µm, unpatterned.

Figure 7.14 $I_c(B_z)$ for four TESs of bilayer side length L, measured close to T_c for all devices. The larger points show data taken with on-chip shielding, whilst the dots of the corresponding colour show data taken without on-chip shielding. For the patterned bilayer with L=10 µm, the data for the shielded device has been shifted by 120 µT for ease of comparison with the unshielded data. All datasets have been normalised to I_c at zero field.

Measurements of critical current as a function of field were taken as in Section 6.3.1, and compared to the corresponding measurements for the unshielded TESs. Again, the oscillations in critical current do not reach zero, but the model given by Equation (6.1) can again be used, using the definition of effective length in Section 6.3.1, which assumes flux threads a region of width equal to the full bilayer width and length $L_{\text{eff}} < L$. Figure 7.14 shows $I_c(B_z)$ for the four devices tested, both without shielding (dots) and without shielding (larger markers). From these plots, the shielding did not change the magnitude of the oscillations in $I_c(\Phi_z)$, but the period of these oscillations I_c was reduced.

This reduction in period is also shown by the difference in effective length in Table 7.2 and Figure 7.15. Table 7.2 shows the effective side lengths for all of the TESs tested both with and without on-chip shielding, and these effective side lengths are plotted in Figure 7.15 as a function of actual side length. The solid black line in this figure indicates the case when $L = L_{\text{eff}}$. The red points show measurements taken with shielding, whilst the black points show measurements taken without shielding. In all cases, the presence of on-chip shielding decreases the effective length by a factor of about 2-4 for all TESs, indicating a reduction in magnetic field sensitivity.

Table 7.2 Effective length for TES bilayers with and without on-chip shielding. This effective length was calculated from the effective area that gave the best fit of Equation (6.1) to the oscillations in $I_c(B_z)$, assuming flux penetration across the full width of the bilayer. For each device, a shielding factor was calculated as the ratio of the effective length without shielding to the effective length with shielding.

Side length/μm	Number of bars	L_{eff}/μm		$L_{\text{eff,unshielded}}/L_{\text{eff,shielded}}$
		Unshielded	Shielded	
40	0	6.7	1.5	4.4 ± 0.2
10	0	2.9	1.0	3.0 ± 0.1
10	3	3.5	1.0	3.6 ± 0.2
5	0	2.1	0.9	2.2 ± 0.1

7.5.2 Current and resistance as a function of field

As in Section 6.3.4, bias current measurements were taken with the device biased at around 0.5 R_n with no applied field. The magnetic field was cycled between no applied field and an applied field of 100 μT using the 3-axis coil system, and the change in bias current was recorded. This measurement was carried out for fields applied in the x, y and z directions.

Figures 7.16a and 7.16b show the effects of applied fields parallel to the TES thin film. The points show measurements without on-chip shielding, whilst the larger markers indicate measurements taken with on-chip shielding. For all three devices tested, for the same applied field in either the x or y direction, the observed change in current was reduced by the use of on-chip shielding. The on-chip shield was only designed to reduce the impact of fields in the z direction, but the presence of the superconducting shield disrupts the fields in the x and y directions as well, which is an extremely valuable result as it shows that on-chip shielding can reduce the impact of all applied fields, regardless of their direction.

Figure 7.17 shows (a) the change in TES current and (b) the change in bias point with applied field in the z direction for the three devices tested, both without on-chip shielding (points) and

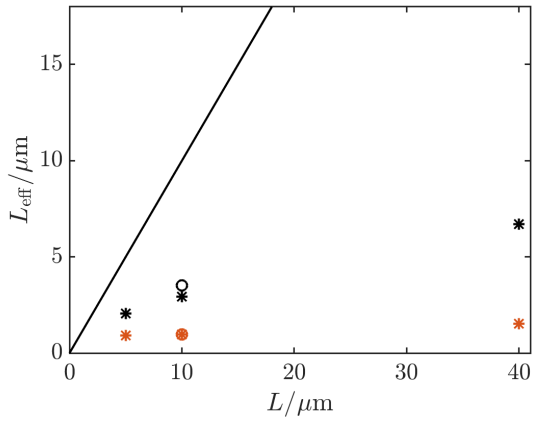

Figure 7.15 Effective length as a function of actual length, where L_{eff} is calculated from the effective area that gives the best fit of Equation (6.1) to the oscillations in $I_{\mathrm{c}}(B_z)$, assuming flux penetration across the full width of the bilayer. The solid black line shows the case when the two lengths are the same. The black points indicate the effective lengths without shielding, whilst the red points indicate the effective lengths with shielding. The asterisks correspond to unpatterned devices whilst the circle corresponds to the device patterned with three partial normal metal bars.

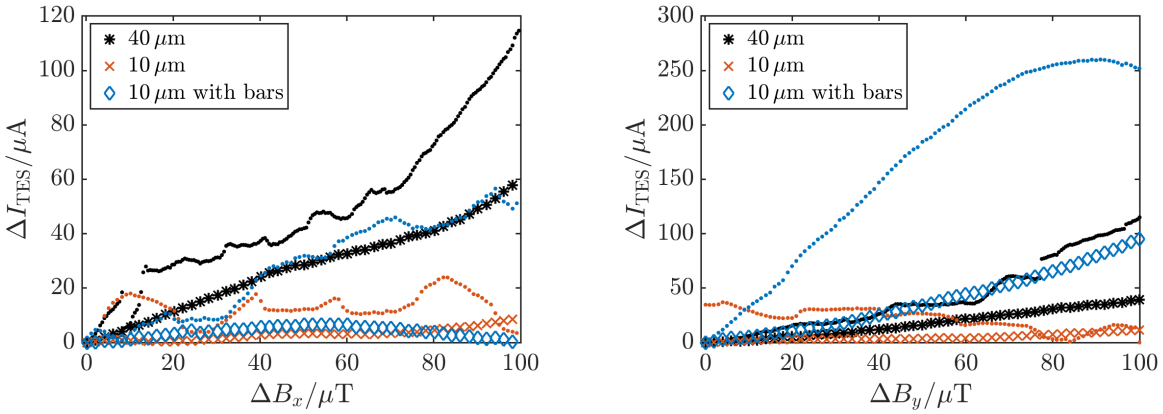

(a) (b)

Figure 7.16 (a) $I(B_x)$ and (b) $I(B_y)$ at a temperature of 90 mK for three TESs with on-chip shielding: one unpatterned TES of bilayer side length 40 µm (black asterisks), one unpatterned TES of bilayer area 10 µm (red crosses), and one TES with bilayer area 10 µm and three normal metal bars (blue diamonds). The dots of the corresponding colour show the measurements taken without on-chip shielding.

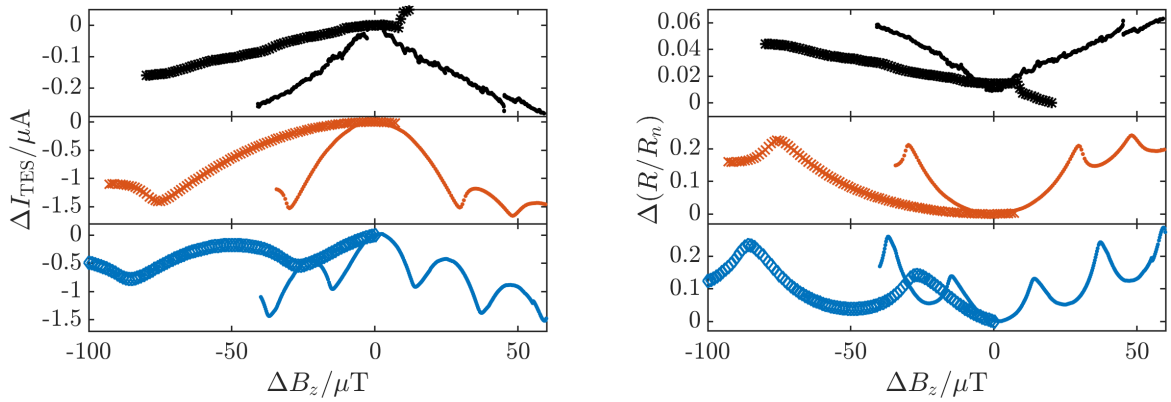

(a) (b)

Figure 7.17 (a) $I(B_z)$ and (b) $R(B_z)$ at a temperature of 90 mK for three TESs with on-chip shielding: one unpatterned TES of bilayer side length 40 µm (black asterisks), one unpatterned TES of bilayer area area 10 µm (red crosses), and one TES with bilayer area 10 µm TES and three normal metal bars (blue diamonds). As there was a large background field for the device with bars, the data is shifted by 120 µT to allow comparison with the other data sets. The dots of the corresponding colour show the measurements taken without on-chip shielding.

with on-chip shielding (larger markers). As in Section 7.5.1, the on-chip shielding reduced the period of the oscillations in field and bias point, and the magnitude of the oscillations is also reduced, indicating that the shielding is effective in reducing the field perpendicular to the TES. The presence of the shielding also considerably reduces the magnetic field sensitivity of the TESs themselves, shown by a reduction in $\Delta I/\Delta B_z$ at zero field. This increased resilience will also reduce any device noise produced by magnetic fields. Overall, this shows that the use of on-chip shielding will significantly improve TES performance.

7.5.3 Spherical scans

Figures 7.18 to 7.20 show the results from spherical scans (a) without and (b) with on-chip shielding, with a target field magnitude of 20 µT. The plots show the direction of the applied field scaled by the current response of the TES. For all three devices, the size of the response surface is reduced in all directions by the on-chip shielding, whilst maintaining the same shape. This indicates that the on-chip shielding reduces the magnitude of the magnetic field experienced by the TESs but does not fundamentally change its magnetic field behaviour.

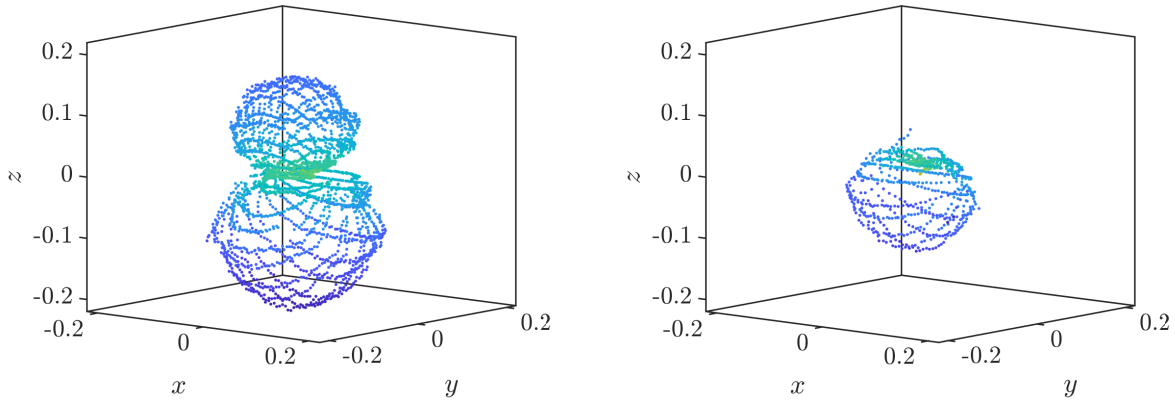

(a) (b)

Figure 7.18 Direction of the applied field scaled by the current response for the TES with an unpatterned 40 µm side length bilayer, for a field magnitude of 20 µT, without (a) and with (b) an on-chip shield. Both measurements were taken at a temperature of 90 mK, at a bias point of 50 % R_n. The colours of the points correspond to the magnitude of the current response.

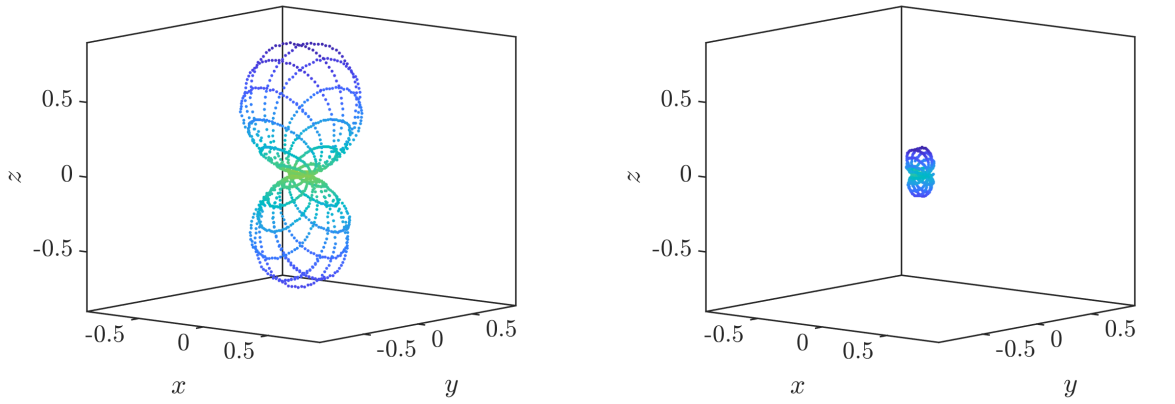

(a) (b)

Figure 7.19 Direction of the applied field scaled by the current response for the TES with an unpatterned 10 µm side length bilayer, for a field magnitude of 20 µT, without (a) and with (b) an on-chip shield. (a) was taken at a temperature of 90 mK, whilst (b) was taken at a temperature of 120 mK. Both measurements are at a bias point of 50 % R_n. The colours of the points correspond to the magnitude of the current response.

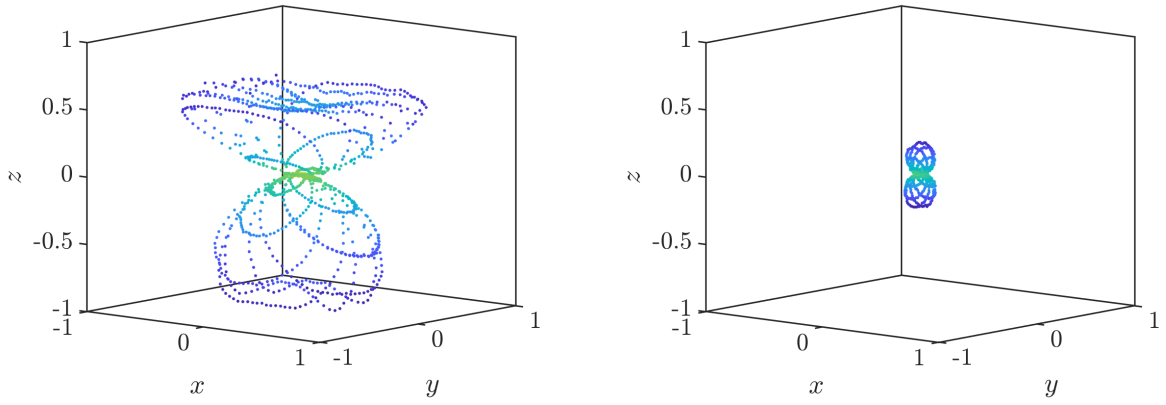

Figure 7.20 Direction of the applied field scaled by the current response for a TES with bilayer side length 10 µm and three normal metal bars, for a field magnitude of 20 µT, without (a) and with (b) an on-chip shield. Both measurements were taken at a temperature of 90 mK, at a bias point of 50 % R_n. The colours of the points correspond to the magnitude of the current response.

7.5.4 Shielding factors

From each of $I_{TES}(B_z)$, $I_c(B_z)$ and the spherical scans, a shielding factors can be defined to describe the difference between the unshielded and shielded results. For $I_{TES}(B_z)$ and $I_c(B_z)$, the shielding factor describes the reduction in oscillation period when shielding is applied, whilst for the spherical scans, the shielding factor describes the reduction in magnitude of the response surface.

Table 7.3 Shielding factors to compare unshielded and shielded measurements of $I_{TES}(B_z)$, $I_c(B_z)$ and spherical scans. Only $I_c(B_z)$ could be measured for the shielded TES with an unpatterned bilayer of side length 5 µm as the first stage SQUID displayed switching behaviour.

Side length/µm	Number of bars	Shielding factor		
		$I_{TES}(B_z)$	$I_c(B_z)$	Spherical scans
40	0	3 ± 0.3	4.4 ± 0.2	2 ± 0.5
10	0	2.5 ± 0.2	3.0 ± 0.1	5 ± 1
10	3	3 ± 0.3	3.6 ± 0.2	5 ± 1
5	0	-	2.2 ± 0.1	-

From Table 7.3, the shielding factors for all of the devices range from 2 to 5, with errors of up to 20 %. The shielding factors are not the same for all three measurements, which may be

due to the differences in conditions between the measurements. The bias current measurements are taken under voltage bias, whilst the critical current measurements are taken at zero voltage.

7.5.5 Noise and response time

In order to ensure that the presence of an on-chip shield does not significantly alter the noise properties and device response time, noise spectra and response time measurements were taken with the on-chip shield in place and compared with the equivalent measurements with no additional shielding.

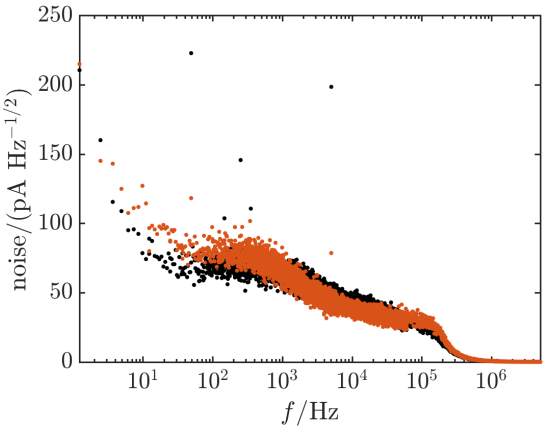

Figure 7.21 Noise spectra for the TES with an unpatterned 10 µm side length bilayer, without an on-chip shield, at a temperature of 77 mK (black points) and with an on-chip shield, at a temperature of 87 mK (red points). The bias voltage is set to a bias point of 30 % R_n and no active field cancellation is applied.

Figure 7.21 shows the noise spectra for the TES with an unpatterned 10 µm side length bilayer without an on-chip shield (black points) and with an on-chip shield (red points). The two spectra are very comparable, despite the spectrum with the shield being taken at a temperature 10 mK higher than the unshielded spectrum. The higher $1/f$ noise for the shielded TES can be attributed to the higher temperature and additional background vibration noise. The spectra were also taken on different days and cooldowns, which will also affect the behaviour. The similarity of the spectra despite the differences in measurement conditions shows that the backing plate does not affect the noise behaviour of the TES.

Figure 7.22 shows the current response to an applied voltage step for the TES with an unpatterned 10 µm side length bilayer without an on-chip shield (black points) and with an on-chip shield (red points). The measurement without shielding was taken with a filter, increasing the noise in the measurement. Exponential fits to the two plots give response times of 0.27 ms without the backing plate and 0.32 ms with the backing plate, suggesting that the

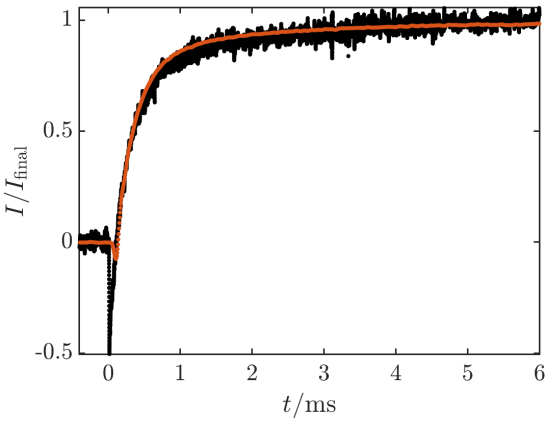

Figure 7.22 Risetime curves for the device with an unpatterned 10 µm side length bilayer without the backing plate, at a temperature of 79 mK (black points) and with the backing plate, at a temperature of 87 mK (red points), normalised to the final amplitude. Exponential fits to the two plots give response times of 0.27 ms without the backing plate and 0.32 ms with the backing plate. No active field cancellation is applied.

presence of the backing plate may slow the TES response slightly. However, since it appears that the current backing plate design traps flux and increases the magnetic field, this slowing in response can be attributed to the increased field when the on-chip shield is in place.

7.6 Conclusions

I have shown that using a superconductor such as aluminium or niobium to make an on-chip shield can theoretically reduce the perpendicular magnetic field component by a factor of 100, whilst also providing a reflective backstop if required. I designed a series of possible on-chip shields were made, using SOI wafers to achieve TES-shield distances of 21 µm. This on-chip shielding was successfully implemented on the SIZE-1 chip tested in the previous chapter and experimental studies were carried out to assess the degree of shielding achieved.

Experimentally, the on-chip shielding reduces the effective lengths of the TESs under test by a factor of about 2-4, halves the oscillation period of $I_{\mathrm{TES}}(B_z)$ and shrinks the response surface from the spherical scan by a factor of around 5, showing a clear reduction in magnetic field sensitivity. The shielding had a negligible impact on other system parameters such as noise and response time. The measured shielding factor is lower than predicted by my modelling, which can be attributed to both the finite size of the on-chip shield and the flux trapped in the Nb. However, I have demonstrated that on-chip shielding produces a reduction in both the magnetic

field experienced by the TES and the field sensitivity of the TES, making it a very attractive proposition for future studies of detector shielding.

The results from my study can be used to inform the design of future on-chip shields. The magnetic field system I used does not allow the niobium shielding to be cooled in zero-field conditions, resulting in significant trapped flux. For my system, this trapped flux could be prevented by adding additional shielding to the exterior of the cryostat or by making the on-chip shield from a lower-T_c superconductor such as Al, which could be cooled under active shielding using the coil system. In general, using a multilayer featuring a high-permeability metal such as μ-metal would provide shielding for the superconducting layer, allowing it to be cooled under zero-field conditions regardless of whether or not there is any other shielding present.

Additionally, the pillar designs used for the on-chip shields in this chapter were chosen to allow a safe level of clearance between the pillar and the edges of the TES well, ensuring that neither the TESs nor the pillars were damaged in the process of fitting the on-chip shield, even if there were errors in the alignment. This meant that the shields were relatively small and so the assumption in my initial modelling, that the shield could be modelled as an infinite superconducting plane, was less valid as edge effects may be significant. The alignment of the TES and the on-chip shield was successful, and showed that it would be possible to increase the size of the on-chip shields. Larger on-chip shields should display fewer edge effects, and will therefore have a shielding factor closer to that predicted by the model. This is an exciting area for future study.

Chapter 8

HEMT modelling

8.1 Introduction

So far, in this thesis, I have considered how TESs may be optimised by modifications to the bilayer geometry and material composition. It is also possible to improve TES performance by modifying the readout system used. Historically, Superconducting Quantum Interference Detectors (SQUIDs) have been used for signal amplification, as they enable the TESs to be operated under electrothermal feedback [15], and provide low input impedance and very low noise [105]. However, the frequency of operation is limited by the SQUID, and so high frequency operation is not possible. In this chapter, I investigate the possibility of using a High Electron Mobility Transistor (HEMT) in parallel with an inductor to read out a TES optimised for this purpose. A HEMT is a field effect transistor which uses a junction between two materials with different band gaps as the channel. It is able to operate at higher frequencies than other transistors, has a high gain and is capable of rapid switching speeds. These rapid switching speeds and high frequency operation would be of huge benefit in applications such as the demodulation of kilopixel arrays. HEMTs are also less sensitive to magnetic fields than SQUIDs, making them more robust and reducing the associated shielding requirements. Such a readout scheme has not been previously modelled or tested.

I provide a description of the model I have developed to describe HEMT readout in Section 8.2, including descriptions of the thermal and electrical bias circuits. I test this model by calculating the device response for typical TES parameters. I then investigate the noise of the HEMT readout system in Section 8.3. Section 8.4 discusses the stability of this configuration, looking at stability measures including input impedance, circuit resonance conditions and the reflection coefficient of the TES. In Section 8.5, I identify the parameters that are most important in optimising a system for HEMT readout, and finally, in Section 8.6, I discuss how knowledge

of these parameters might be incorporated into a TES design to optimise readout both using a HEMT amplifier and using a SQUID amplifier.

8.2 Description and development of HEMT model

In this analysis, I relate changes in input power P and voltage V to the resultant changes in the TES temperature T and current I. This allows me to determine the TES responsivity and suggest how this responsivity might be optimised. In general, TESs are used to study changes in input power P that result from photon absorption, but noise sources may produce voltage fluctuations as well as power fluctuations, and so it is beneficial to understand the TES response to both.

8.2.1 Small signal TES response

I assume that the TES undergoes small-signal sinusoidal perturbations of current I, voltage V, temperature T and power P, all of which are of the form

$$A = A_0 + (A_1 e^{i2\pi ft} + A_1^* e^{-i2\pi ft}), \tag{8.1}$$

where A_0 is the value at the operating point and A_1 is the magnitude of the perturbation. In this small-signal approximation $A_1 \ll A_0$.

8.2.2 Thermal bias circuit

The thermal circuit for the TES is the same as for readout using a SQUID [18], as shown in Figure 8.1. The combined heat capacity of the TES and absorber is modelled as a single heat capacity C, the temperature of the thermal heat sink is T_{bath} and P_{bath} gives the power flow from the TES to the heat bath. There are two additional power terms in this model: $P_{\text{J}} = I^2R$ is the TES Joule power dissipation and P is the signal power.

The thermal differential equation for this circuit is

$$C\frac{\mathrm{d}T}{\mathrm{d}t} = -P_{\text{bath}} + P_{\text{J}} + P. \tag{8.2}$$

The power flow from the TES to the heat bath is assumed to have a power law dependence,

$$P_{\text{bath}} = K(T^n - T_{\text{bath}}^n), \tag{8.3}$$

where n is the thermal exponent and $K = G/(nT^{n-1})$ where $G = \mathrm{d}P_{\text{bath}}/\mathrm{d}T$.

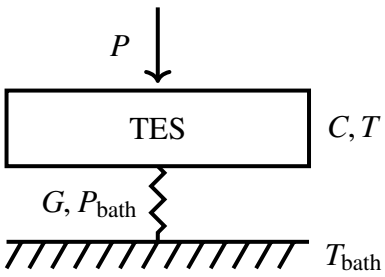

Figure 8.1 Thermal circuit for the TES calorimeter model. Here C is the heat capacity of the TES and absorber, T_{bath} is the temperature of the heat bath, P_{bath} is the power flow from the TES to the heat bath, $P_{\text{J}} = I^2R$ is the TES Joule power dissipation and P is the signal power.

For small-signal sinusoidal perturbations as given by Equation (8.1), the power flow to the heat bath can be written as

$$\begin{aligned} P_{\text{bath}} &= K((T_0 + T_1 e^{i2\pi ft} + T_1^* e^{-i2\pi ft})^n - T_{\text{bath}}^n), \\ &\approx K(T_0^n + nT_0^{n-1}T_1 e^{i2\pi ft} + nT_0^{n-1}T_1^* e^{-i2\pi ft} - T_{\text{bath}}^n), \\ &\approx K(T_0^n - T_{\text{bath}}^n) + nKT_0^{n-1}(T_1 e^{i2\pi ft} + T_1^* e^{-i2\pi ft}), \\ &\approx P_{\text{bath},0} + G(T_1 e^{i2\pi ft} + T_1^* e^{-i2\pi ft}), \end{aligned} \tag{8.4}$$

where any terms of second order or higher are assumed to have a negligible contribution.

The resistance of the TES can be expanded around the bias point to first order as

$$R(T, I) \approx R_0 + \left(\frac{\partial R}{\partial T}\right)_{I_0} (T_1 e^{i2\pi ft} + T_1^* e^{-i2\pi ft}) + \left(\frac{\partial R}{\partial I}\right)_{T_0} (I_1 e^{i2\pi ft} + I_1^* e^{-i2\pi ft}). \tag{8.5}$$

Substituting in the logarithmic temperature and current sensitivities $\alpha_I = (T_0/R_0)(\partial R/\partial T)_{I_0}$ and $\beta_I = (I_0/R_0)(\partial R/\partial I)_{T_0}$,

$$R(T, I) \approx R_0 + \frac{\alpha_I R_0}{T_0}(T_1 e^{i2\pi ft} + T_1^* e^{-i2\pi ft}) + \frac{\beta_I R_0}{I_0}(I_1 e^{i2\pi ft} + I_1^* e^{-i2\pi ft}). \tag{8.6}$$

The Joule power can be written to first order as

$$P_{\text{J}} \approx (I_0 + I_1 e^{i2\pi ft} + I_1^* e^{-i2\pi ft})^2 \left(R_0 + \frac{\alpha_I R_0}{T_0}(T_1 e^{i2\pi ft} + T_1^* e^{-i2\pi ft}) + \frac{\beta_I R_0}{I_0}(I_1 e^{i2\pi ft} + I_1^* e^{-i2\pi ft})\right), \tag{8.7}$$

$$\approx P_{\text{J},0} + 2I_0R_0(I_1 e^{i2\pi ft} + I_1^* e^{-i2\pi ft}) + \frac{\alpha_I P_{\text{J},0}}{T_0}(T_1 e^{i2\pi ft} + T_1^* e^{-i2\pi ft}) + \frac{\beta_I P_{\text{J},0}}{I_0}(I_1 e^{i2\pi ft} + I_1^* e^{-i2\pi ft}).$$

Substituting Equation (8.4) and Equation (8.7) into Equation (8.2), making the small signal approximation given by Equation (8.1), and separating out the terms in f,

$$i2\pi f C T_1 = -G T_1 + 2 I_0 R_0 I_1 + \frac{\alpha_I P_{\mathrm{J},0}}{T_0} T_1 + \frac{\beta_I P_{\mathrm{J},0}}{I_0} I_1 + P_1 C. \tag{8.8}$$

The low-frequency loop gain with constant current is defined as

$$\mathscr{L}_I = \frac{P_{\mathrm{J},0}\alpha_I}{G T_0}, \tag{8.9}$$

and the natural time constant is

$$\tau = \frac{C}{G}. \tag{8.10}$$

There is one more time constant associated with the thermal behaviour,

$$\tau_{\text{therm.}} = \tau \frac{1 + \beta_I + R_\mathrm{S}/R_0}{1 + \beta_I + R_\mathrm{S}/R_0 + (1 - R_\mathrm{S}/R_0)\mathscr{L}_\mathrm{I}}. \tag{8.11}$$

The loop gain and natural time constant can be substituted into Equation (8.8) to give

$$i2\pi f C T_1 = -\frac{C T_1}{\tau} + 2 I_0 R_0 I_1 + \frac{C \mathscr{L}_I}{\tau} T_1 + \beta_I I_0 R_0 I_1 + P_1. \tag{8.12}$$

Grouping together terms in I_1, T_1 and P_1,

$$\left(i2\pi f C + \frac{C(1 - \mathscr{L}_I)}{\tau} \right) T_1 - I_0 R_0 (2 + \beta_I) I_1 = P_1. \tag{8.13}$$

Hard current bias and τ_I

In the case where $I_1 = 0$ (hard current bias) then the situation is the same as for a TES readout with a SQUID [18]. The temperature oscillates at a natural frequency f_T, Equation (8.13) is independent of I_1 and

$$\left(i2\pi f_T + \frac{(1 - \mathscr{L}_I)}{\tau} \right) C T_1 = P_1. \tag{8.14}$$

In the case $P_1 = 0$, this can be rearranged to give

$$\begin{aligned} i2\pi f_T &= -\frac{(1 - \mathscr{L}_I)}{\tau}, \\ 2\pi f_T &= -\frac{(1 - \mathscr{L}_I)}{i\tau}. \end{aligned} \tag{8.15}$$

Substituting this back into Equation (8.1) for temperature,

$$T = T_0 + T_1 e^{-\frac{(1-\mathscr{L}_I)}{\tau}t}, \tag{8.16}$$

showing that in this case the temperature decays exponentially back to the bias point with time constant

$$\tau_I = \frac{\tau}{1-\mathscr{L}_I}. \tag{8.17}$$

If $\mathscr{L}_I > 1$ then $\tau_I < 0$ and the negative time constant indicates that when the TES is current biased there is instability due to thermal runaway.

8.2.3 Electrical bias circuit

The equivalent circuit for TES readout using a SQUID is shown in Figure 8.2.

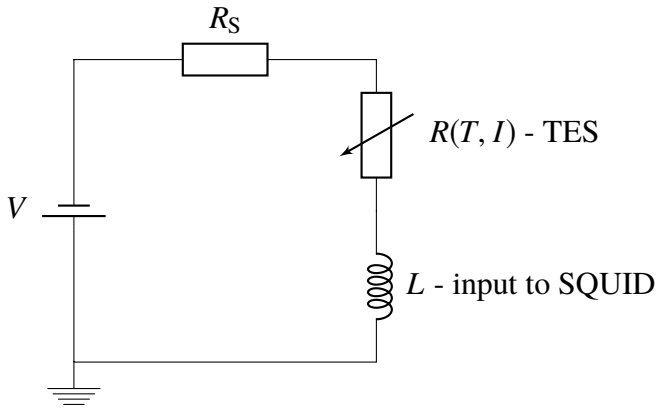

Figure 8.2 Equivalent circuit for TES readout using a SQUID. The TES is represented by a variable resistor, L is the input inductance to the SQUID and R_S is the stray resistance in the circuit.

For readout using a HEMT amplifier, the input inductance to the SQUID is replaced with an input impedance to the amplifier Z_A. For readout at frequencies within the bandwidth of the HEMT, this input impedance will be purely resistive and equal to R_A, and it is this case I consider here. To ensure circuit stability, an inductance L_a is connected across the terminals of the amplifier so that the TES remains under voltage bias. The equivalent circuit is shown in Figure 8.3.

Applying Kirchhoff's voltage law to the circuit in Figure 8.3,

$$V - IZ_S - IR(T, I) - I_A R_A = 0. \tag{8.18}$$

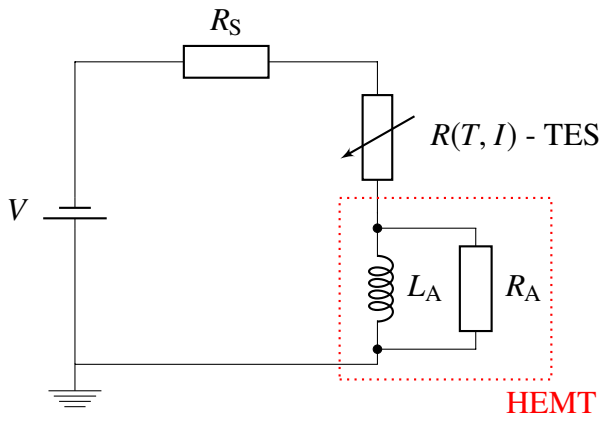

Figure 8.3 Equivalent circuit for TES readout using a HEMT. The TES is represented by a variable resistor, and R_a is the input resistance to the HEMT. An inductor L_a is placed in parallel with the input resistance to the HEMT to stabilise the circuit. R_S is the stray resistance in the circuit.

I_A is determined by the relative values of R_A and Z_L. Equality of voltages across the two parallel components of the amplifier means that

$$I_A R_A = I_L Z_L, \tag{8.19}$$

where $Z_L = i2\pi f L_A$, and application of Kirchhoff's current law gives

$$I = I_L + I_A. \tag{8.20}$$

Substituting Equation (8.20) into Equation (8.19) gives an expression for I_A,

$$\begin{aligned} I_A R_A &= (I - I_A) Z_L, \\ I_A(R_A + Z_L) &= I Z_L, \\ I_A &= \frac{I Z_L}{R_A + Z_L}, \end{aligned} \tag{8.21}$$

that can then in turn be substituted back into Equation (8.18),

$$V = I R_S + I R(T, I) + I \frac{R_A Z_L}{R_A + Z_L}. \tag{8.22}$$

Comparing this with the voltage in the SQUID circuit,

$$V = I R_S + I R(T, I) + I Z_L. \tag{8.23}$$

The equivalent results for the SQUID circuit can therefore be obtained by replacing the impedance combination $\frac{R_A Z_L}{R_A + Z_L}$ with Z_L.

In both cases, at the operating point,

$$V_0 = I_0 R_S + I_0 R_0, \tag{8.24}$$

as the impedance of the inductor is zero when there is no time variation.

For the HEMT circuit, making the small-signal approximation as given by Equation (8.1) in Equation (8.22),

$$(V_0 + V_1 e^{i2\pi ft} + V_1^* e^{-i2\pi ft}) = (I_0 + I_1 e^{i2\pi ft} + I_1^* e^{-i2\pi ft}) R_S + I_1 e^{i2\pi ft} \frac{i2\pi f L R_A}{R_A + i2\pi f L} + I_1^* e^{-i2\pi ft} \frac{(-i2\pi f L) R_A}{R_A - i2\pi f L} \tag{8.25}$$

$$+ (I_0 + I_1 e^{i2\pi ft} + I_1^* e^{-i2\pi ft}) \left(R_0 + \frac{\alpha_I R_0}{T_0} (T_1 e^{i2\pi ft} + T_1^* e^{-i2\pi ft}) + \frac{\beta_I R_0}{I_0} (I_1 e^{i2\pi ft} + I_1^* e^{-i2\pi ft}) \right).$$

Separating out the time-independent terms and collecting terms in f,

$$V_1 = I_1 R_S + I_1 R_0 + \frac{I_0 \alpha_I R_0}{T_0} T_1 + \beta_I R_0 I_1 + I_1 \frac{Z_L R_A}{R_A + Z_L}. \tag{8.26}$$

Grouping terms in I_1, T_1 and V_1,

$$V_1 = \left(R_S + R_0(1 + \beta_I) + \frac{R_A Z_L}{R_A + Z_L} \right) I_1 + \frac{I_0 \alpha_I R_0}{T_0} T_1. \tag{8.27}$$

8.2.4 Limiting case: no loop gain

If the low-frequency loop gain $\mathscr{L}_I$ approaches zero then Equation (8.27) is independent of T_1 and

$$\left(R_S + R_0(1 + \beta_I) + \frac{R_A Z_L}{R_A + Z_L} \right) I_1 = V_1. \tag{8.28}$$

In the case $V_1 = 0$, this equation can be rearranged to find an exact value for f_I, the natural frequency of oscillation of the current,

$$\begin{aligned} R_A i2\pi f L &= -(R_A + i2\pi f_I L)(R_S + R_0(1 + \beta_I)), \\ 2\pi f_I &= -\frac{R_A (R_S + R_0(1 + \beta_I))}{(R_A + R_S + R_0(1 + \beta_I)) iL}. \end{aligned} \tag{8.29}$$

Substituting this back into Equation (8.1) for current,

$$I = I_0 + I_1 e^{-\frac{R_A(R_S+R_0(1+\beta_I))}{(R_A+R_S+R_0(1+\beta_I))L}t}, \tag{8.30}$$

showing that in this case the current decays exponentially back to the bias point with time constant

$$\tau_{el} = \frac{(R_A + R_S + R_0(1+\beta_I))L}{R_A(R_S + R_0(1+\beta_I))}. \tag{8.31}$$

This time constant can be split up into two terms,

$$\tau_{el} = \frac{L}{R_S + R_0(1+\beta_I))} + \frac{L}{R_A}. \tag{8.32}$$

It is helpful to define two electrical time constants, the time constant corresponding to the resistance of the TES and the stray resistance

$$\tau_{elec.} = \frac{L}{R_0(1+\beta_I) + R_S}, \tag{8.33}$$

and the time constant corresponding to the input impedance of the HEMT amplifier,

$$\tau_{amp.} = \frac{L}{R_A}. \tag{8.34}$$

8.2.5 Analytic expressions for circuit response

Combining Equations (8.13) and (8.27) into a single matrix,

$$\begin{pmatrix} R_S + R_0(1+\beta_I) + \frac{R_A i2\pi f L}{R_A + i2\pi f L} & \frac{\mathscr{L}_I G}{I_0} \\ -I_0 R_0(2+\beta_I) & i2\pi f C + \frac{(1-\mathscr{L}_I)C}{\tau} \end{pmatrix} \begin{pmatrix} I_1 \\ T_1 \end{pmatrix} = \begin{pmatrix} V_1 \\ P_1 \end{pmatrix}. \tag{8.35}$$

This can then be inverted to find I_1 and T_1 for a given V_1 or P_1. I simplify the form of the matrix by defining the following quantities:

$$Z_c = R_S + R_0(1+\beta_I) \tag{8.36}$$

$$Z_{amp} = \frac{R_A Z_L}{R_A + Z_L}. \tag{8.37}$$

Using the definition of τ_I from Equation (8.17), the matrix in Equation (8.35) becomes

$$\mathbf{M} = \begin{pmatrix} Z_c + Z_{amp} & \frac{\mathscr{L}_I G}{I_0} \\ -I_0 R_0(2+\beta_I) & i2\pi f C + \frac{C}{\tau_I} \end{pmatrix}, \tag{8.38}$$

with determinant

$$\det \mathbf{M} = \frac{(Z_c + Z_{amp})(i2\pi f C\tau_I + C)}{\tau_I} + \mathscr{L}_I G R_0 (2 + \beta_I). \tag{8.39}$$

Inverting the matrix in Equation (8.35),

$$\begin{pmatrix} I_1 \\ T_1 \end{pmatrix} = \frac{\tau_I}{(Z_c + Z_{amp})(i2\pi f C\tau_I + C) + \mathscr{L}_I G R_0 \tau_I (2 + \beta_I)} \begin{pmatrix} \frac{(i2\pi f C\tau_I + C)}{\tau_I} & -\frac{\mathscr{L}_I G}{I_0} \\ I_0 R_0 (2 + \beta_I) & (Z_c + Z_{amp}) \end{pmatrix} \begin{pmatrix} V_1 \\ P_1 \end{pmatrix}. \tag{8.40}$$

The two components of this equation give the current and temperature response of the TES,

$$I_1 = \frac{\tau_I}{(Z_c + Z_{amp})(i2\pi f C\tau_I + C) + \mathscr{L}_I G R_0 \tau_I (2 + \beta_I)} \left[\frac{(i2\pi f C\tau_I + C)}{\tau_I} V_1 - \frac{\mathscr{L}_I G}{I_0} P_1 \right] \tag{8.41}$$

and

$$T_1 = \frac{\tau_I}{(Z_c + Z_{amp})(i2\pi f C\tau_I + C) + \mathscr{L}_I G R_0 \tau_I (2 + \beta_I)} \left[I_0 R_0 (2 + \beta_I) V_1 + (Z_c + Z_{amp}) P_1 \right]. \tag{8.42}$$

8.2.6 Calculation of the zero-frequency responsivity

From Equation (8.41), when $V_1 = 0, 2\pi f = 0$, the power-to-current responsivity is

$$s_I(0) = -\frac{\tau_I}{\mathscr{L}_I G R_0 \tau_I (2 + \beta_I) + C Z_c} \left(\frac{\mathscr{L}_I G}{I_0} \right). \tag{8.43}$$

This agrees with the zero-frequency impedance found by using symbolic software to computationally invert the matrix in Equation (8.35). The zero-frequency response given by Irwin et al.,

$$s_I(0) = -\frac{1}{I_0 (R_0 - R_S)}, \tag{8.44}$$

assumes strong feedback,

$$\mathscr{L}_I \gg \frac{R_S + R_0 (1 + \beta_I)}{R_0 - R_S}. \tag{8.45}$$

It can be shown that Equation (8.43) reduces to Equation (8.44) in the strong-feedback limit. If the TES bias point resistance R_0 decreases, the strong feedback condition will eventually not be met and the device will become unstable.

8.2.7 Calculation of high-frequency responsivity

To find the high frequency power-to-current responsivity, I take Equation (8.41) and set $V_1 = 0$. I assume that any terms in f are much larger than any other terms, an assumption that has been checked using typical values of TES parameters. In this limit,

$$\left|\frac{I_1}{P_1}\right| \approx -\frac{\mathscr{L}_I G}{C I_0 R_A}\frac{1}{2\pi f}. \tag{8.46}$$

On a logarithmic plot, this will be a line with a constant negative gradient of -1.

The high frequency voltage-to-current responsivity can be found in the same way from Equation (8.41), setting $P_1 = 0$.

$$\left|\frac{I_1}{V_1}\right| \approx \frac{1}{R_A}. \tag{8.47}$$

On a logarithmic plot, this will be a constant.

8.2.8 Simulations of TES response

The TES current response to either an input voltage ($P_1 = 0$) or an input power ($V_1 = 0$) was investigated by solving Equation (8.35) numerically to find I_1, as shown in Figures 8.4 and 8.5. This was then multiplied by the amplifier impedance Z_{amp}, shown in Figure 8.6, to give the voltage output across the terminals of the amplifier, seen in Figures 8.7 and 8.8. As a starting point, typical values of the system parameters for the infrared TESs studied by the Quantum Sensors group were used in the simulations.

Figure 8.4 shows the normalised current response to a power input for the HEMT readout circuit as a function of input frequency. The dashed line in the amplitude plot gives the zero-frequency limit of the response, showing that the analytic zero-frequency limit derived in Section 8.2.6 agrees with the calculated response at low frequency. The three dashed lines indicate the frequencies corresponding to the time constants $\tau_{\text{therm.}}$, $\tau_{\text{elec.}}$ and $\tau_{\text{amp.}}$. The three changes in gradient in the amplitude plot and the three changes of phase in the phase plot occur at the frequencies corresponding to these three time constants, showing that the values of these time constants determine the changes of gradient and phase. At high frequency, the line has constant negative gradient, as predicted by Equation (8.46).

In Figure 8.5, the normalised current response to a voltage input for the HEMT readout circuit is shown as a function of input frequency. The three dashed lines indicate the frequencies corresponding to the time constants $\tau_{\text{therm.}}$, $\tau_{\text{elec.}}$ and $\tau_{\text{amp.}}$. These time constants again dictate the frequencies where the magnitude of the response changes. At high frequency, the amplitude is constant, as predicted by Equation (8.47).

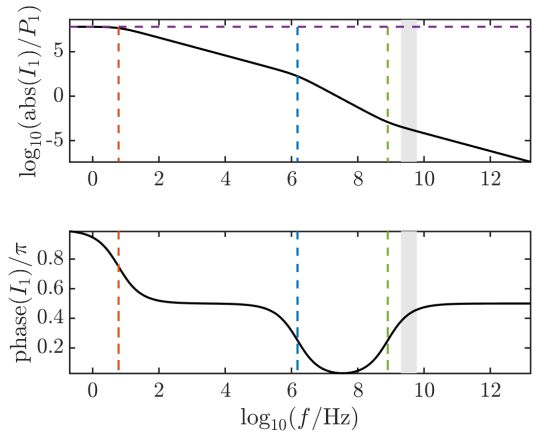

Figure 8.4 Current-power responsivity of the HEMT readout circuit as a function of input frequency f. The inductance across the HEMT terminals is 10 nH, the TES bias point resistance is 15.8 mΩ and the thermal conductance to the heat bath is 0.51 pWK^{-1}. The zero-frequency limit of the current-power responsivity is shown by the purple dashed line. The red, blue and green dashed lines indicate the frequencies corresponding to the time constants $\tau_{\mathrm{therm.}}$, $\tau_{\mathrm{elec.}}$ and $\tau_{\mathrm{amp.}}$ respectively, and the grey shaded region indicates the typical bandwidth of a HEMT amplifier.

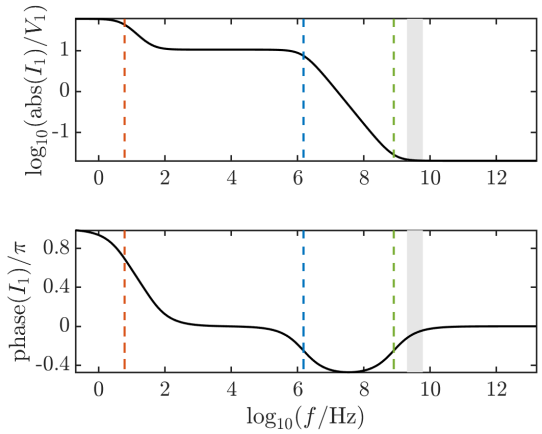

Figure 8.5 Current-voltage responsivity of the HEMT readout circuit as a function of input frequency f. The inductance across the HEMT terminals is 10 nH, the TES bias point resistance is 15.8 mΩ and the thermal conductance to the heat bath is 0.51 pWK^{-1}. The red, blue and green dashed lines indicate the frequencies corresponding to the time constants $\tau_{\mathrm{therm.}}$, $\tau_{\mathrm{elec.}}$ and $\tau_{\mathrm{amp.}}$ respectively, and the grey shaded region indicates the typical bandwidth of a HEMT amplifier.

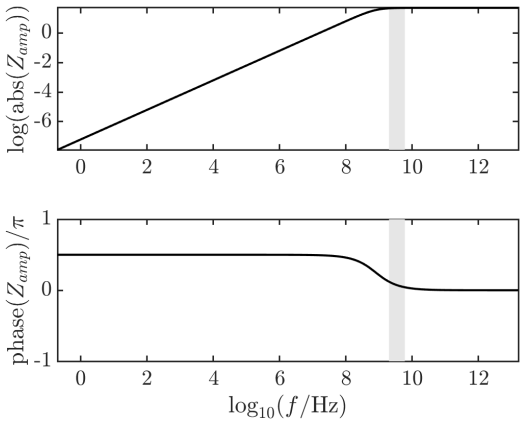

Figure 8.6 Amplitude and phase of the impedance of the parallel HEMT input resistance and inductor for an inductance of 10 nH and a real input impedance to the HEMT of 50 Ω, as a function of frequency f. The grey shaded region indicates the typical bandwidth of a HEMT amplifier.

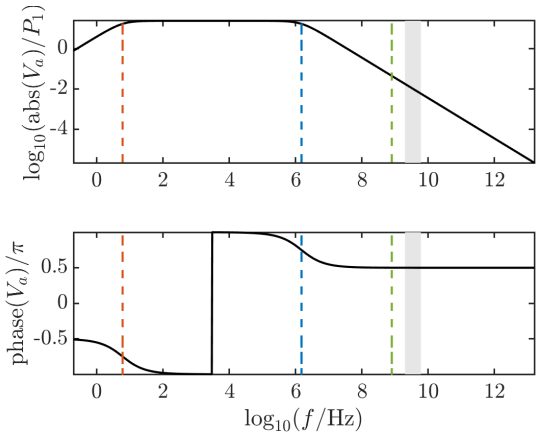

Figure 8.7 Amplitude and phase of the voltage measured across the amplifier terminals as a function of input frequency f, normalised by the power input P_1. The inductance across the HEMT terminals is 10 nH, the TES bias point resistance is 15.8 mΩ and the thermal conductance to the heat bath is 0.51 pWK^{-1}. The red, blue and green dashed lines indicate the frequencies corresponding to the time constants $\tau_{\mathrm{therm.}}$, $\tau_{\mathrm{elec.}}$ and $\tau_{\mathrm{amp.}}$ respectively, and the grey shaded region indicates the typical bandwidth of a HEMT amplifier.

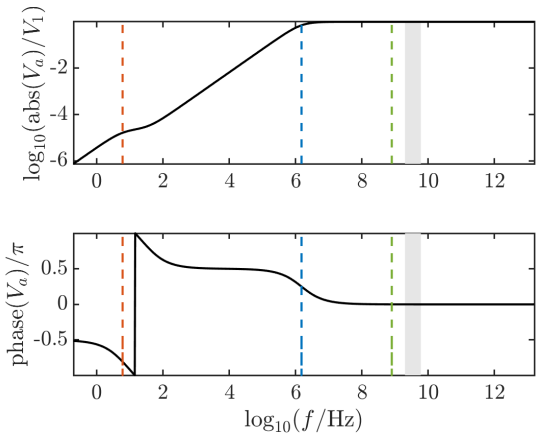

Figure 8.8 Amplitude and phase of the voltage measured across the amplifier terminals as a function of input frequency f, normalised by the voltage input V_1. The inductance across the HEMT terminals is 10 nH, the TES bias point resistance is 15.8 mΩ and the thermal conductance to the heat bath is 0.51 pWK^{-1}. The red, blue and green dashed lines indicate the frequencies corresponding to the time constants $\tau_{\mathrm{therm.}}$, $\tau_{\mathrm{elec.}}$ and $\tau_{\mathrm{amp.}}$ respectively, and the grey shaded region indicates the typical bandwidth of a HEMT amplifier.

Figure 8.6 shows the magnitude and phase of the amplifier impedance, defined as the parallel combination of the inductor and resistor representing the input to the HEMT in Figure 8.3, as a function of frequency. At low frequencies, the HEMT is effectively shorted by the inductor, and at high frequencies, the current all passes through the HEMT, resulting in a constant amplifier impedance.

As the HEMT works as a voltage amplifier, the quantity that is amplified is the voltage across the terminals of the HEMT. Figure 8.7 shows the magnitude and phase of this voltage in response to a power input, as a function of frequency. This is the product of the current response to a power input shown in Figure 8.4 and the amplifier impedance shown in Figure 8.6. The dashed lines indicate the frequencies corresponding to the time constants $\tau_{\mathrm{therm.}}$, $\tau_{\mathrm{elec.}}$ and $\tau_{\mathrm{amp.}}$. The thermal time constant τ influences the position of the first turning point, and $\tau_{\mathrm{elec.}}$ determines the position of the second turning point. $\tau_{\mathrm{amp.}}$ does not correspond to any change in gradient because the changes it produces in the current response and the impedance cancel out.

Figure 8.8 displays the magnitude and phase of the voltage across the terminals of the HEMT amplifier in response to a voltage input, as a function of frequency. This is the product of the current response to a voltage input shown in Figure 8.5 and the amplifier impedance shown in Figure 8.6. The dashed lines show the frequencies corresponding to the thermal and electrical time constants $\tau_{\mathrm{therm.}}$, $\tau_{\mathrm{elec.}}$ and $\tau_{\mathrm{amp.}}$. The frequency linked to the thermal time constant $\tau_{\mathrm{therm.}}$ corresponds to the first change in gradient in the amplitude plot, and is close to

the jump in phase in the phase plot. $\tau_{\text{elec.}}$ dictates the point where the response flattens out and, as in Figure 8.7, $\tau_{\text{amp.}}$ has no effect.

8.3 Discussion of noise sources in different circuits

8.3.1 Noise analysis

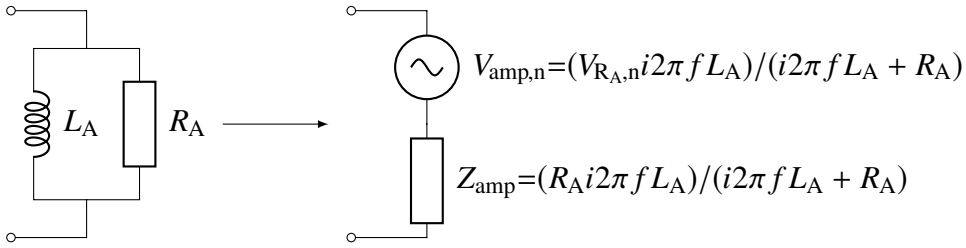

Figure 8.9 Thevenin equivalent noise circuit for the inductor-amplifier combination, where $V_{R_A,n} = \sqrt{4k_B T_{amp,n} R_A}$.

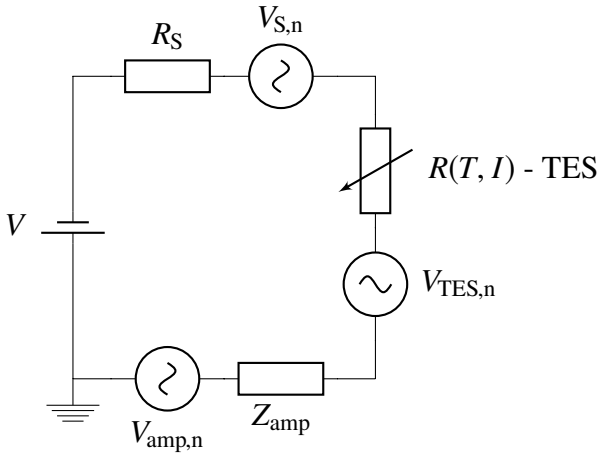

Figure 8.10 Equivalent noise circuit for HEMT readout. The resistors R_S and $R(T, I)$ have an associated noise voltage $V(R, T)_n = \sqrt{4k_B TR}$, where T is the temperature of the resistor and R is its resistance. The inductor-resistor parallel combination has been replaced by its Thevenin equivalent impedance and voltage source as shown in Figure 8.9.

Figure 8.9 shows the replacement of the inductor-amplifier parallel combination by its Thevenin equivalent for the purposes of this noise analysis. Figure 8.10 shows the overall equivalent noise circuit for a TES read out using a HEMT. The current noise produced by each noise source can be calculated by shorting out the other noise sources in the circuit and calculating the contribution from each noise source.

Figueroa-Feliciano [184] gives the general relationship between the input vector for a particular noise source $\mathbf{X}_n$ and its effect on the output $\mathbf{Y}_n$ as

$$\mathbf{Y}_n = \mathbf{S}\mathbf{X}_n. \tag{8.48}$$

The matrix $\mathbf{S}$ is the generalised responsivity and is the inverse of the matrix in Equation (8.35). The subscript n denotes a noise, and so I_n denotes the current noise, for example. The form of the input vector $\mathbf{X}_n = (V_n, P_n)$ depends on the type and position of the noise source in question. Table 8.1 shows the input vectors for the noise contributions from the different noise sources in the readout circuit components. The output vector $\mathbf{Y}_n = (I_n, T_n)$.

Table 8.1 Input vectors corresponding to different noise sources from the readout circuit components.

Type of noise	Noise source	Input vector $\mathbf{X}_n$
Johnson noise	TES	$\begin{pmatrix} \sqrt{4k_\mathrm{B}T_0R_0(1+2\beta_I)} \\ -I_0\sqrt{4k_\mathrm{B}T_0R_0(1+2\beta_I)} \end{pmatrix}$
Electron-phonon coupling	TES	$\begin{pmatrix} 0 \\ \sqrt{4k_\mathrm{B}GT_0^2F(T_0,T_\mathrm{bath})} \end{pmatrix}$
Johnson noise	Stray resistance	$\begin{pmatrix} \sqrt{4k_\mathrm{B}T_\mathrm{b}R_\mathrm{S}} \\ 0 \end{pmatrix}$
Johnson noise	Input resistor to HEMT	$\begin{pmatrix} (i2\pi f L_\mathrm{A}/(R_\mathrm{A}+i2\pi f L_\mathrm{A}))\sqrt{4k_\mathrm{B}T_\mathrm{amp,n}R_\mathrm{a}} \\ 0 \end{pmatrix}$

For TES Johnson noise, the resistance at the bias point R_0 is modified by a factor of $(1+2\beta_I)$ to account for the non-linear behaviour of the TES and the second component of the input vector accounts for the temperature fluctuations produced by the power dissipated by the Johnson noise current in the TES. The function F in the electron-phonon coupling contribution is a unitless function that accounts for the nonlinear thermal conductance. The impedance used to calculate the Johnson noise for the inductor-amplifier parallel combination is its Thevenin equivalent impedance.

Once the input noise vectors are known, the current noise and thermal noise for each noise source and type can then be calculated using Equation (8.48). The current noise can then be used to work out the noise in the amplifier voltage output as the voltage across the amplifier terminals will have voltage noise equal to $\sqrt{|I_nZ_\mathrm{amp}|^2 + |V_\mathrm{amp,n}|^2}$.

From Figure 8.11, the current noise is dominated by thermal fluctuation noise at low frequencies. As the frequency increases, the Johnson noise from the TES becomes more important, and at high frequencies, the noise from the HEMT amplifier dominates. The noise

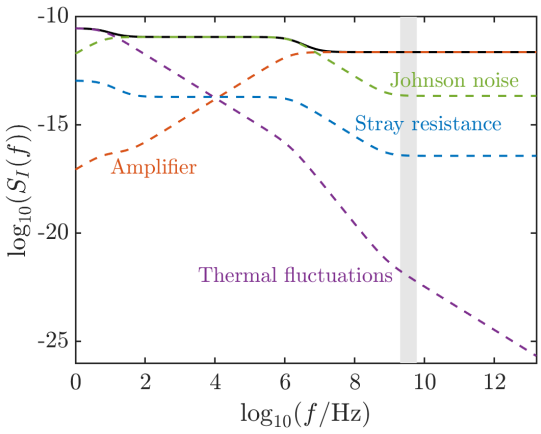

Figure 8.11 Current noise contributions to the overall current noise I_n. The shaded grey region shows the HEMT bandwidth.

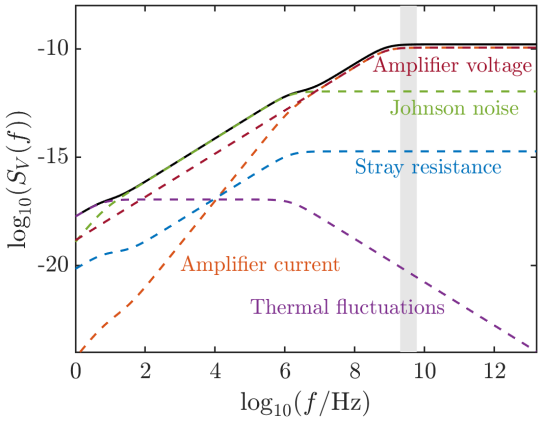

Figure 8.12 Noise contributions to the overall voltage noise V_n. The shaded grey region shows the HEMT bandwidth.

from the stray resistance is never the main contribution at any frequency. The overall current noise reduces as the frequency increases.

In the voltage noise plot in Figure 8.12, again the thermal fluctuation noise dominates at low frequencies, the Johnson noise from the TES at intermediate frequencies and the amplifier voltage noise at high frequencies. The overall current noise increases as the frequency increases because the amplitude of the voltage across the HEMT and inductor increases with increasing frequency.

The NEP is lowest at lower frequencies and increases with increasing frequency, and so to optimise the system for high frequency readout, the NEP at high frequency should be reduced. As longer integration time will result in a smaller bandwidth, and hence an improvement in the NEP, there is a trade off between short integration times and small NEPs.

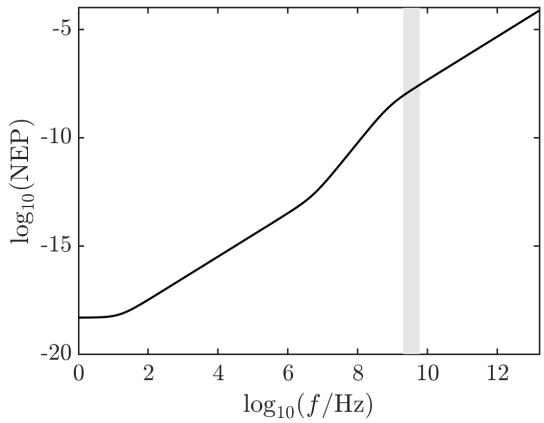

Figure 8.13 Noise equivalent power for readout using a HEMT. The shaded grey region shows the HEMT bandwidth.

8.3.2 Signal to noise ratio

Frequency components of signal

An equation used to fit a typical pulse produced by a TES circuit is given by Portesi et al. [34] as

$$V(t) = V_0 \left[\exp\left(-\frac{(t - t_0)}{\tau_{\text{el}}} \right) - \exp\left(-\frac{(t - t_0)}{\tau_{\text{eff}}} \right) \right]. \tag{8.49}$$

Figure 8.14 shows a typical pulse shape produced by this equation and its frequency components, with the two time constants both set to previously calculated values: τ_{eff}=26.3 ms and τ_{el}=106 ns.

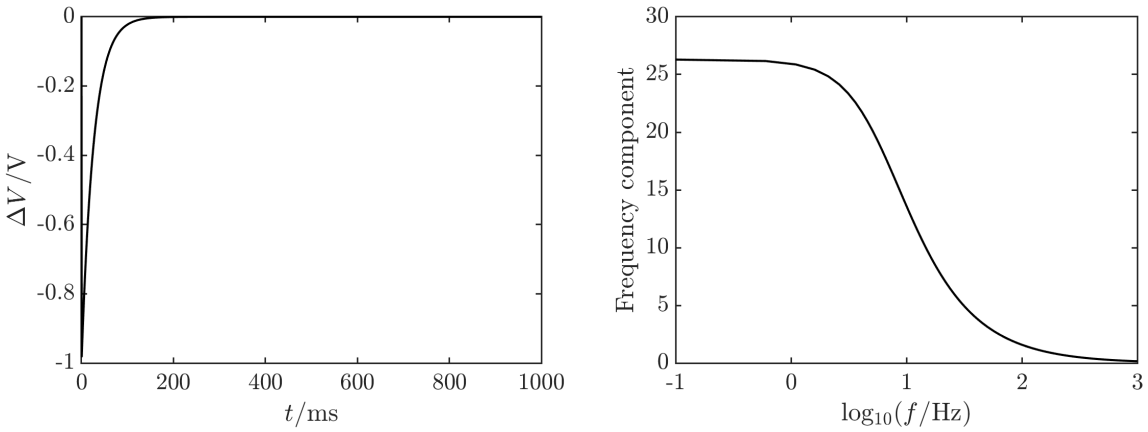

Figure 8.14 TES pulse shape given by Equation (8.49), with τ_{eff}=26.3 ms and τ_{el}=106 ns, in (a) the time domain and (b) the frequency domain.

The frequencies at which the TES response is located are well outside the bandwidth of a typical HEMT, but by reducing the response time of the TES, the response curve broadens and the signal power shifts up in frequency. This means that a greater proportion of the power is at higher frequencies, as shown by Figure 8.15

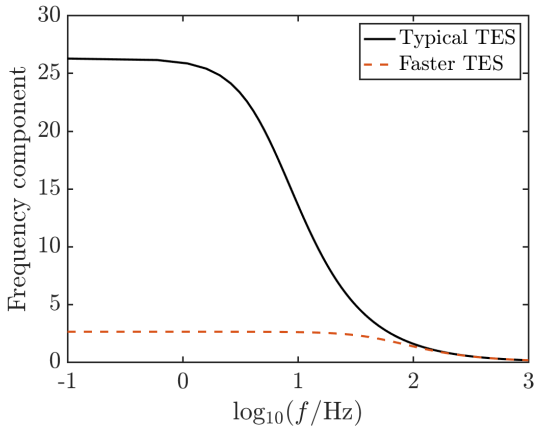

Figure 8.15 TES pulse shape for (black line) a typical TES and (red dashed line) a TES with a response time that is 10 times smaller, producing a faster device.

The time constant $\tau_{\text{eff}} \propto C/G$ so can be reduced by increasing the thermal conductance G and by reducing the heat capacity C. The time constant $\tau_{\text{elec.}}$ can be reduced by increasing the TES resistance and by reducing the value of the inductor in the circuit.

Calculation of signal to noise ratio

The signal I calculated comes from a Fourier transform of an input voltage or current pulse and has units of volts per hertz (V/Hz). The noise has units of volts per root Hertz (V/$\sqrt{\text{Hz}}$), and so taking their ratio does not give a dimensionless value. I therefore needed to multiply by the square root of the frequency spacing of the points, Δf, to make the ratio dimensionless.

Figure 8.16 shows the signal to noise ratio as a function of frequency, calculated for typical values of the TES system parameters. The signal to noise ratio decreases as the frequency increases, with the signal being equal in magnitude to the noise at around 100 MHz. In order to operate at high frequencies, this signal to noise ratio will need to be greater than one at the frequency of interest, and so the noise at high frequencies must be reduced.

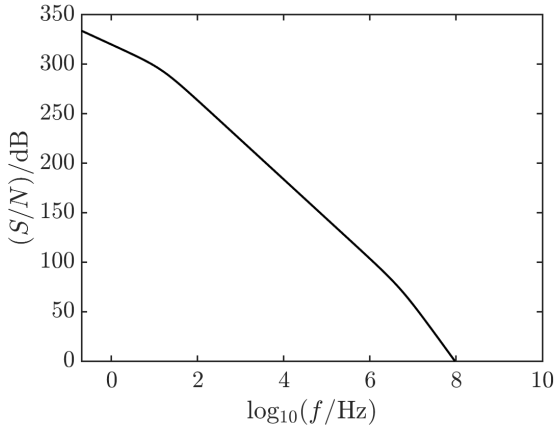

Figure 8.16 S/N in dB as a function of frequency, as calculated for typical TES parameters.

8.4 Stability analysis

8.4.1 TES stability conditions

When considering device stability, there are two different aspects to take into account:

1. The stability of the operating point itself.
2. The stability of the system with respect to small-signal AC perturbations.

8.4.2 Impedance

The complex impedance of the circuit is defined as

$$Z_{\mathrm{circ}} = \frac{V_1}{I_1}. \tag{8.50}$$

This can be evaluated by setting $P_1 = 0$ in Equation (8.41),

$$\begin{aligned} I_1 &= \frac{C(i2\pi f\tau_I + 1)}{\mathscr{L}_1 G R_0 \tau_I (2+\beta_I) + C(Z_{\mathrm{c}} + Z_{\mathrm{amp}})(i2\pi f\tau_I + 1)} V_1 \\ \frac{V_1}{I_1} &= \frac{\mathscr{L}_1 G R_0 \tau_I (2+\beta_I) + C(Z_{\mathrm{c}} + Z_{\mathrm{amp}})(i2\pi f\tau_I + 1)}{C(i2\pi f\tau_I + 1)} \\ Z_{\mathrm{circ}} &= (Z_{\mathrm{c}} + Z_{\mathrm{amp}}) + \frac{\mathscr{L}_1 R_0 \tau_I (2+\beta_I)}{(i2\pi f\tau_I + 1)\tau} \\ Z_{\mathrm{circ}} &= (R_{\mathrm{S}} + R_0(1+\beta_I) + Z_{\mathrm{amp}}) + \frac{\mathscr{L}_1 R_0 (2+\beta_I)}{(i2\pi f\tau_I + 1)(1-\mathscr{L}_1)} \end{aligned} \tag{8.51}$$

The impedance of the TES, accounting for the thermal behaviour, is then

$$Z_{\mathrm{TES}} = Z_{\mathrm{circ}} - Z_{\mathrm{amp}} - R_{\mathrm{S}}, \tag{8.52}$$
$$Z_{\mathrm{TES}} = R_0(1+\beta_{\mathrm{I}}) + \frac{\mathscr{L}_{\mathrm{I}} R_0(2+\beta_I)}{(i2\pi f\tau_I + 1)(1-\mathscr{L}_{\mathrm{I}})}.$$

This is exactly the same as the impedance of the device accounting for thermal behaviour derived by Irwin and Hilton [18], demonstrating that the TES impedance is independent of readout method, as expected.

Figure 8.17 is a plot of the real part of Z against the complex part of Z, showing the characteristic semi-circle corresponding to the impedance of the TES. At low frequencies, the real part of Z is negative, and so there is a particular frequency at which the impedance of the device is purely imaginary. This can be calculated from Equation (8.52) as

$$2\pi f = \pm\frac{1}{\tau_{\mathrm{I}}}\sqrt{\left(\frac{\mathscr{L}_{\mathrm{I}}}{\mathscr{L}_{\mathrm{I}}-1}\right)\left(\frac{2+\beta_{\mathrm{I}}}{1+\beta_{\mathrm{I}}}\right)-1}. \tag{8.53}$$

From this equation, this frequency is real only if $\mathscr{L}_{\mathrm{I}} > 1$, and so for a loop gain less than one the real part of Z will always be positive.

Figure 8.18 shows how the real and imaginary parts of the impedance vary as a function of frequency, both for the analytic TES impedance in Equation (8.52) and for the device impedance calculated by computationally inverting the matrix in Equation (8.35). The dip in the imaginary part of the impedance corresponds to a change in magnitude of the real part of the impedance. There is extremely good agreement between the calculated and analytic TES impedances, showing that computationally inverting the matrix gives the same result for the impedance as the derived expression, as expected.

The input impedance, defined as the sum of the amplifier impedance and the TES impedance, gives information about circuit stability. If this impedance has a negative real part then the circuit may be unstable. For a HEMT circuit, this impedance is

$$Z_{\mathrm{in}} = \frac{R_{\mathrm{A}} i2\pi f L}{R_{\mathrm{A}} + i2\pi f L} + R_0(1+\beta_{\mathrm{I}}) + \frac{\mathscr{L}_{\mathrm{I}} R_0(2+\beta_I)}{(i2\pi f\tau_I+1)(1-\mathscr{L}_{\mathrm{I}})}. \tag{8.54}$$

Collecting together real and imaginary parts,

$$Z_{\mathrm{in}} = \left(\frac{2\pi f^2 L^2 R_{\mathrm{A}}}{2\pi f^2 L^2 + R_{\mathrm{A}}^2} + R_0(1+\beta_{\mathrm{I}}) + \frac{\mathscr{L}_{\mathrm{I}} R_0(2+\beta_I)}{(1+2\pi f^2\tau_I^2)(1-\mathscr{L}_{\mathrm{I}})}\right) + i\left(\frac{2\pi f L R_{\mathrm{A}}^2}{2\pi f^2 L^2 + R_{\mathrm{A}}^2} - \frac{2\pi f\tau_{\mathrm{I}}\mathscr{L}_{\mathrm{I}} R_0(2+\beta_I)}{(1+2\pi f^2\tau_I^2)(1-\mathscr{L}_{\mathrm{I}})}\right). \tag{8.55}$$

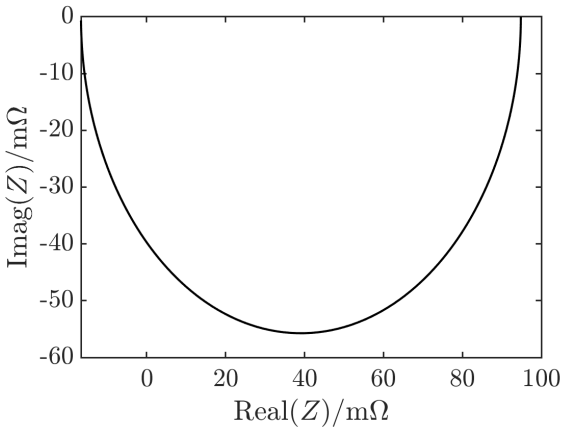

Figure 8.17 Real and imaginary parts of the complex impedance.

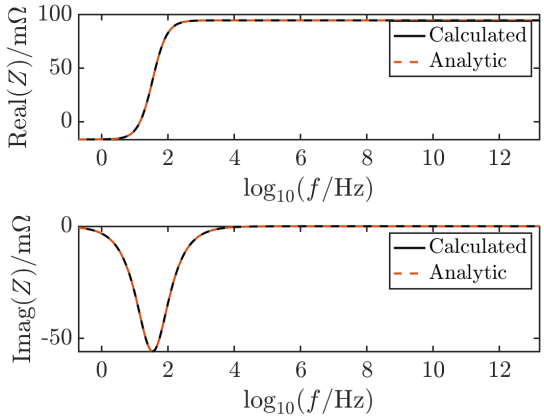

Figure 8.18 Real and imaginary parts of the complex impedance as a function of frequency determined by computationally inverting the matrix in Equation (8.35) and by using the analytic expression in Equation (8.52).

The real part of Equation (8.55) is negative only if $\mathscr{L}_\mathrm{I}$ is much greater than 1, at low frequencies where f is negligible. In this limit,

$$Z_\mathrm{in} \approx -R_0. \tag{8.56}$$

8.4.3 Circuit resonance

For a circuit consisting of two impedances in series, resonance will occur when the real parts of the two impedances are equal and when the imaginary parts are equal in magnitude but opposite in sign. To avoid circuit resonance I therefore wanted to ensure that one of these conditions is never possible. The condition for the imaginary components to be equal in magnitude but

opposite in sign is

$$R_0(1+\beta_I)+\frac{\mathscr{L}_\mathrm{I}R_0(2+\beta_I)}{(1-\mathscr{L}_\mathrm{I})(1+2\pi f^2\tau_I^2)}=\frac{2\pi f^2L^2R_\mathrm{A}}{R_\mathrm{A}^2+2\pi f^2L^2}. \tag{8.57}$$

This leads to the condition that

$$(2\pi f)^2=-\frac{\left(\frac{\mathscr{L}_\mathrm{I}}{\mathscr{L}_\mathrm{I}-1}R_0(2+\beta_I)\tau_I+L\right)R_\mathrm{A}^2}{R_\mathrm{A}^2L+\frac{\mathscr{L}_\mathrm{I}}{\mathscr{L}_\mathrm{I}-1}R_0(2+\beta_I)\tau_IL^2}. \tag{8.58}$$

As long as the loop gain $\mathscr{L}_\mathrm{I}>1$, the right hand side of this equation will always be negative so the circuit resonance conditions will never be achieved.

8.4.4 Reflection coefficient

The reflection coefficient r gives information about the magnitude of the reflected electrical signal relative to the transmitted electrical signal when a voltage perturbation is applied to the circuit. I calculate the reflection coefficient as a function of frequency for voltage signals incident on the TES. It is desirable for the TES reflection coefficient to have a real part with magnitude less than 1, since otherwise the TES is a source of power, which is beneficial for oscillatory circuits but not for amplification circuits. For the HEMT circuit,

$$\begin{aligned} r&=\frac{Z_\mathrm{TES}-(Z_\mathrm{amp}+R_\mathrm{S})}{Z_\mathrm{TES}+Z_\mathrm{amp}+R_\mathrm{S}} \\ &=\frac{R_0(1+\beta_\mathrm{I})+\frac{\mathscr{L}_\mathrm{I}R_0(2+\beta_I)}{(i2\pi f\tau_I+1)(1-\mathscr{L}_\mathrm{I})}-\left(\frac{R_\mathrm{A}i2\pi fL}{R_\mathrm{A}+i2\pi fL}+R_\mathrm{S}\right)}{R_0(1+\beta_\mathrm{I})+\frac{\mathscr{L}_\mathrm{I}R_0(2+\beta_I)}{(i2\pi f\tau_I+1)(1-\mathscr{L}_\mathrm{I})}+\frac{R_\mathrm{A}i2\pi fL}{R_\mathrm{A}+i2\pi fL}+R_\mathrm{S}}. \end{aligned} \tag{8.59}$$

Figure 8.19 shows the variation of the real and imaginary parts of the reflection coefficient as a function of frequency for a TES bias point resistance of 15.8 mΩ, whilst Figure 8.20 shows the variation of the real part of the reflection coefficient for a series of TES resistances. Figure 8.19a shows that the real part of the reflection coefficient has magnitude less than one for frequencies above 10^4 Hz, for a typical TES bias point resistance. From Figure 8.19b, the real part approaches, but does not cross, -1 at high frequencies. From Figure 8.20, as the bias point resistance increases, the frequency above which the reflection coefficient has magnitude less than 1 increases, but even at the highest resistances, this frequency is still below the lower limit of the HEMT bandwidth.

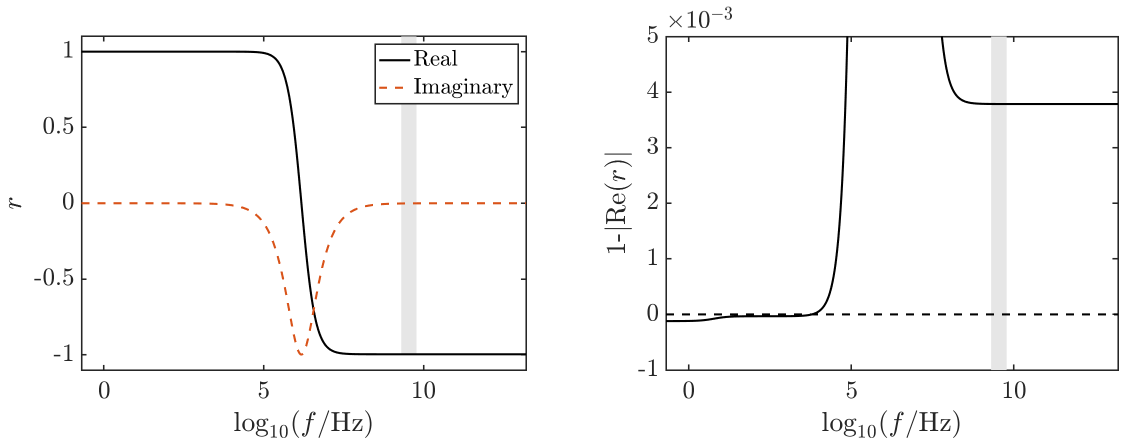

(a) (b)

Figure 8.19 (a) Real and imaginary parts of the TES reflection coefficient as a function of frequency, for a TES resistance of 15.8 mΩ. (b) 1-|Re(r)|, to better indicate the values of frequency for which the reflection coefficient has magnitude fractionally greater than 1. The dashed line indicates when |Re(r)|=1. In both plots, the shaded grey region indicates the bandwidth in which a typical HEMT amplifier operates.

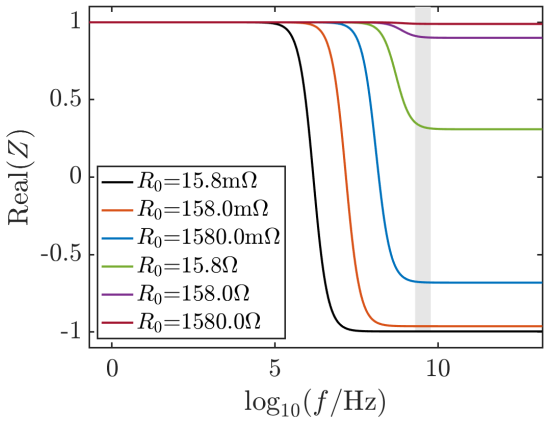

Figure 8.20 Real part of the TES reflection coefficient as a function of frequency, for a series of TES resistances. The shaded grey region shows the bandwidth of the HEMT amplifier.

8.5 Identification of device parameters for optimisation

The effects on the output voltage across the HEMT terminals of varying the TES bias point resistance R_0, the inductance across the HEMT terminals L and the thermal conductance to the heat bath G were then investigated.

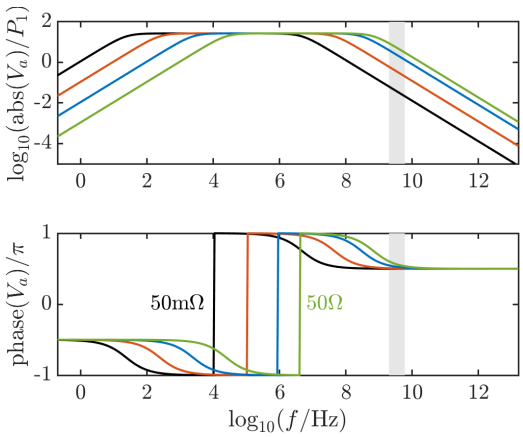

Figure 8.21 Amplitude and phase of the voltage across the amplifier terminals as a function of input frequency f, normalised by the power input P_1, for a range of TES bias point resistances R_0. The inductance across the HEMT terminals is 10 nH and the thermal conductance to the heat bath is 100 pWK^{-1}. The input resistance of the HEMT is 50 Ω, and the grey shaded region indicates the typical bandwidth of a HEMT amplifier.

Figure 8.21 shows the effect on the amplitude and phase of the voltage across the amplifier terminals of changing the TES bias point resistance R_0. From this figure, as the TES bias point resistance is increased the roll off of the amplifier voltage increases in frequency. This is because as R_0 is increased, $\tau_{\text{elec.}} = L/(R0(1 + \beta_I) + R_S)$ decreases so its corresponding frequency increases.The position of the jump in phase also increases in frequency as the TES resistance at the bias point increases. It is therefore desirable to have a TES with a higher normal state resistance and hence bias point resistance for high frequency readout.

Figure 8.22 shows the amplitude and phase of the voltage across the amplifier terminals as the inductance connected across the HEMT terminals varies. As the inductance across the HEMT terminals increases, the circuit response bandwidth narrows and the position of the roll off of the amplifier voltage decreases in frequency but the amplitude of the response increases, meaning that the need for a wide bandwidth response and a response at high frequency must be balanced by the need for a detectable response amplitude.

In Figure 8.23, the effect of changing the thermal conductance to the heat bath G on the amplitude and phase of the voltage across the amplifier is shown. Increasing the thermal conductance to the surroundings increases the point at which the amplifier output voltage

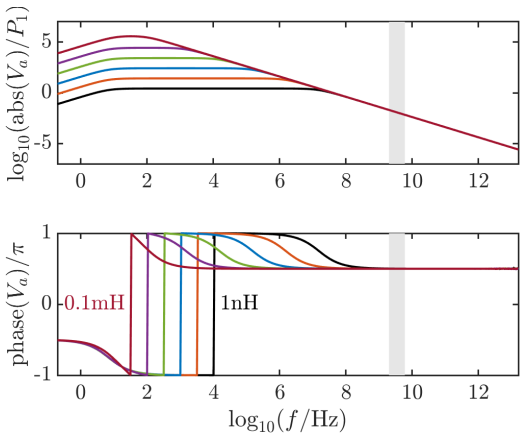

Figure 8.22 Amplitude and phase of the voltage across the amplifier terminals as a function of input frequency f, normalised by the power input P_1, for a range of inductances across the HEMT terminals L. The TES resistance is 50 mΩ and the thermal conductance to the heat bath is 100 pWK^{-1}. The input resistance of the HEMT is 50 Ω, and the grey shaded region indicates the typical bandwidth of a HEMT amplifier.

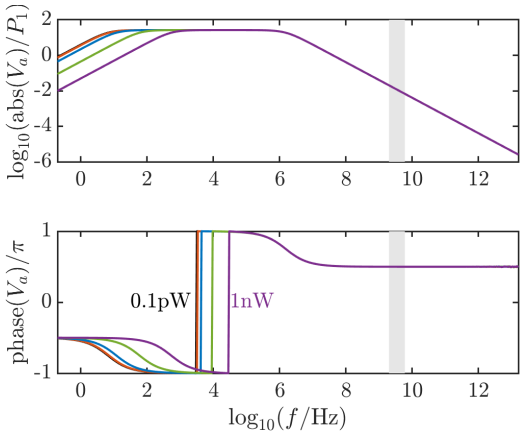

Figure 8.23 Amplitude and phase of the voltage across the amplifier terminals as a function of input frequency f, normalised by the power input P_1, for a range of thermal conductances to the heat bath G. The TES resistance is 50 mΩ and the inductance across the HEMT terminals is 10 nH. The input resistance of the HEMT is 50 Ω, and the grey shaded region indicates the typical bandwidth of a HEMT amplifier.

rises, thereby narrowing the response bandwidth of the circuit. This is because as G increases, $\tau_{\text{therm.}} = C/G$ decreases and hence its corresponding frequency increases. Reduced thermal isolation will therefore increase the bandwidth of the response across the HEMT. As the thermal conductance to the surroundings is increased, the position of the jump in phase also increases in frequency.

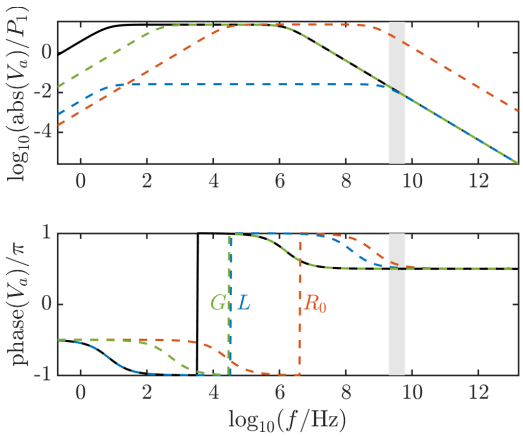

Figure 8.24 Amplitude and phase of the voltage across the amplifier terminals as a function of input frequency f, normalised by the power input P_1, showing the effects of varying the thermal conductance to the heat bath G, the TES resistance R_0 and the inductance across the HEMT terminals L. The input resistance of the HEMT is 50 Ω. The shaded grey region indicates the typical bandwidth of the HEMT amplifier.

Figure 8.24 summarises the effects on the amplitude and phase across the amplifier terminals of varying the thermal conductance G, the TES resistance at the bias point R_0 and the inductance across the HEMT terminals L. Increasing the TES resistance shifts the power plateau up in frequency; decreasing the inductance widens the bandwidth but reduces the amplitude of the response; and increasing the thermal conductance moves the start of the power plateau up in frequency.

8.6 Optimisation of TESs for different readout circuits

The thermal circuits for readout using a TES and a SQUID are the same, the circuits differ only in their electrical components. The equivalent circuit for TES readout using a SQUID is shown in Figure 8.2, and that for readout using a HEMT in Figure 8.3.

The SQUID acts as a current to voltage converter, and so the important parameter to consider is the current flowing through the input inductance to the SQUID. As the HEMT acts as a

voltage to voltage converter, in this case it is the voltage across the terminals of the HEMT that matters.

In order to read out TESs using a HEMT, the response time of the detector must fall within the bandwidth of the HEMT, and so the power plateau needs to be moved to higher frequencies. Figure 8.24 shows that the plateau increases in frequency when the TES resistance is increased, when the thermal conductance to the surroundings is increased, and when the impedance across the HEMT terminals is lowered. To optimise HEMT performance, I therefore wanted to model a circuit with a highly resistive TES with good thermal conductance to its surroundings and a low impedance across the terminals of the HEMT.

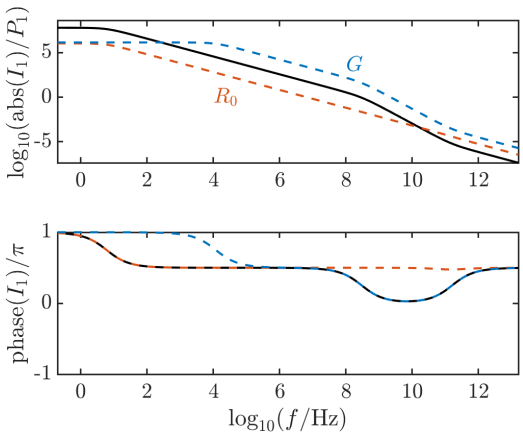

Figure 8.25 Amplitude and phase of the current through the SQUID readout as a function of input frequency f, normalised by the power input P_1, showing the effects of varying the thermal conductance to the heat bath G and the TES resistance R_0 The input inductance to the SQUID is 50 pH.

When optimising SQUID readout, the input inductance to the SQUID is fixed at about 50 pH for a RF SQUID, and so only the TES resistance, the heat capacity and the thermal conductance can be varied. From Figure 8.25, increasing the bias point resistance reduces the overall response of the SQUID, but increasing the thermal conductance increases the overall response and extends the plateau in responsivity, and so it is therefore more desirable to increase the thermal conductance whilst maintaining the same or smaller TES bias point resistance.

Figure 8.26 shows the HEMT bandwidth, indicated by the grey shaded region, falls between the frequency corresponding to the thermal time constant and the frequency corresponding to the electrical time constant due to the HEMT, where the responsivity is flat. Figure 8.27 shows that the responsivity of the current in the SQUID circuit is flat at low frequencies, and so the SQUID is better operated at lower frequencies.

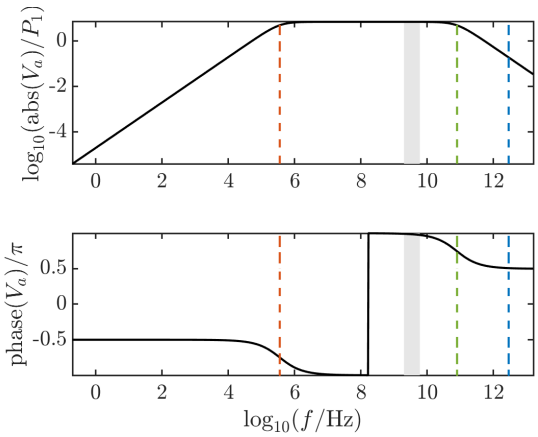

Figure 8.26 Amplitude and phase of the voltage across the amplifier terminals as a function of input frequency f, normalised by the power input P_1. The inductance across the HEMT terminals is 0.1 nH, the TES resistance is 300 Ω and the thermal conductance to the heat bath is 100 pWK^{-1}. The grey shaded region indicates the bandwidth of the HEMT. The red, blue and green dashed lines indicate the frequencies corresponding to the time constants $\tau_{\mathrm{therm.}}$, $\tau_{\mathrm{elec.}}$ and $\tau_{\mathrm{amp.}}$ respectively.

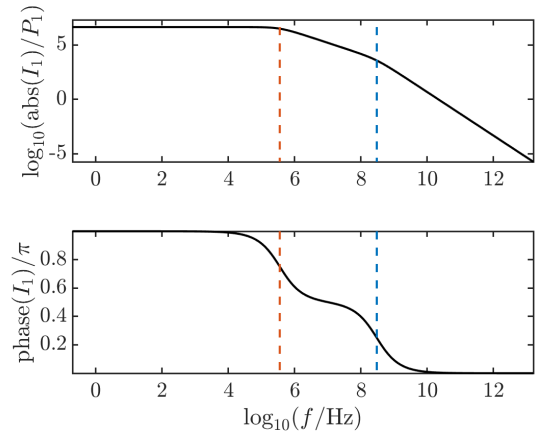

Figure 8.27 Amplitude and phase of the current through the SQUID readout as a function of input frequency f, normalised by the power input P_1. The input inductance to the SQUID is 50 nH, the TES resistance is 15.8 mΩ and the thermal conductance to the heat bath is 100 pWK^{-1}. The red and blue dashed lines indicate the frequencies corresponding to the time constants $\tau_{\mathrm{therm.}}$ and $\tau_{\mathrm{elec.}}$ respectively.

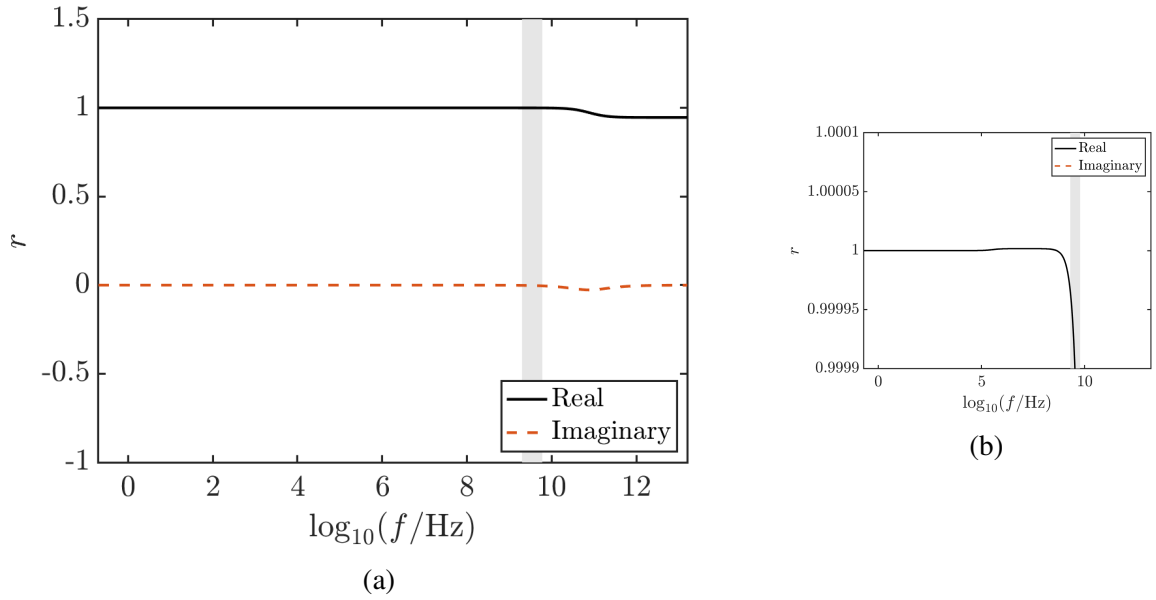

Figure 8.28 Real and imaginary parts of the reflection coefficient of the HEMT circuit as a function of frequency, for a TES resistance of 300 Ω. (b) shows the region around $r = 1$ in more detail, and the grey shaded region indicates the HEMT bandwidth.

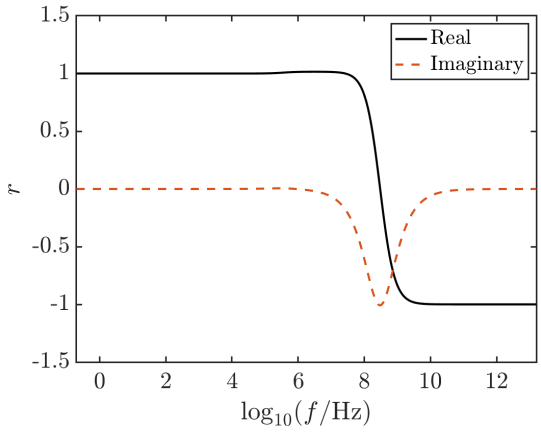

Figure 8.29 Real and imaginary parts of the reflection coefficient of the SQUID circuit as a function of frequency, for a TES resistance of 15.8 mΩ.

In Figure 8.28, the real part of the reflection coefficient is slightly greater than 1 for frequencies less than $10^6 s^{-1}$. For a SQUID, the reflection coefficient is significantly greater than 1 in a similar region, as shown by Figure 8.29.

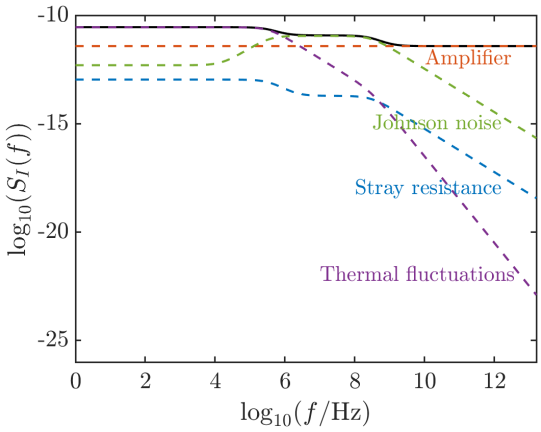

Figure 8.30 Contributions to the overall SQUID current noise I_n.

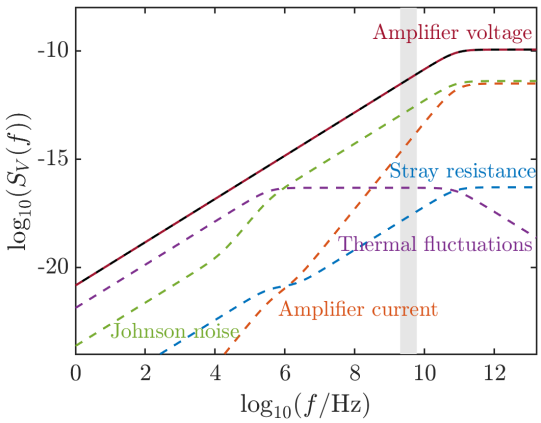

Figure 8.31 Contributions to the overall HEMT voltage noise V_n. The shaded grey region shows the HEMT bandwidth.

For a SQUID, the current noise in the circuit will cause noise in the readout, shown in Figure 8.30. This noise falls off as a function of frequency, with the thermal fluctuations providing the greatest contribution at low frequencies and the Johnson noise from the TES dominating at higher frequencies. In the voltage noise plot for the HEMT in Figure 8.31, the contribution from the noise voltage corresponding to the amplifier dominates the overall noise.

The NEPs for the SQUID and the HEMT are very similar in shape, differing more at high frequencies when electrical effects become more significant, as shown in Figure 8.32. As the overall NEP is flat as a function of frequency up to about $10^{6.5} s^{-1}$, for optimal noise performance

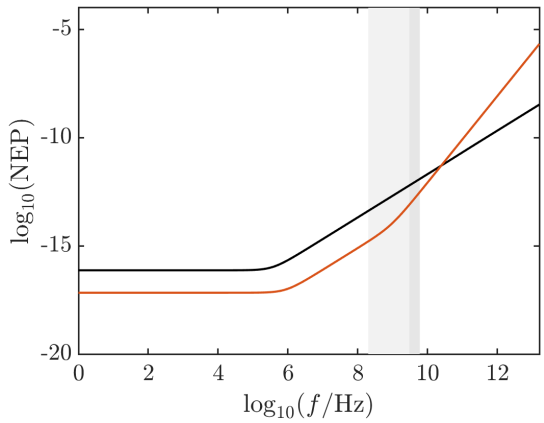

Figure 8.32 Noise equivalent power for readout using a HEMT and a SQUID. The grey shaded region indicates a typical HEMT bandwidth, and the lighter grey shaded region indicates the bandwidth achievable with one of the Low Noise Factory's HEMT amplifiers.

the TES should be operated below this frequency. This is not a problem for amplification using a SQUID. However, the assumed HEMT bandwidth is from about $10^{10}\mathrm{s}^{-1}$ to $10^{10.5}\mathrm{s}^{-1}$ so at this frequency the NEP will be slightly higher. There is the possibility of using a HEMT with a lower operating frequency. The cryogenic noise amplifiers made by the Low Noise Factory (https://www.lownoisefactory.com) can operate at 200MHz, as shown in Figure 8.32, reducing the NEP at operation down to a possible $10^{-13}\mathrm{W}/\sqrt{\mathrm{Hz}}$.

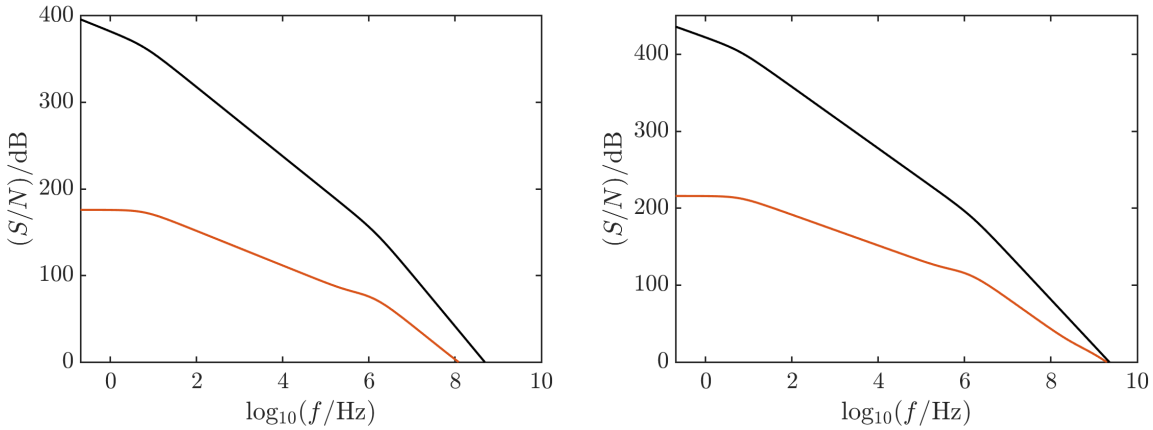

Figure 8.33 Signal to noise ratio for readout using an optimised SQUID (red lines) and an optimised HEMT (black lines). (b) has a signal amplitude two orders of magnitude higher than (a).

The two plots in Figure 8.33 compare the SQUID and HEMT signal to noise ratios, calculated as described in Section 8.3.2. In both plots, the signal to noise ratio drops off much faster as a function of frequency for the HEMT than for the SQUID, but since the signal to noise ratio is initially much higher, the point where its log is zero (and therefore the signal and noise become of equal magnitude) is higher in frequency. Increasing the magnitude of the signal has more of an effect on the signal to noise ratio for the SQUID than for the HEMT, and so using a HEMT for high frequency readout is more advantageous when the signal of interest is small.

8.7 Conclusions

I have developed a model to analyse the thermal and electrical circuits for TES readout using a HEMT amplifier in parallel with an inductor. The model agrees with theoretically calculated limits, with changes in behaviour determined by three time constants: one linked to the thermal behaviour and two related to the electrical behaviour. I have shown mathematically that the readout does not affect the TES impedance. This analysis does not take into account environmental factors that could affect the noise behaviour for readout using a HEMT. For example, fluctuations in fridge temperature and external magnetic fields will both increase the system noise.

The parameters that can be varied to improve performance of this circuit at high frequencies are the thermal conductance to the heat bath G, the impedance connected across the HEMT terminals L and the TES bias point resistance (linked to the normal state resistance, assuming that $R_{\text{bias}}/R_{\text{n}}$ is constant). For high frequency readout, it is desirable to have a TES with a high bias point resistance, with a relatively small inductance across the HEMT terminals and a low thermal conductance to the surroundings.

The noise in the circuit was calculated using a generalised responsivity matrix, showing that the noise is dominated by thermal fluctuations at low frequencies, Johnson noise in the TES at intermediate frequencies, and the amplifier noise voltage at high frequencies. The total noise and hence the NEP increase with frequency, which is not beneficial for high frequency readout. For typical TES parameters, the signal to noise ratio is greater than one below frequencies of about 100 MHz. The readout circuit is stable with respect to a number of different stability metrics, with a positive input impedance at all frequencies and no circuit resonance.

I selected two sets of parameters to optimise the readout circuits using a SQUID and using a HEMT respectively. These optimised parameters give a signal to noise ratio greater than one in the region accessible using a Low Noise Factory HEMT amplifier, showing that it would be possible to use one of these HEMTs for readout at higher frequencies.

Overall, the work described in this chapter provides a good justification to carry out experimental studies of TESs read out using a HEMT amplifier in parallel with an inductor, as such a system would enable readout at higher frequencies and over wider bandwidths without any stability issues. It would be beneficial to create this new readout system in parallel with a series of TESs with high bias point resistance and low thermal isolation, to optimise the devices for HEMT readout.

Chapter 9

Conclusions

At the start of this thesis, I asked to what extent microscopic modelling can be used to predict TES behaviour and to inform device development. The proximity effect model can be used to validate proposed device designs before any processing work takes place. In particular, it allows checks to see whether the electrothermal parameters and the transition temperature meet the design specifications. My research has highlighted that bilayer geometry has a significant effect on the predictive ability of microscopic modelling. Smaller, unpatterned bilayers are well described by the models I have used, whilst larger bilayers display unpredictable magnetic field behaviour, and bilayers with thick normal metal bars exhibit a meander pattern of current flow, resulting in a much larger self-field and requiring complex modelling to describe. Models of on-chip superconducting shielding indicated that perpendicular fields could be reduced by a factor of 100, but experimental testing revealed that these models had not accounted for the effects of trapped flux, demonstrating a shielding factor of 2-5 and indicating that a more complex shield design may be required.

9.1 Review of key findings

During my research, I have developed a proximity effect model to describe the microscopic physics of TES bilayers both with and without normal metal stripes, which was validated against several sets of devices and shown to give a reasonable account of the $I(V)$ curves for most devices tested. I wrote software to implement this model and used it to design an experimental study, investigating the effects of bilayer geometry on TES performance with a particular focus on magnetic field dependence. As part of this study I developed a new system to allow a more detailed study of magnetic field effects and carried out the very first measurements of the directional field dependence of TESs. I identified that bilayers of around 20 µm side length give low field sensitivity and relatively sharp transitions whilst displaying predictable behaviour. I

demonstrated that the use of on-chip shielding has enormous potential to reduce the magnetic field experienced by TESs whilst at the same time providing a reflective backstop. Finally, I investigated an innovative alternative readout scheme using a HEMT in parallel with an inductor and showed that this allows readout at much higher frequencies than a SQUID-based readout method. For each area of research, I summarise the key findings in this chapter.

9.1.1 Proximity effect model

- I developed a 1D model based on the diffusive Usadel equations [91] to describe TES bilayers operating at low temperatures. This model accounts for the effects of normal metal structures on the bilayer, with modified boundary conditions to account for thickness discontinuities whilst ensuring supercurrent conservation.
- I wrote Matlab software to solve the system of equations in this 1D model and make predictions of the critical current of the TES bilayer.
- I used this software to calculate the principal TES characteristics α, β, T_c, $R(T, I)$ and $I_c(\Phi)$ for an idealised bilayer, and demonstrated good qualitative agreement with experimental observations such as oscillation of α, β and I_c with applied field [97], and the reduction of α with the addition of metal bars [88].
- I then applied this model to real devices and used it to predict $I(V)$ curves for a series of different geometries and material combinations. The 1D model gave an excellent account of Ti/Au TESs and a reasonable account of Mo/Au TESs, although for some devices the transition predicted by the model was broader than that observed.
- For the Ti/Au device with bars, an effective T_c was needed for the bars to account for the Ti adhesion layer.
- The model for the Mo/Au TESs is very sensitive to T_c of the bilayer. Since no experimental measurements of this T_c were available, I used the lowest-temperature $I(V)$ curve to calibrate this value. Ideally, no fitting or adjustment should be required.
- The 1D model did not give a good account of devices with thick (>50 nm) normal metal bars, indicating 2D current flow in these devices.

9.1.2 Effect of bilayer geometry

- I designed a set of TESs to enable systematic study of the effects of bilayer geometry on device behaviour, using the proximity effect model software.

- I carried out a series of calibration tests to provide realistic parameters for my modelling work, including measurements of T_c for the different materials.
- Measurements of $R(T)$ for large, unreleased TESs showed that T_c does not vary with side length for very large devices (150 µm side length bilayers).
- TESs with normal metal stripes across the whole bilayer width showed a residual resistance. This was not observed for devices with partial width bars, indicating 2D current flow in a meander pattern.
- I carried out a set of measurements to study the behaviour of TESs with different bilayer geometries, investigating the transition temperature, the critical current as a function of temperature, the small signal parameters α and β, the response time and the device noise.
- I wrote Matlab software to analyse the data collected.
- TESs with smaller bilayers show behaviour that is more consistent with our current understanding of how TESs work, but have higher noise than TESs with larger bilayer areas. These larger bilayers additionally display sharper transitions. TESs with 20 µm side length bilayers provide a good compromise with relatively low noise, fast device response and sharp transitions.

9.1.3 Magnetic field modelling

- I created a simple model to predict the directional field dependence of TES critical current, showing that TESs are most sensitive to applied field perpendicular to the bilayer, especially for small field strengths. For larger field strengths the response surface shows oscillatory behaviour.
- A model to predict the effects of the field generated by current flow in the superconducting leads suggests significant suppression of bias current, α and β for some TESs, which is not observed experimentally [4].
- TESs with odd numbers of bars have a larger self-field so may be less affected by the presence of external magnetic fields.

9.1.4 Magnetic sensitivity

- I designed a new magnetic field system which allows application of a uniform magnetic field in any direction, to study the TES magnetic response in detail. I developed a method

for carrying out spherical scans, in which the field magnitude is fixed and its direction is varied, and implemented this method in the system software.

- I calibrated the fields produced by this system using a Hall probe, showing excellent field stability. I repeated the calibration with a new Hall probe based on a 2D electron gas (2DEG), which was a good verification of the calibration testing as well as demonstrating the improved performance of the 2DEG probe.

- I carried out measurements to indicate the field sensitivity of TESs with different bilayer geometries, studying the variation of bias current, transition temperature, response time, electrothermal parameters, noise and critical current as a function of field magnitude. I also investigated the variation of bias current as a function of field direction.

- TESs with larger bilayer areas show less variation in bias point when magnetic fields are applied, and hence have lower magnetic field sensitivity. However these devices show phase slip behaviour, which is not seen in TESs with smaller bilayer areas.

- Normal metal bars reduce the magnetic field sensitivity, especially for TESs with larger bilayer areas, but also slow down the device response due to the increase in heat capacity.

- Although maxima and minima are observed in the TES current as the applied magnetic field varies, the TESs don't become fully normal. This contradicts the theory, based on a simple model of magnetic phase, that the current should be zero when an integer number of magnetic flux quanta pass through the TES [98]. This shows that other effects, such as the self-field of the bilayer, have a significant influence on device behaviour.

- Whether the bilayer has an odd or even number of bars affects its self field and hence its magnetic field behaviour. As devices with odd numbers of bars are slower but less sensitive to magnetic fields, when considering the number of bars to use, there is a trade off between fast response and reduced sensitivity to external fields.

9.1.5 On-chip shielding

- I wrote software to estimate the reduction in magnetic field possible using on-chip shielding, using a model based on the superconducting method of images.

- Introducing an on-chip shield made from a superconductor such as aluminium or niobium can theoretically reduce the perpendicular field experienced by the TESs by factor of 100 whilst also providing a reflective backstop.

- A silicon-on-insulator wafer was used to make an on-chip shield, with a TES - shield separation of 21 μm.
- This shield reduced the magnetic field experienced by all of the TESs tested in all directions.
- Using a niobium on-chip shield, I measured a shielding factor of between 2-5 for the TESs tested. This is less than the theoretical prediction of 100 due to trapped flux in the niobium thin film.

9.1.6 HEMT readout

- I developed a model to analyse the thermal and electrical circuits for TES readout using a HEMT amplifier in parallel with inductor. This model agrees with the theoretically calculated limits.
- I identified the parameters that can be varied to improve the TES performance at high frequencies. These parameters are the thermal conductance to the heat bath G, the inductance in parallel with the HEMT L and the TES bias point resistance R_0.
- To give a good response at high frequencies, a TES should have a high bias point resistance, a small inductance across the terminals of the HEMT and a low thermal conductance to its surroundings.
- I calculated the noise in this readout scheme using a generalised responsivity matrix approach. For typical device parameters, the S/N is greater than 1 below 100 MHz. Optimised parameters give a S/N above 1 in a region that is accessible using a HEMT from the Low Noise Factory, assuming the noise produced by external sources such as temperature fluctuations and magnetic fields is not significant.

9.2 Improvements and extensions

From the calibration testing in Chapter 4, I have shown that current flow in the bilayers of patterned Mo/Au TESs made by several groups follows a meander pattern, which cannot be described using a 1D model. The 2D flow of the current could therefore be accounted for in a microscopic model to give a good account of the behaviour of bilayer-based TES designs.

As well as this, the thermal coupling between the device and its surroundings must be tuned to allow effective detection and dissipation of the absorbed power [82]. This is achieved either by varying the transition temperature, altering the strength of the electron-phonon thermal

coupling [18], or by modifying the supporting legs [12]. Extending this model to describe the full electrothermal behaviour of the TES would allow me to account for this thermal coupling and make the model even more realistic.

Additionally, TESs may be operated and read out under AC bias, and so this microscopic modelling could be extended to describe the AC behaviour of TESs. An AC model of the microscopic behaviour could give valuable insights as to why AC-biased TESs exhibit higher NEPs, as reported by Akamatsu et al. [157].

The performance of the on-chip shield in my experimental system was degraded by the presence of trapped flux. This trapped flux could be significantly reduced or eliminated by making the shielding layer from a lower-T_c superconductor, which could be cooled in zero-field conditions using the magnetic coil system, or a multilayer of niobium and a high-permeability metal. This would produce a reduction in the field experienced by the TES without the additional stray field due to trapped flux. Trapped flux prevented the on-chip shielding achieving an optimal reduction in field, illustrating the drawbacks of passive shielding. The magnetic field system that I developed can be used as an active shield, allowing the shielded devices to be operated under zero-field conditions. This shows the advantages of having a shielding system with an adjustable shielding factor. The development of new Hall sensors, such as the 2D electron gas sensor tested in this thesis, is making active shielding easier to implement, with these sensors able to operate below 1 K, allowing in-situ monitoring of the background magnetic fields.

The on-chip shields could also be made larger, as the initial set of shields were designed to allow good clearance between the pillar bearing the shield and the edge of the TES well, to prevent damage to either the TESs or the shields if there were any errors in alignment. Larger shields would be less susceptible to any edge effects and would therefore have a shielding factor closer to that predicted using the method of image dipoles.

9.3 Applications and future research outlook

I have already used the proximity effect model to test devices prior to manufacture, when designing the devices for my systematic study. The model enabled me to select a series of lengths that give a good range of transition temperatures whilst ensuring the highest and lowest transition temperatures were still within the temperature range accessible using the ADR. When manufactured, the devices followed the trends predicted by my model and all had transitions within the temperature range of the ADR. I conclude that the proximity effect model provides a valuable tool to validate potential device designs prior to manufacture.

My experimental system allows measurement of the magnetic field dependence of any chip-based superconducting detector, including the directional field dependence, which is an important input to the magnetic shielding design. From my systematic study of bilayer geometry, I have identified an optimal bilayer size of 20 µm side length, which gives a good balance between predictable behaviour, low noise and a fast response. Whether or not normal metal bars optimise performance depends on the specifications required: adding bars will reduce magnetic field sensitivity at the expense of slowing the response time. TESs with rectangular bilayers may provide an excellent compromise, with a small width to suppress any phase slip behaviour and reduce the heat capacity, and a relatively long length to improve noise performance and device stability [177].

On-chip shielding shows excellent potential, allowing the fields experienced by a TES to be reduced with very little additional weight. This is especially important for space applications, where shielding must be designed to add as little extra mass to the spacecraft as possible.

Using a HEMT amplifier in parallel with a resistor would allow readout of TESs at higher frequencies and with a wider bandwidth, with no stability issues. I have used a model of this readout circuit to suggest ways that TESs could be designed for optimal performance under HEMT readout. Following on from the promising results shown by the modelling, this alternative readout scheme should now be tested experimentally.

Throughout my research, a detailed understanding of the microscopic physics of TESs has been hugely beneficial, allowing me to make accurate predictions of the effects of bilayer geometry and magnetic field sensitivity on the performance of the devices. As a result of this, the first set of devices manufactured met the specifications for my systematic study, without any need for iterative design. This emphasises that understanding the microscopic physics of transition edge sensors is vital in optimising TES performance, especially as TESs become more widely used in the near future.

References

[1] J. E. Sadleir, S. J. Smith, S. R. Bandler, J. A. Chervenak, and J. R. Clem, "Longitudinal proximity effects in superconducting transition-edge sensors", Phys. Rev. Lett. **104**, 047003 (2010).

[2] D. J. Goldie, A. V. Velichko, D. M. Glowacka, and S. Withington, "Ultra-low-noise MoCu transition edge sensors for space applications", J. Appl. Phys. **109** (2011) 10.1063/1.3561432.

[3] D. J. Goldie et al., "Performance of horn-coupled transition edge sensors for L- and S-band optical detection on the SAFARI instrument", Proc. SPIE **9914** (2016) 10.1117/12.2232740.

[4] P. Khosropanah et al., "Ultra-low noise TES bolometer arrays for SAFARI instrument on SPICA", Proc. SPIE **9914**, 99140B (2016).

[5] E. Williams et al., "Ultra-low-noise Transition Edge Sensors for Far Infrared Wavelengths : Optical Design , Measurement and Stray Light Control", Proc. SPIE (in prep) (2018).

[6] S. J. Smith et al., "Transition-edge sensor pixel parameter design of the microcalorimeter array for the x-ray integral field unit on Athena", Proc. SPIE **9905**, 99052H (2016).

[7] L. Gottardi et al., "Development of the superconducting detectors and read-out for the X-IFU instrument on board of the X-ray observatory Athena", Nucl. Instruments Methods Phys. Res. A **824**, 622–625 (2016).

[8] A. Puiu et al., "Development of transition edge sensors with rf-SQUID based multiplexing system for the HOLMES experiment", J. Phys. Conf. Ser. **888** (2017) 10.1088/1742-6596/888/1/012069.

[9] A. Puiu et al., "Updates on the Transition-Edge Sensors and Multiplexed Readout for HOLMES", J. Low Temp. Phys. **193**, 1167–1173 (2018).

[10] W. B. Doriese et al., "A practical superconducting-microcalorimeter X-ray spectrometer for beamline and laboratory science", Rev. Sci. Instrum. **88** (2017) 10.1063/1.4983316.

[11] J. N. Ullom et al., "Characterization and reduction of unexplained noise in superconducting transition-edge sensors", Appl. Phys. Lett. **84**, 4206–4208 (2004).

[12] D. Osman, S. Withington, D. J. Goldie, and D. M. Glowacka, "Transition edge sensors with few-mode ballistic thermal isolation", J. Appl. Phys. **116**, 064506 (2014).

[13] E. A. Williams, S. Withington, C. N. Thomas, D. J. Goldie, and D. Osman, "Superconducting transition edge sensors with phononic thermal isolation", J. Appl. Phys. **124** (2018) 10.1063/1.5041348.

[14] S. J. Smith et al., "Small Pitch Transition-Edge Sensors with Broadband High Spectral Resolution for Solar Physics", J. Low Temp. Phys. **167**, 168–175 (2012).

[15] K. D. Irwin, "An application of electrothermal feedback for high resolution cryogenic particle detection", Appl. Phys. Lett. **66**, 1998 (1995).

[16] D. J. Goldie, M. D. Audley, D. M. Glowacka, V. N. Tsaneva, and S. Withington, "Transition edge sensors for bolometric applications: Responsivity and saturation", J. Appl. Phys. **103**, 084509 (2008).

[17] D. J. Goldie et al., "Ultra-low-noise transition edge sensors for the SAFARI L-band on SPICA", Proc. SPIE **8452**, 84520A (2012).

[18] K. D. Irwin and G. C. Hilton, "Cryogenic Particle Detection", *Cryog. Part. Detect.* Vol. 99, edited by C. Enss (Springer-Verlag Berlin Heidelberg, 2005), 63–149.

[19] J. N. Ullom and D. A. Bennett, "Review of superconducting transition-edge sensors for x-ray and gamma-ray spectroscopy", Supercond. Sci. Technol. **28**, 084003 (2015).

[20] L. Howe et al., "Design and characterization of the POLARBEAR-2b and POLARBEAR-2c cosmic microwave background cryogenic receivers", ArXiv e-prints, 1–20 (2018).

[21] M. Hazumi et al., "LiteBIRD: A Satellite for the Studies of B-Mode Polarization and Inflation from Cosmic Background Radiation Detection", J. Low Temp. Phys. **194**, 443–452 (2019).

[22] J. Ding et al., "Optimization of Transition Edge Sensor Arrays for Cosmic Microwave Background Observations with the South Pole Telescope", IEEE Trans. Appl. Supercond. **27** (2017) 10.1109/TASC.2016.2639378.

[23] C. M. Posada et al., "Large arrays of dual-polarized multichroic TES detectors for CMB measurements with the SPT-3G receiver", Proc. SPIE **9914**, 991417 (2016).

[24] D. J. Goldie et al., "First Characterization of a Superconducting Filter-bank Spectrometer for Hyper-spectral Microwave Atmospheric Sounding with Transition Edge Sensors", ArXiv e-prints, 1–13 (2020).

[25] D. Fukuda et al., "Titanium-based transition-edge photon number resolving detector with 98% detection efficiency with index-matched small-gap fiber coupling", Opt. Soc. Am. **19** (2011).

[26] D. Rosenberg, A. E. Lita, A. J. Miller, S. W. Nam, and R. E. Schwall, "Performance of photon-number resolving transition-edge sensors with integrated 1550 nm resonant cavities", IEEE Trans. Appl. Supercond. **15**, 575–578 (2005).

[27] A. J. Miller et al., "Development of wide-band, time and energy resolving, optical photon detectors with application to imaging astronomy", Nucl. Instruments Methods Phys. Res. A **444**, 445–448 (2000).

[28] D. M. Glowacka, D. J. Goldie, and S. Withington, "Comparative Performance of Mo / Cu vs . Mo / Au Transition Edge Sensors for Space Science Applications", ISSTT Proc. **21**, 276–8 (2010).

[29] C. Portesi, E. Taralli, R. Rocci, M. Rajteri, and E. Monticone, "Fabrication of Au/Ti TESs for Optical Photon Counting", J. Low Temp. Phys. **151**, 261–265 (2008).

[30] J. M. Martinis, G. C. Hilton, K. D. Irwin, and D. A. Wollman, "Calculation of TC in a normal-superconductor bilayer using the microscopic-based Usadel theory", Nucl. Instruments Methods Phys. Res. A **444**, 23–27 (2000).

[31] C. M. Posada et al., "Fabrication of Detector Arrays for the SPT-3G Receiver", J. Low Temp. Phys., 1–9 (2018).

[32] E. M. Vavagiakis et al., "Magnetic Sensitivity of AlMn TESes and Shielding Considerations for Next-Generation CMB Surveys", J. Low Temp. Phys. **193**, 288–297 (2018).

[33] A. Suzuki et al., "Multi-chroic dual-polarization bolometric focal plane for studies of the cosmic microwave background", J. Low Temp. Phys. **167**, 852–858 (2012).

[34] C. Portesi, E. Taralli, L. Lolli, M. Rajteri, and E. Monticone, "Fabrication and characterization of fast TESs with small area for single photon counting", IEEE Trans. Appl. Supercond. **25**, 2101004 (2015).

[35] A. Orlando et al., "Antenna-coupled TES Bolometer Arrays for BICEP2/Keck and SPIDER", Proc. SPIE **7741**, 77410H–77410H–10 (2010).

[36] J. Uhlig et al., "High-resolution X-ray emission spectroscopy with transition-edge sensors: present performance and future potential", J. Synchrotron Radiat. **22**, 766–775 (2015).

[37] M. K. Bacrania et al., "Large-area microcalorimeter detectors for ultra-high-resolution X-ray and gamma-ray spectroscopy", IEEE Trans. Nucl. Sci. **56**, 2299–2302 (2009).

[38] P. Roelfsema et al., "SAFARI new and improved: extending the capabilities of SPICA's imaging spectrometer", Proc. SPIE **9143**, 91431K (2014).

[39] B. Reichborn-Kjennerud et al., "EBEX: A balloon-borne CMB polarization experiment", Proc. SPIE **7741**, 77411C (2010).

[40] V. Yefremenko et al., "Design and fabrication of 90 GHz TES polarimeter detectors for the south pole telescope", IEEE Trans. Appl. Supercond. **23**, 2100605 (2013).

[41] S. Dahal et al., "Design and characterization of the Cosmology Large Angular Scale Surveyor (CLASS) 93 GHz focal plane", Proc. SPIE **10708** (2018) 10.1117/12.2311812.

[42] Y. Inoue et al., "POLARBEAR-2: an instrument for CMB polarization measurements", Proc. SPIE (2016) 10.1117/12.2231961.

[43] J. G. Staguhn et al., "GISMO: a 2-millimeter bolometer camera for the IRAM 30 m telescope", Proc. SPIE **6275**, 62751D (2006).

[44] W. S. Holland et al., "SCUBA-2: a large-format submillimeter camera on the James Clerk Maxwell Telescope", Proc. SPIE **4855**, 1 (2003).

[45] S. R. Dicker et al., "MUSTANG: 90 GHz science with the Green Bank Telescope", Millim. Submillim. Detect. Instrum. Astron. IV **7020**, 702005 (2008).

[46] R. Strauss et al., "A detector module with highly efficient surface-alpha event rejection operated in CRESST-II Phase 2", Eur. Phys. J. C **75**, 352 (2015).

[47] S. Roth et al., "Cryogenic composite detectors for the dark matter experiments CRESST and EURECA", Opt. Mater. (Amst). **31**, 1415–1420 (2009).

[48] R. H. den Hartog et al., "Requirements for the detectors and read-out of ATHENA X-IFU", Proc. SPIE **9144**, 91445Q (2014).

[49] S. N. Richards et al., "SOFIA-HIRMES: Looking Forward to the HIgh-Resolution Mid-infrarEd Spectrometer", J. Astron. Instrum. **7**, 1–16 (2018).

[50] J. S. Adams et al., "First Operation of TES Microcalorimeters in Space with the Micro-X Sounding Rocket", J. Low Temp. Phys. (2020) 10.1007/s10909-019-02293-5.

[51] P. Zoller et al., "Quantum information processing and communication", Eur. Phys. J. D **36**, 203–228 (2005).

[52] M. Takeoka and M. Sasaki, "Discrimination of the binary coherent signal: Gaussian-operation limit and simple non-Gaussian near-optimal receivers", Phys. Rev. A **78**, 022320 (2008).

[53] G. Khoury, H. S. Eisenberg, E. J. S. Fonseca, and D. Bouwmeester, "Nonlinear Interferometry via Fock-State Projection", Phys. Rev. Lett. **96**, 203601 (2006).

[54] K. Wakui, H. Takahashi, A. Furusawa, and M. Sasaki, "Photon subtracted squeezed states generated with periodically poled KTiOPO 4", Opt. Express **15** (2007).

[55] A. E. Lita, B. Calkins, L. A. Pellouchoud, A. J. Miller, and S. W. Nam, "High-Efficiency Photon-Number-Resolving Detectors based on Hafnium Transition-Edge Sensors", Proc. Low Temp. Devices, 351–354 (2009).

[56] J. Y. Cheung et al., "The quantum candela: a re-definition of the standard units for optical radiation", J. Mod. Opt. **54**, 2–3 (2007).

[57] N. Gisin, G. Goire Ribordy, W. Tittel, and H. Zbinden, "Quantum cryptography", Rev. Mod. Phys. **74** (2002).

[58] D. Fukuda et al., "Photon number resolving detection with high speed and high quantum efficiency", Metrologia **46**, 288–292 (2009).

[59] K. Niwa, T. Numata, K. Hattori, and D. Fukuda, "Few-photon color imaging using energy-dispersive superconducting transition-edge sensor spectrometry", Nat. Publ. Gr. (2017) 10.1038/srep45660.

[60] R. H. Hadfield, "Single-photon detectors for optical quantum information applications", Nat. Photonics **3**, 696–705 (2009).

[61] G. S. Buller and R. J. Collins, "Single-photon generation and detection", Meas. Sci. Technol. **21**, 012002 (2010).

[62] C. J. Chunnilall, I. P. Degiovanni, S. Kück, I. Müller, and A. G. Sinclair, "Metrology of single-photon sources and detectors: a review", Opt. Eng. **53**, 081910 (2014).

[63] M. D. Eisaman, J. Fan, A. L. Migdall, and S. V. Polyakov, "Invited Review Article: Single-photon sources and detectors", Rev. Sci. Instrum. **82**, 071101 (2011).

[64] Hamamatsu Photonics, *Photomultiplier tubes: H12386 series*, tech. rep. (2016).

[65] ThorLabs, *ThorLabs Single Photon Counting Module*, tech. rep. (2019).

[66] Hamamatsu Photonics, *Si Avalanche Photodiode S14643-02*, tech. rep. (2019), pp. 1–16.

[67] MicroPhotonDevices, *FastGated-SPAD*, tech. rep. (2017).

[68] MicroPhotonDevices, *MicroPhotonDevices PDM-IR*, tech. rep. (2019).

[69] S. Takeuchi, J. Kim, Y. Yamamoto, and H. H. Hogue, "Development of a high-quantum-efficiency single-photon counting system", **74**, 1063–1065 (1999).

[70] D. Fukuda et al., "Titanium superconducting photon-number-resolving detector", IEEE Trans. Appl. Supercond. **21**, 241–245 (2011).

[71] A. E. Lita, A. J. Miller, and S. W. Nam, "Counting near-infrared single-photons with 95% efficiency", Opt. Express **16**, 3032–3040 (2008).

[72] F. Marsili et al., "Detecting single infrared photons with 93% system efficiency", Nat. Photonics **7**, 210–214 (2013).

[73] H. Takesue et al., "Quantum teleportation over 100 km of fiber using MoSi superconducting nanowire single-photon detectors", Conf. Lasers Electro-Optics Eur. - Tech. Dig. **2015-Augus**, 20–23 (2015).

[74] V. B. Verma et al., "High-efficiency superconducting nanowire single-photon detectors fabricated from MoSi thin-films", Opt. Express **23**, 33792 (2015).

[75] J. C. Blakesley et al., "Efficient single photon detection by quantum dot resonant tunneling diodes", Phys. Rev. Lett. **94**, 1–4 (2005).

[76] E. J. Gansen et al., "Photon-number-discriminating detection using a quantum-dot, optically gated, field-effect transistor", Nat. Photonics **1**, 585–588 (2007).

[77] A. M. Datesman et al., "Reduced-scale transition-edge sensor detectors for solar and X-ray astrophysics", IEEE Trans. Appl. Supercond. **27** (2017) 10.1109/TASC.2017.2649839.

[78] T. Gerrits, A. E. Lita, B. Calkins, and S. W. Nam, "Superconducting Transition Edge Sensors for Quantum Optics", *Supercond. Devices Quantum Opt.* (2016), 31–60.

[79] B. Calkins, A. E. Lita, A. E. Fox, and S. W. Nam, "Faster recovery time of a hot-electron transition-edge sensor by use of normal metal heat-sinks", Appl. Phys. Lett. **99** (2011) 10.1063/1.3659686.

[80] J. Zmuidzinas, "Superconducting Microresonators: Physics and Applications", Annu. Rev. Condens. Matter Phys. **3**, 169–214 (2012).

[81] J. Perido et al., "Extending KIDs to the Mid-IR for Future Space and Suborbital Observatories", J. Low Temp. Phys. (2020) 10.1007/s10909-020-02364-y.

[82] K. Rostem, S. Withington, and D. J. Goldie, "Multitone large-signal analysis of superconducting transition-edge sensors for astronomy", J. Appl. Phys. **102** (2007) 10.1063/1.2763976.

[83] D. J. Goldie, M. D. Audley, D. M. Glowacka, V. N. Tsaneva, and S. Withington, "Thermal models and noise in transition edge sensors", J. Appl. Phys. **105**, 074512 (2009).

[84] C. L. Chang et al., "Optical and thermal properties of ANL/KICP polarization sensitive bolometers for SPTpol", J. Low Temp. Phys. **167**, 865–871 (2012).

[85] D. M. Glowacka et al., "A fabrication process for microstrip-coupled superconducting transition edge sensors giving highly reproducible device characteristics", J. Low Temp. Phys. **151**, 249–254 (2008).

[86] S. J. Smith et al., "Characterizing the superconducting-to-normal transition in Mo/Au transition-edge sensor bilayers", J. Low Temp. Phys. **151**, 195–200 (2008).

[87] J. E. Sadleir et al., "Proximity effects and nonequilibrium superconductivity in transition-edge sensors", Phys. Rev. B **84**, 184502 (2011).

[88] G. Wang et al., "Mo/Au bilayer TES resistive transition engineering", IEEE Trans. Appl. Supercond. **25**, 2101105 (2015).

[89] D. Yan et al., "A two-dimensional resistor network model for transition-edge sensors with normal metal features", Supercond. Sci. Technol. **32**, 085010 (2019).

[90] D. A. Bennett, D. R. Schmidt, D. S. Swetz, and J. N. Ullom, "Phase-slip lines as a resistance mechanism in transition-edge sensors", Appl. Phys. Lett. **104** (2014) 10.1063/1.4863664.

[91] A. G. Kozorezov et al., "Microscopic model of a transition edge sensor as a weak link", IEEE Trans. Appl. Supercond. **21**, 250–253 (2011).

[92] A. G. Kozorezov et al., "Modelling the resistive state in a transition edge sensor", J. Low Temp. Phys. **167**, 114–120 (2012).

[93] J. C. Cuevas and F. S. Bergeret, "Magnetic Interference Patterns and Vortices in Diffusive SNS Junctions", Phys. Rev. Lett. **99**, 217002 (2007).

[94] D. S. Swetz, D. A. Bennett, K. D. Irwin, D. R. Schmidt, and J. N. Ullom, "Current distribution and transition width in superconducting transition-edge sensors", Appl. Phys. Lett. **101**, 242603 (2012).

[95] A. Bergen et al., "Design and validation of a large-format transition edge sensor array magnetic shielding system for space application", Rev. Sci. Instrum. **87** (2016) 10.1063/1.4962157.

[96] B. D. Jackson, *Requirements for the shielding of the SAFARI TES and SQUIDs against quasi-static magnetic fields*, tech. rep. (2013).

[97] S. J. Smith et al., "Implications of weak-link behavior on the performance of Mo/Au bilayer transition-edge sensors", J. Appl. Phys. **114**, 074513 (2013).

[98] F. Chiodi et al., "Geometry-related magnetic interference patterns in long S N S Josephson junctions", Phys. Rev. B **86**, 064510 (2012).

[99] R. A. Hijmering et al., "Effects of Magnetic Fields on Highly Sensitive TiAu TES Bolometers", IEEE Trans. Appl. Supercond. **23**, 2101505 (2013).

[100] Y. Hatsukade, T. Inaba, Y. Maruno, and S. Tanaka, "Mobile cryocooler-based SQUID NDE system utilizing active magnetic shielding", IEEE Trans. Appl. Supercond. **15**, 723–728 (2005).

[101] S. J. Smith et al., "Characterization of Mo/Au Transition-Edge Sensors with Different Geometric Configurations", J. Low Temp. Phys. **176**, 356–362 (2014).

[102] A. Catalano et al., "Characterization and physical explanation of energetic particles on Planck HFI instrument", J. Low Temp. Phys. **176**, 773–786 (2014).

[103] S. L. Stever, F. Couchot, N. Coron, R. M. J. Janssen, and B. Maffei, "A new pulse shape description for alpha-particle pulses in a highly-sensitive sub-Kelvin bolometer", ArXiv e-prints (2018) 10.1117/12.2313968.

[104] S. Molendi et al., *AREMBES (ATHENA Radiation Environment Models and X-Ray Background Effects Simulators): Radiation Background Data Analysis & Lessons Learned from Previous X-ray Missions*, tech. rep. (2017).

[105] T. M. Lanting et al., "A frequency-domain SQUID multiplexer for arrays of transition-edge superconducting sensors", IEEE Trans. Appl. Supercond. **13**, 626–629 (2003).

[106] R. H. den Hartog et al., "Frequency domain multiplexed readout of TES detector arrays with baseband feedback", IEEE Trans. Appl. Supercond. **21**, 289–293 (2011).

[107] K. Sakai et al., "Study of Dissipative Losses in AC-Biased Mo/Au Bilayer Transition-Edge Sensors", J. Low Temp. Phys. **193**, 356–364 (2018).

[108] J. D. Gard et al., "A Scalable Readout for Microwave SQUID Multiplexing of Transition-Edge Sensors", J. Low Temp. Phys. **193**, 485–497 (2018).

[109] A. S. Kher, "Superconducting Nonlinear Kinetic Inductance Devices", PhD thesis (2017).

[110] S. J. Smith et al., "Toward 100,000-Pixel Microcalorimeter Arrays Using Multi-absorber Transition-Edge Sensors", J. Low Temp. Phys. (2019) 10.1007/s10909-020-02362-0.

[111] K. D. Usadel, "Generalized diffusion equation for superconducting alloys", Phys. Rev. Lett. **25**, 507–509 (1970).

[112] R. C. Harwin, D. J. Goldie, and S. Withington, "Modelling proximity effects in transition edge sensors to investigate the influence of lateral metal structures", Supercond. Sci. Technol. **30**, 084001 (2017).

[113] L. N. Cooper, "Bound Electron Pairs in a Degenerate Fermi Gas", Phys. Rev. **104**, 1189–1190 (1956).

[114] L. N. Cooper, "Superconductivity in the neighbourhood of metallic contacts", Phys. Rev. Lett. **6**, 689–690 (1961).

[115] C. W. J. Beenakker, "Random-Matrix Theory of Quantum Transport", ArXiv e-prints **69**, 85 (1996).

[116] A. A. Golubov, M. Y. Kupriyanov, and E. Il'ichev, "The current-phase relation in Josephson junctions", Rev. Mod. Phys. **76**, 411–469 (2004).

[117] N. W. Ashcroft and N. D. Mermin, *Solid State Physics* (Brooks Cole, 1976).

[118] A. M. Kadin, "Spatial Structure of the Cooper Pair", J. Supercond. Nov. Magn. **20**, 285–292 (2007).

[119] S. Zhao, D. J. Goldie, C. N. Thomas, and S. Withington, "Calculation and measurement of critical temperature in thin superconducting multilayers", Supercond. Sci. Technol. **31** (2018).

[120] Y. V. Fominov and M. V. Feigel'man, "Superconductive properties of thin dirty SN bilayers", Phys. Rev. B **63**, 094518 (2001).

[121] R. A. Hijmering et al., "Comparison of the Effects of Magnetic Field on Low Noise MoAu and TiAu TES Bolometers", J. Low Temp. Phys. **176**, 316–322 (2014).

[122] K. K. Likharev, "Superconducting weak links", Rev. Mod. Phys. **51**, 101–159 (1979).

[123] J. P. Heida, B. J. van Wees, T. M. Klapwijk, and G. Borghs, "Nonlocal supercurrent in mesoscopic Josephson junctions", Phys. Rev. B **57**, R5618 (1998).

[124] A. S. Vasenko, A. A. Golubov, M. Y. Kupriyanov, and M. Weides, "Properties of tunnel Josephson junctions with a ferromagnetic interlayer", Phys. Rev. B **77**, 134507 (2008).

[125] W. Belzig, F. K. Wilhelm, C. Bruder, G. Schön, and A. D. Zaikin, "Quasiclassical Green's function approach to mesoscopic superconductivity", Superlattices Microstruct. **25**, 1251 (1999).

[126] G. Brammertz et al., "Generalised proximity effect model in superconducting bi- and trilayer films", J. Appl. Phys. **90**, 355–364 (2001).

[127] A. V. Zaitsev, "Quasiclassical equations of the theory of superconductivity for contiguous metals and the properties of constricted microcontacts", Zh. Eksp. Teor. Fiz. **86**, 1742 (1984).

[128] M. A. Lindeman et al., "Percolation model of excess electrical noise in transition-edge sensors", Nucl. Instruments Methods Phys. Res. A **559**, 715–717 (2006).

[129] K. Rostem et al., "Multitone harmonic-balance simulations of an x-ray transition-edge sensor characterized at BESSY II", J. Appl. Phys. **108**, 024509 (2010).

[130] L. Gottardi et al., "Development of TES-based detectors array for the X-ray Integral Field Unit (X-IFU) on the future X-Ray Observatory Athena.", Proc. SPIE **9144**, 91442M (2014).

[131] A. G. Kozorezov et al., "Modelling the resistive state in a transition edge sensor", Appl. Phys. Lett. **99**, 063503 (2011).

[132] M. Y. Kupriyanov and V. F. Lukichev, "Influence of boundary transparency on the critical current of "dirty" SS'S structures", Sov. Phys. JETP **67**, 1163–8 (1988).

[133] W. T. Coffey, Y. P. Kalmykov, S. V. Titov, and L. Cleary, "Smoluchowski equation approach for quantum Brownian motion in a tilted periodic potential", Phys. Rev. E **78**, 031114 (2008).

[134] W. Gautschi and J. Slavik, "On the Computation of Modified Bessel Function Ratios", Am. Math. Soc. **32**, 865–875 (1978).

[135] T. Kuhn, V. Anghel, J. P. Pekola, M. Manninen, and Y. M. Galperin, "Heat transport in ultrathin dielectric membranes and bridges", Phys. Rev. B **70** (2004) 10.1103/PhysRevB.70.125425.

[136] K. Rostem, D. M. Glowacka, D. J. Goldie, and S. Withington, "Thermal conductance measurements for the development of ultra low-noise transition-edge sensors with a new method for measuring the noise equivalent power", Proc. SPIE **7020**, 70200L (2008).

[137] D. J. Goldie, A. V. Velichko, D. M. Glowacka, and S. Withington, "Towards ultra-low-noise MoAu transition edge Sensors", J. Low Temp. Phys. **167**, 248–253 (2012).

[138] L. Gottardi et al., "Josephson effects in an alternating current biased transition edge sensor", Appl. Phys. Lett. **105**, 162605 (2014).

[139] R. Gross and A. Marx, "Applied Superconductivity: Josephson Effect and Superconducting Electronics", (2005).

[140] L. Gottardi et al., "Study of the dependency on magnetic field and bias voltage of an ac-biased TES microcalorimeter", J. Low Temp. Phys. **167**, 214–219 (2012).

[141] A. D. Beyer et al., "Effect of Mo / Cu Superconducting Bilayer Geometry Sensor Performance", IEEE Trans. Appl. Supercond. **23**, 3–6 (2013).

[142] R. C. Harwin et al., "Proximity effect model for x-ray transition edge sensors", High Energy, Opt. Infrared Detect. Astron. VIII, 49 (2018).

[143] B. Cabrera et al., "Detection of single infrared, optical, and ultraviolet photons using superconducting transition edge sensors", Appl. Phys. Lett. **73**, 735–737 (1998).

[144] B. Calkins et al., "High quantum-efficiency photon-number-resolving detector for photonic on-chip information processing", Opt. Express **21**, 22657 (2013).

[145] A. Lamas-Linares et al., "Nanosecond-scale timing jitter for single photon detection in transition edge sensors", Appl. Phys. Lett. **102**, 1–5 (2013).

[146] A. E. Lita et al., "Tuning of tungsten thin film superconducting transition temperature for fabrication of photon number resolving detectors", IEEE Trans. Appl. Supercond. **15**, 3528–3531 (2005).

[147] C.-L. Kuo et al., "Antenna-coupled TES bolometer arrays for CMB polarimetry", Proc. SPIE, 70201I–70201I–14 (2009).

[148] G. Fujii et al., "Thin gold covered titanium transition edge sensor for optical measurement", J. Low Temp. Phys. **167**, 815–821 (2012).

[149] A. Luukanen et al., "Transition edge microcalorimeter in Corbino disk geometry for XEUS NFI", Proc. Work. XEUS (2002).

[150] A. S. Hoover et al., "Microcalorimeter arrays for ultra-high energy resolution X- and gamma-ray detection", J. Radioanal. Nucl. Chem. **282**, 227–232 (2009).

[151] D. J. Goldie, D. M. Glowacka, K. Rostem, and S. Withington, "Transition Edge Sensor Thermometry for On-chip Materials Characterization", ISSTT Proc. **21**, 6 (2010).

[152] M. A. Lindeman et al., "Characterization and reduction of noise in Mo/Au transition edge sensors", Nucl. Instruments Methods Phys. Res. A **520**, 348–350 (2004).

[153] D. M. Glowacka, M. Crane, D. J. Goldie, and S. Withington, "A fabrication route for arrays of ultra-low-noise MoAu transition edge sensors on thin silicon nitride for space applications", J. Low Temp. Phys. **167**, 516–521 (2012).

[154] A. R. Miniussi et al., "Performance of an X-ray microcalorimeter with a 240 um absorber and a 50 um TES bilayer", J. Low Temp. Phys. **193**, 337–343 (2018).

[155] C. A. Jhabvala et al., "Kilopixel backshort-under-grid arrays for the primordial inflation polarization explorer", Proc. SPIE, 91533C–91533C (2014).

[156] C. Pobes et al., "Development of Cryogenic X-Ray Detectors Based on Mo/Au Transition Edge Sensors", IEEE Trans. Appl. Supercond. **27**, 2101505 (2017).

[157] H. Akamatsu et al., "Performance of TES X-ray microcalorimeters with AC bias read-out at MHz frequencies", J. Low Temp. Phys. **176**, 591–596 (2014).

[158] C. N. Bailey et al., "Implications of Weak Link Effects on Thermal Characteristics of Transition-Edge Sensors", J. Low Temp. Phys. **167**, 121–128 (2012).

[159] F. W. Carter et al., "Tuning SPT-3G Transition-Edge-Sensor Electrical Properties with a Four-Layer Ti–Au–Ti–Au Thin-Film Stack", J. Low Temp. Phys., 1–8 (2018).

[160] V. Yefremenko et al., "Impact of Electrical Contacts Design and Materials on the Stability of Ti Superconducting Transition Shape", J. Low Temp. Phys. **193**, 732–738 (2018).

[161] M. Piat et al., "QUBIC: The Q&U bolometric interferometer for cosmology", J. Low Temp. Phys. **167**, 872–878 (2012).

[162] A. J. Anderson et al., "Performance of Al–Mn Transition-Edge Sensor Bolometers in SPT-3G", J. Low Temp. Phys., 1–9 (2019).

[163] A. S. Bergman et al., "280 GHz Focal Plane Unit Design and Characterization for the Spider-2 Suborbital Polarimeter", J. Low Temp. Phys. **193**, 1075–1084 (2018).

[164] K. T. Crowley et al., "Advanced ACTPol TES Device Parameters and Noise Performance in Fielded Arrays", Proc. SPIE (2018).

[165] K. Nandra et al., "The Hot and Energetic Universe: A White Paper presenting the science theme motivating the Athena+ mission", ArXiv e-prints, 1–18 (2013).

[166] X. Barcons et al., "Athena: the X-ray observatory to study the hot and energetic Universe", J. Phys. Conf. Ser. **610**, 012008 (2015).

[167] D. Barret et al., "The Hot and Energetic Universe: The X - ray Integral Field Unit (X - IFU) for Athena+", ArXiv e-prints, 1–17 (2013).

[168] L. Dunlop, D. M. Glowacka, D. J. Goldie, S. Withington, and G. Yassin, "Characterising the electrothermal properties of microstrip-coupled TES detectors", Proc. SPIE, 627507 (2006).

[169] S. Zhang et al., "Mapping of the resistance of a superconducting transition edge sensor as a function of temperature, current, and applied magnetic field", J. Appl. Phys. **121**, 074503 (2017).

[170] M. Kofferlein, "KLayout: Free Open Source Software for HW design", (2018).

[171] Lakeshore Cryotronics, *Hall Generators: application note*, tech. rep. (Lakeshore Cryotronics, 2010).

[172] R. C. Harwin, *2Dex Hall Sensors: Planar Hall Effect Investigation in Cryogenic Environment*, tech. rep. (2019).

[173] D. Drung, J. Beyer, M. Peters, J.-H. Storm, and T. Schurig, "Novel SQUID current sensors with high linearity at high frequencies", IEEE Trans. Appl. Supercond. **19**, 772–777 (2009).

[174] K. D. Irwin, "Phonon-Mediated Particle Detection Using Superconducting Tungsten Transition-Edge Sensors", PhD thesis (1995).

[175] S. Withington, E. Williams, D. J. Goldie, C. N. Thomas, and M. Schneiderman, "Thermal elastic-wave attenuation in low-dimensional SiNx bars at low temperatures", J. Appl. Phys. **122**, 054504 (2017).

[176] M. A. Lindeman et al., "Impedance measurements and modeling of a transition-edge-sensor calorimeter", Rev. Sci. Instrum. **75**, 1283–1289 (2004).

[177] N. Wakeham et al., "TES pixel optimization for the ATHENA X-IFU instrument", Low Temp. Detect. (2019).

[178] J. F. Cochran and D. E. Mapother, "Superconducting Transition in Aluminium", Phys. Rev. **111**, 132–142 (1958).

[179] M. Bahte, F. Herrmann, and P. Schmuser, "Magnetization and Susceptibility Measurements on Niobium samples for Cavity Production", Part. Accel. **60**, 121–133 (1998).

[180] K. Chang, *Microwave Solid-State Circuits and Applications* (1994), pp. 75–95.

[181] M. A. Washington and T. A. Fulton, "Observation of flux trapping threshold in narrow superconducting thin films", Appl. Phys. Lett. **40**, 848–850 (1982).

[182] Q. Geng and E. Goto, "Flux trapping in superconducting thin films in weak magnetic fields", J. Appl. Phys. **74**, 6293–6296 (1993).

[183] A. L. Fetter and P. C. Hohenberg, "The mixed state of thin superconducting films in perpendicular fields", Phys. Rev. **159**, 330–343 (1967).

[184] E. Figueroa-Feliciano, “Complex microcalorimeter models and their application to position-sensitive detectors”, J. Appl. Phys. **99**, 114513 (2006).